

Polarization Switching in
Ferroelectric Films of P(VDF-TrFE) Copolymer

Dissertation
zur Erlangung des Grades
des Doktors der Ingenieurwissenschaften
der Naturwissenschaftlich-Technischen Fakultät II
- Physik und Mechatronik -
der Universität des Saarlandes

von
Manfang Mai

Saarbrücken
2013

Tag des Kolloquiums: 22.11.2013

Dekan: Prof. Dr. C. Wagner

Mitglieder des
Prüfungsausschusses: Prof. Dr.-Ing. habil. H. Kliem
Hon.-Prof. Dr. rer. nat. W. Arnold
Prof. Dr.-Ing. C. Xu
Dr.-Ing. A. Tschöpe

Zusammenfassung

Das ferroelektrische Material Poly(vinylidenfluorid/trifluoroethylen) [P(VDF-TrFE)] ist ein vielversprechendes Material für eine Anwendung in nichtflüchtigen Speichern. In dieser Arbeit wird das Umschalten des Polarisationszustandes in P(VDF-TrFE) Filmen, welche als Metall-Ferroelektrikum-Metall Strukturen aufgebaut sind, untersucht.

Die Proben werden mit der Langmuir-Blodgett (LB) Technik und durch ein Spin Verfahren mit einer großen Dickenvariation von Nanometern bis Mikrometern hergestellt, was eine Untersuchung von Finite-Size Effekten erlaubt. Das ferroelektrische Verhalten von sowohl LB Filmen als auch aufgeschleuderten Filmen wird untersucht und verglichen unter Berücksichtigung von Hystereschleifen, Koerzitivfeldern, remanenter Polarisation, transienter Polarisation, Speichereigenschaften und Alterungsverhalten. Der Einfluss von Elektrodeneffekten und dielektrischen Schichten auf die ferroelektrische Systemantwort wird diskutiert. Es wird gezeigt, dass LB- und Spin-Filme vergleichbares Schaltverhalten aufweisen. Die Ergebnisse zeigen, dass Proben mit einer Dicke von 60-100nm günstig für Niederspannungsanwendungen mit einer relativ schnellen Schaltgeschwindigkeit sind.

Der Effekt der Polarisationsrelaxation, welcher durch einen stetigen Anstieg der Polarisation in den transienten Schaltkurven charakterisiert wird, entspricht einem ausgeprägten Kohlrausch-Verhalten bzw. $t^{-\alpha}$ -Gesetz der Stromdichte im Langzeitbereich. Wir beschreiben dieses Verhalten unter Benutzung eines Modells bestehend aus asymmetrischen Doppelmuldenpotentialen mit einer Verteilung von Relaxationszeiten, in welchen Dipole thermisch aktiviert zwischen zwei Minima fluktuieren. Im Depolarisationsstrom wird ein ausgeprägtes Minimum über der Zeit, welches begründet ist durch eine Injektion von Elektronen und ihr anschließendes Trappen und Austrappen, beobachtet.

Ein interessanter Dickeneffekt wird im Verlauf des transienten Schaltstromes gefunden. Es zeigt sich, dass das Erscheinen eines Strommaximums während des Umschaltens der Polarisation von der Probendicke abhängt. Darüberhinaus ist die Form des Schaltstromes feld- und temperaturabhängig. Eine Änderung der Form des Schaltstromes deutet auf eine Veränderung des Schaltmechanismus hin.

Die wichtigen Merkmale, welche den Phasenübergang in P(VDF-TrFE) charakterisieren wie die thermische Hysterese, die Temperaturabhängigkeit der Hystereseschleife und die remanente Polarisation, werden untersucht. PVDF Filme, hergestellt mit der LB Technik, werden im nanoskaligen Dickenbereich untersucht. In dem Dickenintervall von $\Delta l = 13 - 20nm$ verschwindet der ferroelektrische Phasenübergang und ein

Übergang vom ferroelektrischen zum pyroelektrischen Zustand findet bei Zunehmender Schichtdicke statt. Dieses Phänomen wird durch den Finite-Size Effekt auf der Nanoskala unter Benutzung der Landau-Ginzburg-Devonshire (LGD) Theorie und durch das Weiss Mean-Field Modell erklärt. Zusätzlich wird der thermische Barkhausen Effekt, welcher mit einer Änderung der Polarisierung verknüpft ist und welcher zumeist bei der Phasenübergangstemperatur erscheint, zum ersten Mal in P(VDF-TrFE) Copolymerfilmen beobachtet.

Abstract

Ferroelectric material poly(vinylidene fluoride/trifluoroethylene) [P(VDF-TrFE)] is a promising candidate for nonvolatile memory applications. In this thesis, polarization switching in P(VDF-TrFE) films as metal-ferroelectric-metal (MFM) structure is investigated.

The samples are prepared by Langmuir-Blodgett (LB) deposition and spin coating with a large thickness range from nanometer to micron, which permits a study of finite size effects. Ferroelectric behavior of both LB films and spun films are investigated and compared in terms of hysteresis loops, coercive fields and remanent polarization, transient polarization, retention properties and fatigue behavior. The influences of electrode effects and dielectric layer on the ferroelectric responses are discussed. It is shown that both types of films exhibit similar switching behavior. The results suggest that samples in the range of 60-100nm are attractive for low voltage operation with a relatively fast switching speed.

The polarization relaxation effect characterized by a continuous increase of polarization in the switching transients corresponds to a $t^{-\alpha}$ law of the current density in the long time range, showing a pronounced Kohlrausch behavior. We described this behavior using an asymmetric double well potential model with a distribution of relaxation times in which dipoles are fluctuating thermally activated between the two minima. Charge injection sets in at higher temperature during charging. A pronounced minimum in time is observed in the depolarization current, which is due to injection of electrons and their subsequent trappings and retrappings.

An interesting size effect is found in the profiles of the switching current transients, that is, whether there is a current maximum occurs during polarization switching depends on the sample thickness. Moreover, the switching current profile is also field and temperature dependent. The change of switching current profile indicates a transformation of switching mechanism.

The important features which characterize phase transition in P(VDF-TrFE) including dielectric thermal hysteresis, temperature dependence of hysteresis loop and remanent polarization are examined. The PVDF LB films are investigated at the nanoscale. In the film thickness interval of $\Delta l = 13 - 20nm$, ferroelectric phase transition disappears and transition from ferroelectric to pyroelectric state takes place. This phenomenon is explained by the finite size effect at the nanoscale using Landau-Ginzburg-Devonshire (LGD) theory and by the Weiss mean field model. Furthermore, thermal Barkhausen effect is observed in P(VDF-TrFE) copolymer films for the first

time, which is connected to the change of polarization and occurs mostly at the phase transition temperature.

Contents

Contents	i
1 Introduction	1
1.1 Motivation	1
1.2 Overview of thesis	3
2 Theoretical Basics	5
2.1 Ferroelectricity	5
2.2 Domain	7
2.3 Phenomenological theory	11
2.4 Properties of P(VDF-TrFE) copolymers	13
2.5 Applications	15
2.6 List of important material data	17
3 Experimental details	18
3.1 Sample preparation	18
3.1.1 Langmuir-Blodgett technique	18
3.1.2 Spin coating method	21
3.2 Annealing and morphology	21
3.3 Thickness determination	23
3.4 Electrical measurements	26
3.4.1 <i>CV</i> measurements	27
3.4.2 Hysteresis loop measurements	28
3.4.3 Time domain polarization	29
3.4.4 Current transients	31
3.4.5 Retention and fatigue tests	31
3.5 High and low temperature measurement setups	32

4	Ferroelectric properties of P(VDF-TrFE) thin films	35
4.1	Comparative study of LB films and spun films	35
4.1.1	Hysteresis loops	36
4.1.2	Coercive fields and remanent polarization	42
4.1.3	Transient polarization	44
4.1.4	Retention properties and fatigue behavior	53
4.2	Electrode effects	57
4.2.1	The influence of electrode effects on $P(E)$ and CV curves	58
4.2.2	The influence of electrode effects on switching transients	61
4.3	Influence of dielectric layer	64
4.4	Frequency and amplitude dependence of $P(E)$	67
4.4.1	Frequency dependence of $P(E)$	67
4.4.2	Amplitude dependence of $P(E)$	74
4.5	Conclusions	76
5	Polarization relaxation and charge injection	77
5.1	Kohlrausch relaxation	77
5.2	Polarization and depolarization transients	80
5.3	The physical model for the Kohlrausch relaxations	88
5.4	Temperature dependence and charge injection	93
5.5	Conclusions	99
6	Switching mechanisms in P(VDF-TrFE) thin films	100
6.1	Overview of existing theoretical models for ferroelectric switching	100
6.2	Thickness and field dependence of switching process	108
6.3	Temperature dependence of switching process	113
6.4	Extrinsic switching vs. intrinsic switching	125
6.5	Conclusions	130
7	Phase transition	132
7.1	Phase transition in P(VDF-TrFE) thin films	132
7.2	The thickness dependence of the phase transition temperature in PVDF	138
7.2.1	Thermal hysteresis and butterfly hysteresis	138
7.2.2	Landau-Ginzburg-Devonshire theory	141
7.2.3	The Weiss mean field model	143
7.3	Observation of Barkhausen effect	146
7.3.1	Barkhausen pulses of P(VDF-TrFE) on polyimide substrate	147

CONTENTS

7.3.2	Barkhausen pulses of P(VDF-TrFE) on glass substrate	151
7.4	Conclusions	153
8	Summary and Outlook	154
	Bibliography	158
	Publications	176
	Acknowledgments	178

Chapter 1

Introduction

1.1 Motivation

In many applications, there is a demand towards small size ferroelectric driven by miniaturized electronics. For nonvolatile memory devices, low-voltage operation is crucial which requires fabrication of ferroelectric films as thin as possible [1]. Generally, ferroelectrics exhibit a striking finite size effect [2]. The switching time and the coercive field increase with decreasing film thickness while reversely the remanent polarization and the phase transition temperature decrease with decreasing thickness. Therefore, the investigated ferroelectric films should be thin enough for low operation voltage at the same time they should have sufficient and stable ferroelectric properties to maintain the memory functionality.

Polyvinylidene fluoride (PVDF) and its copolymer with trifluoroethylene (TrFE) is a promising material for the next generation nonvolatile high-density memory applications which can replace perovskite ceramics currently used in the commercial ferroelectric random access memories (FRAMs) [3-5]. It has many attractive advantages including low temperature processing, low-cost solution processing, outstanding chemical stability and nontoxicity [6,7]. In the past few years, there have been considerable research activities to combine P(VDF-TrFE) films as nonvolatile memory cells such as metal-ferroelectric-insulator-semiconductor (MFIS) diode [8-12] and ferroelectric-field-effect-transistor (FeFET) [13-16]. The key issues which include switching time, switching voltage, retention and endurance still need to be overcome. Consequently, the study of the switching kinetics in P(VDF-TrFE) films is critically important in understanding the switching behavior and the switching processes. The material quality in terms of processing and properties could be evaluated and improved.

The discovery of Langmuir-Blodgett (LB) ferroelectric polymer films in 1995 [17] led to investigation of ferroelectric properties at the nanoscale. For P(VDF-TrFE) films, the ferroelectricity and polarization switching have been found for two monolayers ($l = 1nm$) [18]. It opened the way for investigation of finite size effect at the nanoscale. Since then, it has been a subject of intensive study not only in theoretical aspects but also in technical applications. The results on P(VDF-TrFE) LB films provide many new insights into the fundamental physics: the existence of two-dimensional ferroelectrics with nearly absence of finite size effects on the bulk transition (a first order phase transition with a transition temperature nearly equal to the bulk value) [18], the transition from extrinsic (switching with nucleation and domain wall motion) to intrinsic (switching without domain) ferroelectric switching in the context of Landau-Ginzburg mean-field theory below a thickness of 15nm [19], etc. However, there have been strong debates of the theoretical models used to explain the experiments. Scott pointed out that the presence of two apparent phase transition temperatures interpreted as true two-dimensional surface ferroelectricity by the Moscow-Nebraska group, instead, can be explained by the seminal Tilly-Zeks theory and its extension by Duiker to first order phase transition [20]. Several groups spoke against the intrinsic nature of the switching as the experiments are lack of several key features of intrinsic switching [21-25]. Lately, the Moscow-Nebraska group demonstrated some new experiment evidences to support their claim of domain-free Landau switching in P(VDF-TrFE) LB films [26,27] as well as in ultrathin $BaTiO_3$ films [28], suggesting homogeneous switching in ultrathin films is a common phenomenon for all ferroelectric materials. Since ferroelectric nonvolatile memories will be about 80-200nm thick [29], the investigation of the existence of intrinsic switching is primarily of academic interest. From technical's point of view, switching behavior of P(VDF-TrFE) LB films and spun films is investigated and compared in the thickness range of 30-300nm in the thesis. For fundamental physics, we investigate PVDF LB films at the nanoscale (7-69nm) to study the finite size effect in terms of phase transition. Up to date, the switching process in P(VDF-TrFE) thin films is not fully understood yet. The explanations for the switching behavior are still controversial.

It is the aim of this thesis to investigate the polarization switching in P(VDF-TrFE) thin films, which is very critical for intentional design and preparation of materials for various purposes. First, P(VDF-TrFE) thin films prepared by both Langmuir-Blodgett technique and spin coating method are compared at the same thickness scale in terms of coercive field, remanent polarization, switching time, switching voltage, retention and fatigue behavior, providing necessary information for the ferroelectric copolymer

films used as nonvolatile memory elements. Later, we focus on the physical nature of some ferroelectric phenomena. Polarization relaxation, switching mechanism and phase transition are investigated experimentally and theoretically.

1.2 Overview of thesis

The thesis is organized as following:

Chapter 2 presents a general theoretical basics for the conducted research. The fundamental concepts including ferroelectricity, domain, phenomenological theory as well as the state-of-the-art applications of P(VDF-TrFE) copolymers are introduced.

Chapter 3 gives a description for the sample preparation and characterization. The two preparation methods including Langmuir-Blodgett deposition and spin coating are introduced. The measurement methods as well as the measurement systems are presented in detail.

Chapter 4 demonstrates a comprehensive study of ferroelectric properties for P(VDF-TrFE) thin films. The ferroelectric behavior of LB films and spun films are investigated and compared through polarization switching measurements. The hysteresis loops, coercive fields and remanent polarization, transient polarization, retention properties and fatigue behavior are analyzed systematically. Moreover, we discuss the influences of electrode effects and dielectric layer on the ferroelectric responses, as well as the frequency and amplitude dependence of hysteresis loops.

In chapter 5, we study the polarization relaxation effects and charge injection. The polarization relaxation in time domain corresponds to a $t^{-\alpha}$ law of the current density in the long time range, showing a pronounced Kohlrausch behaviour. This $t^{-\alpha}$ current at a constant electric field is independent of the sample thickness and saturates at high fields. A physical model is proposed to explain this behavior. Charge injection sets in with increasing temperature. A space charge relaxation current with a pronounced minimum in time is observed in the depolarization current. The physical origin corresponding to this behavior is discussed.

In chapter 6, the switching mechanisms in P(VDF-TrFE) thin films are investigated. We begin with a summary of the existing theoretical models for ferroelectric switching. Then we examine the switching process of ferroelectric P(VDF-TrFE) thin films mainly through switching current transient measurements. The switching current profile is thickness, field and temperature dependent, showing a strong size effect. This chapter finishes with a discussion on the possibility of determination of extrinsic/intrinsic switching.

In chapter 7, the phase transition behavior in PVDF and P(VDF-TrFE) copolymer films is studied. The important features which characterize phase transition including dielectric thermal hysteresis, temperature dependence of hysteresis loop and remanent polarization are examined. The thickness dependence of the phase transition temperature in PVDF is evaluated. The film thickness interval, where ferroelectric phase transition disappears and transition from ferroelectric to pyroelectric state (the melting temperature is lower than the possible phase transition point) takes place is obtained. This phenomenon is explained by the finite size effect at the nanoscale using Landau-Ginzburg-Devonshire (LGD) theory and by the Weiss mean field model. The thermal Barkhausen effect in P(VDF-TrFE) copolymer films is observed for the first time.

Chapter 8 concludes the results and achievements in this thesis. The recommendations for future work are stated.

Chapter 2

Theoretical Basics

A general review of the theoretical background is presented in this chapter.

2.1 Ferroelectricity

The term ferroelectricity is used to describe a material which does not have a center of symmetry or electric dipole moment above a certain temperature called the Curie temperature [30]. The distinguishing feature of ferroelectricity is that the spontaneous polarization in ferroelectric materials can be switched upon the application of an external electric field and can store a remanent polarization after the removal of the field.

Ferroelectricity was discovered in 1920 in Rochelle salt by Valasek [31]. This effect was not considered for some time since that Rochelle salt lost its ferroelectric properties if the composition was slightly changed, making it rather unattractive for industrial applications. It wasn't until a few decades ago that the study of ferroelectricity accelerated rapidly with the discovery of barium titanate. Later it came a period of rapid proliferation with more than 100 new ferroelectric materials leading to their wide use as capacitors, transducers and thermistors, accounting for about one-half of electroceramic components [32].

For a ferroelectric, the charge displacement under an applied electric field consists of a linear and a nonlinear part,

$$D = \varepsilon_0 \varepsilon_r E + P \tag{2.1}$$

where ε_0 and ε_r are the dielectric permittivities of free space and the ferroelectric material, respectively. P is the polarization stemming from the permanent dipole moments

which can change their orientation depending on the direction of the field E . Electronic polarization (present in all materials) and ionic polarization (present only in materials made of two or more different kinds of atoms that form ions due to the sharing of the valence electrons of one or more atoms with the others [33]) contribute to the linear part in respond to the electric field. They are classified as induced dipole moments which are slightly dependent on temperature because they are intramolecular phenomena. The permanent polarization P is strongly temperature dependent since the orientation of dipoles involves the energy required to overcome the resistance of the surrounding molecules. It is determined by the total dipole moment per unit volume, i.e.,

$$P = \frac{\sum_i \mu_i}{V} \quad (2.2)$$

with μ_i the dipole moment and V the volume.

In analogy to ferromagnetics, the dielectric displacement D and polarization P in ferroelectrics varying with the electric field E is in the same general manner as the magnetic flux density B and the magnetic polarization I varying with the magnetic field H , yielding a hysteresis loop. A typical hysteresis loop is shown schematically in Fig. 2.1. Several distinctive characteristics can be described here. The saturation polarization P_s , is the linear extrapolation at zero field of the high field polarization which refers to the total polarization attributable to the switching of the spontaneous polarization. The remanent polarization P_r , is the polarization at zero field. The coercive field E_c , is the minimum field required to switch polarization and it is determined by the half width of the hysteresis loop. In an ideal single crystal, P_r and P_s are identical. In polycrystalline ferroelectric, P_r is smaller than P_s because when the field is reduced to zero, some dipoles may return to their original positions (back switching) due to the local elastic or electric fields [34].

Starting from an original state (point O), the polarization first increases linearly with the field when the field is small. This is due mainly to field induced polarization since the field is not large enough to cause orientation of dipoles. At higher fields, polarization increases nonlinearly with increasing field because dipoles start to orient toward the direction of the field. At high fields, polarization reaches a saturation value in which most dipoles are aligned toward the direction of the applied field (point A). As the field is gradually decreased (A \rightarrow B), the polarization decreases and remains P_r at zero field (point B). After a field applied in the opposite direction, the polarization diminishes and comes to zero value at $-E_c$ (point C). Finally, if a sufficiently strong electric field is applied in the reverse direction, the polarization will reach its maximum

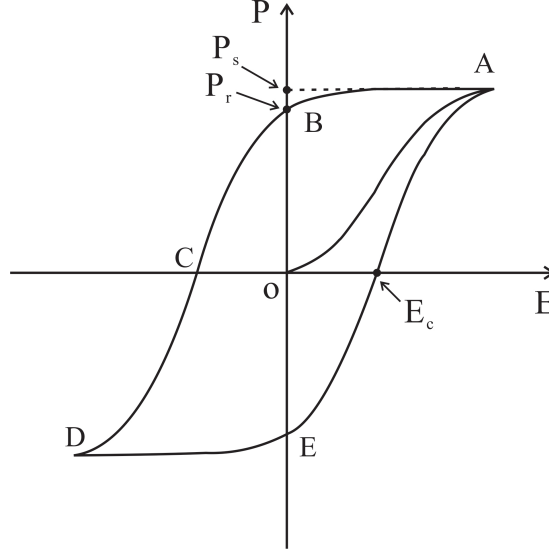


Figure 2.1: Schematic diagram of a typical ferroelectric hysteresis loop. The switching process is shown from an original state ($P = 0$).

value again in the opposite direction (point D) followed by a remanent polarization $-P_r$ in the opposite sign after the removal of the field (point E). Ferroelectric switching results in the majority of the dipoles aligned with the external field. The total area of the hysteresis loop corresponds to the energy loss during switching.

2.2 Domain

Domain in a ferroelectric material is the region that the dipole moments align in one of the symmetry-permitted polarization directions [35]. The interfaces between adjacent domains are called domain walls, which have a typical thickness of 1-2 unit cells. Domains and domain walls are fundamental issues in ferroelectrics which dominate their physical and electrical properties such as strain, switching, aging and fatigue.

Domain structures in ferroelectric materials are formed in an attempt to minimize the free energy of the system. Considering the change of spontaneous polarization at inhomogeneities, the spatial variation of the dielectric displacement D and the charge density ρ (free charges in the metal electrodes and bound charges inside the material) must satisfy Poissons equation [36],

$$\text{div}\vec{D} = \rho \quad (2.3)$$

With equation (2.1), we get the following one with respect to the divergence of the electric field and the ferroelectric polarization,

$$\operatorname{div}\vec{E} = \frac{1}{\varepsilon_0\varepsilon_r} \left(\rho - \operatorname{div}\vec{P} \right) \quad (2.4)$$

In an ideal infinite ferroelectric the spontaneous polarization \vec{P} is uniform so that $\operatorname{div}\vec{E} = \frac{\rho}{\varepsilon_0\varepsilon_r}$, as in non-ferroelectric dielectrics. In finite ferroelectric, \vec{P} decreases to zero at the surface or may differ from the perfect crystal in the neighborhood of defects, therefore $\operatorname{div}\vec{P}$ acts as the source for a depolarization field. In contrast to the magnetic equivalent, this depolarization field can be compensated by the flow of free charges inside the crystal and outside the surrounding medium

$$\delta_s = \int_0^t \sigma \cdot E dt \quad (2.5)$$

where δ_s is the surface charge density and σ is the electric conductivity of the crystal. Since the conductivities of ferroelectric materials and the surrounding air are usually low, the equilibrium for compensation is reached slowly. Furthermore, accumulation of surface charges by conduction satisfies the requirement that the field vanishes both outside and inside the crystal but not necessarily in the region just below the crystal surface [36].

If a ferroelectric material with homogeneous polarization between two parallel metal plates locates in a electric field (Fig. 2.2(a)), the depolarization field is compensated by the metal electrodes and therefore it is equal to zero. If the polarization has a distribution of $P(z)$ within the material (Fig. 2.2(b)), the depolarization field is in opposite direction to the polarization in the central region of the material and it is in the same direction as the polarization close to the interfaces.

The formation of the domains depends on the energy associated with the depolarization field W_E . The energy W_E would be zero for a totally compensated crystal in equilibrium. For an insulating crystal in an insulating environment with the distribution of polarization within the crystal, the equilibrium is reached very slowly. The magnitude of W_E depends on the crystal geometry and the distribution of $P(z)$ within the crystal [36]. When a crystal is cooled from a paraelectric phase to a ferroelectric phase in the absence of applied fields, there is only a limited number of possible directions of the spontaneous polarization. In order to minimize W_E , different regions polarize in one of those directions, thus results in the domain structure. A domain is a homogenous region, in which all of the dipole moments have the same orientation. If no electric field

is applied, the crystal usually shows zero net polarization.

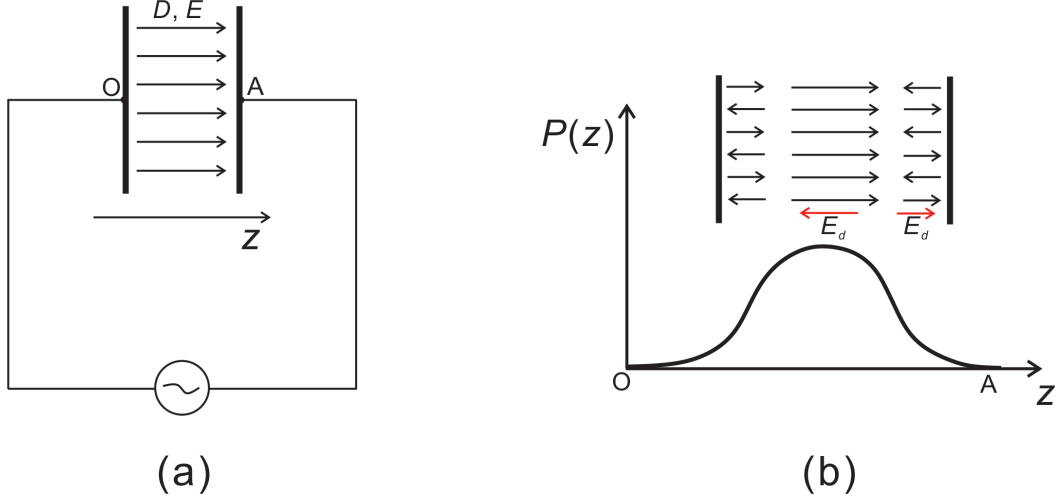


Figure 2.2: Schematic diagram of (a) a ferroelectric between two parallel metal plates, (b) distribution of polarization inside a ferroelectric. OA is the distance between two metal plates.

The domain wall energy W_w is the other contribution to the domain formation. The final domain configuration is determined by minimizing the total energy of W_E and W_w . In ferroelectric films, mechanical clamping by the substrate is another factor for the formation of domain patterns [1]. When all depolarization fields are compensated, theoretically a single domain structure should evolve. In reality, this is rarely achieved due to the presence of surfaces, local imperfections and external boundary conditions.

Depending on the crystal structure of the ferroelectric, the possible polarization directions and their available domain orientations may vary. For example, a rhombohedral crystal structure gives rise to 180° , 109° or 71° domain walls. In a tetragonal structure, the available domain walls can be 180° or 90° . 180° domain walls are purely ferroelectrically active, while the non- 180° domain walls are both ferroelectrically and ferroelastically active [32,37]. The domain structures in ferroelectric single crystals are optically visible while they are invisible in ceramics and thin films. The domain patterns in films can be visualized experimentally using different techniques, e.g. scanning force microscopy (SFM) [38], transmission electron microscopy (TEM) [39], and scanning nonlinear dielectric microscopy (SNDM) [40].

Domain nucleation and domain wall motion mechanism for polarization reversal was established early by Merz [41] and Little [42] and later by Miller [43,44] and Fatuzzo [45]. The studied ferroelectric material was barium titanate ($BaTiO_3$). Based on the

electrical measurements combined with optical observations, Merz proposed that the switching process in $BaTiO_3$ was accomplished by (1) the nucleation of new domains with opposite polarization when a reverse field was applied, and (2) the growth of these domains accompanied by domain wall motions. Fatuzzo extended the switching mechanism incorporating sideways growth and coalescence, as shown in Fig. 2.3. When a field is applied with the opposite polarity, small nuclei of domain with reverse polarization direction appear, usually at the interfaces or grain boundaries (Fig. 2.3(a)). Each nucleus grows parallel or anti-parallel to the applied field until it becomes a domain and reaches the opposite side (Fig. 2.3(b)). The domain formed in this way starts expanding sideways (Fig. 2.3(c)). After some time these domains are large enough to join each other and become coalescence (Fig. 2.3(d)). The above successive processes will repeat until the polarization is completely reversed in the whole sample.

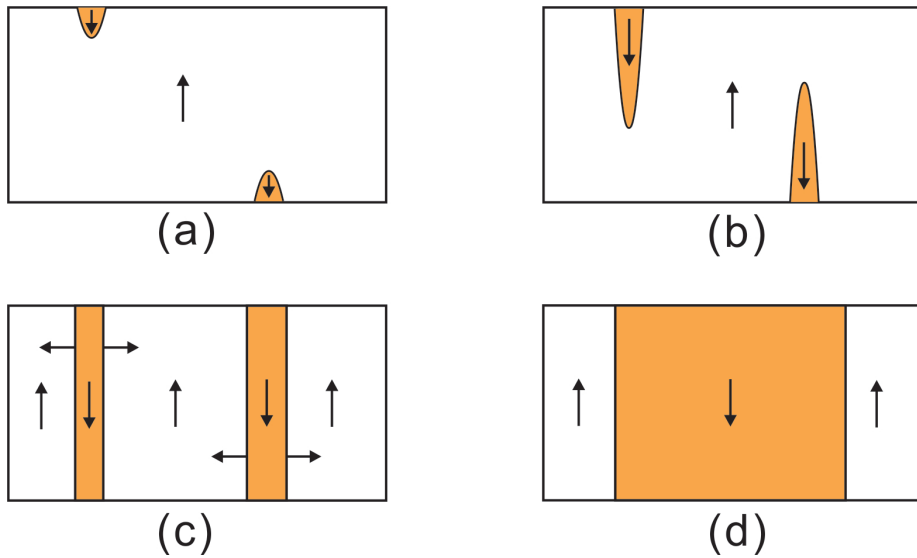


Figure 2.3: The evolution of the domain structure in ferroelectric during switching under an application of electric field (a) nucleation of new domains, (b) forward growth, (c) sideways expansion and (d) coalescence. After [45].

Numerous models have been proposed to quantify domain phenomena and their effects on ferroelectric switching. The classical model to describe ferroelectric switching kinetics is the Kolmogorov-Avrami-Ishibashi (KAI) model [2,46,47], which is based on the study of statistical behavior and the probability of nucleation and growth of domains. An alternative model is the nucleation-limited switching (NLS) model for thin films developed by Tagantsev et al. [35,48]. The details of these theories would be addressed in chapter 6.

2.3 Phenomenological theory

Landau theory is a symmetry-based analysis of equilibrium behavior near a phase transition [49-51]. Later study showed that the Landau theory is valid even for temperature far away from the phase transition [99], which indicates that the Landau theory is a generalised phenomenological theory. Ginzburg and Devonshire developed the Landau theory to study ferroelectrics using a thermodynamic approach [52,53]. As a macroscopic model, Landau-Ginzburg-Devonshire (LGD) theory has been successful in describing the phenomenological behavior of phase transitions in ferroelectrics.

Based on this theory, the free energy of a ferroelectric material in the vicinity of a phase transition, in the absence of an electric field and applied stress can be written as a Taylor expansion in terms of the order parameter, polarization P . If a sixth order expansion is used, the free energy in one dimension expression is given by:

$$G = \frac{1}{2}\alpha_0 (T - T_0) P^2 + \frac{1}{4}\beta P^4 + \frac{1}{6}\gamma P^6 \quad (2.6)$$

where G is the free energy, T_0 is the Curie-Weiss temperature, α_0 , β , γ are coefficients related to the crystal symmetry which can be determined either by fit to experiments or from first-principles calculations.

The equilibrium state is obtained by minimizing the free energy G , where we shall have $\frac{\partial G}{\partial P} = 0$. This gives us

$$E = \alpha_0 (T - T_0) P + \beta P^3 + \gamma P^5 \quad (2.7)$$

α_0 and γ are both positive in all known ferroelectric [36,54]. There are two cases depending on the sign of β . If $\beta > 0$, the free energy curve has a single minimum at $P = 0$ for $T > T_0$ and double minima at non-zero values of P for $T < T_0$, as shown in Fig. 2.4(a). The values of P at the minima corresponding to the spontaneous polarization $\pm P_s$ are determined by the solution of Eq. (2.7) at $E = 0$, i.e.,

$$\alpha_0 (T - T_0) P + \beta P^3 + \gamma P^5 = 0 \quad (2.8)$$

With increasing temperature, the spontaneous polarization P_s will decrease continuously to zero at T_0 (Fig. 2.4(b)). Here T_0 coincides with the Curie point T_c . This transition is called a second order transition.

In the other case, if $\beta < 0$, there is a temperature range from T_0 to T_1 where a single minimum at $P = 0$ and double minima at $P = \pm P_s$ coexist, seen in Fig. 2.5(a).

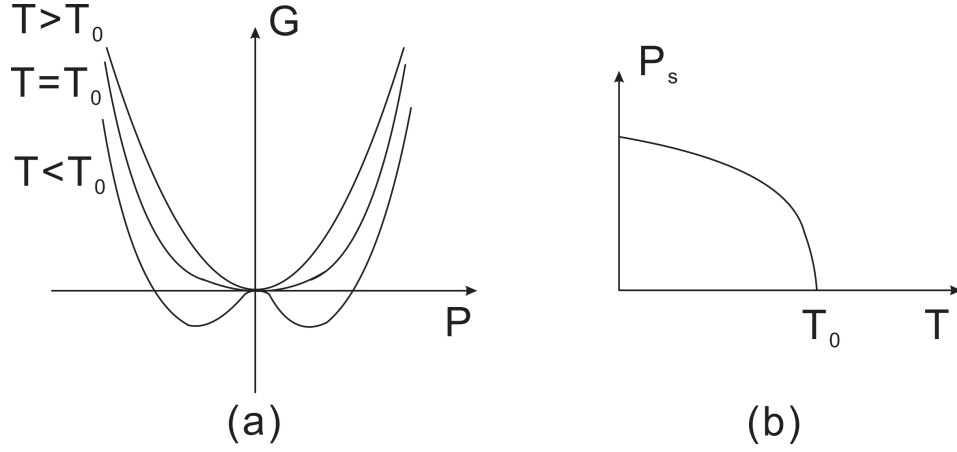


Figure 2.4: Second order phase transition. (a) the free energy as a function of the polarization at $T > T_0$, $T = T_0$, and $T < T_0$; (b) the spontaneous polarization as a function of temperature.

T_1 refers to ferroelectric limit temperature [55]. The most important feature of this transition is that the spontaneous polarization P_s jumps discontinuously to zero at T_c (Fig. 2.5(b)). This type of phase transition is defined as a first order transition.

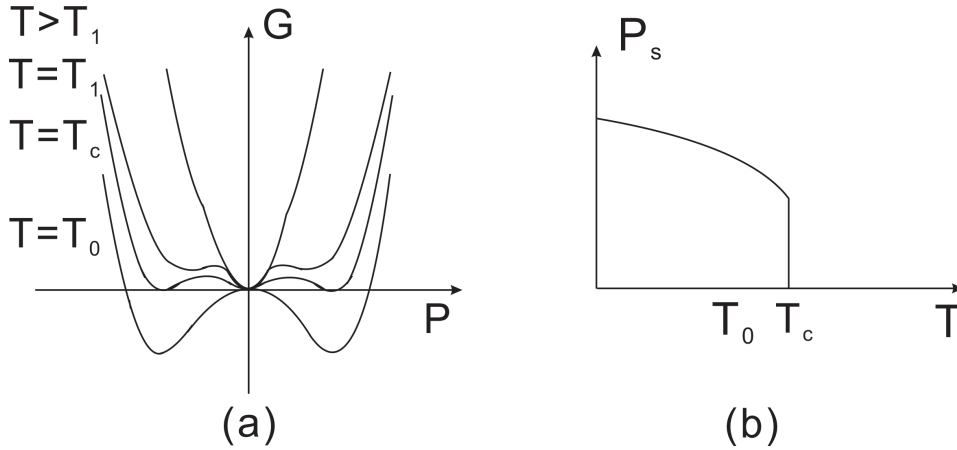


Figure 2.5: First order phase transition. (a) the free energy as a function of the polarization at $T > T_1$, $T = T_1$, $T = T_c$, and $T = T_0$; (b) the spontaneous polarization as a function of temperature.

Most ferroelectrics in practical applications are of first order phase transition, such as barium titanate, lead zirconium titanate, PVDF and its copolymers. In a first order phase transition, the samples behavior at $T = T_c$ will depend on whether it is approaching T_c from lower or higher temperature, thus the sample manifests a thermal

hysteresis. Another feature of a first order phase transition is that, above T_1 , ferroelectric state still can be induced by applying an external electric field. The polarization versus the electric field exhibits a double hysteresis loop.

The Landau-Ginzburg-Devonshire theory also predicts at a constant temperature a variety of nonlinear relations between P and E , i.e., a hysteresis loop, according to Eq. (2.7). The theoretical value of the coercive field E_c , which is determined from the intersection at E axis where P jumps from the positive branch to the negative branch, is usually much higher than the experimental E_c [36]. A comparison with experiment values in P(VDF-TrFE) is given in chapter 4.

2.4 Properties of P(VDF-TrFE) copolymers

Ferroelectric materials contain both organic and inorganic compounds. Among the organic ones, polyvinylidene fluoride (PVDF) and its copolymers with polytrifluoroethylene (PTrFE) are the representatives and the most important ferroelectric materials [56]. The piezoelectricity in poled PVDF was discovered in 1969 [57] followed by the discovery of the pyroelectricity in PVDF in 1971 [58]. However, it wasn't until the late 1970's that the ferroelectricity in PVDF was confirmed [59,60]. The distinguishing characteristics of PVDF and its copolymers include highly compact structure, high chemical stability, large permanent dipole moment, ease of fabrication and low annealing temperature which can be integrated with other materials and processes, e.g. silicon microfabrication.

PVDF and its copolymers with TrFE exhibit four polymorphic crystalline forms: α , β , γ and δ phases, whose formations depend on crystallization conditions, electrical poling and mechanical drawing. The β phase has an orthorhombic structure with an all-trans (TTTT) molecule conformation possessing a large spontaneous polarization and is responsible for the ferroelectric and piezoelectric properties. The dipoles in the β -PVDF extend from the electronegative fluoride atoms to the slightly electropositive hydrogen atoms perpendicular to the polymer chain direction, producing a dipole moment of $7 \times 10^{-30} C \cdot m$ (2 Debyes), as shown in Fig. 2.6. The introduction of TrFE, which has three fluoride atoms per monomer, to copolymerize with PVDF, can enhance the all-trans conformation associated with the β phase. This is because the fluoride atom is larger than hydrogen atom and therefore it can induce a stronger steric hindrance [6]. In addition, the copolymer with TrFE can be annealed to much higher crystallinity than pure PVDF [61].

Another feature for the introduction of TrFE is that it can lower the phase transition

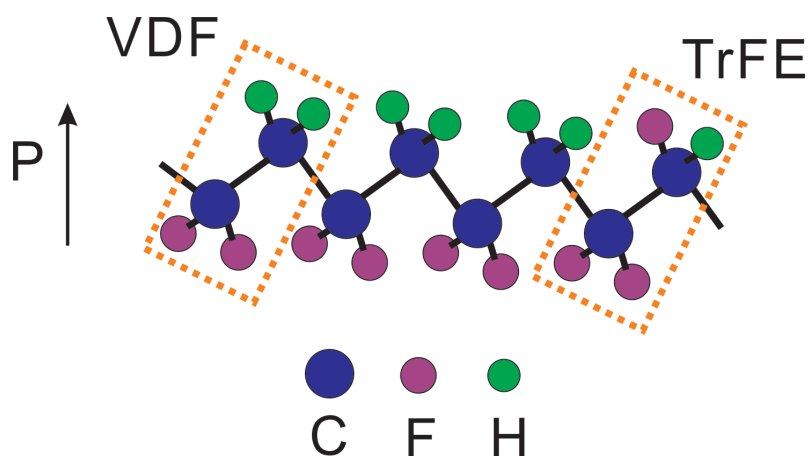


Figure 2.6: Schematic of molecular structure of P(VDF-TrFE) in the β phase. The polarization direction points from fluoride to hydrogen atoms.

temperature T_c in the copolymers. P(VDF-TrFE) with molar ratios of 50 – 80% of PVDF undergoes a clear ferroelectric-paraelectric phase transition with a measurable Curie point. The T_c increases with increasing PVDF content from 70°C at 50 *mol%* to 140°C at 80 *mol%*. The transition is an order-disorder type while the disorder is a random mixture of trans and gauche combinations in the conformation of the molecules. Moreover, the transition tends to change from a first order to a second order as the PVDF content decreases to a 52/48 composition with evidence of the disappearance of thermal hysteresis [62]. In the bulk PVDF the phase transition is not accessible with experiments because the melting temperature of this ferroelectric polymer ($\sim 170^\circ\text{C}$) is lower than the point of the possible phase transition T_c . Until very recently, a first order ferroelectric phase transition in the Langmuir-Blodgett ultrathin PVDF films was observed for the first time [63]. We have found the thickness interval, where ferroelectric phase transition disappears and transition from ferroelectric to pyroelectric state takes place in PVDF Langmuir-Blodgett films and explain the shift of T_c by the finite size effect at the nanoscale using Landau-Ginzburg-Devonshire theory and the Weiss mean field model, which is presented in chapter 7.

The switching in P(VDF-TrFE) is obtained by a rotation of the molecule chain along the chain axis changing the direction of the dipole moment. The rotation is not continuous but discrete due to the discrete potential energy for the chain rotation. A plausible model is that the rotation is changed by 60° steps during polarization based on x-ray [64] and IR transmission [65] measurements as well as energy favor calculations [59]. An alternative model is a single 180° rotation. This model becomes unfavorable

due to the lack of enough evidences, although both models can reproduce the observed switching curves by computer simulations with the employ of nucleation and domain growth mechanism [67].

2.5 Applications

PVDF and its copolymers have a wide range of practical applications in industry. Conventionally, PVDF has been used as sensors and actuators in the areas of adaptive optics [68], active and vibration control of structures [69-71] associated with their piezoelectricity and pyroelectricity. Nowadays the new potential applications of P(VDF-TrFE) films as nonvolatile memory devices are very attractive and prospective [3].

The principle of nonvolatile ferroelectric random access memories (FRAMs) is based on the polarization reversal by an external applied electric field. The binary logic states ‘1’ and ‘0’ are represented by the nonvolatile storage of the positive or negative remanent polarization states. The nonvolatile property is due to that the sample can hold the polarization state when the external field is removed. Compared to other nonvolatile memories, e.g. flash, electrically erasable and programmable read-only memories (EEPROM), FRAMs have faster write and read times, lower power consumption and high write and read endurance. A summary of the performances for different devices is given in table 2.1. FRAMs can be applied in a variety of consumer products, such as smart cards, power meters, printers, video games and radio-frequency identification (RFID) tags.

Table 2.1: Comparison of the performances for different types of nonvolatile memories. Data gathered from [72-74].

Type	Area/Cell (normal- ized)	Read ac- cess time	Write access time	Energy per 32b write	Energy per 32b read	Endurance
EEPROM	2	50ns	10 μ s	1 μ J	150pJ	> 10 ⁶
Flash	1	50ns	100ns	2 μ J	150pJ	10 ⁴
FRAMs	2-5	100ns	100ns	1nJ	1nJ	> 10 ¹⁵

The available commercial FRAMs are based on perovskite-type ferroelectrics such as lead zirconium titanate (PZT) and strontium barium titanate (SBT). Researchers have

overcome many difficulties including degradation and retention. Besides, perovskites generally require high annealing temperature ($> 400^{\circ}\text{C}$), which is harmful to other components on the chip. Therefore, the perovskite memory chips require buffer layers and complex mask sets [3,75]. P(VDF-TrFE) copolymer is the promising material to replace perovskites which has attractive advantages: the device can be achieved by low-temperature processing ($< 200^{\circ}\text{C}$) and solution-processing techniques, which would enable its use in ultra-low-cost applications; the copolymer has outstanding chemical stability which barely reacts to other components and it is nontoxic. However, the Curie point of P(VDF-TrFE) ($\sim 104^{\circ}\text{C}$ for the ratio of 70/30) is too low for practical applications in the integrated circuits. Thin films of pure PVDF with higher operation temperature for memory applications should be considered in the future.

There are three main memory elements based on ferroelectric films: metal-ferroelectric-metal (MFM) capacitor, metal-ferroelectric-insulator-semiconductor (MFIS) diode and ferroelectric-field-effect-transistor (FeFET). The MFM capacitors can be connected to the transistors to integrate into 1T1C (one-transistor-one-capacitor) or 2T2C (two-transistor-two-capacitor) memory cells [29]. MFIS devices based on P(VDF-TrFE) films have been investigated by several groups [8-12]. Earlier relatively thick P(VDF-TrFE) films ($> 100\text{nm}$) with SiO_2 buffer layer were used resulting in a higher operation voltage ($> 10\text{V}$). More recently, using sub-100nm P(VDF-TrFE) films, a $\pm 3\text{V}$ CV loop with a memory window of 1V was achieved in a stack consisting of a 10nm SiO_2 layer and a 36nm P(VDF-TrFE) LB film [10], and a $\pm 4\text{V}$ loop with a large memory window of 2.9V was obtained using a 3nm Ta_2O_5 buffer layer and a 100nm P(VDF-TrFE) spin coated film [11]. In Ref. [12], the authors fabricated MFM and MFIS devices using epitaxially grown P(VDF-TrFE) thin films (20-30nm). A memory window of 2.4V with applied $\pm 5\text{V}$ was obtained in MFIS and their printed micropattern application was demonstrated. All-organic FeFET devices based on P(VDF-TrFE) have been reported in [5,13-16]. High-performance solution-processed FeFETs were first reported in 2005 by Naber et al. [14] using P(VDF-TrFE) film as the gate insulator and MEH-PPV (poly (2-methoxy-5-(2-ethyl-hexyloxy)-p-phenylene-vinylene)) as a semiconductor. The FeFETs have a long retention time ($>$ one week) with a stable $I_{\text{on}}/I_{\text{off}}$ of 10^4 , a high programming cycle endurance (> 1000 cycles) and a short programming time of 0.3ms. However, with 60V operation voltages, the devices need to be scaled down. Lately, Gerber et al. [16] fabricated FeFET with very thin P(VDF-TrFE) films prepared by Langmuir-Blodgett technique. The memory element consists of a 10nm thick SiO_2 layer and a 35nm thick P(VDF-TrFE) film, which can operate at 4V but with very short retention time ($< 10\text{s}$).

In spite of these efforts, to commercialize P(VDF-TrFE) based nonvolatile memory devices, there are two important technical obstacles must be overcome. First, an appropriate approach must be found to control switching dynamics in the copolymer films. Second, the solution-processing technology must be scaled up and incorporated into the semiconductor-manufacturing process [3].

In this thesis, the investigated devices based on P(VDF-TrFE) thin films were fabricated as MFM structure. For technical applications, switching time, switching voltage, retention properties and fatigue behavior are considered, which are discussed in chapter 4. Furthermore, we go insight into the physical nature of the ferroelectric behavior in P(VDF-TrFE) thin films including polarization relaxation, switching mechanism and phase transition, which are presented in the following chapters.

2.6 List of important material data

The important material data for pure PVDF and P(VDF-TrFE) (70/30) used in this thesis is summarized in table 2.2.

Table 2.2: The important material data for pure PVDF and P(VDF-TrFE) (70/30).

Parameter	PVDF	P(VDF-TrFE) (70/30)
Dielectric constant	$12 \pm 10\%$	$10 \pm 10\%$
Dipole moment	$7 \times 10^{-30}\text{Cm}$	$5 \times 10^{-30}\text{Cm}$
Dipole density	$1.9 \times 10^{28}\text{m}^{-3}$	$1.85 \times 10^{28}\text{m}^{-3}$
Spontaneous polarization	$13\mu\text{C}/\text{cm}^2$	$10\mu\text{C}/\text{cm}^2$
Piezocoefficient	$D_{33} = -16 \pm 20\%\text{pC}/\text{N}$, $D_{31} = 6 \pm 20\%\text{pC}/\text{N}$	$D_{33} = -20 \pm 10\%\text{pC}/\text{N}$, $D_{31} = 6 \pm 10\%\text{pC}/\text{N}$
Curie point	not measurable	$\sim 104^\circ\text{C}$ at heating and $\sim 74^\circ\text{C}$ at cooling
Melting temperature	$\sim 170^\circ\text{C}$	$\sim 152^\circ\text{C}$

Chapter 3

Experimental details

This chapter describes the procedures of P(VDF-TrFE) thin film preparation and their electrical property characterizations. Two preparation methods: Langmuir-Blodgett deposition and spin coating, are introduced and the experimental steps are specified. The measurement systems with temperature controlled setups are also presented.

3.1 Sample preparation

In order to obtain a wide range of sample thickness (7nm-600nm), two preparation techniques are employed in this thesis.

3.1.1 Langmuir-Blodgett technique

Langmuir-Blodgett deposition, a novel technique for construction of multilayered and superlattice structures, can control layer composition precisely, including alternating ferroelectric and nonferroelectric films. The principle of Langmuir-Blodgett technique is the amphiphilic property of molecules which are composed of a hydrophilic part and a hydrophobic part [76]. Amphiphilic molecules are trapped at the interface with one type of bonding being attracted to polar media such as water and the other type of bonding being much less water soluble. The film can be produced by sweeping a barrier over the water surface causing the molecules to come close together and eventually to form a compressed and ordered monolayer, known as a Langmuir film. The Langmuir-Blodgett (LB) films are achieved through subsequent transfer of monolayers from gas-liquid interface onto a solid substrate. The transfer can be done by either vertical or horizontal dipping with the latter one called horizontal Langmuir-Schaefer method, as shown in Fig. 3.1.

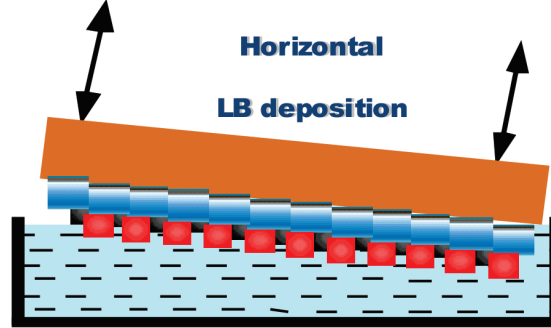


Figure 3.1: Sketch of the Langmuir-Schaefer monolayer deposition method, after [78].

The first ultrathin ferroelectric Langmuir-Blodgett films of P(VDF-TrFE) were prepared in institute of Crystallography of the Russian Academy of Sciences in 1995 [17]. Although P(VDF-TrFE) copolymer is not amphiphilic, the large molecular weight of polymers with low solubility in water can be dispersed to form a sufficiently stable layer on water with a repeatable pressure area isotherm [77]. Therefore, it permits the possibility to fabricate P(VDF-TrFE) ultrathin films by LB technique. The advantage of using LB technique to prepare P(VDF-TrFE) films is that it allows precisely control the film thickness down to 1nm [78] by the number of monolayer transfer. Besides, the crystallinity in LB films is much higher than that by other conventional thin film preparation methods.

In this work, a commercial Langmuir-Blodgett trough from NIMA Technology with model of 601S was employed which allowed a horizontal Langmuir-Schaefer deposition. The glass substrates with area of $10 \times 10 \text{mm}^2$ were ordered from Praezisions Glas & Optik GmbH, Germany. The surface roughness (root mean square) of the substrates measured with an Atomic Force Microscope (AFM) was within 20nm. It should be noted that the surface roughness of the substrates played an important role in the property performance of the films since the investigated thickness range of LB films was in nanometer scale. The effect of the surface roughness had been observed by comparison with normal glass slides which were not scrapes and salients free. The leakage current was higher for the LB films deposited on the normal glass slides than that on the low surface roughness substrates.

The substrates were cleaned by ultrasonic in 2-propanol and then dried by nitrogen flow before use in order to remove the contamination from the surface. Two aluminum stripes served as bottom electrodes with a width of $200 \mu\text{m}$ and a thickness of 100nm

were deposited onto the substrates by vacuum thermal evaporation through a shadow mask at a chamber pressure of $2 - 3 \times 10^{-6}$ mbar. The electrode deposition rate was about $0.1 - 0.2$ nm/s.

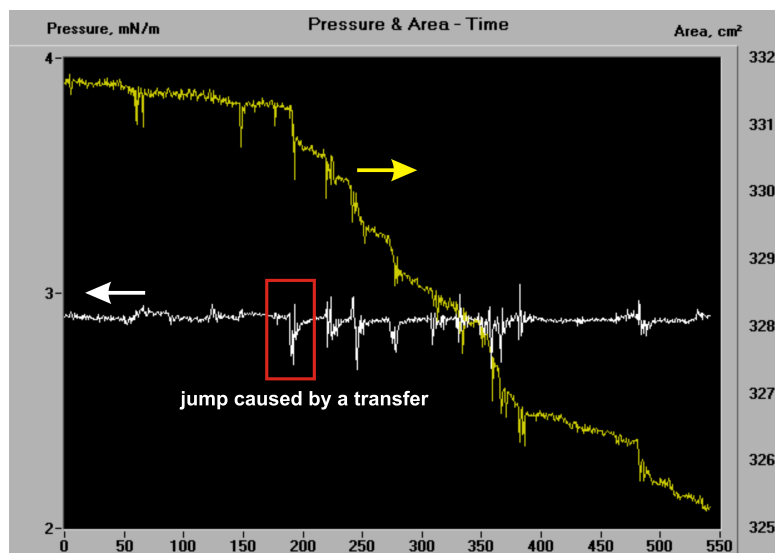


Figure 3.2: The evolution of surface pressure and area in dependence of time during LB deposition. The target pressure is kept constant (white line) while the compressed area is decreasing (yellow line). The red frame indicates a jump of pressure caused by a transfer.

The starting material of P(VDF-TrFE) copolymers used here was pellet form in a ratio of 70/30 (Piezotech S.A., France). The copolymer pellets were dissolved in dimethylsulfoxide (DMSO) to form a solution with concentration of 0.02% by weight. The trough was filled with ultrapure ($18\text{M}\Omega \cdot \text{cm}$) water. A clean surface in the trough should be checked and ensured at the beginning characterized by an almost flat pressure area isotherm indicating no significant change of the surface pressure on the surface. Then about 0.5ml of the P(VDF-TrFE)/DMSO solution was dispersed dropwise onto the water subphase with area of 600cm^2 . The dripping of the solution can be done either by directly using a syringe or by draining slowly over a slightly inclined glass slide. After the evaporation of the solvent (usually took about 40 minutes), the surface layer was compressed by closing the trough barrier at a rate of $40\text{cm}^2/\text{min}$. The target pressure was set to 3mN/m , much below the collapsing pressure. Once the target pressure was reached and the surface pressure remained constant, the film was ready to be transferred to a substrate. Attention should be paid on lowering immersion of the substrate to the surface slowly to avoid the formation of air bubbles and to ensure

smooth film adhesion. The substrate should be parallel to the liquid surface during dipping and then slowly removed from the subphase at a small angle. Every transfer causes a jump in the pressure versus time curve (Fig. 3.2). The transfer ratio, which is defined as the area of monolayer removed from subphase at a constant pressure divided by the area of substrate immersed in water, can evaluate how well a film has been transferred to a substrate. A transfer ratio of higher than 70% was ensured in this work.

The film thickness depends on the preparation conditions including temperature, humidity, solution concentration and target pressure. Here, samples prepared by 10-100 transfers yielded thicknesses of 7-140nm.

3.1.2 Spin coating method

Spin coating is a fast and easy method to generate thin films basically from 50nm to micrometers. It is very attractive for researchers due to its ease of processing and uniform quality of film surface. The physics behind spin coating bases on a balance between centrifugal forces controlled by spin speed and viscous forces which are determined by solvent viscosity [79].

The copolymer pellets were dissolved in 2-butanone. The spin coating was realized with a spin-coater of KW-4A from Chemat Technology. The film was formed firstly spin coated at a low spin rate (hundreds of rpm) for several seconds to spread out the solution then at a higher rate (thousands of rpm) fixing spin time at one minute to generate a homogenous film. The sample thickness was controlled by varying the solution concentrations from 0.5% to 5%, and rotating speeds from 1000 to 4000rpm. The samples showed good reproducibility. In this work, P(VDF-TrFE) spun films with thicknesses in the range of 50- 600nm were investigated.

3.2 Annealing and morphology

All the samples were annealed at 125°C for 2h in air with heating and cooling rate of 1°C/min to improve the crystallinity. The anneal temperature was above the Curie point of the copolymer. Some studies showed that samples annealed in paraelectric phase exhibited better crystallinity because paraelectric phase behaved significant plastic flow which was helpful for crystallization [80].

The microstructure of the thin films was checked with an Atomic Force Microscope (AFM) from Veeco Instruments Inc. Fig. 3.3 depicts the surface morphology of P(VDF-TrFE) LB films with 4ML on silicon substrates under different anneal conditions. The

as-prepared sample without annealing treatment shows the monolayer material has good adhesion to the substrate with smooth and dense surface (Fig. 3.3(a)). No obvious peeling off is observed. With the heat treatment (Fig. 3.3(b)), the material starts to crystallize and joins into oblong and lamella structure. As the holding time at the anneal temperature increases to 20min (Fig. 3.3(c)), there is more joining of the grains leaving larger void. Further increasing the holding time to 1h (Fig. 3.3(d)), the surface structure of the sample does not show significant change. The group of S. Ducharme called the nanostructure of LB films with only several monolayers as ‘nanomesa’ and ‘nanowell’. They pointed out the potential applications of this structure in high-density nonvolatile random-access memories, acoustic transducer/infrared imaging arrays, as well as templates for nanoscale molding or contact-printing [3,81,82].

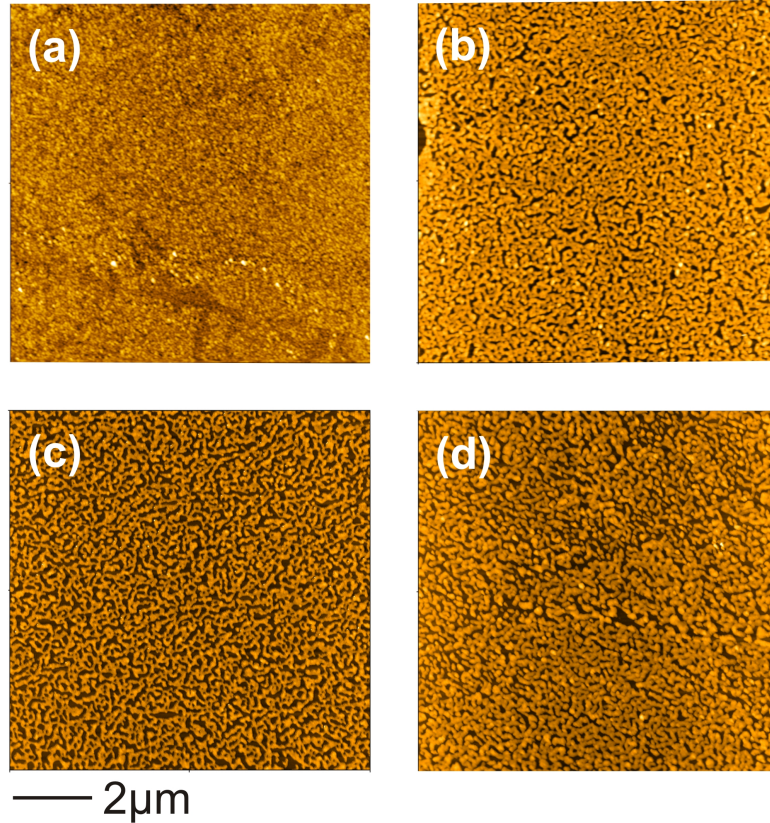


Figure 3.3: AFM images of the samples with 4ML (a) as-prepared, (b) heat up to 125°C and cool down immediately, (c) heat up at 125°C kept for 20min and cool down, (d) heat up at 125°C kept for 1h and cool down.

After anneal, a second set of aluminum stripes was evaporated on the top of the film to form a plane parallel capacitor structure. The top electrodes were perpendicular

to the bottom electrodes. The overlapped area of the top and the bottom electrodes determined the active area. The LB film samples and the spun film samples had the same structure. There were four capacitors available for the electrical measurements, as shown in Fig. 3.4. Each capacitor in the crossover area was electrically isolated from the others by scratching the electrode stripes.

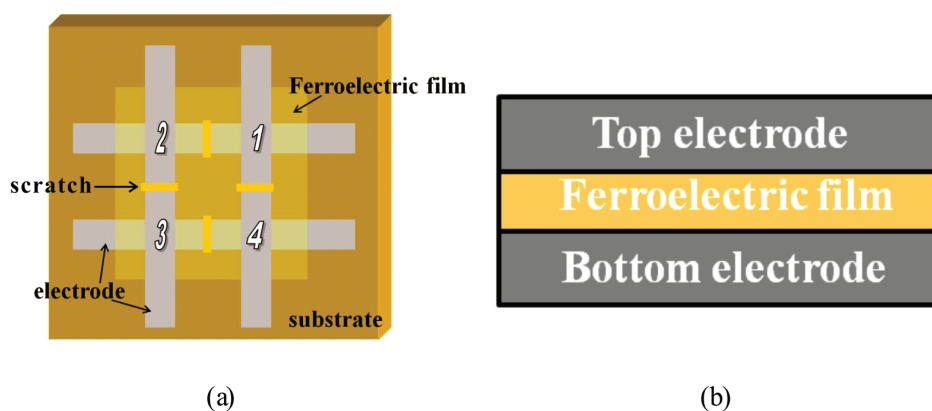


Figure 3.4: MFM stack consisting of P(VDF-TrFE) as ferroelectric layer (a) front view and (b) cross sectional view.

Aluminum was the mainly used electrode material in this work due to its low melting point for evaporation, no obvious diffusion and high reproducibility of the switching properties. Gold had a diffusion to the ferroelectric films observed before which caused a serious short circuit and therefore it was not suitable to serve as electrodes for P(VDF-TrFE) films. Other metal electrode materials, e.g. copper and platinum, were also used. Their influences on the switching behaviour are investigated which are discussed in chapter 4. Deposition of platinum electrodes was through electron beam evaporation due to its high melting point (1771°C). Besides, only the platinum bottom electrodes were evaporated since the high evaporation temperature would be harmful for the polymer films.

3.3 Thickness determination

The thicknesses of the films were measured with either an ellipsometer or an AFM.

Ellipsometry is typically used for thickness measurements for films with thicknesses ranging from sub-nanometers to a few microns. The measurement is based on the change of polarization state of light reflected from the surface of a sample. Briefly, as

indicated in Fig. 3.5, light from a laser passes a polarizer to a sample, for example, a P(VDF-TrFE)/Al₂O₃/Al structure in our case. The polarized light is refracted and reflected on the sample and then received by the detector through an analyzer. The measured value is represented as complex reflectance ratio ρ , which is parametrized by the amplitude component Ψ , and the phase difference Δ , written as [83]

$$\rho = \tanh(\Psi) e^{i\Delta} \quad (3.1)$$

The procedure used to deduce the film thickness is following: first, an optical model is built describing the sample structure using the information (thickness, refractive index n and extinction coefficient k) about the sample. In our case, a P(VDF-TrFE)/Al₂O₃/Al structure is constructed. Since the thickness of the aluminum bottom electrode of 100nm is much higher than the penetration range of light, the bottom electrode can be considered as an infinite half-space. The native oxide layer has a thickness of about 2nm as measured from the Al₂O₃/Al model. Second, a set of theoretical data is generated from the optical model that corresponds to the experimental data (Ψ and Δ). In the data analysis, generated data is compared with experimental data. Unknown parameters in the optical model, such as film thickness or optical constants or both, are varied to try and produce a best fit to the experimental data. Regression algorithms are used to vary unknown parameters and minimize the difference between the generated and experimental data.

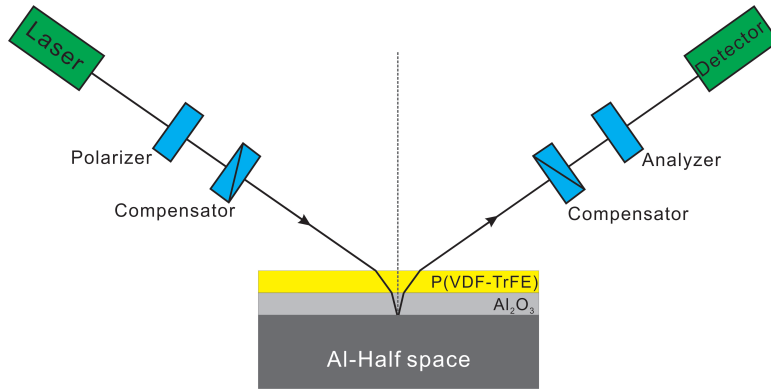


Figure 3.5: Schematic model for the ellipsometric measurements.

In this work, measurements were performed using a Sentech SE500adv ellipsometer. For thin films, multiple angle mode with incidence angle from 30° to 70° at a wavelength of $\lambda = 632.8\text{nm}$ was employed. For thicker films (thicker than 400nm), a white light reflection method under normal incidence (spectroscopic ellipsometry, SE) was used to

provide more reasonable and precise values.

The film thickness was also determined with an AFM which was achieved by scratching the film to create a step and then scan the step height. It should be noted that the thickness values measured by ellipsometer agreed very well with those determined by AFM.

Table 3.1 shows the thickness of a set of LB films prepared under the same condition measured by ellipsometer and also confirmed by AFM. The film thickness increases gradually with the increase of transfer number. The average thickness per transfer is more or less constant of value around 1.2nm. It is reported that the thickness of a single monolayer is about 0.5nm [78]. Therefore, in the LB deposition, nearly two monolayers are transferred at one time.

Table 3.1: The thickness of LB films with different transfers.

Number of transfer	Thickness(nm)	Average thickness per transfer(nm)
20	28	1.4
30	37	1.23
40	44	1.1
50	53	1.06
60	69	1.15
70	94	1.34
80	103	1.29
100	139	1.39

As mentioned above, the thickness of spun films can be varied by the spin speed and concentration of the solution in a wide range. Fig. 3.6 shows the film thickness versus the spin speed for different concentrations of the solution. Generally, the thickness is in 50nm range with a solution of 0.5% in weight and it increases to a range around 600nm generated with a solution of 5% in weight. At a specific solution concentration, the thickness slightly decreases with increasing spin speed.

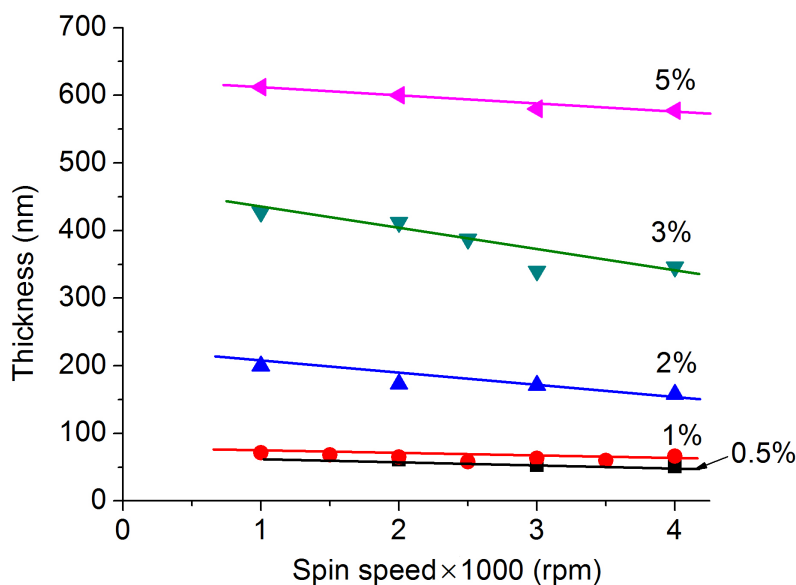


Figure 3.6: Thickness dependence on spin speed at different solution concentrations from 0.5% to 5%. The curves are guides for the eyes.

3.4 Electrical measurements

For all electrical measurements, the samples were placed in a shielded measurement cell which was directly connected to a vacuum pump, as sketched in Fig. 3.7. The O-ring was used to create a seal at the interface between the cover and the chamber under vacuum. The chamber cover was secured by four bolts to the chamber. Point probes were used for making electrical connection between the measurement system, e.g. LCR meter, and the sample. Detailed setup of the probe station for the electrical measurements can be seen in Fig. 3.7. The sample was placed in a metal sample stage. Two probes were equipped with two metallic spring tips (radius of 0.5mm) which mechanically contacted to the top and the bottom electrodes of the sample. Synchronously, the probes were connected through coaxial cables to the measurement system. The cables were kept as short as possible in order to reduce noise caused by parasitic capacitance. For capacitance and loss tangent measurements, the cable length was 1 meter. The fastener adjusted the position for clamping. The inner chamber allowed a heat up and cool down setup for varied temperature measurements which would be discussed later.

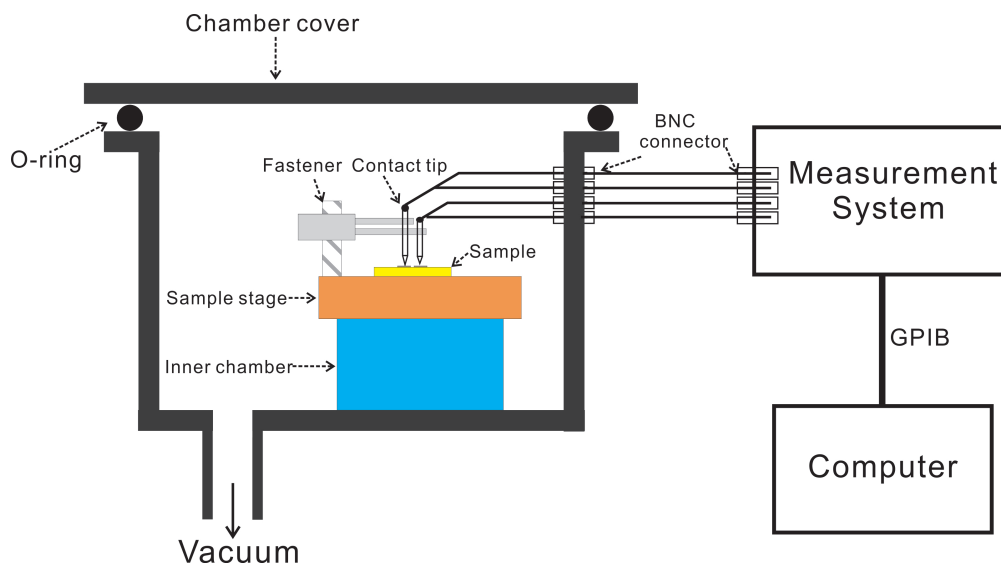


Figure 3.7: Schematic representation of the probe station for the electrical measurements.

3.4.1 *CV* measurements

The capacitance at different voltages represents the change of polarization in the film. For ferroelectric materials, capacitance-voltage sweep usually shows a ‘butterfly’ hysteresis curve. The CV profile is actually a measure of $\frac{\partial P}{\partial E}$. The peak in the CV curve corresponds to the ferroelectric dipoles switching from one orientation to another.

The CV measurements were performed using an Agilent 4294A precision impedance analyzer. The sample under test placed in the cell was connected through four BNC connectors to the LCR meter. The capacitances and loss tangents were recorded by a computer via a GPIB cable and an IEEE interface card. Before test, calibration should be done. An abnormal gap in the frequency dependent capacitance was observed at around 5 MHz before which could be eliminated by appropriate calibration. For the temperature dependent capacitance measurements, a set of copper pads was deposited onto the aluminum stripes which allowed a directly soldered contact of the inner conductor of a coaxial line to the copper pads in order to eliminate measurement errors and obtain reproducible results [84,85].

All the measurements, unless otherwise specified, were performed under a small AC signal of 100mV (rms) at frequency of 1 kHz. The voltage was ramped at 0.1V/s with a step of 0.1V. A typical CV characteristic for a 70ML LB film is shown in Fig. 3.8. A symmetrical butterfly loop is observed. The peaks at voltages of $\pm 4V$ correspond

to the coercive voltage of the sample. At voltages higher than the peak voltage, the capacitance is reduced. Small shift and a little asymmetry in the CV curves are usually observed [2], which can be caused by the built-in field resulting from the difference of the electrodes and/or the defects in the sample.

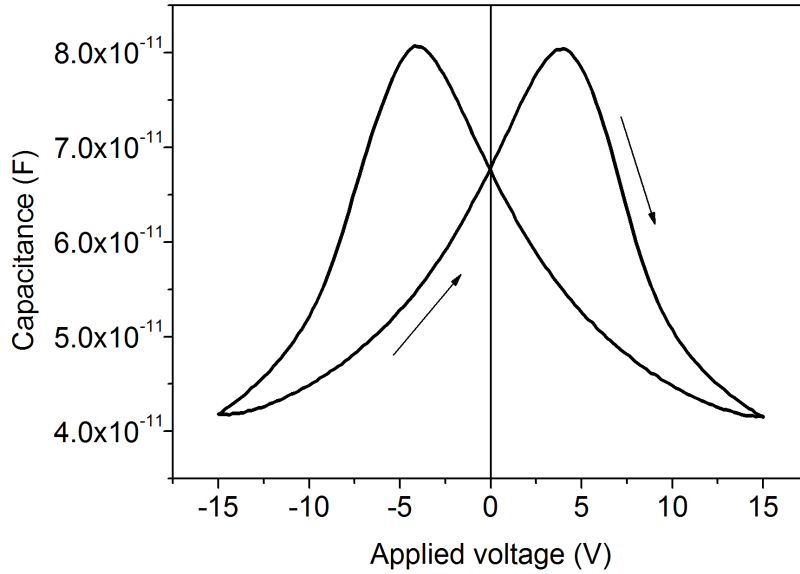


Figure 3.8: The CV characteristic of a LB film with 70ML.

The dielectric constant can be calculated by $\epsilon_r = \frac{1}{\epsilon_0} \cdot \frac{Cd}{A}$. ϵ_0 is the vacuum permittivity ($8.85 \times 10^{-12} \text{ Fm}^{-1}$); C is the capacitance; d is the thickness of the film; and A is the area of the capacitor. P(VDF-TrFE) thin films have a typical dielectric constant of 10-12 at zero bias.

3.4.2 Hysteresis loop measurements

The standard circuit for ferroelectric hysteresis measurements is the well-known Sawyer-Tower circuit (Fig. 3.9) [86]. The sample is connected in series to a low loss reference capacitor. The voltage source generates a triangular signal. The voltage at the reference capacitor can be measured with an electrometer with high input impedance to avoid discharge of the capacitor. With the measured voltage $U_c(t)$ the charge $Q(t)$ on the capacitor can be calculated which is the same as the charge on the sample. The polarization can be derived from the charge with an area A of the sample, i.e. $P(t) = Q(t)/A$. The reference capacitor should be chosen to have a capacitance of

100 times larger than the capacitance of the sample. Therefore, the voltage drop at the reference capacitor is negligible and the applied voltage is almost the same as the voltage drop at the sample. However, if the capacitance of the reference capacitor is too high, the resolution would be reduced and the respond signal would be distorted. A typical value of 100nF was chosen in the experiments based on the sample capacitance.

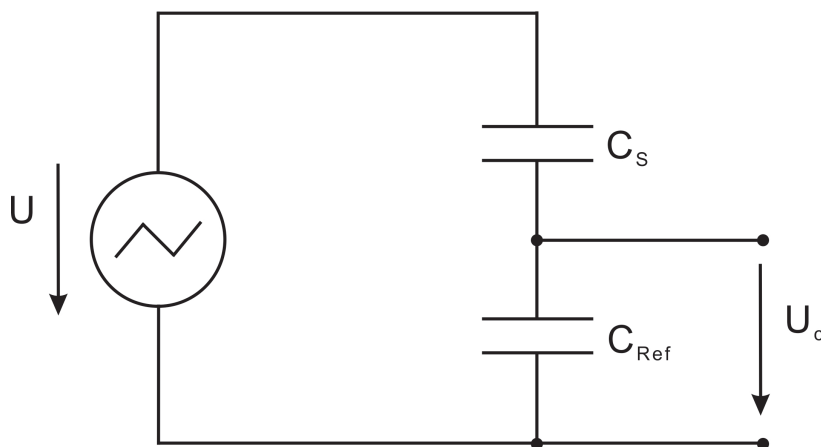


Figure 3.9: Schematic diagram for Sawyer-Tower circuit.

The hysteresis loops were measured by a home-made system using a data acquisition card (NI PCI-6251, National Instruments) to generate signal and amplified by a voltage amplifier which allowed a triangular signal from 1 mHz to 1 kHz. For high frequency measurements, a function generator (HAMEG 8130 (10 MHz), Germany) was equipped with a fast voltage amplifier (WMA-300 (5 MHz), Falco Systems, Netherlands) to generate output signal.

3.4.3 Time domain polarization

Polarization build up in time domain characterizes the switching kinetics in ferroelectric. The time domain polarization measurement has advantage for smaller dynamic range in $P(t)$ and therefore one single measurement is sufficient to receive the complete set of data over a wide time range. In this work, measurements were performed with a modified Sawyer-Tower method developed by Dr. B. Martin (Fig. 3.10) [87]. Three measurement capacitors are implemented which are switched off one after another during the measurement. In the short time range, two additional capacitors (C_1 and C_2) and pre-amplifiers with shorter rise times but lower input impedances are employed. A data acquisition system (ADDA-card, 9812, AdLink) with a high sample rate of 20 MHz and a resolution of 12 bit is used to record the voltages. For the long time (after

t_2), only the device with the high input impedance to avoid self-discharge is active measuring U_3 and a commercial slower data acquisition system with higher resolution (INA116, BurrBrown, $R = \sim 10^{16}\Omega$) is used. In this way, the polarization of the sample can be determined in a time range from $10^{-6}s$ to 10^4s , over 10 decades, with one single run.

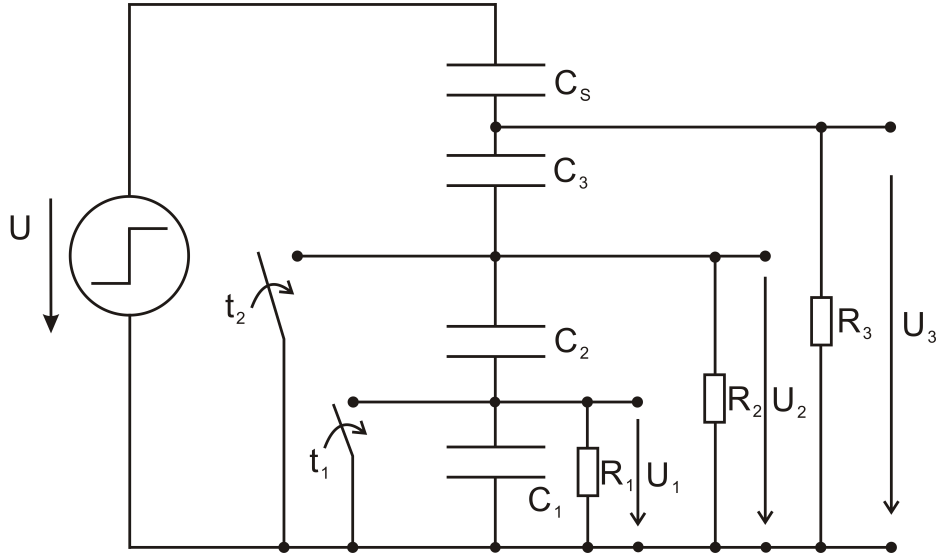


Figure 3.10: Modified Sawyer-Tower measurement system with three measurement capacitors and different data acquisition systems, after [87].

A three pulse method was employed using this measurement system whose configuration is shown in Fig. 3.11 [21]. By applying a first negative pulse with sufficient amplitude and width, all the dipoles in the sample were switched to the negative saturation state of the polarization. After a waiting time, a second positive pulse switched the sample to the positive state. During the application of this positive pulse, the measured charge contained the ferroelectric polarization and all side effects including space charge polarization and charge injection. When the applied voltage was set to zero during the waiting time, the electrometer was reset. With the third pulse of the same positive pulse strength, only the side effects were detected since the sample had already switched in the second positive pulse. Thus, time dependent ferroelectric polarization $P(t)$ was obtained by subtraction of the charges of the second and the third positive pulse resulting in only the contribution from pure ferroelectric switching.

In addition, the depolarization charge after switching off the applied voltage can also be measured with this measurement system.

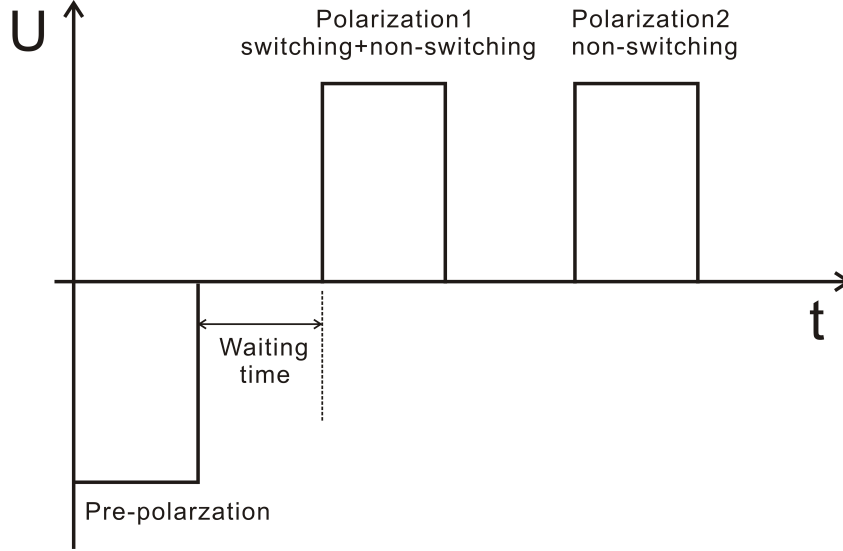


Figure 3.11: The three pulse method used in pulse switching measurements.

3.4.4 Current transients

Polarization current $j(t)$ can be calculated by the time derivative of the polarization, i.e. $j(t) = \frac{dP(t)}{dt}$. Besides, the current response flowing through the ferroelectric film can be recorded directly. For the short time range (nanosecond to microsecond range), the current was measured in a modified Sawyer-Tower circuit by replacing the reference capacitor with a resistor of 50Ω , as shown in Fig. 3.12. This defined the experimental time constant $\tau_{RC} = R \times C_s$, which was much shorter than the ferroelectric switching time in the sample. The voltage drop over the resistor was monitored with an oscilloscope (HAMEG 1508, sampling rate: 1 GSa/s, Germany). The current transient was determined by $i(t) = \frac{U_R(t)}{R}$. For longer time range (from several microsecond), the current was measured with a fast current amplifier (Keithley 428, rise time of $2\mu s$) and monitored with the oscilloscope. For a time range longer than 1s, the current was recorded using a Keithley 6514 electrometer which had higher resolution. The depolarization current was measured in the same way.

3.4.5 Retention and fatigue tests

Retention properties and fatigue behavior were measured with the same modified Sawyer-Tower measurement system as shown in Fig. 3.10. The retention behavior was measured by the two pulse method. The sample was first switched to the negative saturated polarization state by a negative pulse. After a short circuit waiting time

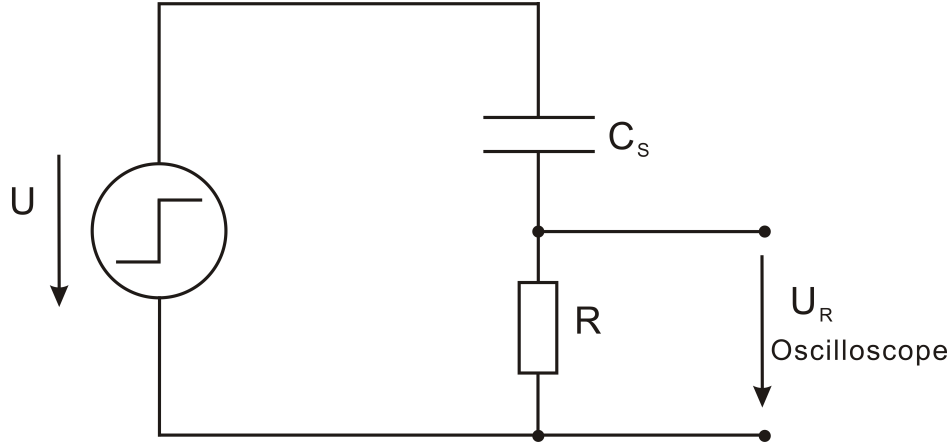


Figure 3.12: Modified Sawyer-Tower circuit used in current transient measurements.

of 10s, to release the space charge polarization, the sample was then switched to the positive saturated state by a positive pulse. Charges were recorded after the removal of the positive pulse. In this way the remanent polarization of the sample was measured as a function of time.

The fatigue tests of ferroelectric films were performed by applying alternating rectangle-shaped switching voltage pulses with a frequency at 1 kHz and amplitude of 6-45V for samples with different thicknesses, equaled to an electric field of 150 MV/m, which was high enough to cause ferroelectric switching in the samples. The hysteresis loops were measured at intervals of the fatigue process using a triangular voltage pulse at a frequency of 1 Hz to determine the remanent polarization change with cumulative switching cycles. Special attention should be paid on the waiting time between the alternating pulses, which would be discussed in more detail in chapter 4. The employ of pulse train in the long term reliability evaluation including retention and fatigue has advantage that it is more relevant to the ferroelectric memory since the memory uses square pulses to operate ‘read’ and ‘write’.

3.5 High and low temperature measurement setups

The high temperature (room temperature to 400K) measurements could be achieved in the measurement cell under vacuum described above (Fig. 3.7). The temperature was controlled with a resistance temperature detector (RTD) of Pt100 resistor in which resistance value was converted to the temperature value through a multimeter. The Pt100 resistor was mounted close to the sample on a glass substrate which had the

same thickness as the sample. In addition, another Pt100 sensor was mounted directly on the sample stage to monitor the temperature difference between the stage and the glass surface. Thermal paste was used to glue the sample to the stage in order to increase the heat transfer at the interface. In the high temperature measurements, the two sensors showed identical temperature values.

Heating was performed by a copper coil embedded beneath the metal stage in the inner chamber. The bottom side of the big chamber was covered by thermal insulation (styrofoam) to reduce thermal loss to the ambient. The metal stage where the sample placed was shielded by a glass cover evaporated with aluminum. A window in one side of the cover for the cable entrance was veiled with copper foils. This design was used to reduce heat circulation on the top of the sample, and therefore reduced the cooling of the sample surface, and increased thermal uniformity. The heating and cooling rate and the set temperature could be controlled by a programme in the computer through a PID regulator. Compressed air flow to the inner chamber could be used to increase the cooling rate in the cool down process especially in the temperature range just above room temperature where the natural cooling rate could be very slow. Capacitance, loss tangent, temperature and current or voltage could be collected simultaneously by the computer via an IEEE interface card.

The low temperature (room temperature to 180K) measurements were performed by a liquid nitrogen evaporator. Fig. 3.13 shows the schematic for the measurement setup. The liquid nitrogen was stored in a thermo-insulation container. A bung which was covered by the insulating materials fitted tightly into the top of the container with four screw bolts. The bung had two electrical leads through it for attachment to the resistive heater coil and the external power circuit, as well as an exit tube for the nitrogen gas. The nitrogen gas was generated using a heater coil. The heater coil should always be totally immersed in the nitrogen bath during the experiment. The heater caused the liquid nitrogen to boil, and the nitrogen gas generated was led through the copper tube whose outside part was fixed with a teflon nozzle. The nitrogen gas flow rate depended on the adjustable power supply for the heater which could provide constant current up to 3A. The higher the current was set the faster the nitrogen gas flowed and therefore the lower the temperature could achieve. When an appropriate amount of nitrogen gas vented, the tube could be connected to the inner chamber where the sample placed and the cooling process started.

The cover for shielding the sample stage was the same as that in the high temperature measurement setup. The tube connected the tank to the inner chamber was protected by the insulating materials to reduce unwanted thermal exchange with the

external ambient. The big chamber was first pumped to a vacuum level of $\sim 10^{-3}$ Torr, to minimize heat transfer and to reduce the presence of residual humidity that could be detrimental to the measurements at very low temperatures. The temperature was also monitored by the Pt100 resistors. It should be mentioned that the thermal conductivity of glass decreased with decreasing temperature [88]. The low thermal conductivity of glass substrate at low temperature could cause temperature difference between the sample stage and the glass surface as we observed the different read-out of the two Pt100 sensors mounted at different positions described above. This effect could be eliminated by careful gluing the bottom and the four sides of the substrate with thermal paste to increase the thermal conductivity. Besides, the set temperature should be stabilized for 15 minutes and the temperature oscillation was within $\pm 1\text{K}$ before the measurement performed.

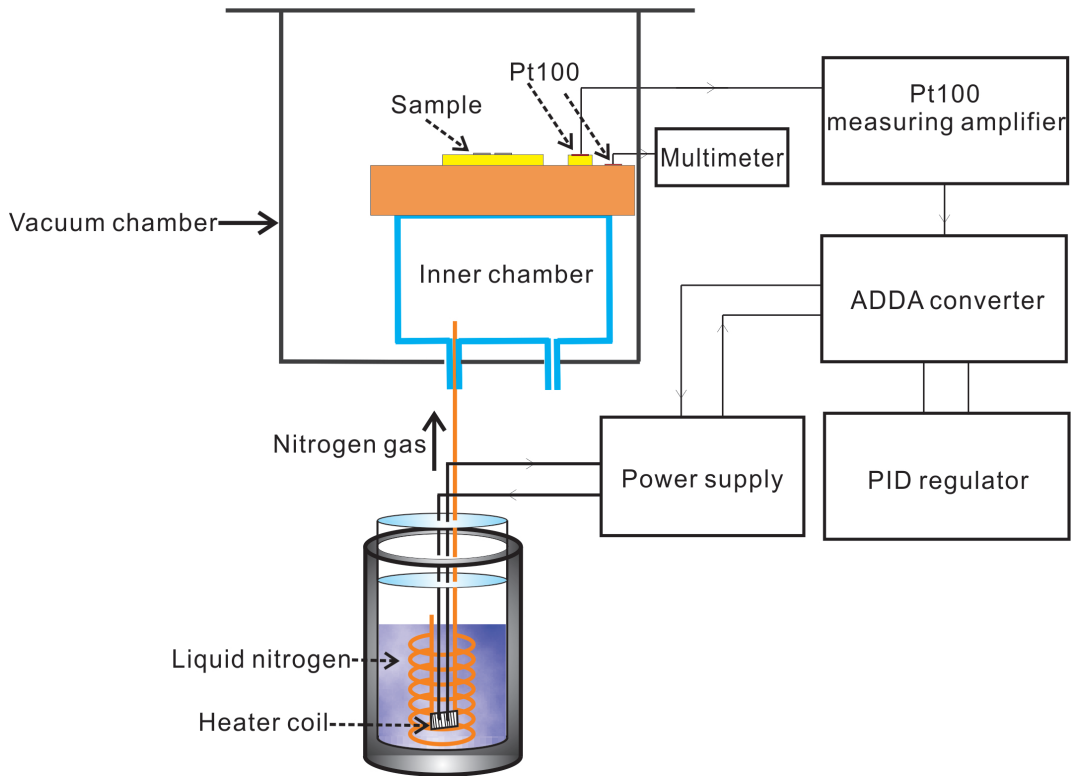


Figure 3.13: Schematic of the connection for the low temperature experiment setup. For simplicity, the details of the vacuum chamber one can refer to Fig. 3.7.

Chapter 4

Ferroelectric properties of P(VDF-TrFE) thin films

In this chapter, ferroelectric behavior of poly(vinylidene fluoride/trifluoroethylene) copolymer thin films prepared by Langmuir-Blodgett deposition ($d = 37 - 139nm$) and spin coating method ($d = 53 - 327nm$) has been investigated and compared through polarization switching measurements. Their hysteresis loops, coercive fields and remanent polarization, transient polarization, retention properties and fatigue behavior are addressed systematically. Furthermore, the influences of electrode effects and dielectric layer on the ferroelectric responses, as well as frequency and amplitude dependence of hysteresis loop are discussed.

4.1 Comparative study of LB films and spun films

In recent years, numerous researches on poly(vinylidene fluoride/trifluoroethylene) [P(VDF-TrFE)] copolymer thin films have shown their great potential in nonvolatile memory applications [3,4,18,21,78,82,89-94]. One of the technical challenges is to achieve low-voltage operation due to their relatively high coercive field of $\sim 50MV/m$ [6]. Therefore, fabrication of ultrathin films (below 100nm) attracts much interest. Conventionally, high quality ferroelectric films thinner than 60nm could not be fabricated by solvent spinning method [3,78], thus investigation of the finite size effect for ferroelectric films was limited for nearly ten years. A main breakthrough was the development of Langmuir-Blodgett (LB) deposition for fabrication of ferroelectric copolymer films in 1995 [17], which allows precise control of film thickness down to one monolayer. Since then, great achievements have been reached not only in theoretical investigation but

also in technical applications [3,18,21,78,82,89,90]. Lately, with the improvement of experimental conditions, some groups can produce ferroelectric copolymer films even down to 10nm by spin coating [92,93]. Thus the properties of LB films and spun films including switching mechanism and phase transition can be compared at the same scale.

Despite this, no group has directly compared the properties of LB films and spun films up to now. Although some data of both types of films are compiled and summarized in some literatures [3,21,78], the measurement procedures differ in different groups. In this thesis, we prepare P(VDF-TrFE) copolymer films by both Langmuir-Blodgett deposition and spin coating method. Measurements of polarization hysteresis loops and switching transients are carried out. Moreover, the thickness effects in both types of films are investigated.

4.1.1 Hysteresis loops

Fig. 4.1(a) and (b) show the D-U hysteresis loops of the P(VDF-TrFE) copolymer LB films and spun films for various thicknesses. The thicker films exhibit nearly square hysteresis loops. As the sample thickness decreases, the hysteresis curve tends to slant more observably. The surface oxidation layer of Al_2O_3 , which is between the Al electrode and the ferroelectric film can cause a depolarization field and therefore a slanted hysteresis loop results [95]. Considering a series model of the ferroelectric film with a surface oxidation layer (Fig. 4.2), the boundary condition for the dielectric displacement yields

$$\varepsilon_0\varepsilon_{ox}E_{ox} = P_{fe} + \varepsilon_0\varepsilon_{fe}E_{fe} \quad (4.1)$$

where P_{fe} is the polarization of the ferroelectric film; ε_0 , ε_{fe} and ε_{ox} are permittivities of free space, ferroelectric film and the oxidation layer, respectively. In addition, the voltage divided by the ferroelectric film and the oxide layer should be fulfilled

$$U = E_{ox}d_{ox} + E_{fe}d_{fe} \quad (4.2)$$

with d_{fe} and d_{ox} being the thicknesses of the ferroelectric film and the oxidation layer. E_{fe} and E_{ox} are the electric fields in the ferroelectric film and the oxide layer. Combining Eqs. (4.1) and (4.2) one can derive

$$E_{fe} = \frac{\varepsilon_{ox}U}{\varepsilon_{ox}d_{fe} + \varepsilon_{fe}d_{ox}} - \frac{P_{fe}d_{ox}}{\varepsilon_0(\varepsilon_{ox}d_{fe} + \varepsilon_{fe}d_{ox})} \quad (4.3)$$

The depolarization field can be expressed as

$$E_{de} = \frac{P_{fe}d_{ox}}{\varepsilon_0(\varepsilon_{ox}d_{fe} + \varepsilon_{fe}d_{ox})} \quad (4.4)$$

It is obvious that the depolarization field becomes higher in the thinner ferroelectric films.

The thickness of the oxidation layer measured by the ellipsometry is about 2nm. Here, we assume the oxidation layer has the same thickness $d_{ox} = 2nm$, $\varepsilon_{ox} = 8$, $\varepsilon_{PVDF} = 10$, then we can apply the shear straight line technique to gain the material hysteresis loops [89,95]. The details of the shearing process consist of three steps,

- (1) The axes of the voltage U is scaled by $\varepsilon_{ox}/(\varepsilon_{ox}d_{fe} + \varepsilon_{fe}d_{ox})$.
- (2) The shear straight line $\Delta E_{fe}(P) = -Pd_{ox}/(\varepsilon_0(\varepsilon_{ox}d_{fe} + \varepsilon_{fe}d_{ox}))$ is constructed in the diagram.
- (3) To each point of the hysteresis the amount of $\Delta E_{fe}(P)$ is added.

This yields the material hysteresis $P(E_{fe})$ from $P(U)$. To get the material hysteresis $D(U_{fe})$, the voltage can be derived as $U_{fe} = U - U_{ox} = U - \frac{DA}{C_{ox}} = U - \frac{Dd_{ox}}{\varepsilon_0\varepsilon_{ox}}$. Similar to the above process, the shear straight line is constructed as $\Delta U_{fe}(D) = -Dd_{ox}/\varepsilon_0\varepsilon_{ox}$. Measured hysteresis and material hysteresis reconstructed by the shear straight line technique of LB films with 37nm and 139nm are compared in Fig. 4.3. The material hysteresis shows increased squareness ratio and the remanent polarization is higher. The change of the remanent polarization for the sample with 139nm is slight. The series oxidation layer has higher influence on the thinner samples. Nevertheless, this effect is negligible for samples thicker than 100nm. In addition, the coercive field remains unchanged since the polarization is zero at E_c and the depolarization field is zero according to Eq. (4.4).

In order to further evaluate the influence of the Al_2O_3 layer on the hysteresis loop shape of the samples, we grow the Al_2O_3 layer on the Al bottom electrodes thermally (MILA-5000 infrared lamp heating system). The Al_2O_3 layers of 8.3nm and 23nm are grown in a dry oxidation process at 500°C for different time intervals (30-120min) and their thicknesses are determined by ellipsometry. The ferroelectric films used here are prepared by LB technique with 60 monolayers and they have nearly the same thickness of 90nm. As shown in Fig. 4.4 (a), with increasing thickness of the Al_2O_3 layer, the hysteresis loops show reduced squareness ratio and tend to slant more considerably, which is the same behavior as observed in the thinner LB films and spun films due to the higher volume concentration of the oxide layer. Meanwhile, the remanent polarization decreases and the coercive field slightly increases. After reconstruction by the

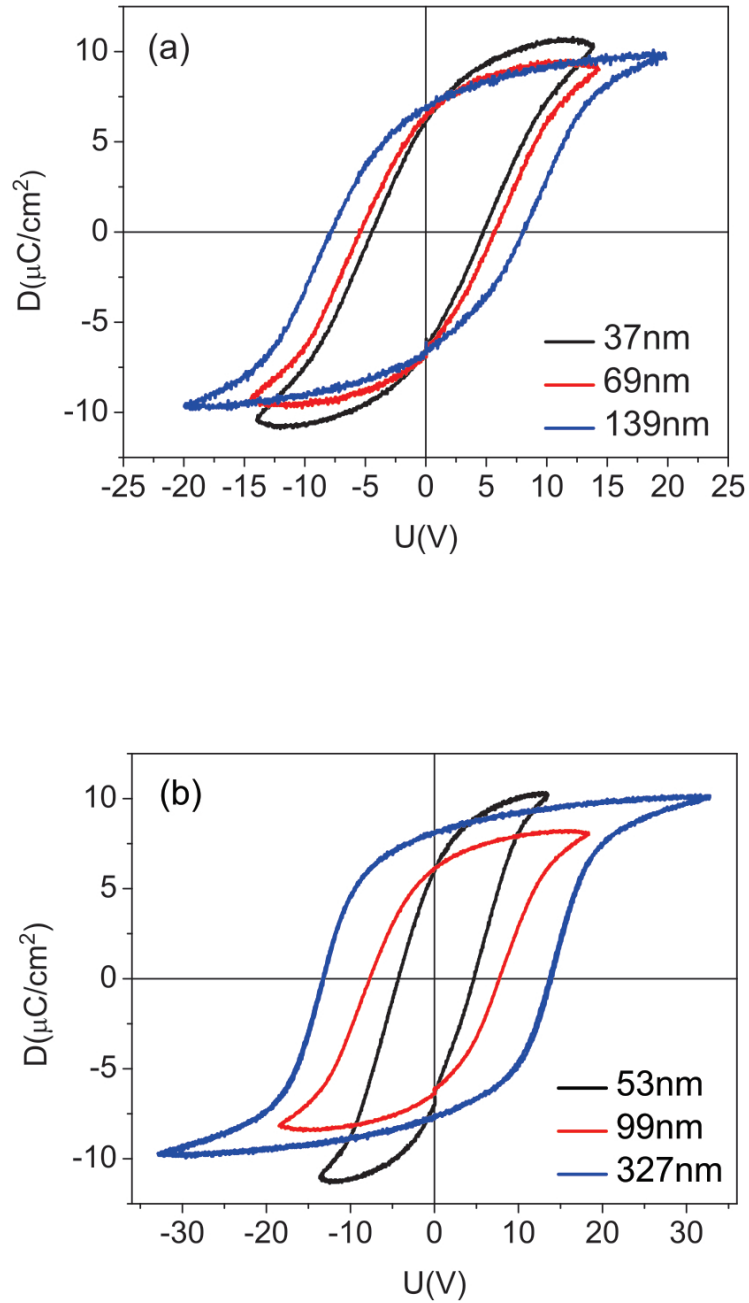


Figure 4.1: D-U hysteresis loops of (a) LB films and (b) spun films with varying thicknesses. Measurements were carried out with a triangular signal at 1 Hz.

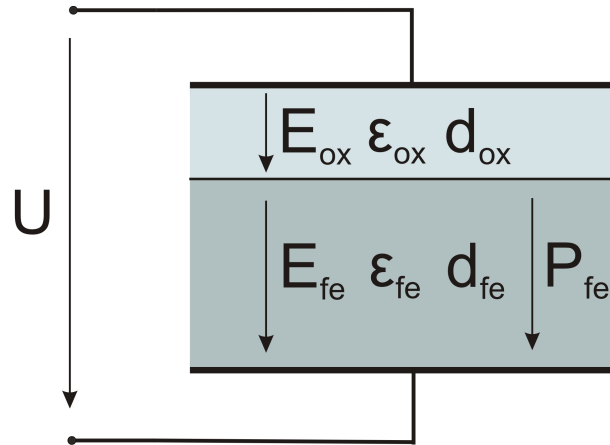
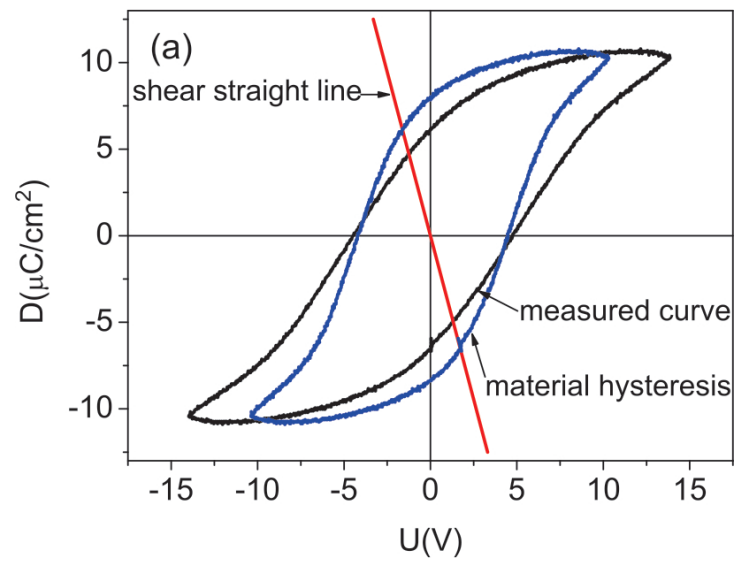


Figure 4.2: A series capacitor structure consisting of a ferroelectric film and an oxide layer.



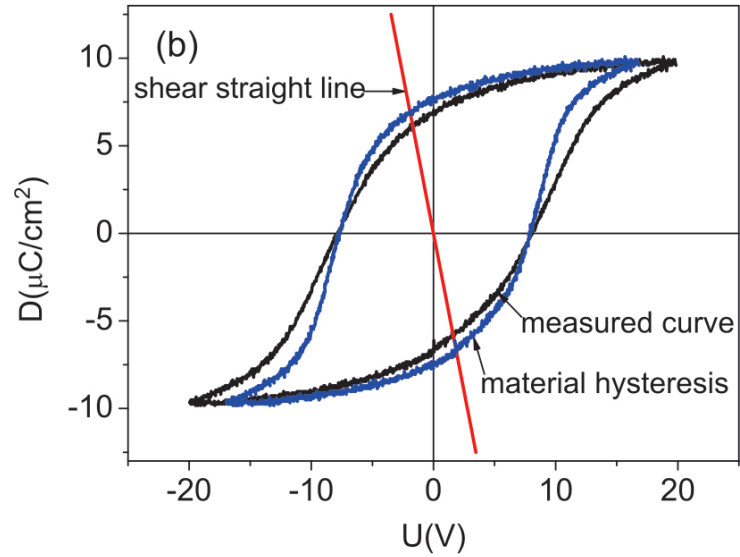
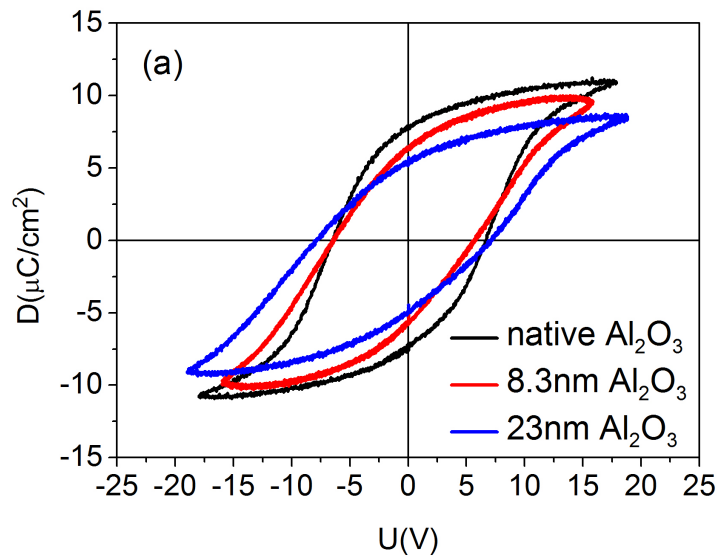


Figure 4.3: Measured hysteresis and material hysteresis reconstructed by the shear straight line technique of LB films with (a) 37nm and (b) 139nm.



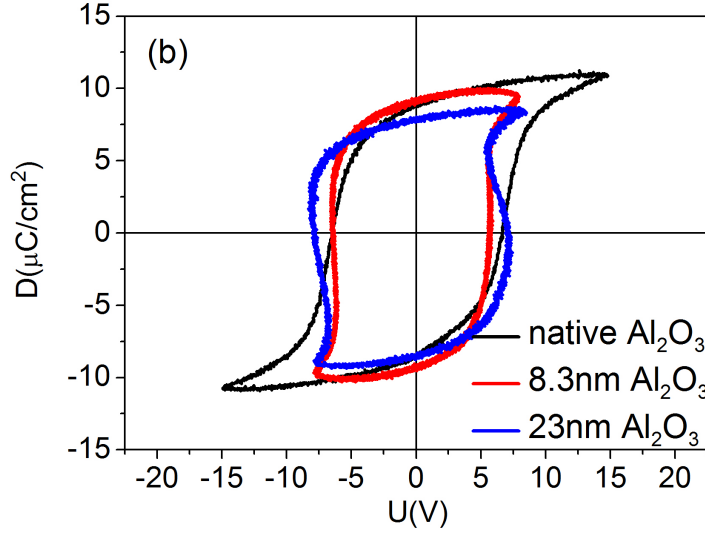


Figure 4.4: (a) Measured hysteresis loops and (b) material hysteresis loops reconstructed by the shear straight line technique for samples (LB films thickness of 90nm) with native Al_2O_3 layer and grown layer thicknesses of 8.3nm and 23nm. Measurements were carried out with a triangular signal at 1 Hz.

shear straight line technique, the material hysteresis loops for samples with different thicknesses of the Al_2O_3 layer are shown in Fig. 4.4 (b). The material hysteresis loops have an almost square shape with nearly constant remanent polarization. However, the master material hysteresis loops are not identical. For samples with thicker Al_2O_3 layer, the slope of the shear straight line $D(U) = -\varepsilon_0\varepsilon_{ox}\frac{U}{d_{ox}}$ is lower. Therefore, the amount of back shear for the material hysteresis is higher. After reconstruction, the material hysteresis of the sample with 8.3nm Al_2O_3 has a slight ‘negative slope’, which becomes more pronounced for the the sample with 23nm Al_2O_3 . This characteristic of hysteresis with a negative slope is also shown in the ‘real’ hysteresis loops in nanometer-scale ferroelectric films after excluding the depolarization field [193], which is a feature of domain structure governed mainly by electrostatics. The negative slope is also predicted in Ref. [194] for an ideal ferroelectric plate between perfect metallic electrodes with a voltage drop across thin dead layers. The large depolarization field in samples with thicker Al_2O_3 layer partly contributes to the negative slope here. In addition, the Al_2O_3 layer causes a built-in field in the sample which is shown in the later section. Therefore, the axes of the voltage U should be shifted to $U + U_{bi}$ when the external voltage is in the same direction as the built-in potential U_{bi} and should be shifted to

$U - U_{bi}$ when the external voltage is in the opposite direction to the built-in potential.

According to Arlt's electrostatic model [95], three main effects can be induced in the measured hysteresis including the slanting of the curve by the depolarization field, the shift of the hysteresis curve by the internal bias field and the change in the coercive field. Besides surface oxidation layer effects, defects and grain boundaries in thin films can also play an important role in the thickness dependence of the switching kinetics [82]. The slanting of the hysteresis curve can also be induced by the defects in the thinner films since they can behave as a non-ferroelectric second phase in the ferroelectrics. Moreover, it is believed that aluminum is a reactive electrode and it can react with PVDF to produce other layers such as AlF_3 [96]. The interaction between the PVDF dipoles and the Al electrode can cause some orientational rotation of the dipoles. Whether such influence of dipole orientation is also responsible for the inferior ferroelectric properties should be a subject of further study by using different electrode materials.

4.1.2 Coercive fields and remanent polarization

The coercive fields and remanent polarizations can be obtained from the hysteresis loops. The coercive fields of LB films and spun films are compiled in Fig. 4.5. The data of both kinds of films are comparable and exhibit an increasing coercive field with decreasing thickness. The data points have the tendency to follow a power law,

$$E_c \sim d^{-\alpha} \quad (4.5)$$

with the parameter α close to 0.58. This is the empirical rule first discovered by V. Janovec [97]. The coercive field of a LB film with 37nm is 125MV/m, which is lower than the value obtained in Ref. [21]. There is no saturation of the coercive field found in this study, the same as our previous results [21], which suggests an extrinsic switching. Meanwhile, the coercive voltages of both kinds of films, which are useful for technical applications, are also compiled in the right Y axis in Fig. 4.5. For thinner samples, the coercive voltage seems to find saturation, whereas it increases as the sample thickness increases. If the applied voltage divided by the oxide layer is excluded, the coercive voltage should increase with increasing sample thickness following a power law with an exponent about 0.4. The more pronounced influence of the oxide layer on the thinner samples accounts for the apparent saturation.

Fig. 4.6 shows the thickness dependence of the remanent polarization for both LB films and spun films. For samples from 37 to 158nm, the remanent polarization is nearly

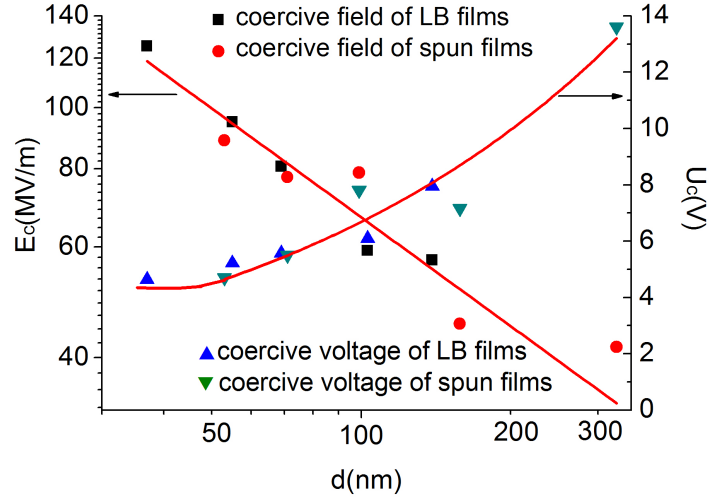


Figure 4.5: Coercive field E_c and coercive voltage U_c determined from the measured hysteresis loops versus the sample thickness. The red line for coercive field represents a fit by a power law. The red line for coercive voltage is guide for the eyes.

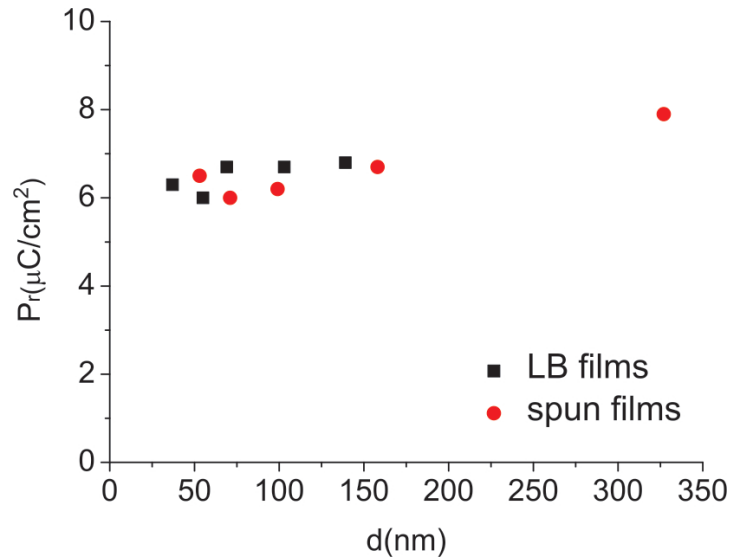


Figure 4.6: The remanent polarization P_r determined from the measured hysteresis loops of LB films and spun films as a function of the sample thickness. The data points marked as squares are LB films. The points marked as circles are spun films.

constant. The remanent polarization is slightly higher in the spun film with 327nm. Less influence of electrode effects and surface oxidation layer effects are responsible for this improvement.

4.1.3 Transient polarization

Time domain measurements of polarization reversal with the three pulse method are carried out to investigate the switching dynamics in the ferroelectric films. For thinner samples (approximately thickness less than 300nm), we observe a monotonically decreasing current in the linear scale of the current transient. The polarization switching transients can be approximately described by the stretched exponential function [21],

$$P(t) = P_s(U) \left(1 - \exp \left(- \left(\frac{t}{\tau_{tp}} \right)^\alpha \right) \right) \quad (4.6)$$

where α with $0 < \alpha \leq 1$ is a stretching factor related to the deviation of $P(t)$ from an exponential behavior. $P_s(U)$ is the switched polarization from a negative value resulting from the negative pulse to the positive polarization, which depends on the applied voltage. τ_{tp} is the switching time defined as the turning point of the transient polarization curve (Fig. 4.7). The best fit of the curve by Eq. (4.6) gives a τ_{tp} . For samples thicker than 300nm, there is a peak found in the current transient (Fig. 4.8). This peak value increases and shifts to shorter times with increasing applied voltage. The time to peak τ_p is taken as a measure for the switching time [98].

Fig. 4.7 shows typical polarization switching transients of a LB film with a thickness of 103nm under various applied voltages. At high applied voltage, the amount of reversed polarization is nearly constant. Switching is faster with increasing applied voltage. The switching curves exhibit a two step increase: a rapid increase of polarization followed by a continued slow increase over several decades. The retarded stages of the transients in the long time range are related to a field independent current of polarization and depolarization which can be interpreted by a double well model with dipoles fluctuating between two equilibrium positions. The detailed explanation is addressed in chapter 5. It should be mentioned that our system for time domain measurements can record charges in a time range from $2\mu s$. A fast jump of the polarization at times below $2\mu s$ is observed as applied voltage increases, which indicates polarization reversal starts below $2\mu s$. In the future the use of faster data acquisition systems with higher resolutions should be employed to measure shorter times [87].

Switching transients of LB films for various thicknesses measured at 150MV/m are

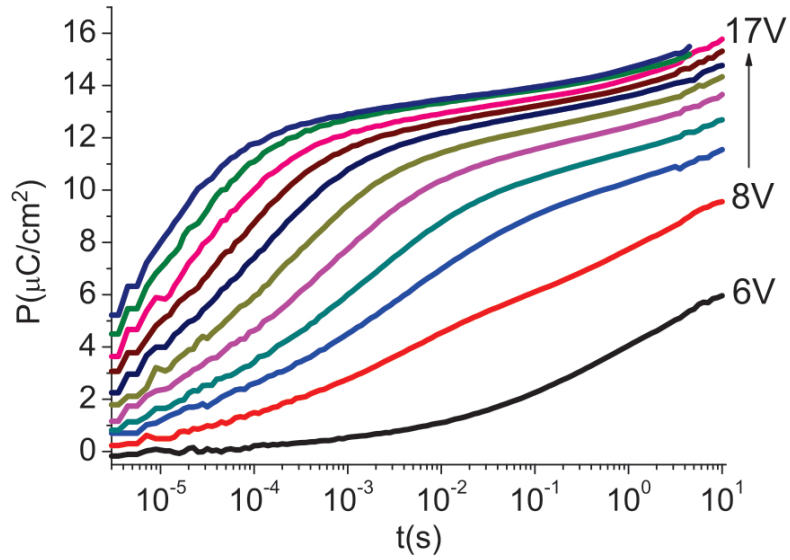


Figure 4.7: Typical polarization switching transients of a LB film with thickness of 103nm.

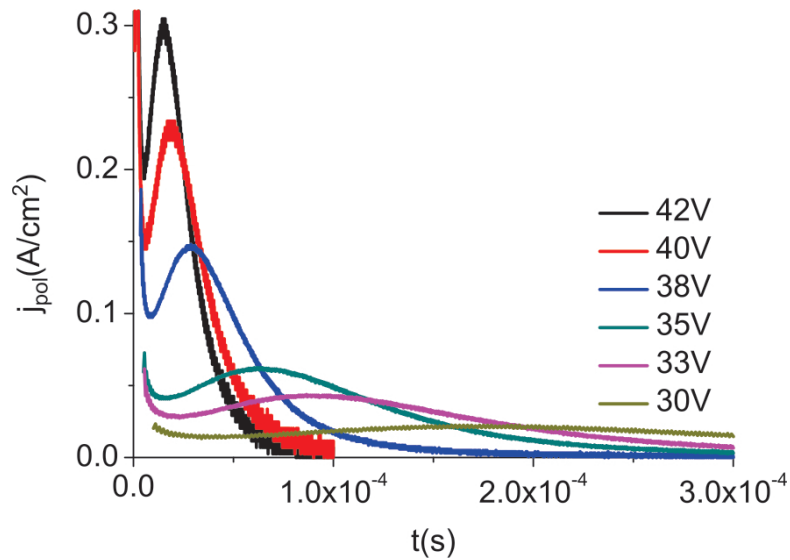


Figure 4.8: Typical current transients of a spun film with thickness of 360nm.

shown in Fig. 4.9. The thicker films exhibit faster switching at the same applied field. Besides, the transient curve is broader in thinner films. This can be due to the thickness distribution effect becoming more pronounced and higher coercive field in thinner films. The applied field is equaled to three times of the 139nm thick sample's coercive field while it is only equaled to 1.5 times of the 37nm thick sample's coercive field, as can be seen in Fig. 4.5.

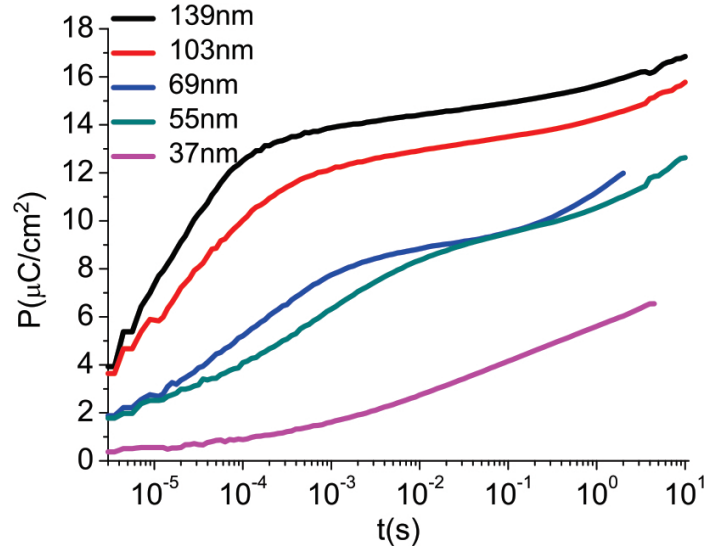


Figure 4.9: Thickness dependence of switching transients of LB films at 150MV/m.

We summarize the stretching factor α and the switching time τ_{tp} by fitting with Eq. (4.6) in terms of the normalized applied field dependences for LB films with various thicknesses in Fig. 4.10 and Fig. 4.11. The stretching factor increases with increasing sample thickness and increasing applied field. It is obvious that the transient curve is closer to an exponential shape with stretching factor closer to 1. As shown in Fig. 4.9, the thinner films have a broader transient curve related to the smaller value of α . The field dependence of the stretching factor α for different thicknesses follows an exponential law (Fig. 4.10), which is already found in Ref. [21].

The switching time, as shown in Fig. 4.11, can be described by an exponential law

$$\tau_{tp} = \tau_{tp0} \cdot \exp\left(-\gamma \frac{E}{E_c}\right) \quad (4.7)$$

where τ_{tp0} and γ depend on the sample thickness.

Samples with thickness of 37nm and 55nm show slower switching, which arises from the surface oxidation layer. As we discuss above the shear straight line effect is more

pronounced in thinner samples and a higher depolarization field results. For samples thicker than 69nm, the switching time is nearly the same at the same applied field, which indicates the switching time in LB films is nearly independent of thickness down to 69nm (Fig. 4.12).

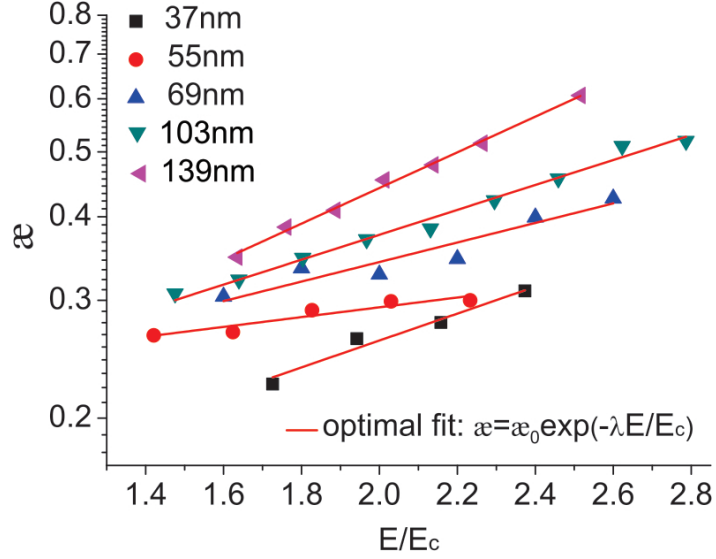


Figure 4.10: Field dependence of stretching factor α for LB films with various thicknesses. The data points are fitted with an exponential function.

For technical applications, switching time and switching voltage are of interest. From Fig. 4.13, it is found that, at the same switching time, the switching voltage first decreases then increases with increasing thickness, which indicates an optimal thickness range for low voltage operation. E.g. for sample with thickness of 69nm, the switching time is $4 \times 10^{-4}s$ at an applied voltage of 10V. This is attractive for practical applications. Moreover, the voltage dependence of the switching time follows an exponential law. The data points slightly deviate from the exponential fittings at high applied voltage and thicker films. It appears that polarization reversal is governed by the nucleation of new domains at lower applied voltage, which has an exponential dependence on voltage, and by the domain-wall motion at higher applied voltage, which has a power law or linear dependence [101].

Switching transients of spun films for various thicknesses measured at 150MV/m (Fig. 4.14) exhibit similar behavior as in LB films. The polarization curve is broadening as the thickness reduces. Their stretching factors, which are shown in Fig. 4.15, have a higher value in thicker samples and higher applied fields. Fig. 4.16 depicts the field dependence of switching time fitted by an exponential function the same as Eq. (4.7).

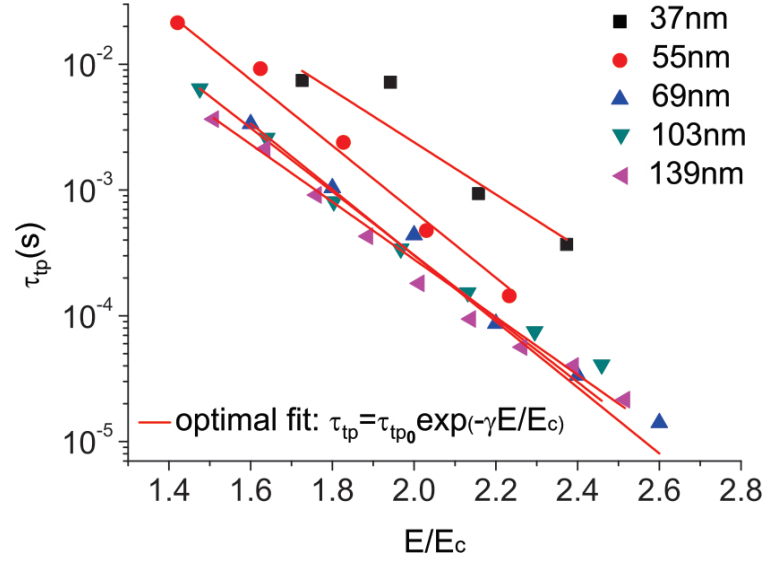


Figure 4.11: The switching time τ_{tp} of the turning point for LB films with various thicknesses as a function of the normalized applied field. Every set of the data points is fitted with an exponential function.

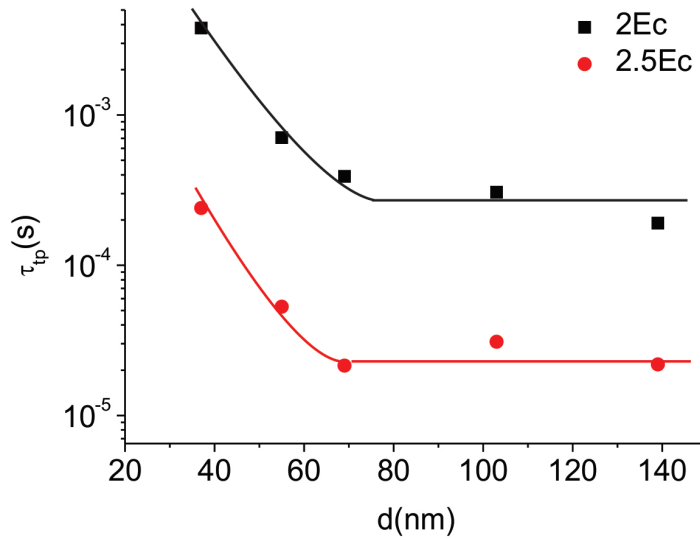


Figure 4.12: The thickness dependence of the switching time τ_{tp} at constant normalized applied fields for LB films. The lines are guides for eyes.

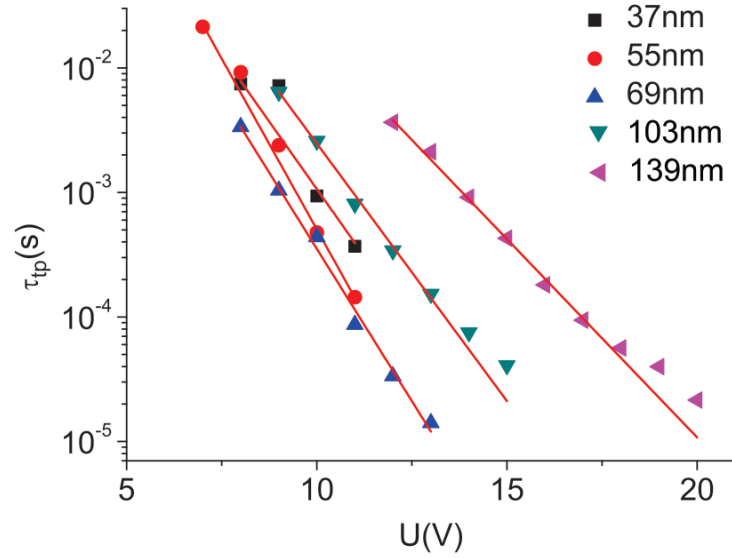


Figure 4.13: The switching time τ_{tp} of the turning point for LB films with various thicknesses as a function of the applied voltage. Every set of the data points is fitted with an exponential function.

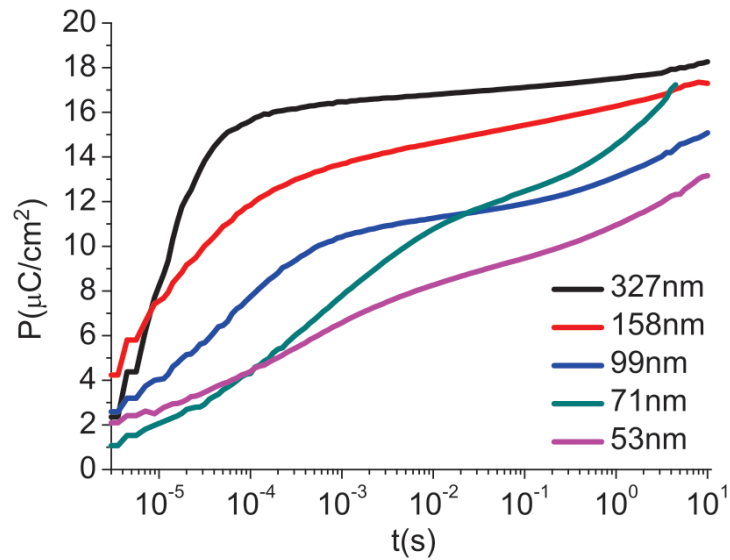


Figure 4.14: Thickness dependence of switching transients of spun films at 150MV/m.

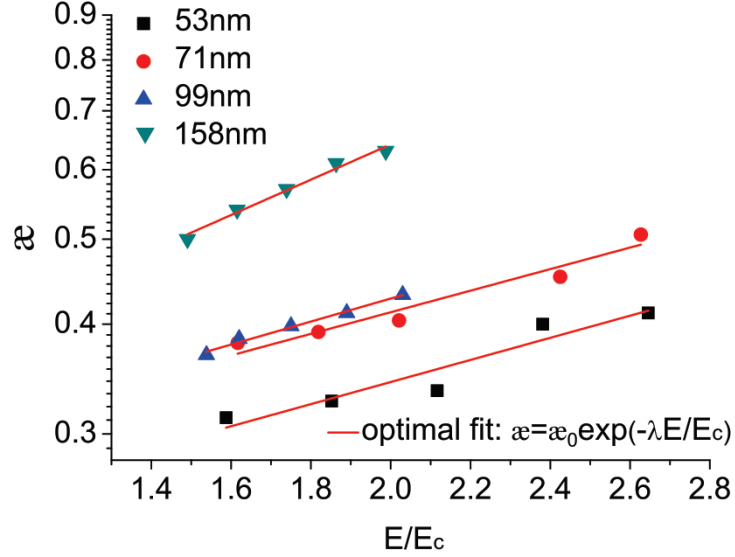


Figure 4.15: Field dependence of stretching factor α for spun films with various thicknesses. The data points are fitted with an exponential function.

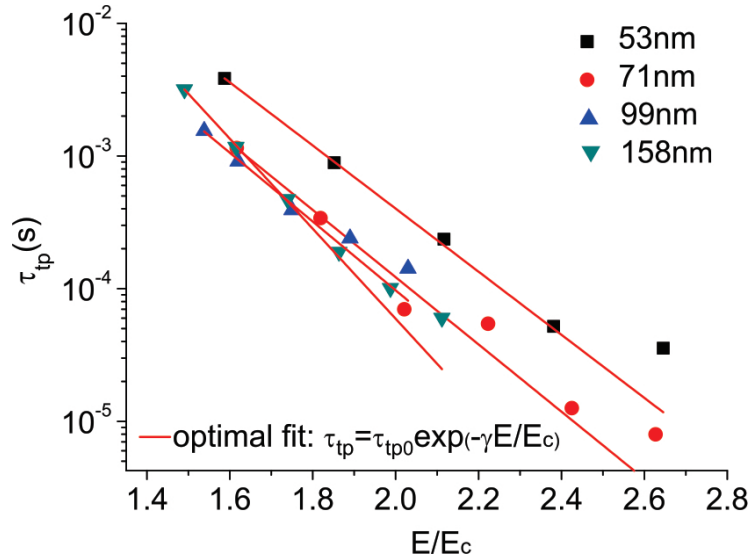


Figure 4.16: The switching time τ_{tp} of the turning point for spun films with various thicknesses as a function of the normalized applied field. Every set of the data points is fitted with an exponential function.

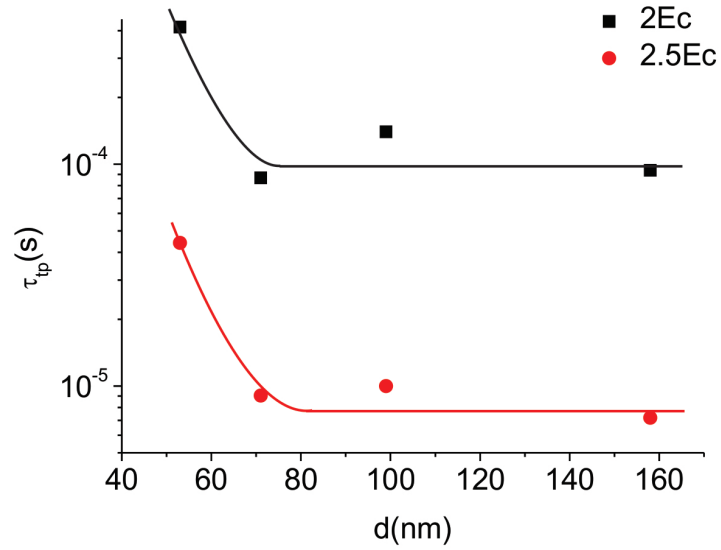


Figure 4.17: The thickness dependence of the switching time τ_{tp} at constant normalized applied fields for spun films. The lines are guides for eyes.

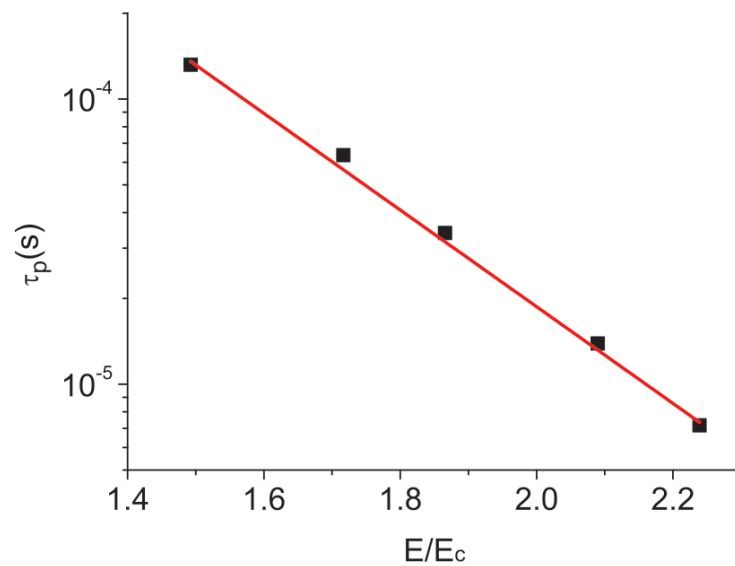


Figure 4.18: The peak time τ_p for the spun film of 327nm.

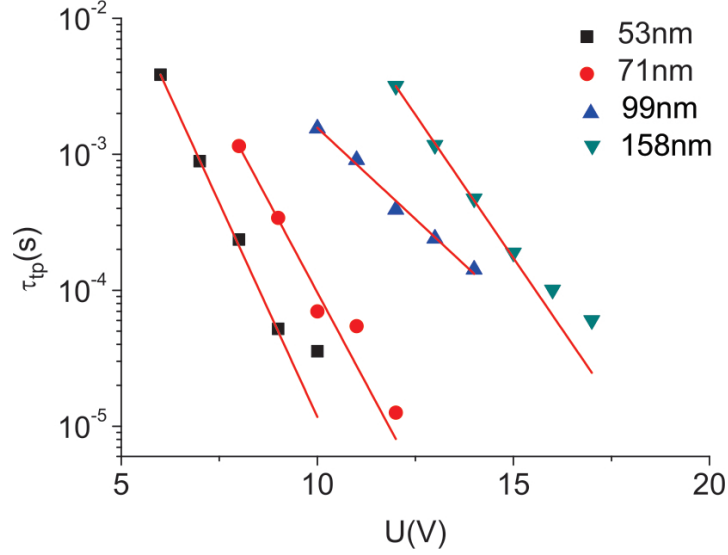


Figure 4.19: The switching time τ_{tp} of the turning point for spun films with various thicknesses as a function of the applied voltage. Every set of the data points is fitted with an exponential function.

The data points slightly deviate from the exponential fitting at high fields. Again, the sample with 53nm exhibits slower switching due to the surface oxidation layer effect (see also in Fig. 4.17). The values of switching time for spun films thicker than 71nm are very close, the same behavior as in LB films (Fig. 4.17). Furukawa et al. show that the switching time is independent of thickness down to 50nm using Au electrode in Ref. [4]; we found that the switching time is independent of thickness down to 69nm in LB films and 71nm in spun films here. Both results are consistent and the different thickness values are attributed to the different electrodes.

Since a maximum is observed in the current transient in the spun film with thickness of 327nm, the switching time can be characterized by the peak value τ_p , which also has an exponential dependence on the electric field as shown in Fig. 4.18. The slope in the exponential fitting in Fig. 4.18 characterized by γ in Eq. (4.7) has the same order as the average slopes of the fittings in Fig. 4.16.

In fact, the polarization transients for thicker samples can be approximately described by the compressed exponential function, which has the same format as Eq. (4.6) with $\varkappa > 1$. The current density can be obtained by the time derivative of the polarization,

$$j(t) = \frac{dP(t)}{dt} = P_s \frac{\varkappa}{\tau_{tp}} \left(\frac{t}{\tau_{tp}} \right)^{\varkappa-1} \exp \left[- \left(\frac{t}{\tau_{tp}} \right)^{\varkappa} \right] \quad (4.8)$$

Whether there is a peak in the current transient depends on the value of α . As can be seen in Eq. (4.8), the exponential part $\exp\left[-\left(\frac{t}{\tau_{tp}}\right)^\alpha\right]$ is a decreasing function while the power law part $\left(\frac{t}{\tau_{tp}}\right)^{\alpha-1}$ would be decreasing for $\alpha < 1$ and be increasing for $\alpha > 1$. With an increasing power function and a decreasing exponential function a current maximum is produced mathematically.

At the current peak τ_p , we have $\frac{dj(t)}{dt} = 0$ and therefore τ_p is derived as

$$\tau_p = \tau_{tp} \left(\frac{\alpha - 1}{\alpha}\right)^{1/\alpha} \quad (4.9)$$

The peak time τ_p is slightly smaller than the turning point τ_{tp} at where $\frac{\partial^2 P}{\partial(\log t)^2} = 0$ in Eq. (4.6) with $\alpha > 1$. Therefore, their exponential dependence on the field should have the same order of slope.

As shown in Fig. 4.19, samples thinner than 100nm could be operated below 10V at a relatively fast switching speed (up to $3 \times 10^{-5}s$) and therefore it is promising in practical applications. Similar to LB films, the data points slightly deviate from the exponential fitting at high applied voltages, which suggests a nucleation mechanism at low applied voltages and a domain-wall motion mechanism at higher applied voltages. Compared to LB films in Fig. 4.13, both kinds of samples with similar thicknesses exhibit almost the same switching speed at constant applied voltages.

4.1.4 Retention properties and fatigue behavior

The long term reliability including retention and fatigue behavior is an important issue for ferroelectric nonvolatile memories. For the measurement system one can refer to chapter 3. A time dependence of normalized remanent polarization for both LB films and spun films is illustrated in Fig. 4.20. In general, all the samples show similar retention decay tendency. The polarization loss consists of a slight decrease before 1000s and a rapid decrease after 1000s. The thinnest sample of 37nm has a polarization loss of 62% within 10^4s at room temperature, while the thickest sample of 327nm has a polarization loss of 51%. The difference can be due to the higher depolarization field in the thinner samples.

Retention performance at different temperatures is useful for device evaluation. In Fig. 4.21, retention characteristics of a sample with 103nm are measured from room temperature to 80°C, which is close to the upper limit of the standard temperature range for ferroelectric memory operation. As we can see here, retention is strongly temperature dependent. There is nearly no change of the retention behaviour measured

at room temperature and 40°C before 1000s. Nevertheless, the sample measured at 40°C shows faster reduction of polarization after 1000s. Almost the same retention behaviour is observed up to 60°C. When temperature reaches 80°C, we observe a significant deterioration of the remanent polarization with value almost zero after 1000s. This is because the temperature approaches the Curie point and a transition from ferroelectric to paraelectric could happen.

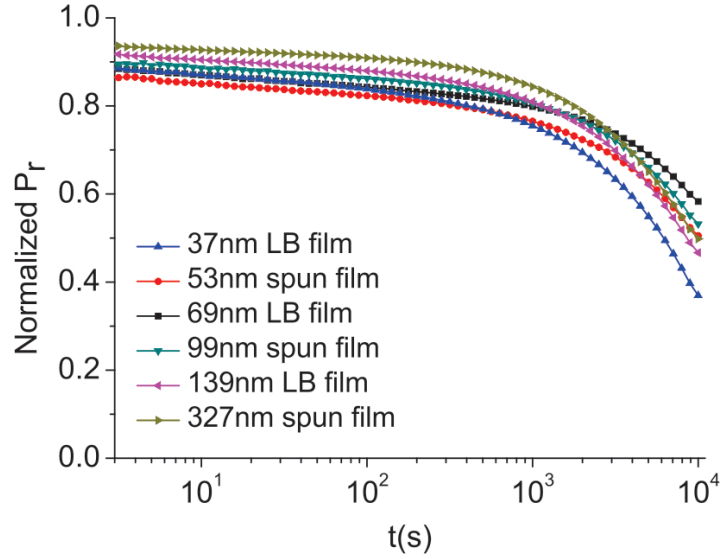


Figure 4.20: Retention characteristics of LB films and spun films with various thicknesses obtained by pulse-switching measurements.

Fig. 4.22 shows the remanent polarization degradation of P(VDF-TrFE) copolymer thin films under rectangular alternating electric fields of 150MV/m at 1 kHz. The remanent polarization of both kinds of films remains nearly unchanged after 10^3 cycles and then starts to decrease rapidly. The thicker samples exhibit a faster drop in P_r than the thinner samples. The remanent polarization of the 37nm LB film drops to 88% of its initial value after 10^4 cycles, whereas the remanent polarization of the 327nm spun film drops to 65% of its initial value after the same cycles of switching. The thinner samples show improved polarization fatigue endurance under the same electric field. In a thin sample the heat produced at each cycle can diffuse faster to the sample surface and be released faster than in a thicker sample. Considering the effect of the oxide layer, since the thermal conductivity of aluminum oxide ($18\text{W}/(\text{K}\cdot\text{m})$) is nearly 100 times higher than the thermal conductivity of PVDF ($0.19\text{W}/(\text{K}\cdot\text{m})$) and the oxide layer is much thinner than the polymer, the heat diffusion is believed to be governed by the ferroelectric layer. Both LB films and spun films have the same tendency in

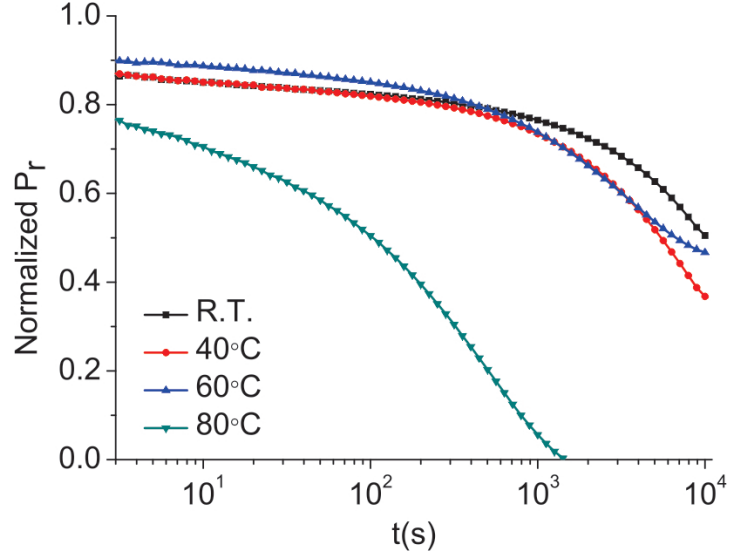


Figure 4.21: Retention characteristics of a LB film (103nm) measured at different temperatures.

remanent polarization degradation. The effect of heat generation can be illustrated in Fig. 4.23. There are some breakdown points appear in the electrode surface of the sample after fatigue measurements, as indicated by the red circles.

Fatigue endurance is usually studied by continued switching with hysteresis loops measured at the intervals of the fatigue process [102,103]. The energy loss produced in each cycle is proportional to the area of the polarization hysteresis loop. Microscopically, charge or dipole flips will produce heat energy during the switching process so as to increase the local temperature, known as ‘self-heating’. The local temperature could be very high and cannot be neglected as continued switching proceeds. However, the local temperature is very difficult to measure. We consider a waiting time between each switching pulse may somewhat release the produced heat and have an influence on the fatigue behaviour of the samples. A measurement with the same pulse amplitude and width but a waiting time of 1s between each pulse is compared with the usually continued switching measurement for two samples having similar thicknesses, as shown in Fig. 4.24. The sample measured by continued switching appears to have better fatigue endurance before 10^4 cycles. Nevertheless, the fatigue rate of the sample measured by interrupted switching slows down for longer cycles and the decrease of P_r is 30% after 10^6 switching cycles compared with 47% loss of P_r for the sample measured by continued switching. X. J. Lou et al. proposed a switching-induced charge-injection model to explain fatigue phenomenon [103]. Higher temperature may decrease fatigue

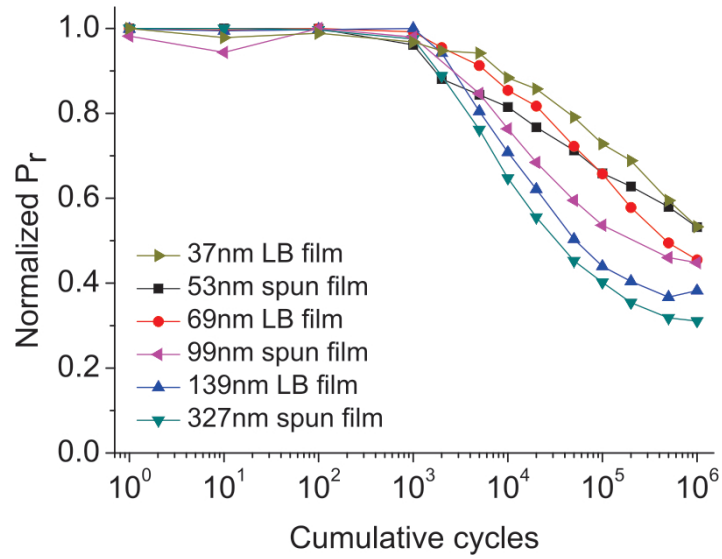


Figure 4.22: Fatigue characteristics of LB films and spun films with various thicknesses. Measurements were carried out under the cycling of an *ac* electric field of 150MV/m at 1 kHz.

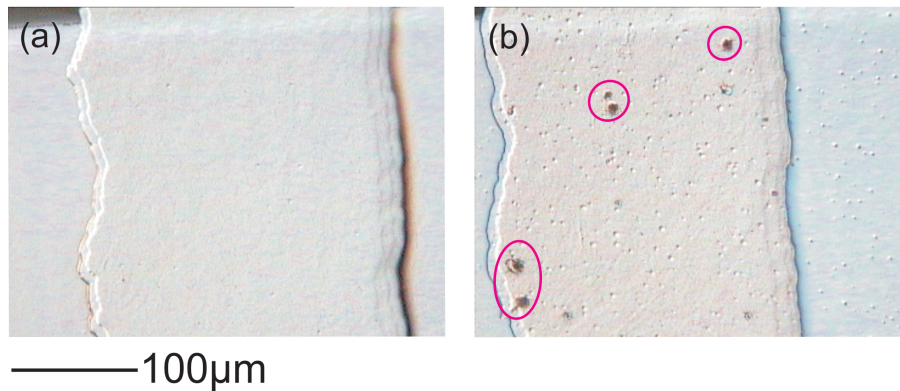


Figure 4.23: Electrode surface of a sample before (a) and after (b) fatigue measurements. The red circles indicate the breakdown points caused by the generated heat during switching.

resistivity for local phase degradation, but a lower P_r of samples at higher temperature may increase fatigue resistivity. Therefore, a qualitative interpretation of local temperature effect is difficult. However, we believe investigation of fatigue endurance under different waiting times for switching will give some guidance on read and write operations of memories in practice.

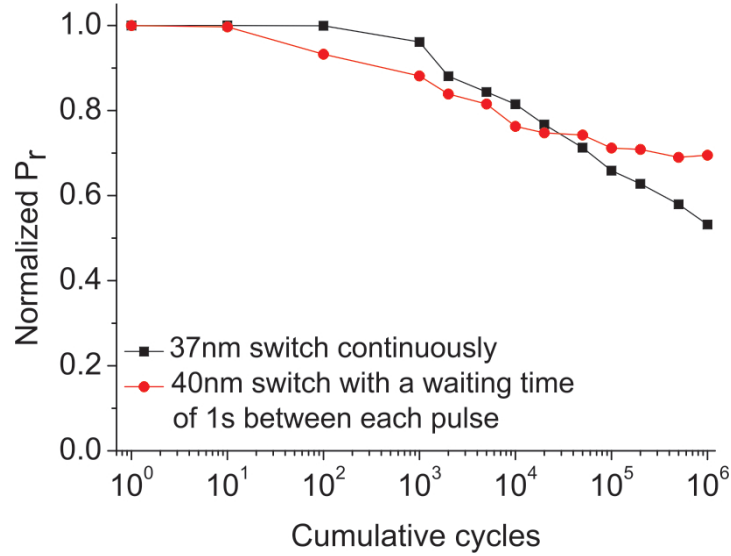


Figure 4.24: Fatigue characteristics of LB films (37nm and 40nm) measured by continued switching and interrupted switching with a waiting time between each pulse.

4.2 Electrode effects

The electrode material used in the sandwich structure (metal/ferroelectric film/metal) can be a very important factor in determining the electrical properties of the ferroelectric film. Studies of the selection and processing of electrode materials over the past decades have illustrated the electrode effects on ferroelectric device performance [104,105]. The basic function of electrodes is to provide electrical contact to the device. Ideally, the electrode should not alter the electrical properties of the ferroelectric itself. However, in many cases, the interaction between the electrode and the ferroelectric film occurs resulting in a non-ohmic contact and causing asymmetric device characteristics due to a self-biased heterojunction effect at the ferroelectric electrode interface [2]. When a ferroelectric material is considered as a wide-band-gap semiconductor, a Schottky barrier at the metal/ferroelectric interface can exist [106]. It is reported that P(VDF-TrFE) copolymer films have a n -type characteristic [107], therefore the barrier

height is described by $\phi_{Bn} = \phi_m - \chi_s$, with ϕ_{Bn} and χ_s being the metal work function and the semiconductor electron affinity, respectively. In general, the influence of electrode materials on the electrical properties of ferroelectric includes the bulk effect and interface effect [108]. The bulk effect indicates the built-in field caused by different work functions when dissimilar electrodes are used. The interface effect is due to the interaction between the electrode and the ferroelectric, e.g. diffusion, reaction and oxidation.

The criteria of consideration for the electrode choice include: (1) chemical reactivity, (2) diffusivity, and (3) leakage current and breakdown voltage. In general, the higher the work function of the metal electrode is the higher the breakdown field becomes [29]. Therefore, the metal with high work function should be chosen for the devices, e.g. platinum with a work function of about 5.3eV.

Different materials have served as electrodes for P(VDF-TrFE) films including aluminum [18,109,110], platinum [108,111], gold [92,96,112], silver [96,112], copper [108], nickel [108], indium [93], sodium [113] and conducting PEDOT/PSS copolymer [94]. For P(VDF-TrFE) films, the most commonly used electrode is aluminum. The advantages of aluminum electrode are its low deposition temperature, chemical passivation and suppressing of charge injection from the metal electrode. However, the formation of the oxide layer (Al_2O_3) between the electrode and the ferroelectric film inhibits fast switching of the films. In the early experiments, we found a serious diffusion problem in gold into the film when the samples were kept for long time. Here, aluminum, platinum and copper are chosen and a comparative study of their influence on the ferroelectric responses of P(VDF-TrFE) thin films is presented.

4.2.1 The influence of electrode effects on $P(E)$ and CV curves

The metals used for the bottom electrode (the electrode on the glass substrate) are Al, Cu and Pt and for the top electrode (the one evaporated on the free surface of the film) are Al and Cu. Pt was not used as top electrode because the high evaporation temperature of Pt would destroy the film. Here, the configuration of the samples is referred to as bottom electrode/ferroelectric/top electrode. The positive voltage is taken as that the potential of the bottom electrode is higher than the potential of top electrode. Five types of devices for Al/F/Al, Al/F/Cu, Cu/F/Al, Cu/F/Cu and Pt/F/Al are investigated. The films are deposited by Langmuir-Blodgett technique with 80ML. Comparison is made in samples having almost the same thickness between 100nm and 120nm. Fig. 4.25 shows the CV curves for samples with different configurations. The

samples with the same electrode pairs exhibit nearly symmetrical curves (Fig. 4.25(a) and (b)) while the samples with dissimilar electrode pairs show asymmetrical curves (Fig. 4.25(c) and (d)). Note that the two peaks are almost of equal height, but there is an offset in the asymmetrical curves. The work functions of Al and Cu are 4.28eV and 4.7eV, respectively. When dissimilar electrodes are used, there is a built in bias voltage pointing from the high work function electrode to the low work function electrode, i.e. $U_{bi} = (\phi_1 - \phi_2)/q$, where ϕ_1 and ϕ_2 are the work functions for the high and the low work function electrodes, respectively. In this case, the internal field points from Cu to Al. When positive voltage is applied, the total voltage would be $U - U_{bi}$ for Al/F/Cu structure and $U + U_{bi}$ for Cu/F/Al structure. As we can see in Fig. 4.25(c), there is a small offset towards positive bias indicating a negative built in voltage in the Al/F/Cu sample. In contrast, there is a small offset towards negative bias indicating a positive built in voltage in the Cu/F/Al sample (Fig. 4.25(d)). This is in accordance with the anticipation of work function difference. The offset is 1.23V in the Al/F/Cu sample and 1.4V in the Cu/F/Al sample which is higher than the difference caused by the work function. The interface effect is responsible for the larger offset. In the case of Al, electrons injected from the electrodes during the previous switching are trapped at Al/Al₂O₃ interface, causing a negative bias pointing from Cu top to Al/Al₂O₃ bottom for Al/F/Cu structure and a positive bias pointing from Cu bottom to Al/Al₂O₃ top for Cu/F/Al structure. Therefore, the apparent offset in the CV curve is the sum of the work function difference and the bias due to the oxide layer.

Fig. 4.26 shows the hysteresis loop comparisons for the samples with the same electrodes (Fig. 4.26(a)) and dissimilar electrodes (Fig. 4.26(b)). The Al/F/Al and Cu/F/Cu samples have almost symmetrical hysteresis. The coercive voltage U_c is slightly lower which is also indicated in the CV curve and the remnant polarization P_r is higher using the higher work function metal Cu. Besides, the hysteresis of Al/F/Al sample is more slanted. This is due to the depolarization effect caused by the oxide layer between Al and the film. Again, we see the asymmetrical hysteresis in Al/F/Cu and Cu/F/Al samples with positive shift in Al/F/Cu and negative shift in Cu/F/Al (Fig. 4.26(b)), which are consistent with the CV measurements. Their remnant polarizations are comparable. The asymmetry is caused by the work function difference combined with the interfacial effect. It should be noted that the shifts of both CV and PV curves are polarity dependent. If negative voltage is applied, the curve will shift to the opposite direction. Since the shift of the direction depends on the total voltage being $U + U_{bi}$ (the applied voltage has the same direction as the built in voltage) or $U - U_{bi}$ (the applied voltage is in the opposite direction of the built in voltage). The Pt/F/Al

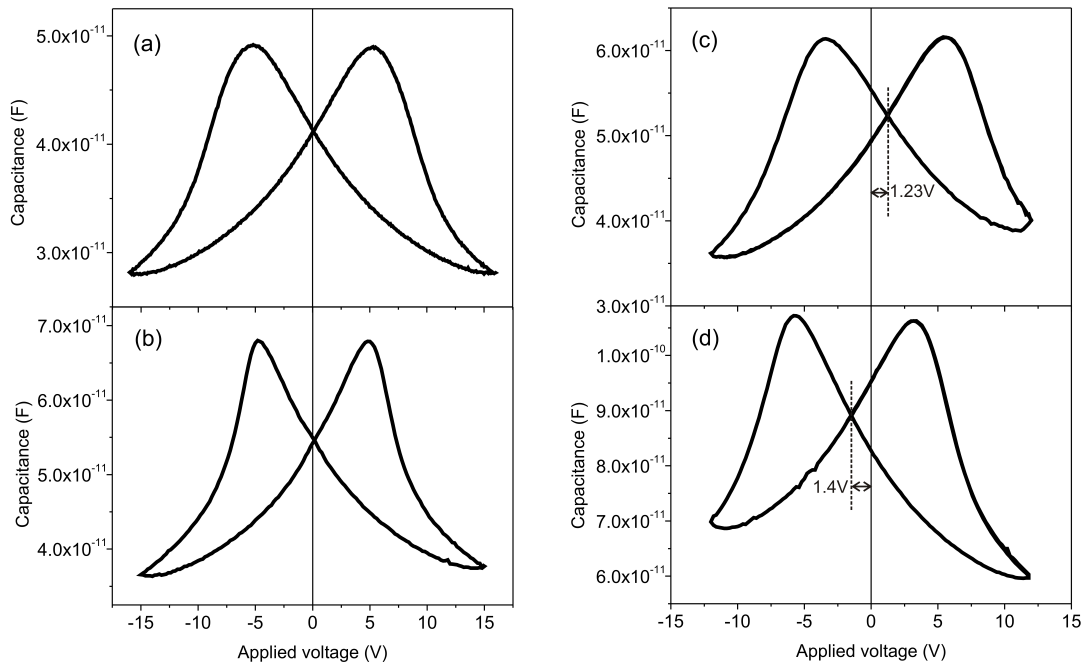
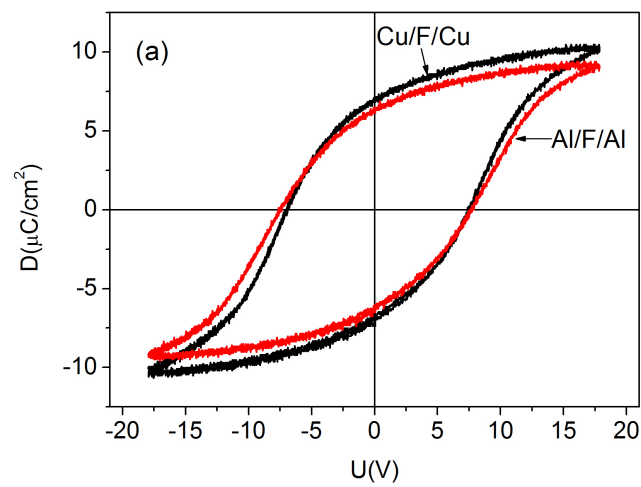


Figure 4.25: The capacitance versus applied voltage for (a) Al/F/Al, (b) Cu/F/Cu, (c) Al/F/Cu and (d) Cu/F/Al samples.



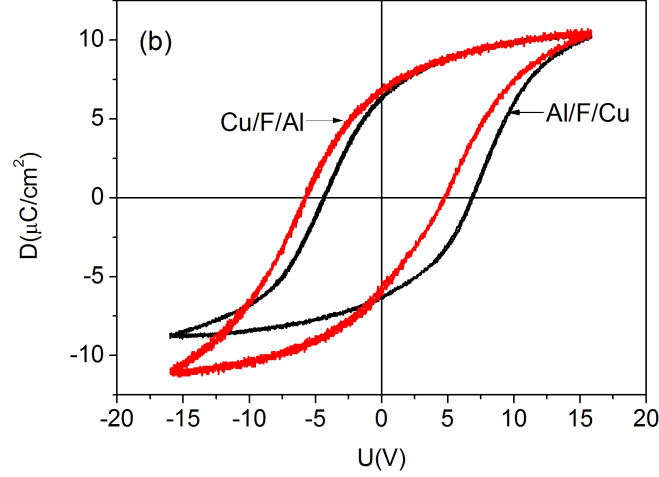


Figure 4.26: Hysteresis loops for (a) Al/F/Al and Cu/F/Cu, (b) Al/F/Cu and Cu/F/Al samples. Measurements were carried out with a triangular signal at 1 Hz.

sample shows similar results with asymmetrical butterfly loop and hysteresis loop.

4.2.2 The influence of electrode effects on switching transients

The main disadvantage of Al electrodes is the inhibition of fast switching due to the depolarization field induced by the surface oxide layer. The reported fastest switching time is 25ns for a 20nm thick P(VDF-TrFE) film under an electric field of 840MV/m using Au electrodes [92]. However, this switching behaviour is only limited in fresh samples since Au will diffuse to the films as samples kept for longer time. Beside, the applied voltage should have a pulse width in microsecond range to avoid electric breakdown due to the short circuit problem. The fast switching behaviour of P(VDF-TrFE) films using other electrode materials is seldom reported. The possibility of decreasing switching time using Cu and Pt electrodes is the main concern here.

Fig. 4.27 shows the comparison of the polarization build up for the samples with dissimilar electrode pairs. The switching curves for the Al/F/Cu and Cu/F/Al system can also be described by the stretched exponential function using Eq. (4.6). Switching speed increases with increasing applied voltages. The switchable polarization saturates at high applied voltages. Other systems including Al/F/Al, Cu/F/Cu, and Pt/F/Al have similar switching curves. The switching time of the turning point τ_{tp} and the stretching factor α for the five systems are extracted from the fitting with Eq. (4.6),

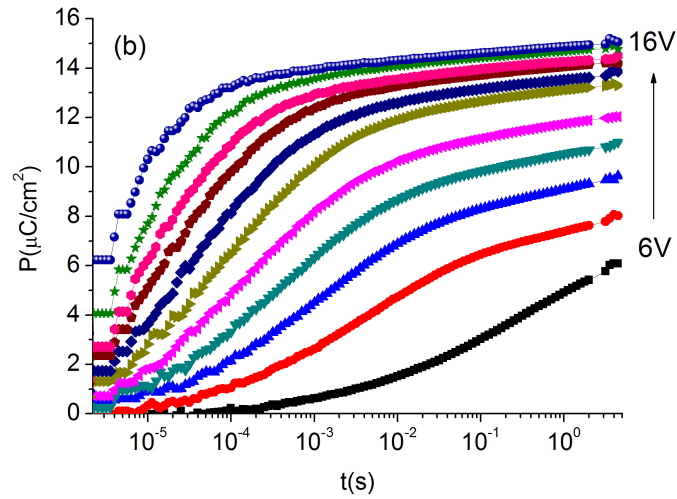
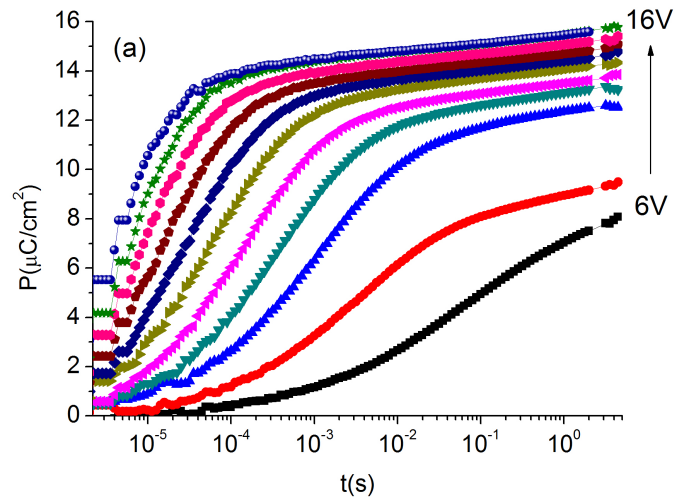


Figure 4.27: Polarization switching transients for the samples with dissimilar electrode pairs (a) Al/F/Cu and (b) Cu/F/Al.

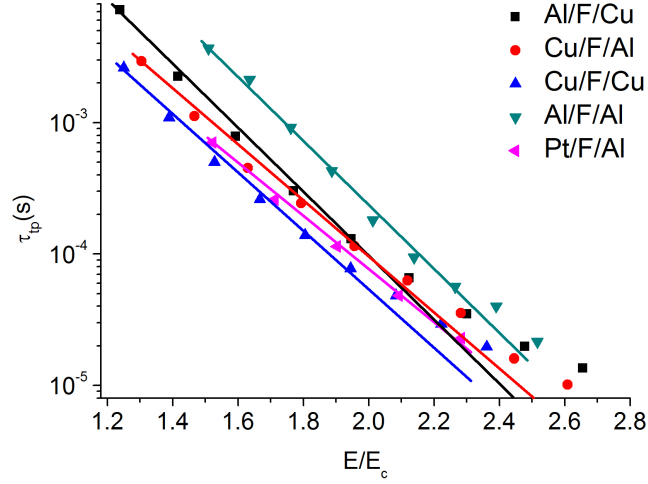


Figure 4.28: The switching time τ_{tp} of the turning point for samples with different configurations as a function of the normalized applied field. Every set of the data point is fitted with an exponential function, $\tau_{tp} = \tau_{tp0} \exp(-\gamma E/E_c)$.

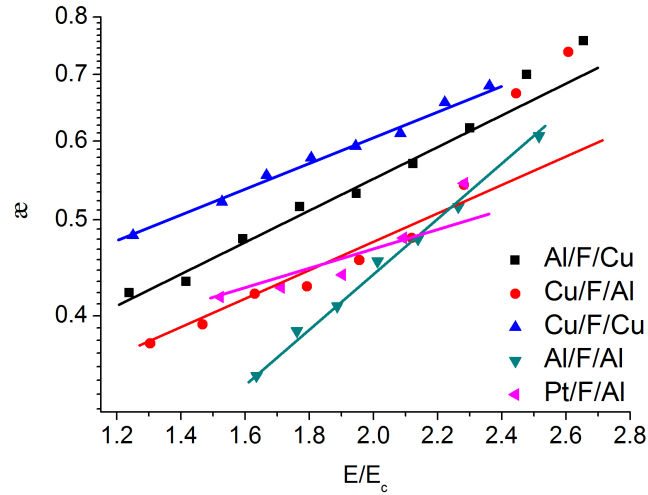


Figure 4.29: Field dependence of stretching factor æ for samples with different configurations. The data points are fitted with an exponential function $\text{æ} = \text{æ}_0 \exp(-\gamma E/E_c)$.

as shown in Fig. 4.28 and Fig. 4.29. Every set of the switching time can be fitted by the exponential function of Eq. (4.7). Slight deviations of the data points from the exponential fittings at high applied fields are observed. The switching time for samples with higher work function metal electrodes exhibit faster switching. The Al/F/Al sample shows the slowest switching at the same normalized applied field. Switching time can be reduced by just replacing either electrode with a higher work function metal. Under the positive pulse, Pt/F/Al and Cu/F/Al systems have shorter switching time than the Al/F/Cu system due to the positive built-in field. The stretching factors for all the samples have exponential dependence on the applied field (Fig. 4.29). The Cu/F/Cu sample has the highest stretching factor at the same normalized applied field, which indicates the switching curve is closer to an exponential shape. The higher the work function of the metal electrode is, the thinner the oxide layer becomes. Therefore the smaller the depolarization field is according to Eq. (4.4) and the faster the switching speed could achieve, which is also revealed in Fig. 4.33 in the next section.

4.3 Influence of dielectric layer

It is well known that there is an oxide layer grown on the surface of aluminum. The Al_2O_3 layer has a low dielectric constant around 8 which is less than the dielectric constant of P(VDF-TrFE) film (10-12). During the application of external voltage, part of the applied voltage will drop on the oxide layer. Even a very thin low dielectric constant layer can have a pronounced effect on the dielectric and ferroelectric responses of the device [2]. A ferroelectric with an interface layer can be modeled by two capacitors in series [95,114], which is illustrated in Fig. 4.30. The interface layer can have a non-switchable polarization P_1 . For a simplified model, the interface layers at both the top and bottom electrodes can be combined and represented electrically as a single layer with a thickness equal to the sum of the interface layer thicknesses. According to this model, the total capacitance of the sample, which is expressed as $\frac{1}{C} = \frac{1}{C_i} + \frac{1}{C_f}$, with C_i and C_f being the capacitance of the interface layer and the ferroelectric film respectively, is reduced. The effect becomes more pronounced the thinner the sample is and it is responsible for a lower peak in the thermal hysteresis of capacitance for a thin sample [85].

A shifted and slant hysteresis loop caused by the oxide layer has been discussed in section 4.1. Besides the hysteresis loop, the oxide layer can also influence the CV characteristics and switching transients of the sample. Fig. 4.31 shows the CV curves for samples with different thicknesses of Al_2O_3 layer while P(VDF-TrFE) film thickness

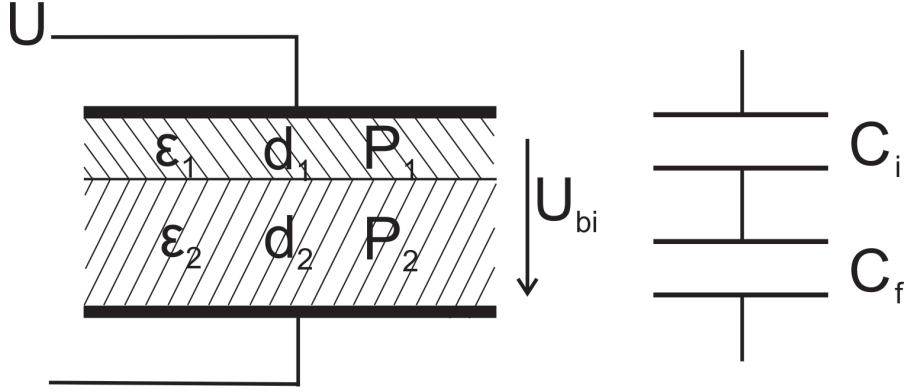


Figure 4.30: The two layer capacitor model and the electrical representation of a ferroelectric capacitor in series with an interface layer.

is kept almost the same of 90nm. The high potential output was connected to the top Al electrode. There is a small positive offset for samples with grown Al_2O_3 layer which indicates a negative built-in field pointing from Al/Al_2O_3 bottom to Al top. The built-in field increases with increasing Al_2O_3 layer thickness. This is consistent with the work function measurements by AFM on different sample surfaces. In the Kelvin probe force microscopy mode of AFM, the contact potential difference, that is, the difference between the work functions of the sample and of the tip of the microscope, can be locally measured, which is defined as: $U_{CPD} = (\phi_{sample} - \phi_{tip})/e$ [66]. ϕ_{sample} and ϕ_{tip} are the work functions of the sample and tip, and e is the electronic charge. The results reveal that there is an increase of the work function by about 0.4eV for sample with Al_2O_3 layer of 9nm and by about 0.5eV for sample with Al_2O_3 layer of 17nm.

Fig. 4.32 shows the polarization switching transients for the samples with different thicknesses of Al_2O_3 layer. Since the total thickness is different in different samples, a pulse strength of two times of the sample's coercive voltage determined from the hysteresis loop was applied on each sample. The sample with native Al_2O_3 layer exhibits a faster switching. The switching curve becomes broader with increasing the thickness of Al_2O_3 layer which is caused by the depolarization field. The switching time of the turning point is extracted and the comparison for different samples is shown in Fig. 4.33. Each set of the data points can be fitted by the exponential law of Eq. (4.7). The switching time increases with increasing the thickness of Al_2O_3 layer at the same normalized applied field. This is due to, first, the applied voltage (U_a) is divided into the voltage across the ferroelectric film (U_f) and that across the oxide layer (U_i), which

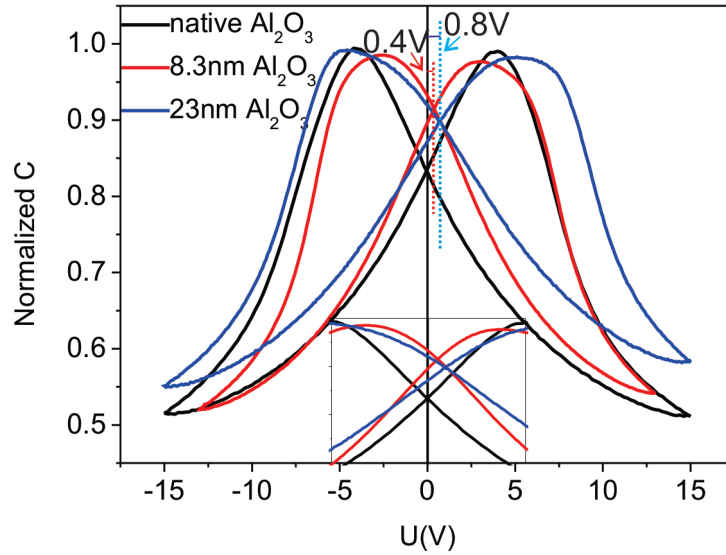


Figure 4.31: CV curves for samples (LB films with thicknesses of 90nm) with native Al_2O_3 layer and grown Al_2O_3 layer thicknesses of 8.3nm and 23nm. The inset shows the enlargement for the offsets.

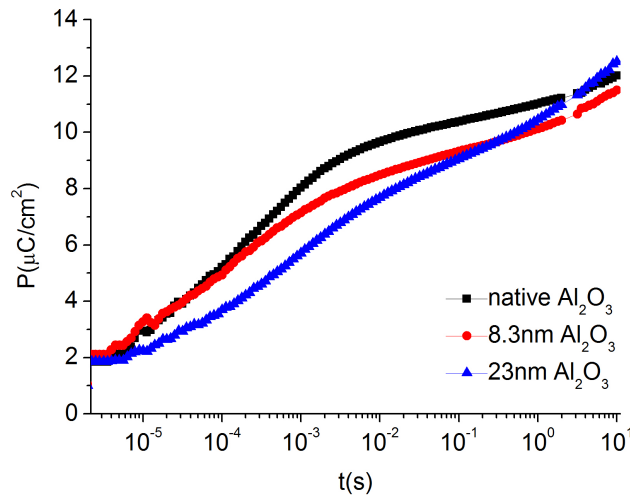


Figure 4.32: Polarization switching transients for the samples (LB films with thicknesses of 90nm) with native Al_2O_3 layer and grown Al_2O_3 layer thicknesses of 8.3nm and 23nm at applied voltages of two times of the samples' coercive voltages.

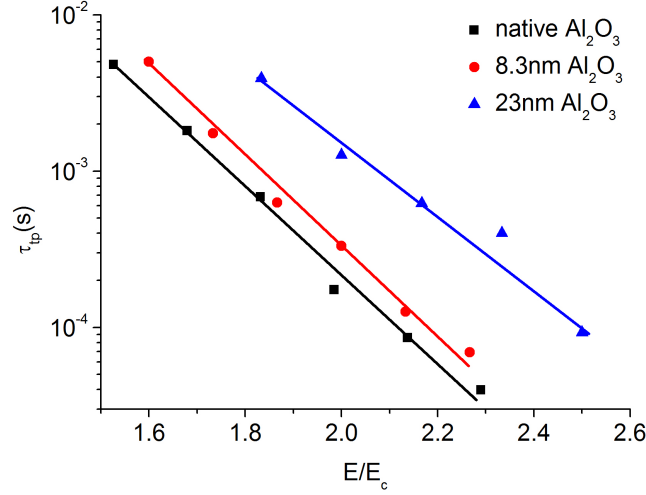


Figure 4.33: Field dependence of the switching time τ_{tp} of the turning point for samples (LB films with thicknesses of 90nm) with native Al_2O_3 layer and grown Al_2O_3 layer thicknesses of 8.3nm and 23nm. The data points are fitted with an exponential function $\tau_{tp} = \tau_{tp0} \exp(-\gamma E/E_c)$.

has the relation of $U_a = U_f + U_i$. The voltage drop on the oxide layer is the higher the thicker the oxide layer is. Furthermore, the depolarization field according to Eq. (4.4) is also the higher the thicker the oxide layer is.

4.4 Frequency and amplitude dependence of $P(E)$

4.4.1 Frequency dependence of $P(E)$

For extrinsic switching, ferroelectrics do not exhibit well-defined coercive fields generally [115]. Activation of nucleation permits switching at arbitrarily small fields if enough time is given. Switching experiments are typically carried out with an ac field therefore the apparent coercive field is actually a function of frequency. The extrinsic coercive field determined experimentally from hysteresis loop measurements is much smaller (less than 10%) than the intrinsic value predicted by Landau-Ginzburg (LG) theory [19,116]. For the applications of non-volatile ferroelectric random access memories, the coercive field at a specific frequency determines the lowest operational voltage, which is of fundamental interest for the extraction of parameters for write- and read-cycles including applied voltage and pulse length.

Fig. 4.34 presents the hysteresis loops for a 580nm-thick spun film measured at a

frequency from 10 Hz to 100 kHz with triangular signal. Limited to the experimental conditions, triangular signal with frequency > 100 kHz is not achievable. The hysteresis widens and the coercive field increases as increasing frequency firstly. Moreover, the remnant polarization is almost independent of frequency below the frequency of 5 kHz. As the frequency further increases, the hysteresis starts to shrink and the coercive field is reduced. The remnant polarization also starts to decrease above 5 kHz. The shape of the hysteresis loop depends on the competition of the dipole switching time and the period of the external signal. If the switching time is shorter than about a quarter of the period, the sample is completely switched and the remnant polarization should be independent of frequency. As the frequency increases, the dipoles become more difficult to catch up with the external signal and a higher coercive field is expected. Otherwise, at high frequencies where the switching time is longer than about a quarter of the period the switching of the dipoles is suppressed and the amount of the switched polarization depends on the period. As the frequency further increases, both the coercive field and remnant polarization decrease and a shrunken hysteresis should be observed.

For comparison, the hysteresis loops measured with sinusoidal signal at a frequency from 10 Hz to 1 MHz are shown in Fig. 4.35. The hysteresis also depends on the pulse shape. In general, the sinusoidal input signal has a higher derivative at 0V and remains near its amplitude for a comparatively longer time. As we can see in Fig. 4.35, the frequency dependence of hysteresis has a similar tendency as that measured with triangular pulse. The hysteresis widens and the coercive field increases as increasing frequency below 5 kHz. At frequency higher than 5 kHz, the hysteresis shrinks and the coercive field decreases. At frequencies up to 1 MHz, the hysteresis has a nearly linear behaviour which indicates dipole switching is almost impossible here. The coercive field extracted as half width of the hysteresis at different frequencies for both triangular and sinusoidal input signals is depicted in Fig. 4.36. The coercive field first increases with increasing frequency in both cases. After reaching to a peak value at around 5 kHz, the coercive field decreases with increasing frequency. The switching time can be estimated of $\sim 10^{-4}$ s according to the peak position, which is consistent with the switching transient measurement in time domain. The coercive field has a slightly higher value and increases faster when sinusoidal pulses are applied.

When the switching time is shorter than a quarter of the period of the external signal, the empirical relationship between the coercive field E_c and frequency f can be expressed as [117]

$$E_c = C f^\beta \quad (4.10)$$

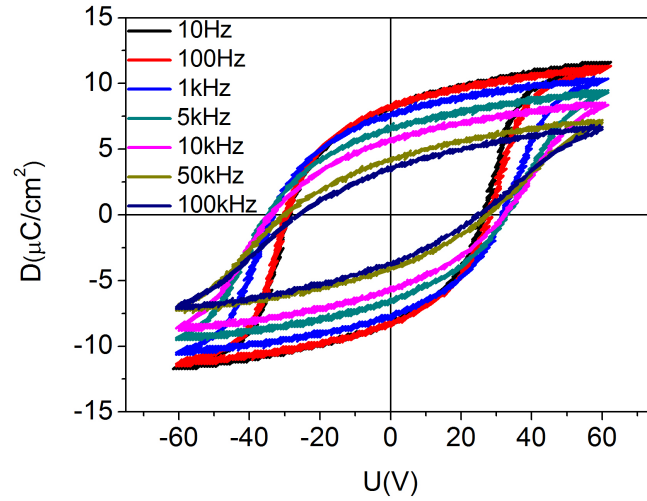


Figure 4.34: Hysteresis loops of a 580nm-thick film as a function of frequency using triangular pulses.

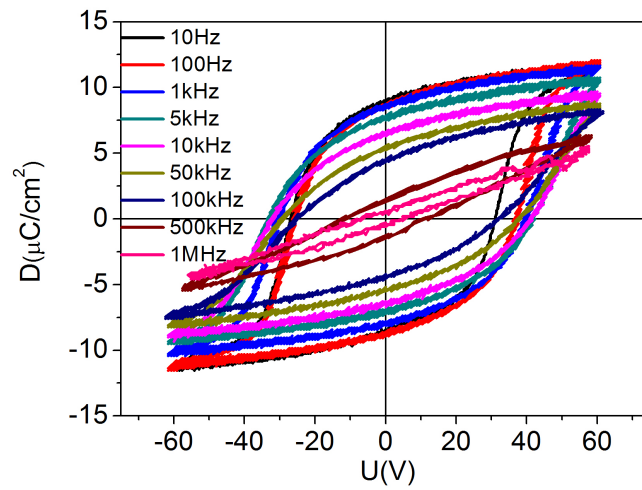


Figure 4.35: Hysteresis loops of a 580nm-thick film as a function of frequency using sinusoidal pulses.

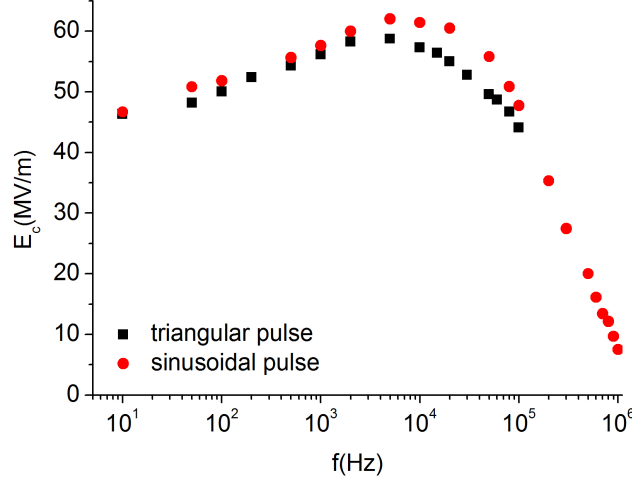


Figure 4.36: Coercive field as a function of frequency for a 580nm-thick film using triangular pulses and sinusoidal pulses.

where C is a constant, β is equal to $n/6$ with n being the effective dimensionality (can be a non-integer value if the system is a mixture of different dimensionalities) of the system in the Kolmogorov-Avrami-Ishibashi (KAI) theory. This relationship predicts E_c increases with increasing f . The linear fit of the frequency dependence of E_c when the sample has completely switched in the log-log scale plot (Fig. 4.37) gives a β value of 0.042 for triangular input and a β value of 0.046 for sinusoidal input, which are much smaller than the value (between $1/6$ and $2/6$) predicted above. The presence of defects or the clamping effect due to the substrate can reduce the effect dimensions and therefore results in a lower value of β . In the case of aluminum electrode, the depolarization field caused by the oxide layer which suppresses the switching can also contribute to the lower values of β . Some studies show that the frequency dependence of E_c in the ferroelectric thin films is not clear yet. For example, in $\text{SiBi}_2\text{Ta}_2\text{O}_9$ films with Pt electrodes, the exponent β is about 0.1 [118], while the value is about an order of magnitude less in BaTiO_3 [119] thin films and PZT 40/60 epitaxial thin films [120]. W. Li et al proposed an exponential dependence on frequency with respect to coercive field in epitaxial PZT thin films, which differs from the empirical power-law relationship. Their calculation was based on the pulse switching polarization transient measurements combined with hysteresis loop measurements [121]. However, in our case, the exponential relationship is less applicable. The increase of E_c with increasing frequency can be well described by the Weiss mean field model taking into account the

piezoeffect [179].

It should be noted that in the high frequency hysteresis loop measurements using Sawyer-Tower circuit, the series resistance in the circuit and the input impedance of the digitizer (here it is oscilloscope in our measurement setup) have to be considered. Prior measurements show that if the series resistance is too high, the output signal will be heavily distorted. As shown in Fig. 4.38, the hysteresis loop has a distortion as the input signal frequency increases. Similar results can be found in Ref. [122], considering the resistive leakage from the reference capacitor.

This behaviour can be modeled by the well-known circuit simulator SPICE. A dummy circuit consists of a linear capacitor C_1 of 33pF which is close to the capacitance value of the sample, a series reference capacitor C_2 of 100nF, which is more than 100 times larger than C_1 and a series resistor R_1 of 50 Ω , as shown in Fig. 4.39. At the output node, the oscilloscope has an input impedance of 1M Ω (R_3) buffered with a capacitor C_3 of 13pF. Two cases are considered: the reference capacitor C_2 connects to a 50 Ω terminator R_2 (Fig. 4.39(a)) and the reference capacitor C_2 is grounded (Fig. 4.39(e)). The input signal is a symmetric triangular wave. In the first case, the output signal becomes distorted with increasing the input frequency, as shown in Fig. 4.39(b), (c) and (d). The distortion is the more pronounced the higher the frequency is. On the contrary, there is no distortion in the output signal in the second case (Fig. 4.39(f), (g) and (h)). The capacitor C_1 has an ideal linear dependence of the applied voltage with respect to the charge.

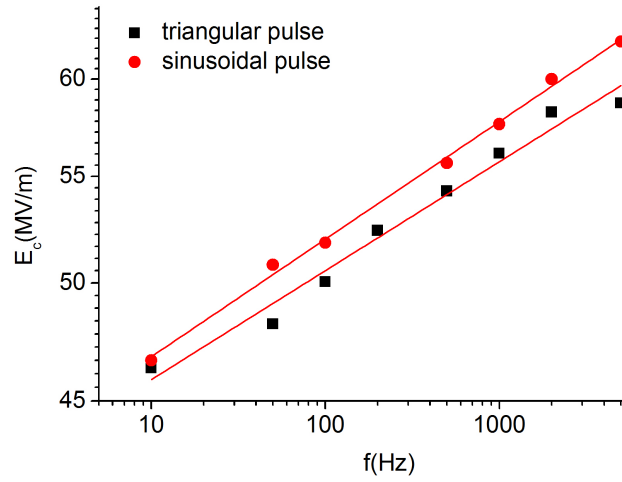


Figure 4.37: log-log scale plot of coercive field versus frequency. The data points are fitted with the power law of Eq. (4.10).

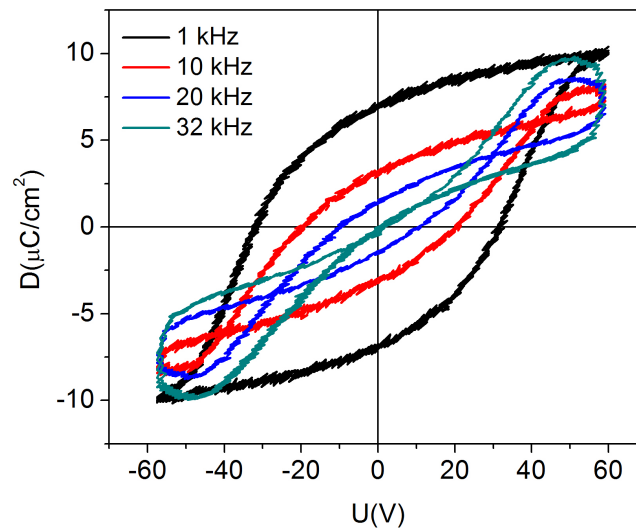


Figure 4.38: Distorted output signal at high frequencies using a triangular wave.

Chapter 4. Ferroelectric properties of P(VDF-TrFE) thin films

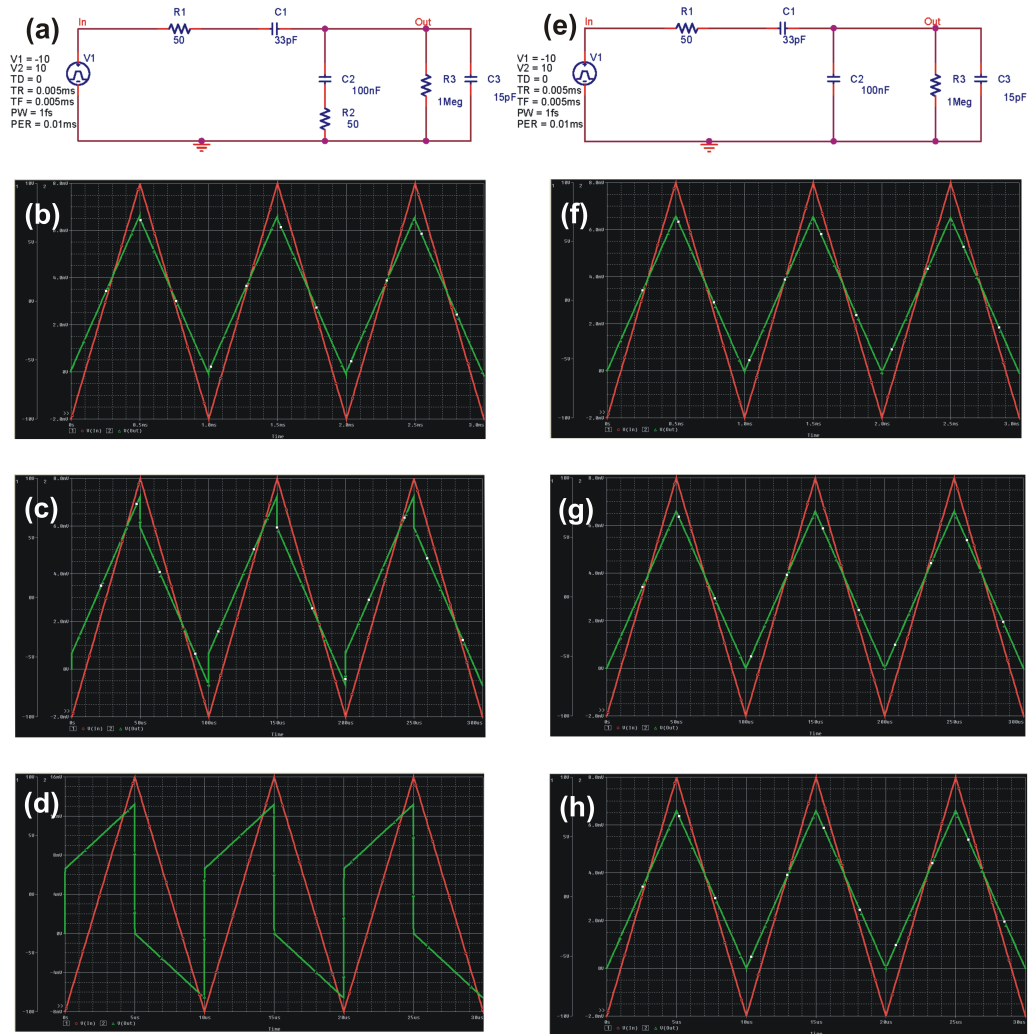


Figure 4.39: Dummy circuit (a) with series resistor R_2 and (e) without series resistor R_2 . Respond signal of dummy circuit (a) at (b) 1 kHz, (c) 10 kHz and (d) 100 kHz. Respond signal of dummy circuit (e) at (f) 1 kHz, (g) 10 kHz and (h) 100 kHz. The red line indicates the input voltage and the green line indicates the output voltage.

4.4.2 Amplitude dependence of $P(E)$

In addition to frequency, the amplitude of the input signal affects the observed hysteresis loop. Coercive field is also a function of the amplitude of the applied field. Fig. 4.40 shows a set of hysteresis loops with a variety of electric field amplitudes. With increasing the amplitude of the applied field, the hysteresis loop widens and the coercive field increases. The hysteresis loop almost gets saturation at an applied voltage of 40V. The slope at a given field is nearly independent of the applied field amplitude for saturated loops. In high field region, the increase of polarization is due to electronic polarization. It has been reported that the coercive field depends on the maximum electric field by [123]

$$E_c = \frac{1}{3}(\varepsilon_r + 2)pN\alpha \left(1 - \frac{T}{T_c}\right)^{3/2} \tanh\left(\frac{\lambda p E_{max}}{kT}\right) \quad (4.11)$$

where ε_r is the dielectric constant, p is the dipole moment per unit volume, N is the number of dipoles, α is a coefficient measuring the tendency of the dipoles to align in one direction, λ is the correction factor and T is temperature. For a given sample, all other variables remain constant. Therefore the coercive field increases with increasing the maximum electric field E_{max} in a hyperbolic tangent function form. Eq. (4.11) is based on the assumption that the number of dipoles contributing to the polarization varies with the applied electric field magnitude similar to anhysteretic curve, in order to obtain the theoretical results close to the experimental results. In the framework of the static Weiss model, the coercive field is determined by the intersection point of the straight lines and the hyperbolic tangent jumping from one quadrant to the other quadrant [153]. Therefore, it is independent of the amplitude of the applied field at a constant temperature. The amplitude dependence of coercive field can be obtained in the dynamic Weiss model.

The coercive voltage determined from Fig. 4.40 and its fitting with Eq. (4.11) as a function of applied voltage is plotted in Fig. 4.41. The coercive voltage first increases rapidly and later has a tendency to get saturation, which can be described by Eq. (4.11).

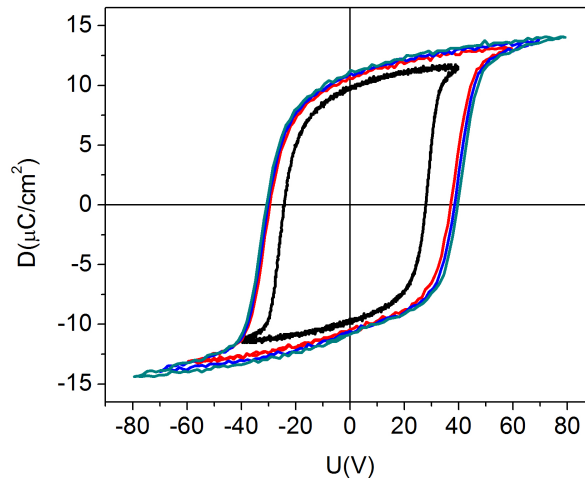


Figure 4.40: Hysteresis loops as a function of the amplitude of the applied field for a spun film of 600nm at 100 Hz.

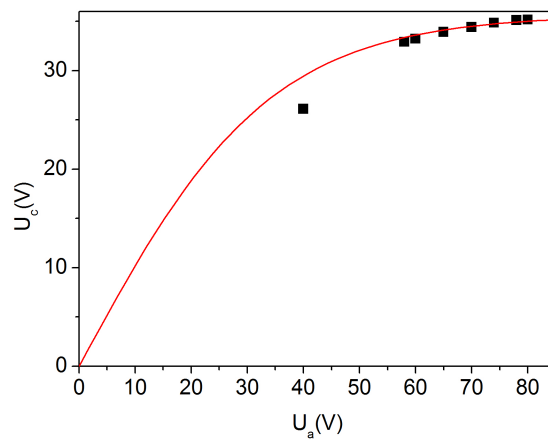


Figure 4.41: Coercive voltage as a function of the amplitude of the applied voltage for a spun film of 600nm at 100 Hz. The solid line is fitted with Eq. (4.11).

4.5 Conclusions

The switching dynamics of ferroelectric P(VDF-TrFE) copolymer Langmuir-Blodgett films and spun films are investigated and compared. In general, both types of films show similar switching behavior. It is considered that LB films and spun films are both inhomogeneous on a larger scale. The thickness dependence of the coercive field in LB films and spun films follows a power law, whereas the remanent polarization is nearly constant. Reduced thickness causes a slant in the hysteresis loops and a broadening in the switching transients. The switching time is dependent on the applied field with an exponential function and is nearly independent of thickness down to 69nm in LB films and 71nm in spun films, while slower switching is observed with thickness below 60nm in both LB films and spun films due to the surface oxidation layer effect. Ferroelectric films in the range of 60-100nm are promising for low voltage operation with a relatively fast switching speed. Retention behavior is temperature dependent. The thicker films exhibit better retention performance due to the lower depolarization field. The fatigue tests by continued switching show that the thinner films have improved polarization fatigue endurance under the same electric field due to faster heat diffusion out of the sample. Furthermore, fatigue endurance seems to be influenced by the waiting time between each switching pulse which induces a change of the local temperature. Both kinds of films exhibit similar remanent polarization decay tendency for retention and fatigue.

Faster polarization switching is observed in metal electrodes with higher work function. Coercive field is lower and switching time is shorter using Cu and Pt electrode due to a thinner oxide layer. CV and PE curves are symmetric with electrodes of same work function and asymmetric with electrodes of different work function.

The Al_2O_3 dielectric layer between the ferroelectric film and electrode can induce a depolarization field. A shift and slanted hysteresis loop is observed. Its influence on ferroelectric properties includes decreasing remanent polarization and increasing coercive field as well as switching time.

Coercive field is a function of both frequency and amplitude of the input signal. For complete switching, the coercive field increases with increasing frequency according to a power law. Besides, the coercive field increases as the maximum electric field increases.

The results presented in this chapter provide necessary information for ferroelectric copolymer films used as nonvolatile memory cells.

Chapter 5

Polarization relaxation and charge injection

In this chapter, polarization relaxation effects and charge injection in P(VDF-TrFE) thin films are investigated in a thickness range between 60nm and 400nm. A $t^{-\alpha}$ (Kohlrausch law) behavior of the current density in the polarization and depolarization processes is demonstrated, which is corresponding to a second step of polarization build up in time domain. The $t^{-\alpha}$ currents at a constant electric field are independent of the sample thickness as expected for a relaxational volume polarization effect. Furthermore, the isochronal polarization and depolarization currents saturate at high fields. A physical model based on an asymmetric double well potential with dipoles fluctuating between the wells is proposed to explain this behavior. Charge injection is observed in polarization currents at higher temperature, which results in a deviation of the $t^{-\alpha}$ law. Two relaxation processes are identified in the depolarization currents: the dipole relaxation process with $t^{-\alpha}$ behaviour at short times and the space charge relaxation process with a pronounced minimum in time at long times. The mechanism responsible for this behavior is discussed.

5.1 Kohlrausch relaxation

For transient, time dependent polarization processes stretched exponential functions and power laws are referred to as Kohlrausch relaxation, which is often observed in disordered dielectrics [124,125]. Ferroelectric materials are no exception to this rule. In general, the relaxational polarization currents in the time domain can have over several

decades the form

$$j(t) = A(E, T)t^{-\alpha(T)}, \alpha \approx 1 \quad (5.1)$$

The prefactor A depend on the applied field strength E and the temperature T . The exponent α is approximate to one and only weakly temperature dependent. This behavior has been observed as early as 1854 by R. Kohlrausch in Leyden jar [126]. Later on this behavior is also called Curie-von Schweidler law which has been found either in the time or in the frequency domain. The depolarization current flowing through the material after the removal of the electric field is usually a mirror image of the polarization current except that the ferroelectric dipole switching current and conduction current are absent in the former for polar materials.

Regardless of the physical and chemical properties, Kohlrausch relaxations can be observed in a wide range of materials, e.g. aluminum oxide [127], silicon oxide [128,129], silicon nitride [130,131], polyethylene oxide [132], polyimide [133], anodic tantalum oxide [134], PVDF [135,136], and vanadium phosphate glass [137]. Recently, P(VDF-TrFE) copolymer films have been shown a remarkable Kohlrausch behaviour in a wide range of electric field and temperature [85,148]. The reason why this behavior is found to be valid in many classes of materials over large ranges of frequency and time as well as wide ranges of temperature points to that some features of the polarization processes are common to all materials exhibiting the Kohlrausch relaxation behavior. There are many different theories which try to explain this behavior. A frequent used interpretation is the assumption of a distribution and linear supposition of relaxation times. Every single Debye relaxation process $P_i(t)$ is described by an exponential function solving a linear first-order differential equation,

$$\tau_i \frac{dP_i}{dt} = P_i(t \rightarrow \infty) - P_i(t) \quad (5.2)$$

The sum of these independently exponential polarization processes leads to the $t^{-\alpha}$ current

$$j(t) = \sum_i \frac{P_i(t \rightarrow \infty)}{\tau_i} e^{-t/\tau_i} \quad (5.3)$$

which can be visualized in Fig. 5.1.

For the physical origin of the distribution function, H. Kliem proposed a model based on a proton fluctuation in double well potentials between adjacent oxygens in disordered oxides, for example in amorphous aluminum oxide [138] (Fig. 5.9). The energy minima in the wells are separated by an energy barrier W_0 which depends on the distance R between the oxygen shells. The potential becomes asymmetric if the sur-

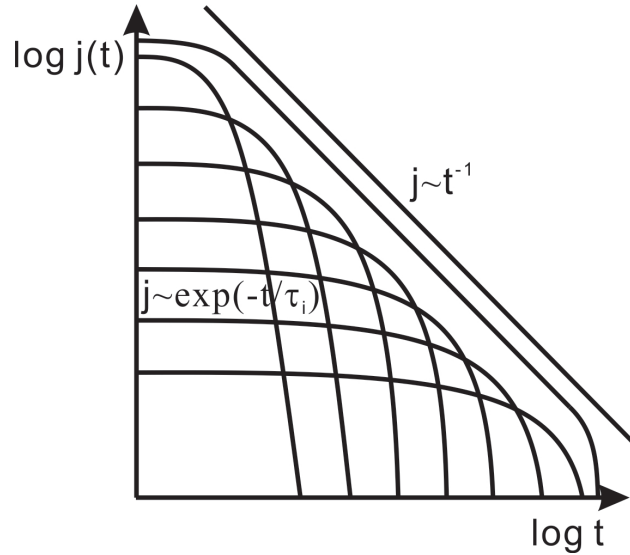


Figure 5.1: The superposition of single exponential currents with different relaxation times and prefactors corresponding to a $t^{-\alpha}$ current in the time domain.

roundings are asymmetric by the distances between negatively charged oxygen atoms and positively charged aluminum atoms. An external field can cause a shift of the double well potentials. A transition for the proton between the two minima is possible by either thermal activation or tunneling. A narrow distribution of atomic center distances can cause a drastically broad distribution of relaxation times by the strong nonlinearity of the exponential function transforms. An alternative physical interpretation for the distribution of relaxation times is based on a charge carrier hopping in the electronic gap of insulating materials [139]. Charge carriers were hopping between energy states located energetically by the band gap and spatially by the random distribution of donor atoms. A distribution of the energetic and spatial separation of the states results in the Kohlrausch relaxations. Recently, it is shown that the dipolar interaction caused by electrostatic forces between dipoles of the same kind in the double well potentials can result in Kohlrausch relaxations without a distribution of any property [100,140]. Another model applicable to solid polymer electrolytes is that ionic charges are attracted towards the electrodes due to the image forces. After application of an external voltage this charge attraction leads to the power law external current [141,142]. Other interpretations for the power law current include correlation function approaches [143], diffusive boundary conditions, interfacial phenomena and the Maxwell-Wagner effect [124]. The list is far away from being complete.

In the present study we examine the polarization relaxation effects in ferroelectric

thin films of P(VDF-TrFE) copolymer with different thicknesses which is responsible for a retarded increase stage in the polarization transients. An asymmetric double well potential model with charges fluctuating between the two minima is proposed [138]. Analyses of polarization currents and depolarization currents in the time domain have been carried out. The charge injection process at higher temperature results in an observation of two relaxational currents during short-circuiting [191].

5.2 Polarization and depolarization transients

The switching dynamics in the ferroelectric films are investigated by polarization reversal measurements in the time domain. Fig. 5.2 shows typical polarization switching transients of a LB film with 139nm under various applied voltages by the three pulse method. The polarization switching rate is faster with increasing applied voltage. The switching curves exhibit a two step increase: a rapid increase of polarization followed by a continuous slow increase over several decades. The retarded stages of the transient curves have nearly the same slope at high applied voltages. This anomalous stage deviates from the stretched exponential function [21] which is usually employed to describe the polarization switching transients representing a saturation in the long time range.

This behavior of switching transients with retarded stages at long times was also reported by several authors [144-146]. Some authors [144,145] briefly explained the second step was due to the conduction current in the samples. However, in our measurements by the three pulse method the contribution of leakage current can be eliminated. Therefore, the explanation of conduction induced polarization is excluded. Other authors [146] believed that the retardation in the end of the polarization reversal was caused by the depolarization effect arising from the oxide layer between the aluminum electrode and the ferroelectric film. The depolarization field is the higher the thinner the sample is. For samples thicker than 100nm, the depolarization effect by the oxide layer becomes negligible [110]. Since we still observed this retarded stage in samples as thick as 400nm, the depolarization field is not strong enough to cause such remarkable retardation of switching. In the following, we will give a qualitative explanation for our observations based on an asymmetric double well potential model.

The retarded stage in the polarization transient corresponds to a t^{-1} behaviour of the current density in the long time range, as shown in Fig. 5.3. The current value measured directly is almost identical to the value of the time derivative of the polarization transient. The polarization current transient consists of a single exponential-like current with a single relaxation time indicating the switching time of the ferroelectric

at short times and a power law current (t^{-1}) which is the superposition of single exponential currents with different relaxation times at long times. For samples as thick as 400nm, there is a maximum of current density visible in linear time scale [110]. The time dependent polarization in the long time range can be approximately described by $P(t) = P_0 + P_1 \log(t)$, therefore the current density is expressed as $j = \frac{dP}{dt} = P_1 t^{-1}$, depending on the slope value of P_1 . As we can see in Fig. 5.3, the t^{-1} currents at long times are nearly field independent corresponding to the nearly same slope of the second step in the polarization reversal transients (Fig. 5.2). Furthermore, we find that these currents in the long time range are also independent of the sample thickness as expected for a relaxational volume polarization effect (Fig. 5.4). In Fig. 5.4(a), the switching time characterized by the exponential current is faster in thicker samples and the currents become almost equivalent at long times. In Fig. 5.4(b), the depolarization currents in which the dipole switching current and the conduction current are not present are identical for samples with different thicknesses, if the samples are subjected before to the same field strength.

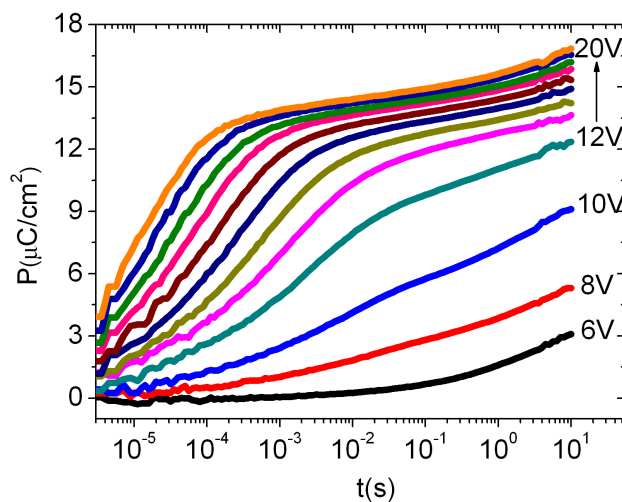


Figure 5.2: Typical polarization switching transients of a LB film with a thickness of 139nm measured by the three pulse method.

Besides the exponential-like switching currents the $t^{-\alpha}$ polarization currents in Fig. 5.4 and Fig. 5.5 at a constant time are higher than the depolarization currents. We have checked that the depolarization current from the first negative pulse does not affect the polarization current in Fig. 5.4 and Fig. 5.5 significantly. Fig. 5.5 shows the direct comparison of the polarization and depolarization currents by the three pulse method.

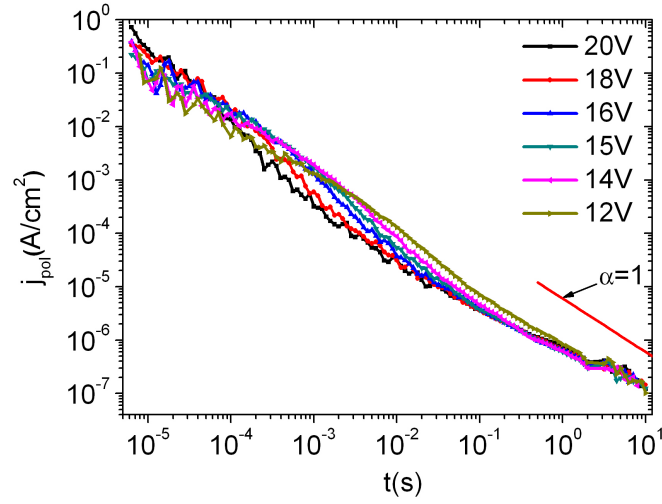
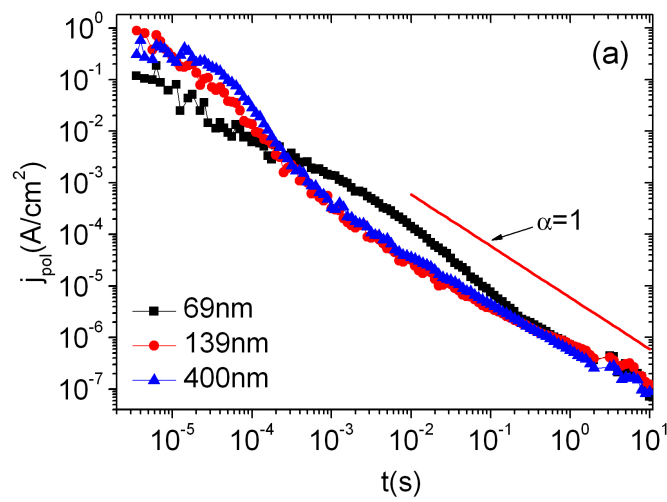


Figure 5.3: The polarization currents of the 139nm LB film under various applied voltages in the time domain obtained by the time derivative of the polarization switching transients in Fig. 5.2.



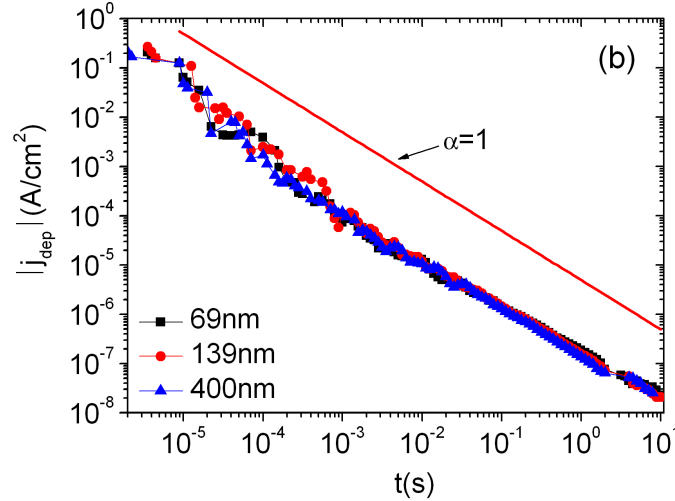


Figure 5.4: (a) The polarization currents in the first positive pulse and (b) depolarization currents after the first positive pulse of samples with different thicknesses under an applied field of 150MV/m in the time domain obtained by the time derivative of the polarization switching transients.

In the first positive pulse where polarization switches from the negative state to the positive state, the polarization current is higher than the depolarization current (Fig. 5.5(a)). A part of the relaxing dipoles contributing to the $t^{-\alpha}$ current does not switch back but remain in its position directed by the field applied before. This part seems to interact with the ferroelectric system. In the second positive pulse when polarization switching is absent, the polarization current is identical to the depolarization current at short times ($< 1s$). At longer times, the polarization current becomes higher than the depolarization current due to conduction (Fig. 5.5(b)). The depolarization currents after the first and second pulse are almost identical.

In order to further investigate the $t^{-\alpha}$ behaviour, polarization and depolarization currents have been also directly measured with higher resolution at long times. Firstly, the influence of the charging pulse length on the depolarization current is checked. Fig. 5.6 shows the depolarization currents after the application of a voltage step with different lengths. For a small applied voltage of 2V (Fig. 5.6 (a)), the depolarization currents which decline faster than t^{-1} depend on the pulse length. The depolarization currents are nearly the same for charging length longer than 100s and decline faster than t^{-1} at about 80s. This can partly be explained by the distribution of relaxation times. A time limited charging pulse affects only those polarization processes which

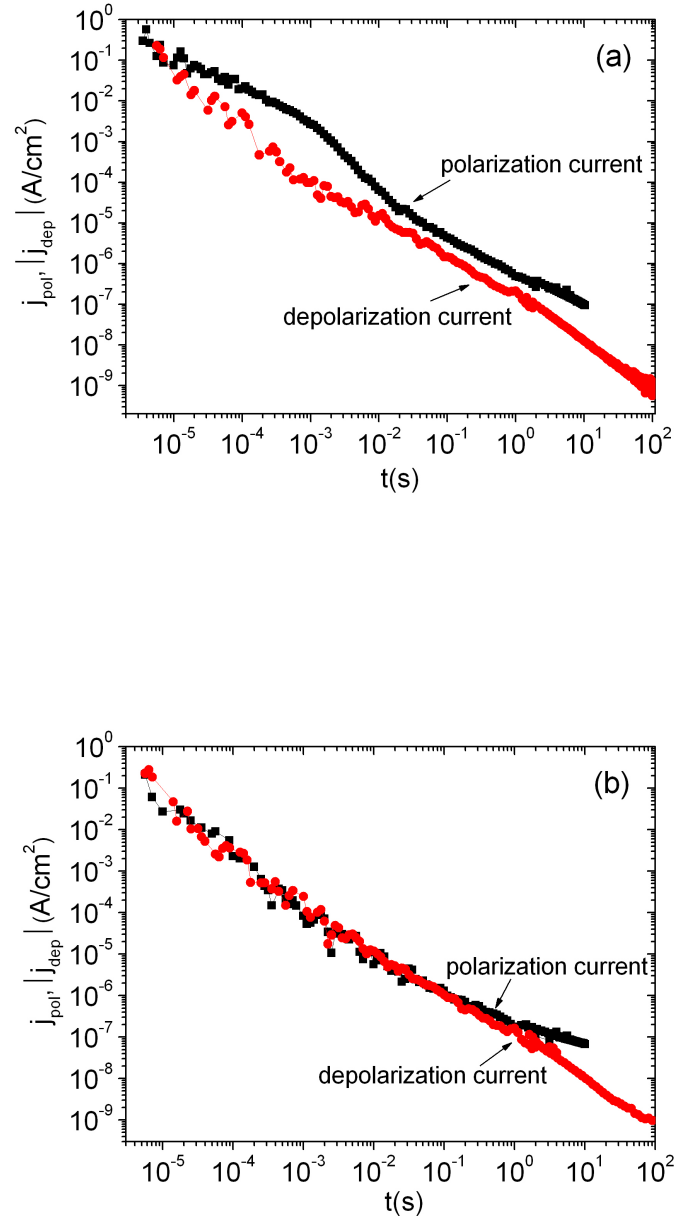


Figure 5.5: The polarization and depolarization currents using the three pulse method for (a) the first positive pulse and (b) the second positive pulse at an applied field of 150MV/m.

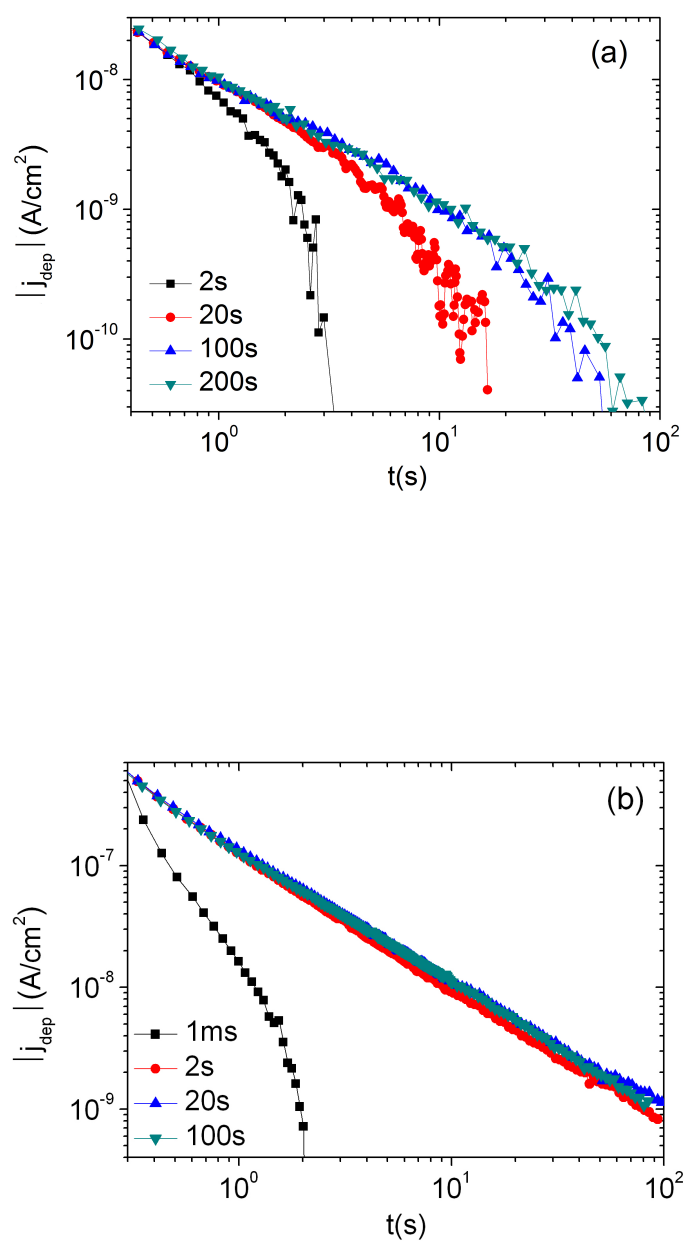


Figure 5.6: The depolarization currents of the 139nm LB film after a charging pulse with different lengths for (a) non-switching of 2V and (b) switching of 20V.

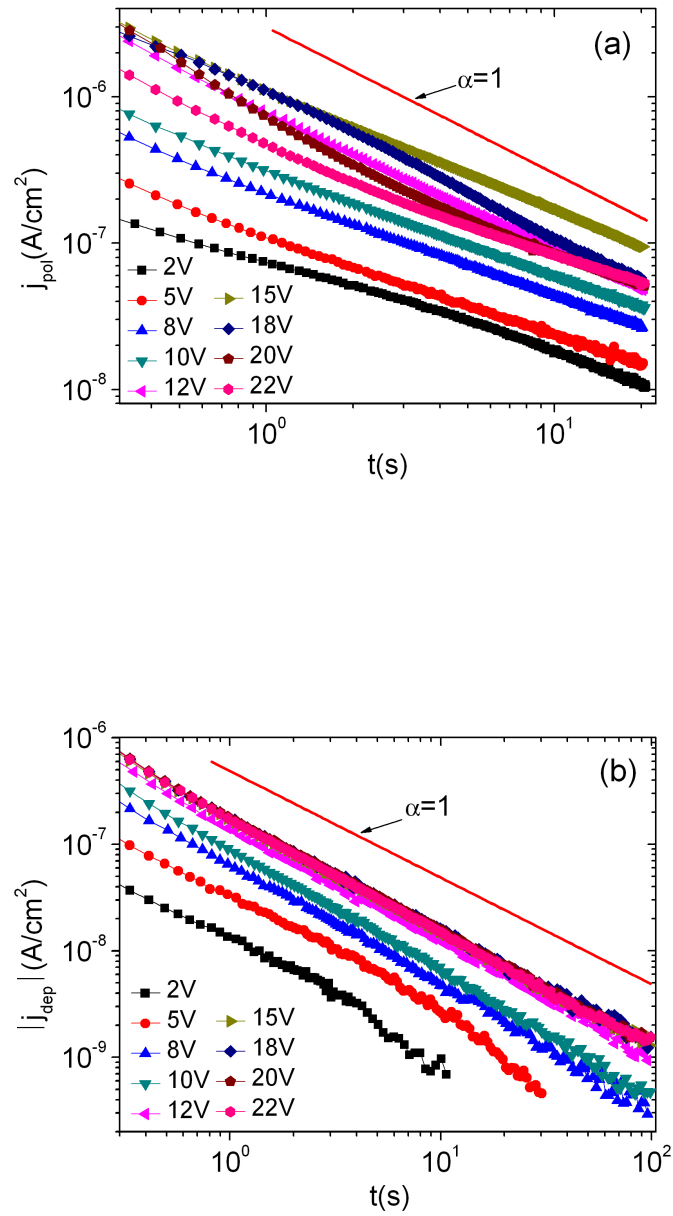


Figure 5.7: The time dependence of the (a) polarization currents and (b) depolarization currents after a voltage step for the sample with 139nm under various applied voltages at room temperature measured by the electrometer.

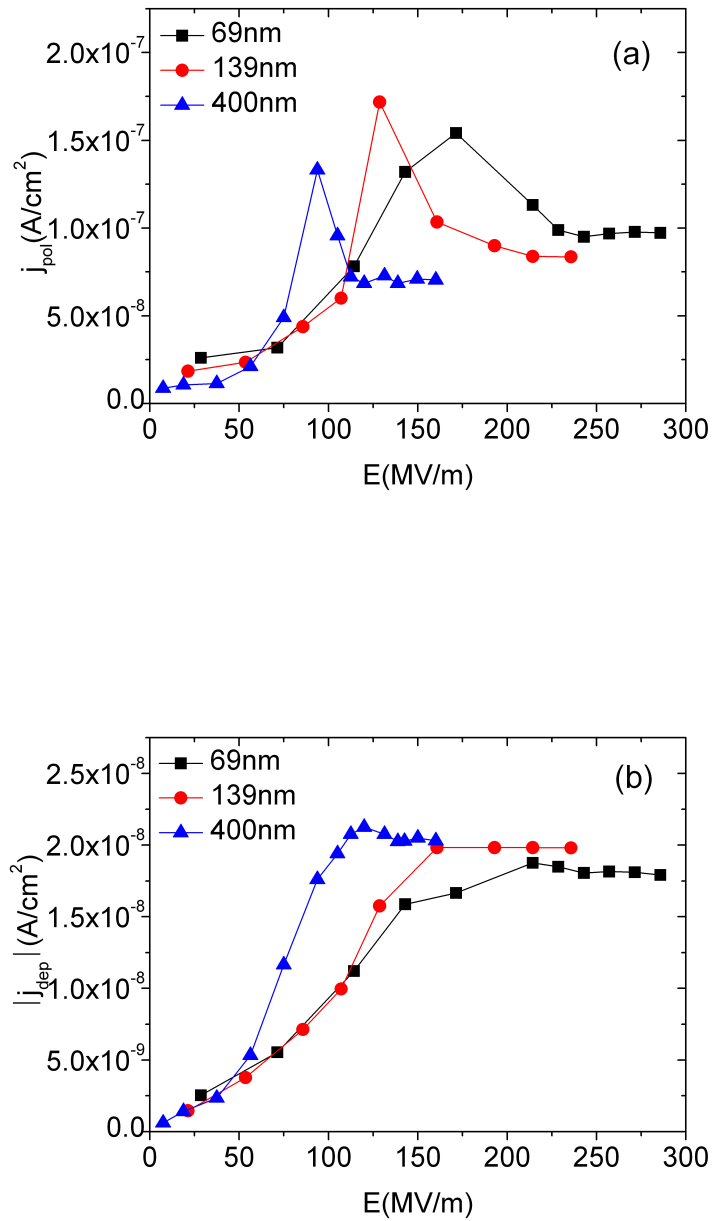


Figure 5.8: (a) The polarization currents and (b) depolarization currents at a time of 10s for samples with different thicknesses as a function of applied field at room temperature.

have a relaxation time within this limit of time. Processes with longer relaxation times are not influenced by the field and after the pulse they cannot contribute to the short circuit current [147]. The time where the depolarization current declines faster than t^{-1} is slightly different from the charging length. However, it was found by the field reversal measurements that the Kohlrausch dipole system has interactions [148]. The behavior shown in Fig. 5.6 (a) reveals the distribution of relaxation times, which is in contrast to Fig. 5.6(b) where the depolarization currents become identical for pulse length longer than 2s for a high voltage step of 20V applied before causing complete switching of dipoles. A part of the dipoles has interaction with the ferroelectric system. If the switching is not completed, e.g., for a pulse length as short as 1ms, the discharge currents for different charging lengths deviate from each other indicated by the faster than t^{-1} decline (Fig. 5.6(b)).

Fig. 5.7 shows the time and field dependence of the charging and discharging currents for the 139nm LB film (see also Fig. 5.3) in a limited time window to get a better resolution. Both currents exhibit the Kohlrausch dependence in general. The isochronal currents at $t = 10s$ saturate for high fields. However due to ferroelectric switching the isochronal polarization current has a peak (Fig. 5.8(a)) before the saturation region sets on. This is caused by the field accelerated switching events.

Peak and saturation of the isochronal currents are independent of the sample thickness thus revealing volume polarization effects (Fig. 5.8). However the currents in thinner samples saturate at higher fields due to their higher coercive fields. Again with Fig. 5.7 and Fig. 5.8 one can see that charging and discharging currents are different by a factor of 4.

We conclude that there are two dipole systems: the ferroelectric system and the relaxing dipoles having a distribution of relaxation times. A part of the relaxing dipoles is interacting with the ferroelectric system.

5.3 The physical model for the Kohlrausch relaxations

The total current in a dielectric after the application of an electric field is given by:

$$j_{tot}(t) = j_D(t) + j_c(t) + j_{dis}(t) = \frac{dP(t)}{dt} + \sigma E(t) + \varepsilon_0 \varepsilon_r \frac{dE(t)}{dt} \quad (5.4)$$

where j_D , j_c , and j_{dis} represent dipole polarization current, conduction current, and displacement current, respectively. ε_0 and ε_r are permittivities of vacuum and the dielectric. $P(t)$ is the polarization caused by dipole orientation. $E(t)$ is the electric

field in the dielectric. The dipole polarization current includes ferroelectric switching current and Kohlrausch relaxation current. The displacement current only affect at very short time range since the RC constant in this system is at nanosecond scale. In the depolarization current, the dipole switching current and conduction current are not present during the short circuit. The depolarization current value after the decrease of j_{dis} is determined by the dipole relaxation and the redistribution of the excess charges in the material, which can be expressed as,

$$j_{dep}(t) = j_{sc}(t) + j_p(t) \quad (5.5)$$

where j_{sc} is the space charge contribution to the external discharge current density and j_p is the contribution of dipole depolarization processes. The long-lasting discharge current is due to some long relaxation processes which are polarization processes and/or processes associated with the release of trapped space charges. Here we present a physical model only considering the Kohlrausch relaxation current.

The saturation effect at high field strengths (Fig. 5.8(b)) has been observed and explained in aluminum oxide and silicon nitride in our group's previous work [131,138,149, 150]. This effect can be described using an asymmetric double well potential model. In the case of P(VDF-TrFE) copolymers, dipoles can fluctuate between two minima which have a built-in potential difference V even without an external field (Fig. 5.9).

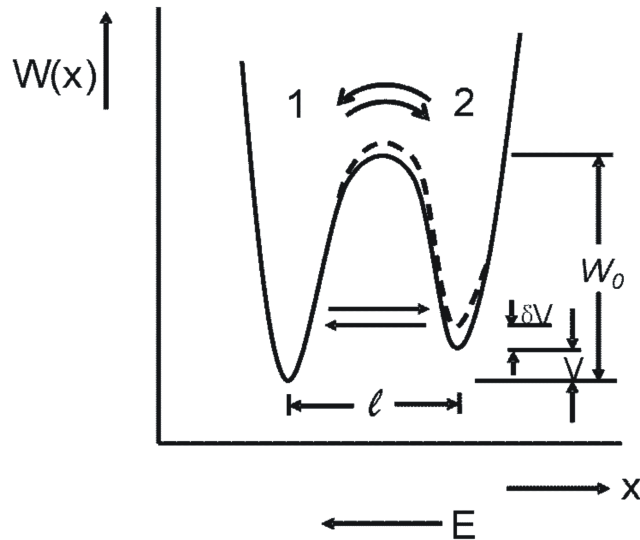


Figure 5.9: The asymmetric double well potential model. The intrinsic asymmetry V can be shifted to $V + \delta V$ by an external field E .

An external field can shift the asymmetry V to $V + \delta V$ leading to a redistribution of the dipoles. Similar to Froehlich's model [151], the transition probabilities for the thermal activation is

$$w_{12} = v_0 \exp\left(-\frac{W_0}{kT}\right) \quad (5.6)$$

$$w_{21} = w_{12} \exp\left(-\frac{V + \delta V}{kT}\right) \quad (5.7)$$

For the tunnelling transition we have

$$w_{21} = v_0 \exp\left(-\frac{4\pi}{h} \sqrt{2m} \int_{-l/2}^{+l/2} \sqrt{W(x)} dx\right) \quad (5.8)$$

$$w_{12} = w_{21} \exp\left(-\frac{V + \delta V}{kT}\right) \quad (5.9)$$

Assuming $f(W_0)$ as the distribution density function of W_0 , dn is the density of dipoles in an interval dW_0 belonging to W_0 . n_0 is the total dipole density: $dn = n_0 f(W_0) dW_0$, dn_1 and dn_2 being the dipole densities in wells 1 and 2. With the assumption of first order rate equations for the temporal change of the dipole densities after a perturbation from equilibrium we have

$$\frac{\partial}{\partial t} dn_1(t) = -dn_1(t)w_{12} + dn_2(t)w_{21} \quad (5.10)$$

$$\frac{\partial}{\partial t} dn_2(t) = dn_1(t)w_{12} - dn_2(t)w_{21} \quad (5.11)$$

$$dn = dn_1 + dn_2 = \text{const} \quad (5.12)$$

Considering no dipole-dipole interaction the asymmetry δV is caused solely by the external electric field. It can be expressed as

$$\delta V = elE \cos \beta \quad (5.13)$$

where β is the angle between the electric field E and the dipole length l . Integration over all directions in space yields for the tunneling and the thermally activated transition a

static polarization $dP(t \rightarrow \infty)$

$$dP(t \rightarrow \infty) = dn \frac{el}{4\pi} \int_0^{2\pi} \int_0^\pi \sin \beta \cos \beta \tanh \left[\frac{V + elE \cos \beta}{kT} \right] d\beta d\gamma \quad (5.14)$$

The time dependent polarization after a step of the electric field is

$$dP(t) = dP(t \rightarrow \infty) \left[1 - \exp \left(-\frac{t}{\tau} \right) \right], \tau = \frac{1}{w_{12} + w_{21}} \quad (5.15)$$

The polarization current density is obtained by the time derivative of Eq. (5.15)

$$dj(t) = \frac{\partial}{\partial t} dP(t) \sim dP(t \rightarrow \infty) \quad (5.16)$$

The asymmetric double well potential model is giving that a distribution of W_0 yields the distribution of transition probabilities, which causes a distribution of relaxation times. The superposition of the exponential currents with different relaxation times yields the power law current: $j \sim t^{-\alpha}$ [138]. Moreover, the asymmetry V causes the nonlinearity in $j(E)|_{t=const.}$ [131,149,150]. Fig. 5.10 shows the static polarization which is proportional to the polarization current density as calculated from the model with a variation of asymmetry V at room temperature ($t = const.$). After a stronger than linear increase, the polarization current density saturates at high fields. The static polarization can be numerically solved either with asymmetry V or dipole length l as parameter. By fitting the curves, the dipole length can be calculated from measurements of the depolarization currents at a constant time. Fig. 5.11 shows the depolarization currents at a constant time of 10s in dependence of the normalized field for the 69nm sample. The dipole length is calculated to be around 0.2nm from the fittings with $\tanh((V + \delta V)/kT)$ in a series of different asymmetrical energies and dipole lengths. This value is a usual distance between positive hydrogen and negative fluorine atoms which form a permanent dipole moment [152]. The asymmetry V is calculated to be between 52 and 78meV. The asymmetry can partly be caused by the ferroelectric polarization which generates a field ηP_{ferro} so called the Weiss field at the location of the dipoles [153] thus introducing an interaction between the dipoles. The local field then is the superposition of the external field and the Weiss field: $E = E_a + \eta P_{ferro}$. The field reversal experiments suggest that the dipoles in P(VDF-TrFE) copolymer are interacting below the Curie point while the system becomes linear and time invariant above the Curie point indicating noninteracting dipoles [148]. In the future a quantitative model based on the interaction of dipoles should be considered.

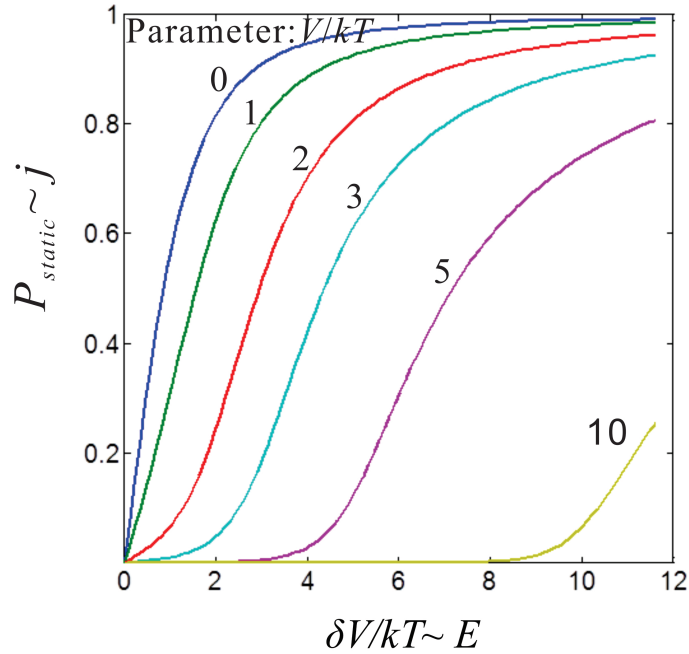


Figure 5.10: The static polarization as calculated from the model with asymmetry V as parameter at 298K.

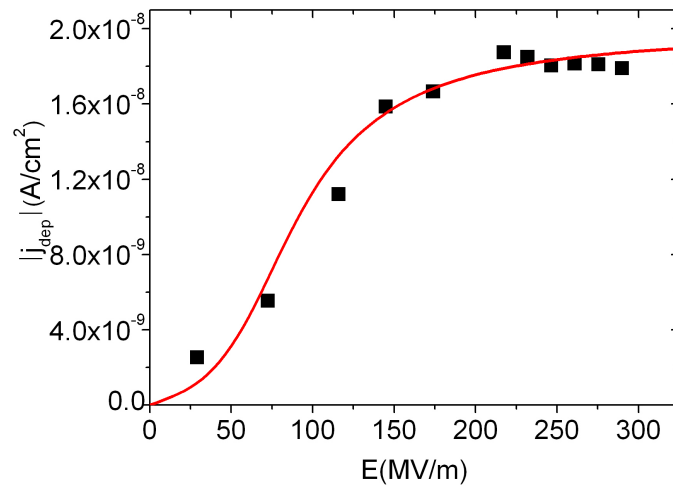


Figure 5.11: The depolarization currents at a constant time of 10s after switching off the voltage step for the 69nm sample as a function of applied field at room temperature. The currents are non-linear and show a saturation effect. The data points are fitted with $\tanh((V + \delta V)/kT)$ with $l = 0.2nm$ and $V = 52meV$.

5.4 Temperature dependence and charge injection

Charge injection becomes considerable with increasing temperature. Fig. 5.12 shows the time variation of the polarization current of the sample with 139nm at a constant electric field of 150MV/m at different temperatures. The polarization current increases with the increase of temperature. At room temperature, the polarization current follows the power law of $t^{-\alpha}$. As temperature increases, the α value falls slightly from 1 to 0.8 at short times and the current departs from the $t^{-\alpha}$ law reaching to a constant value at long times.

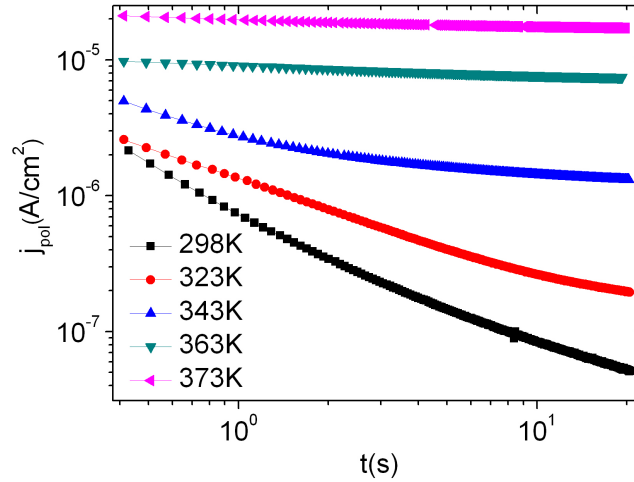


Figure 5.12: The time dependence of the polarization currents of the sample with 139nm at a field strength of 150MV/m over the temperature range of 298K to 373K.

Fig. 5.13 illustrates the polarization current versus the applied voltage at a constant time of 10s at different temperatures. The saturation effect is observed at room temperature and 323K suggesting a low level injection here. Above the temperature of 343K, the saturation effect disappears and the I-V curve is linear showing ohmic behaviour, which suggests the conduction current is dominant at high temperature. This is also revealed in Fig. 5.12 as the polarization current becomes constant at long times above 343K. A similar phenomenon with no appreciable thickness dependence is observed in samples with 69 and 400nm.

The depolarization transients after removal of an electric field of 150MV/m (charging for 20s) at different temperatures are shown in Fig. 5.14. There is an anomalous characteristic observed at shorter times and higher temperatures. The currents were

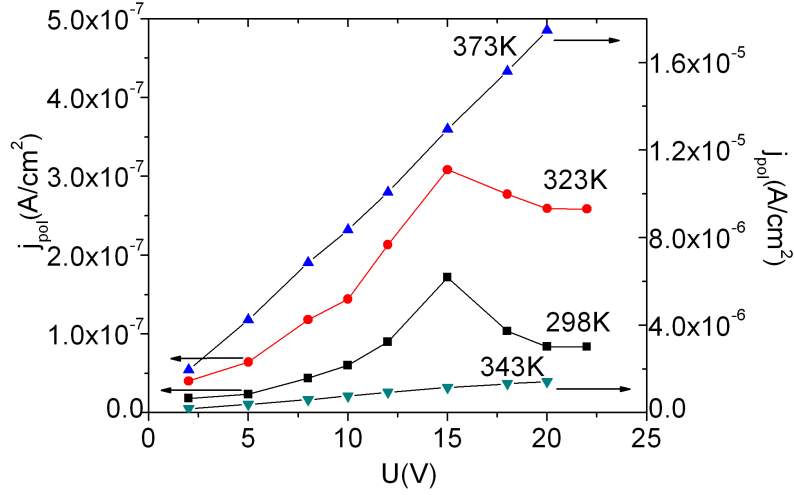


Figure 5.13: The polarization currents of the sample with 139nm under different applied voltages at a constant time of 10s over the temperature range of 298K to 373K. Data for 298K are taken from Fig. 5.7(a).

recorded in a time range from $2\mu\text{s}$ to 1000s over almost ten decades to check the short time and long time behaviour. The currents were measured with a fast current amplifier and monitored with an oscilloscope for times shorter than 1s and then measured with the electrometer at long times. At room temperature, the depolarization currents obey $t^{-\alpha}$ with α equal to 1 in the whole observed time range. In striking contrast to the depolarization current at room temperature, we observe at higher temperature a distinct minimum of $j_{dep}(t)$ at a time denoted with τ_{sc} . Two relaxation processes are identified: one is the dipole relaxation process which still follows t^{-1} at short times; the second is a space charge relaxation process which deviates from t^{-1} and probably relates to the injected carriers during charging at long times. The dipole relaxation current at short times is found to be nearly independent of temperature. Nevertheless the space charge relaxation current considerably depends on temperature and it increases with increasing temperature. The starting point of τ_{sc} at which the space charge relaxation process sets in is observed to shift to shorter times with increasing temperature, as indicated by the arrows in Fig. 5.14. The value of τ_{sc} is about 19s at 323K and becomes 0.03s at 373K. The temperature dependence of τ_{sc} is approximately of the Arrhenius type showing an exponential tendency, as shown in Fig. 5.15. The activation energy of the space charge relaxation is formally calculated to be 1.3eV. It is suggested that the detrapping of space charges in the depolarization currents is a thermally activated

process. It should be noted that from an observation of macroscopic quantities the microscopic properties cannot necessarily be deduced [154].

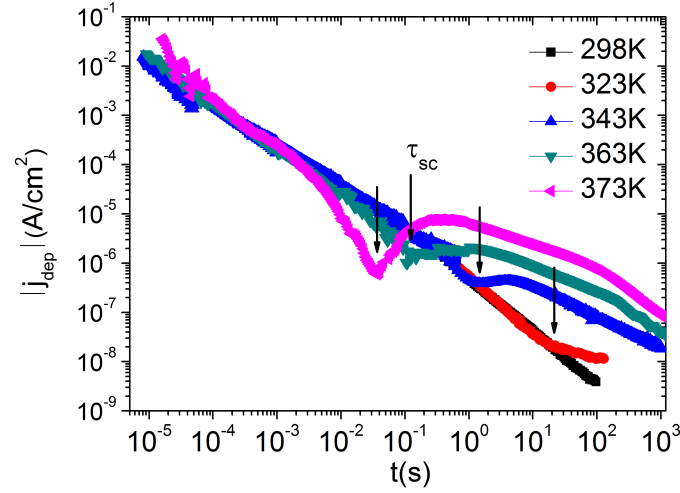


Figure 5.14: The time dependence of depolarization currents of the sample with 139nm after switching off a field strength of 150MV/m over the temperature range of 298K to 373K.

Since the time constant of τ_{sc} at which the space charge relaxation process sets in is about 2s at 343K in which the time range can be directly observed by electrometer, we examine this anomalous behaviour in dependence of the amplitude of charging voltage step, pre-polarization state and pulse length of charging step at 343K. The typical effects of charging voltage step on the depolarization transients at a constant temperature of 343K are shown in Fig. 5.16. The depolarization currents increase with increasing charging voltages and then change only slightly at higher charging steps. The time constant of τ_{sc} shifts slightly to shorter values at low charging voltages and later changes negligibly at high charging voltages.

In order to justify whether this anomalous behaviour in the depolarization currents is related to the ferroelectric switching of the sample, different amplitudes of the first negative poling step keeping the same pulse length of 20s are applied to change the pre-polarization state of the sample with the same charging pulse of 10V for 20s, as presented in Fig. 5.17(a). The depolarization transients are not influenced by the pre-polarization state which is consistent with our assumption that the anomalous current at long times is due to charge injection during the charging process. Fig. 5.17(b) shows the depolarization transients in dependence of the pulse length of the charging step

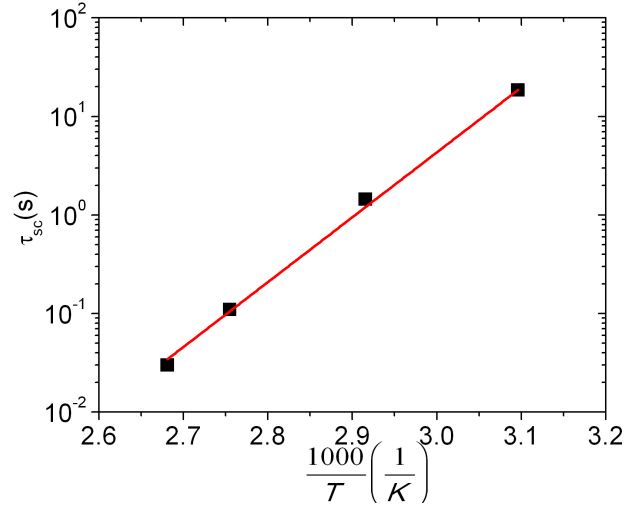


Figure 5.15: Arrhenius plot of the time constant τ_{sc} at which the space charge relaxation process sets in in the depolarization currents.

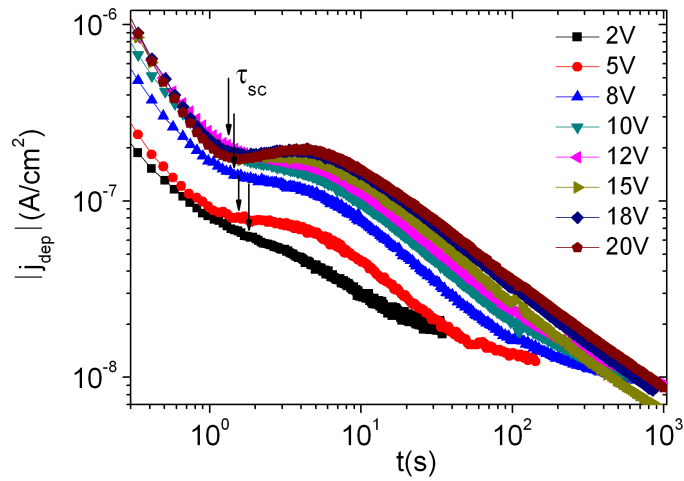


Figure 5.16: The time dependence of depolarization currents of the sample with 139nm after switching off different applied voltage steps at 343K.

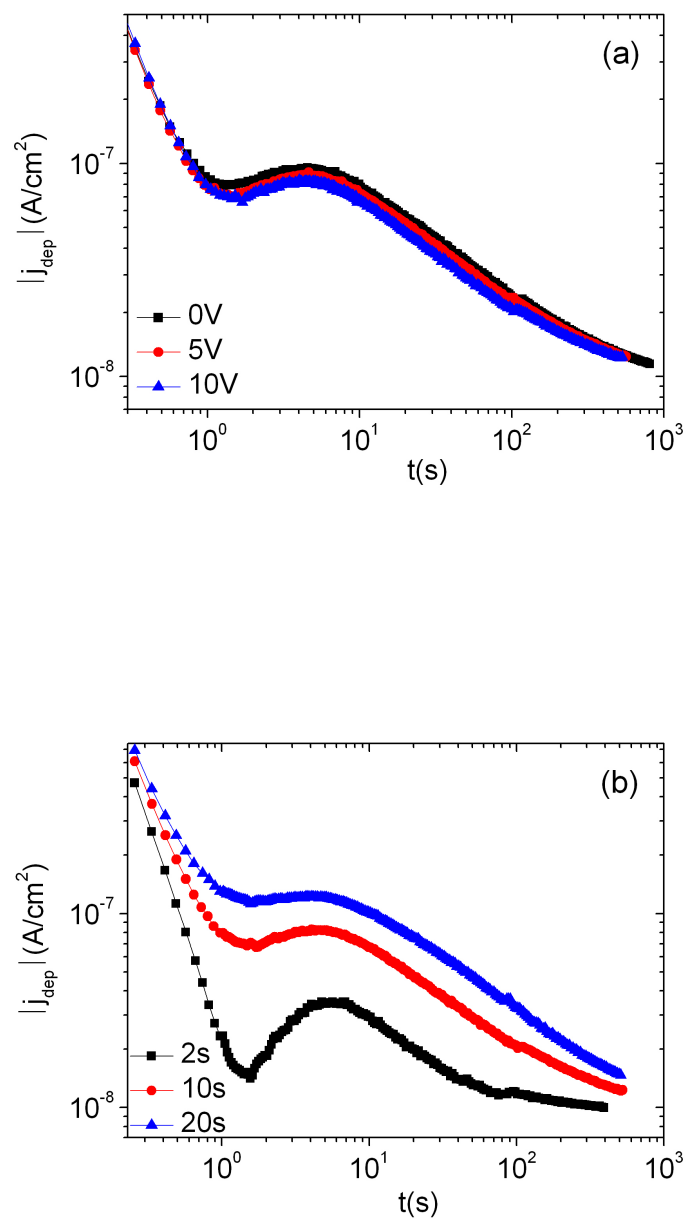


Figure 5.17: The time dependence of depolarization currents of the sample with 139nm (a) at different pre-polarization states and (b) after different pulse lengths of charging step at 343K.

with the same pulse amplitude of 15V. Decreasing the pulse length results in a lower current value and a sharper peak occurs. Thus, the anomalous depolarization current is closely connected with the charging step which determines the charge injection. This further confirms our assumption before.

As discussed above, the space charge relaxation process presents the following characteristics: (1) it is only observed at higher temperature; (2) the time constant of τ_{sc} at which it sets in shifts to shorter times with increasing temperature and it also shifts to shorter values with increasing charging field at low fields; (3) it is not influenced by the ferroelectric switching; (4) the shorter the pulse length of the charging field is the lower the depolarization current is as well as the sharper the depolarization current peak appears. A maximum in the discharging current was also observed in polyethylene oxide (PEO) films in our group and a similar process was observed in polyimide films [155] which are not ferroelectric materials. The discharging currents in polyimide films at high relative humidity have a $t^{-\alpha}$ behaviour at short times and are superimposed by an exponential current at long times which is related to the relaxation of excess charges injected before. In Ref. [156], Murata et al. also observed a current peak in the discharge current in P(VDF-TrFE) copolymer sheets, but that current peak only occurred at high temperature above the ferroelectric to paraelectric transition temperature. Therefore they concluded this behaviour was likely due to a retarded discharge process of ionic charge bound in the paraelectric phase of the copolymer. In our thin films of P(VDF-TrFE) copolymer, the Curie temperature is measured to be 373K during heating and 346K during cooling by $\epsilon(T)$. The current peaks in depolarization transients were observed in both the ferroelectric and paraelectric phase. As we can see in the polarization process (Fig. 5.13), the saturation effect is still present at 323K. At this temperature, the space charge relaxation process in the depolarization current slightly sets in at longer times. Above 343K, the current-voltage characteristic has a linear relationship which suggests one-carrier injection [157] and the space charge relaxation process characterized by a current peak (Fig. 5.14) becomes pronounced here.

After removal of the voltage in the short circuit condition, the injected excess charges would generate an electric field with a zero-field plane in the sample. Then the internal carriers would flow to both electrodes and it is possible that the external current would be zero for a single trapping level [157]. A distribution of trappings and probably retrappings tend to result in a long lasting space charge relaxation current especially at higher temperature. The internal ions inside the sample and electrons injected from the electrodes can serve as the moving charges. After switching off the external field,

the charges will flow to the electrodes. The space charge relaxation process observed in the depolarization transients is due to the charges injected from the electrodes and their subsequent trappings and retrappings.

5.5 Conclusions

A two-step polarization build up is observed in the switching transients with the latter step related to Kohlrausch relaxation effect. This effect is thickness independent as expected for a relaxational volume polarization. A pronounced saturation effect is observed in both isochronal polarization currents and depolarization currents at high fields which is qualitatively explained by an asymmetric double well potential model with dipoles fluctuating between the wells. The model assumes a distribution of barrier heights yielding the distribution of transition probabilities which causes the power law current $j \sim t^{-\alpha}$. An asymmetry V causes the nonlinearity in $j(E)|_{t=const.}$. A charge injection process sets in at higher temperature during charging. The charging currents deviate from the $t^{-\alpha}$ behaviour and become constant at long times. Two relaxation processes are identified in the depolarization currents: the dipole relaxation process with $t^{-\alpha}$ behaviour at short times and the space charge relaxation process at long times. The time constant of τ_{sc} at which the space charge relaxation process sets in considerably depends on temperature as well as the charging field and it is thermally activated. The mechanism responsible for this behaviour appears to be due to injection of charges and their subsequent trappings and retrappings.

Chapter 6

Switching mechanisms in P(VDF-TrFE) thin films

In this chapter, the switching mechanisms in P(VDF-TrFE) thin films are investigated. First, the existing theoretical models for ferroelectric switching are summarized. Then we examine the switching process of ferroelectric P(VDF-TrFE) thin films mainly through switching current transient measurements. The thickness and field dependence as well as temperature dependence of switching behaviour are evaluated. The changes of switching current profile and temperature dependence behavior indicate a transformation of switching kinetics. Finally, the possibility of determination of extrinsic/intrinsic switching is discussed.

6.1 Overview of existing theoretical models for ferroelectric switching

More than fifty years ago, Merz [41] firstly investigated the ferroelectric polarization reversal on single crystals of barium titanate ($BaTiO_3$). He observed a pronounced maximum in the switching current transient flowing to the sample by application of a voltage step. The maximum current and the switching time followed an exponential dependence on the external field. Based on the electrical measurements combined with optical observations, he considered that the switching process in $BaTiO_3$ was accomplished by the nucleation of domains with opposite polarization when a reverse field was applied, and the growth of these domains accompanied by domain wall motions.

After Merz, polarization reversal in ferroelectric materials has been intensively investigated both experimentally and theoretically [2,6,18,21,35,45,48,78,89,154,158-160].

So far, the existing theoretical models for ferroelectric switching are summarized as following:

(1) Kolmogorov-Avrami-Ishibashi (KAI) model

The classical model to describe ferroelectric switching kinetics is the Kolmogorov-Avrami-Ishibashi (KAI) model [2,46,47]. It has been found that this model is very useful for analyzing the switching process in many materials including single crystals [35,158] as well as epitaxial thin film ferroelectrics [159]. In the scope of KAI model, the ferroelectric media where the polarization reversal takes place is infinite. The area of the reversed domain $S(t, \tau)$ at time t after the start of polarization reversal can be written as [2]

$$S(t, \tau) = C [v(t - \tau)]^d \quad (6.1)$$

where C is a constant; v is the velocity of the motion of the domain walls which is assumed to be constant; τ is the nucleation time for the reversed domains and d represents the dimensionality of the shape of reversed domains, as shown in Fig. 6.1.

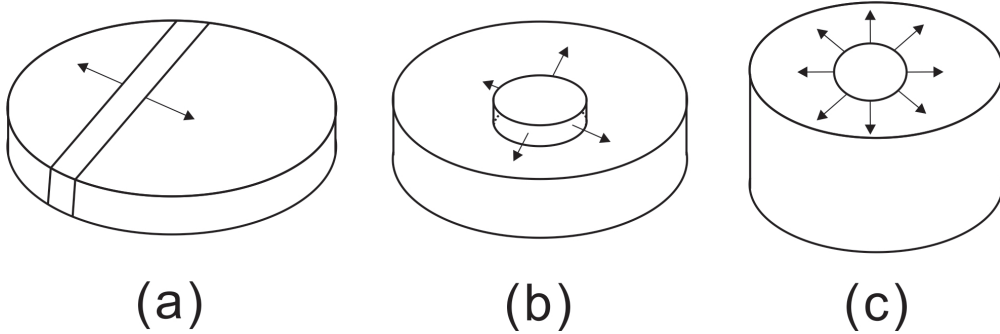


Figure 6.1: (a) one ($d = 1$), (b) two ($d = 2$) and (c) three ($d = 3$) dimensional domains.

The nucleation probability $J(\tau)$ at time τ which means the number of appearing nuclei per unit area per unit time is assumed to be spatially homogeneous. Then, the probability that no nucleus appears in $S(t, \tau)$ during a short time $\Delta\tau$ at time τ is given as $1 - J(\tau)S(t, \tau)\Delta\tau$. Dividing time t by a unit as $\Delta\tau, 2\Delta\tau, 3\Delta\tau, \dots, k\Delta\tau$, we can write $t = k\Delta\tau$ and $\tau = i\Delta\tau$. Taking a point P on an infinite plane, the probability $q(t)$ that P is not included at time t in the reversed domains can be obtained as

$$q(t) = \prod_{i=0}^k [1 - J(i\Delta\tau)S(k\Delta\tau, i\Delta\tau)\Delta\tau] \quad (6.2)$$

Reducing $\Delta\tau \rightarrow 0$ and taking a logarithm of $q(t)$, the above equation can be written as

$$\begin{aligned}\ln q(t) &= \sum \ln [1 - J(i\Delta\tau)S(k\Delta\tau, i\Delta\tau)\Delta\tau] \\ &\approx - \sum J(i\Delta\tau)S(k\Delta\tau, i\Delta\tau)\Delta\tau \\ &= - \int_0^t J(\tau)S(t, \tau) d\tau\end{aligned}\quad (6.3)$$

Therefore, the probability $c(t)$ that the point P , arbitrarily chosen, is included in the reversed domains, i.e., the fraction of the reversed domains can be calculated as:

$$c(t) = 1 - q(t) = 1 - \exp \left[- \int_0^t J(\tau)S(t, \tau) d\tau \right] \quad (6.4)$$

Considering two cases for $J(\tau)$, one is the case that the nucleation takes place with a constant rate, known as α -model, which is homogeneous. Another case is that the nucleation takes place only at $t = 0$, known as β -model, which is inhomogeneous. More realistic, both categories work simultaneously and the fraction of the reversed domains can be written as

$$c(t) = 1 - \exp \left[- \left(\frac{t}{t_\alpha} \right)^{d+1} - \left(\frac{t}{t_\beta} \right)^d \right] \quad (6.5)$$

where t_α and t_β are constants regarding to α -model and β -model, respectively. For simplicity, the above equation can be rewritten as

$$c(t) = 1 - \exp \left[- \left(\frac{t}{t_0} \right)^n \right] \quad (6.6)$$

allowing n to take a non-integer value. The characteristic time t_0 is often taken as switching time.

Now the reversed polarization $P(t)$ and the switching current $I(t)$ can be deduced,

$$P(t) = 2P_s \left(1 - \exp \left[- \left(\frac{t}{t_0} \right)^n \right] \right) \quad (6.7)$$

$$I(t) = 2P_s S_0 \frac{n}{t_0} \left(\frac{t}{t_0} \right)^{n-1} \exp \left[- \left(\frac{t}{t_0} \right)^n \right] \quad (6.8)$$

where P_s is spontaneous polarization and S_0 is electrode area.

For one-dimensional growth, $n = 2$ for α -model and $n = 1$ for β -model. For two-dimensional growth, $n = 3$ for α -model and $n = 2$ for β -model. For the mixture of

α -model and β -model or crossover between the one- and two-dimensional growth, we would have n as non-integer value between 1 to 3. A plot of the switching current profiles for different values of n according to Eq. (6.8) is depicted in Fig. 6.2. The tick labels in the axes would be different for a variation of parameters P_s , S_0 and t_0 in different samples. Fig. 6.2 shows qualitatively different shapes of the switching currents. For $n > 1$, there is a peak in the current transients. For $n \leq 1$, it is not possible to identify a current maximum. However, there is no physical meaning in the framework of KAI model for an n value less than 1 since the growth dimensionality could never be less than 1. Therefore a current maximum should always exist in the switching transient when the sample is suppressed by a field above the coercive field in the framework of KAI model. Moreover, KAI model describes a thermally activated switching.

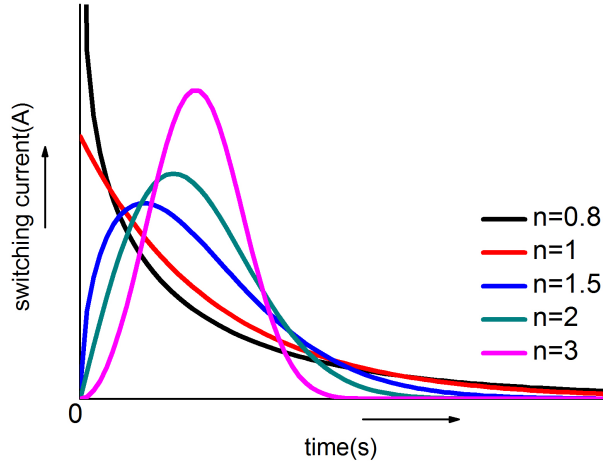


Figure 6.2: Switching current profiles for n with different values according to Eq. (6.8).

The KAI model assumes unrestricted domain growth in an infinite media. Due to the simplified assumptions, it encounters problems when it comes to precisely describe the switching behaviour in real finite ferroelectrics especially for polycrystalline films and ceramics. Therefore, later on new models are constructed to give a more realistic and appropriate description of polarization reversal.

(2) Nucleation-limited switching (NLS) model

Tagantsev et al. [48] developed an alternative scenario of a nucleation-limited switching (NLS) model which is successful to describe the switching kinetics in Pb(Zr,Ti)

O₃ thin films. This model assumes that the film consists of many areas, which switch independently. The switching in an area is considered to be triggered by an act of the reverse domain nucleation. They used a distribution function of the switching times to describe the ensemble of the elementary regions. In the framework of the NLS model, the nucleation time is assumed to be much longer than the time of domain wall motion and a distribution of switching time is modified in the expression of the time dependence of polarization, written as [48]

$$P(t) = 2P_s \int_{-\infty}^{\infty} \left(1 - \exp \left[- \left(\frac{t}{t_0} \right)^n \right] \right) F(\log t_0) d(\log t_0) \quad (6.9)$$

where $F(\log t_0)$ is the distribution function for $\log t_0$. It meets the normalizing condition,

$$\int_{-\infty}^{\infty} F(\log t_0) d(\log t_0) = 1 \quad (6.10)$$

The value of n is assumed to be 2 for thin film ferroelectrics and 3 for bulk ferroelectrics [48]. The switching dynamic extended in a wide time range can be described in terms of this model with a simple shape of the spectrum $F(\log t_0)$. The temperature dependence of the switching time spectrum is of thermal activation nature.

Both KAI model and NLS model neglect the size of nuclei and domains. Fatuzzo [45] reported that the switching current maximum in time could be as broad as that of a single relaxation process regardless of the domain growth dimensions, if the size of nuclei is taken into consideration. Numerical simulations in small systems using a local field method combined with dynamic Monte Carlo steps results in a monotonic decrease in the switching current [100].

(3) The Weiss mean field model

One hundred years ago Pierre Weiss [161,162] proposed a model to describe phase transition in ferromagnetic materials. This model is actually a positive feedback model. The magnetic dipoles mutually evoke a field at the location of other dipoles that results in an alignment of all dipoles into the same direction. This local field which is also called Weiss field is only defined at the location of the dipoles. This model for magnetism was later applied to ferroelectrics [98].

In dielectrics H. A. Lorentz [163] developed a similar local field model. The local field at induced point dipoles for an infinite cubic lattice can be expressed as

$$E_{loc} = E_a + \frac{P}{3\epsilon_0} \quad (6.11)$$

with E_a the applied field and P the polarization of the matter.

Eq. (6.11) illustrates the local field vice versa produce the dipole moments at the lattice points. It is the superposition of the applied field and the dipolar field which is proportional to the polarization itself and is defined only at the location of the dipoles. There are two types of dipoles: permanent dipoles fluctuating thermally activated in double well potentials and induced dipoles. The interaction between all these dipoles is considered with mean fields averaged over all particular local fields. If only permanent dipoles are present, the local field within the Weiss model is assumed to be similar to Eq. (6.11),

$$E_{loc} = E_a + \alpha P \quad (6.12)$$

P is the macroscopic polarization which can be spontaneous below T_c or paraelectric above T_c . α is a coupling factor describing the strength of the interaction between the dipoles. The model is a mean field approach. It also contains microscopic elements including the properties of the double wells with the magnitude of the fluctuating dipole moments, the dipole densities and the coupling constant α . Therefore the model can be considered as a link between phenomenological descriptions and molecular modeling [153].

With the Weiss model, several ferroelectric properties can be described, i.e. ferroelectric hysteresis loop, the temperature dependence of the coercive field, the Curie-Weiss law for the electrical susceptibility, the butterfly curves of the susceptibility in an external field, and a second order ferroelectric to paraelectric transition with its typical protraction in an applied electric field [153,164,165]. It has been shown that if additionally a strain in the material caused by the piezoelectric effect, i.e. by the polarization itself is taken into account, a second order phase transition changes to a first order [166]. In addition, the appearance of a double hysteresis close to the Curie temperature can be explained [167].

Lately, Kliem et al. [154] presented an analytical approach using the Weiss molecular mean-field model combined with the fluctuation of dipoles in double-well potentials to simulate the switching process with a maximum in the switching current as observed by Merz. The time-dependent switching process and the static polarization hysteresis loop are simulated which are in good qualitative agreement with experiments. This theory is exact in the limit of infinite dimensions with homogeneous state and single domain.

(4) The homogenous non-domain switching

Recent studies using poly(vinylidene fluoride/trifluoroethylene) (P(VDF-TrFE))

copolymer Langmuir-Blodgett ultra-thin films suggested the switching kinetics in these films is different from the rules of nucleation and domain wall motion (extrinsic switching). This type of switching is called intrinsic switching which is defined by the absence of nucleation center and domain. It has a threshold field the intrinsic coercive field which is as high as $10^9 V/m$. The polarization switching exhibits a critical behaviour characterized by a pronounced slowing just above the threshold field [160]. In 2000 Ducharme et al. [19] reported that the intrinsic coercive field predicted by the Landau-Ginzburg theory of ferroelectricity was observed in P(VDF-TrFE) LB films below a thickness of 15nm for the first time. They found that with decreasing thickness the coercive field first increases and then saturates for samples thinner than 15nm, to a value of 5MV/cm which is in good agreement with the theoretical intrinsic value.

In intrinsic switching, the dipoles in the systems are highly correlated and tend to switch coherently or not at all. It can be described by Landau-Khalatnikov equations in the context of mean-field theory,

$$\xi \frac{dP}{dt} = -\frac{\partial G}{\partial P} \quad (6.13)$$

$$G = \alpha(T - T_0)P^2 + \beta P^4 + \gamma P^6 - EP \quad (6.14)$$

where P , G , E and T are the polarization, the free energy, the electric field and the temperature, respectively. ξ is a damping coefficient, T_0 is the Curie-Weiss temperature. α , β and γ are constants assumed to be independent of temperature. By minimizing the free energy G in Eq. (6.14), a steady state hysteresis loop $P(E)$ can be derived, as shown in Fig. 6.3 [160]. The solid lines in Fig. 6.3(a) denote stable (AB and A'B') or metastable (BC and B'C') minima in the free energy. The dotted line (COC') denotes unstable minima. Starting from a stable state B, if an opposite electric field which has an amplitude lower than the coercive field is applied, the polarization will remain in the metastable state (BC), then return to its initial state B after the field is removed. On the contrary, if a field larger than the coercive field is applied, the polarization will switch to the other state (A'B') and remain in B' when the field is suppressed. The vertical dashed lines mark the limits of the quasi steady state hysteresis loop. The evolution of the polarization from a negative polarization state to a positive polarization state in Fig. 6.3(b) is obtained by numerical integration of Eq. (6.13). There is switching only for $E > E_c$. Any field larger than E_c results in the same polarization value.

The switching time τ_{in} in intrinsic homogenous switching frame can be defined as the time needed by the polarization from a stable state (e.g. $+P_r$) to cross the zero axis

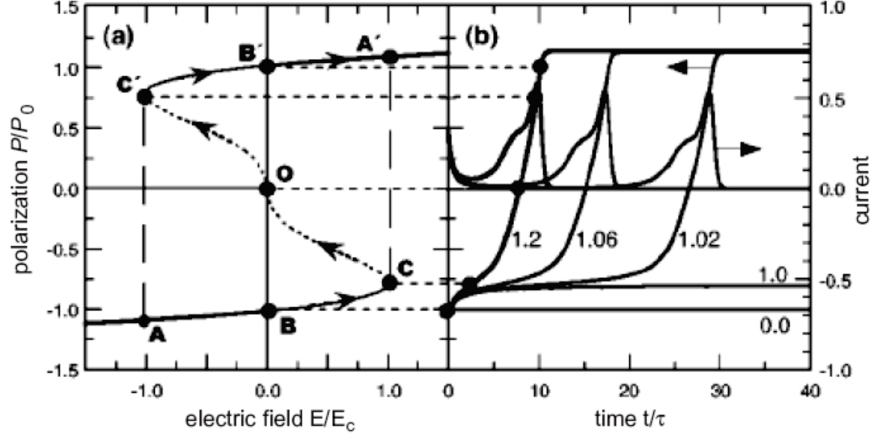


Figure 6.3: (a) The theoretical hysteresis loop $P(E)$ calculated from Eqs. (6.13) and (6.14) for $T \approx T_0$. The solid lines represent stable or metastable states and the dotted line denotes unstable states. (b) Time evolution of the normalized polarization and current during switching at $T = T_0$ for several values of the normalized electric field. The horizontal dashed lines connect corresponding points in (a) to states in (b) [160].

of the polarization (e.g. $B \rightarrow O$ in Fig. 6.3(a)) [21]. From the relationship between the derivative of the polarization P and the free energy G in Eqs. (6.13) and (6.14) the reciprocal switching time τ_{in} is found to have a square-root critical dependence of the form, [160]

$$\frac{1}{\tau_{in}} \approx \frac{1}{\tau_0} \left(\frac{E}{E_c} - 1 \right)^{1/2} \left(1 - \frac{T - T_0}{T_1 - T_0} \right)^{1/2} \quad (6.15)$$

where $\tau_0 \approx 6.3\gamma\xi/\beta^2$, $T_1 = T_0 + 3\beta^2/4\gamma\alpha$. From this equation it can be seen that the switching time τ_{in} will go to infinity as the applied field E approaches to E_c or the temperature increases to T_1 . There is a true coercive field that for fields below this value no switching should occur. In addition, the temperature dependence of switching process is different from a thermally activated behaviour which has an exponential dependence.

Followed by the observation of intrinsic switching in ultra-thin P(VDF-TrFE) LB films, several groups argued against the intrinsic nature of the switching [21-25]. In Ref. [21] the authors found that the experiments are lack of several key features of intrinsic switching: the coercive field does not saturate with decreasing film thickness; the electric field and temperature dependence of the switching time are not well described by the intrinsic switching dynamics in Eq. (6.15); the films have switching below the coercive field. R. C. G. Naber et. al. [25] presented measurements using gold electrode for spin coated P(VDF-TrFE) films down to 60nm. A thickness independence of

coercive field is found which leads to the conclusion that the thickness dependence of coercive field in LB films is due to the influence of the electrode interfaces. Very recently, the same group in Ref. [19] demonstrated new experiment evidences to confirm the existence of intrinsic switching kinetics in ultra-thin ferroelectric copolymer films [26,27]. They used piezoresponse force microscopy (PFM) to switch the sample at the nanoscale. The dependence of the switching rate on voltage for a 54nm thick film exhibits extrinsic nucleation and domain growth kinetics without true threshold coercive field, and is qualitatively different from the behaviour of an 18nm thick film, which exhibits intrinsic switching kinetics with a true threshold coercive field. The absence of top electrode on the sample can exclude the effect of electrode interface. Nevertheless, the depolarization field should be compensated by the tip of the PFM or by the flow of free charges within the sample and in the surrounding medium when the tip is not in contact with the sample surface. Intrinsic homogeneous switching is also found in ultrathin ferroelectric $BaTiO_3$ films [28] by PFM and ultrathin epitaxial $PbTiO_3$ films [168] by in situ synchrotron X-ray scattering measurements. Consequently, the authors claimed that homogeneous switching in ultrathin films is a common phenomenon for all ferroelectric materials.

Up to date, the switching process in P(VDF-TrFE) thin films is not fully understood. The explanations for the switching behavior are still controversial. In this chapter, we firstly investigate the switching current transients in P(VDF-TrFE) thin films with different thicknesses systematically. The important characteristic of the switching current, i.e., whether there is a maximum in time appearing during polarization reversal, is presented. Then we reveal the different temperature dependence of switching behavior in thin and thick films. The physical origins corresponding to the differences are discussed. At last, switching measurements are performed to try to distinguish whether the switching kinetics is extrinsic or intrinsic.

6.2 Thickness and field dependence of switching process

The most meaningful method to study the polarization reversal in a ferroelectric material is to measure the current flowing to the sample during switching as a function of time. We performed the switching current transient measurements started from the negative remanent polarization $-P_{rem}$ by applying a negative pulse, after a waiting time in the short circuit, a positive pulse was applied and the switching currents were recorded. Fig. 6.4 shows the applied voltage dependence of switching current responses of the P(VDF-TrFE) film with a thickness of 600nm. There is a remarkable peak ob-

served in the current transients. Since the RC constant in this system is at nanosecond scale, much shorter than the switching time of the sample in the observed range, the RC peak has negligible influence on the switching current peak. The switching time, which can be defined as the time difference between the time when the application of the reversed field starts and the time when the switching current approaches zero [41], more often, can be defined as the instant at which the current reaches its maximum [169]. Here, we take the time at maximum τ_{max} as a measure for the switching time. As can be seen in Fig. 6.4, the current maximum increases with increasing applied voltage and shifts simultaneously to shorter times.

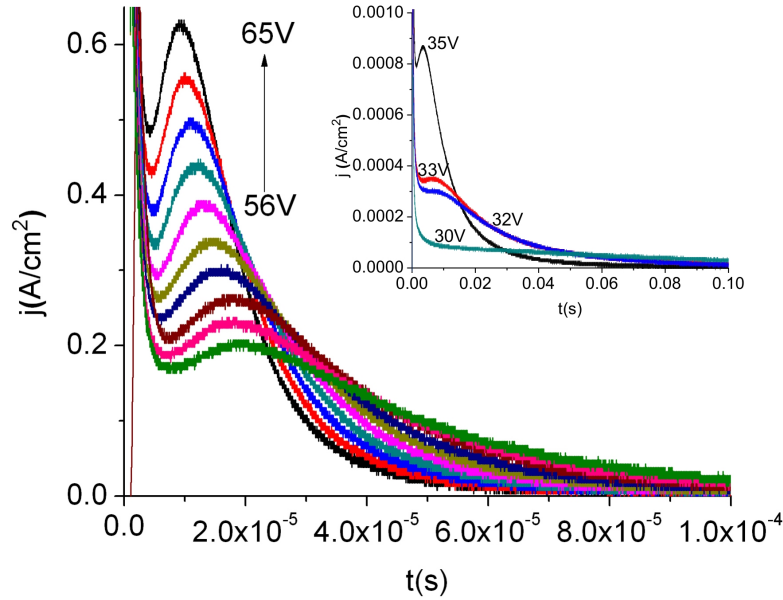


Figure 6.4: Switching current transients for the P(VDF-TrFE) film with a thickness of 600nm under various applied voltages. A peak in the current is observed. Inset shows the switching current transients at low external voltages. The current peak disappears in the vicinity of the coercive voltage.

The inset of Fig. 6.4 shows the current maximum becomes less pronounced as decreasing applied voltage and disappears in the vicinity of the sample's coercive field (U_c is 30V determined by the hysteresis loop at 1Hz), which suggests that coercive field is the critical field for the appearance of current peak. This peculiarity is in agreement with the simulation results in Ref. [154]. For P(VDF-TrFE) films as thick as 600nm, the switching behaviour is similar to single crystals, that is, above the coercive field a

current maximum occurs during polarization switching.

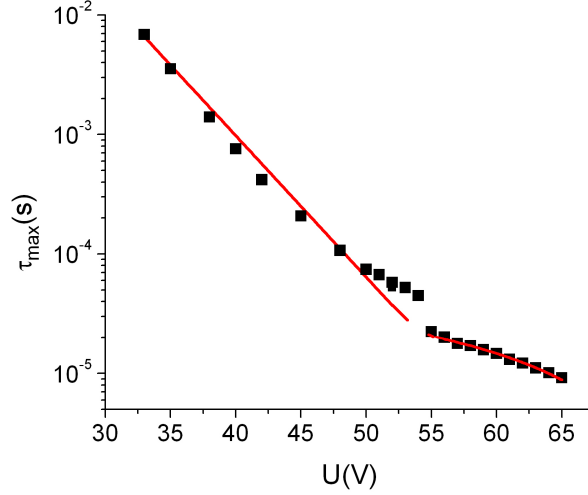


Figure 6.5: Peak time in the current transients as a function of the applied voltages. The lower applied voltage region is fitted with an exponential function while the higher applied voltage region is fitted with a power law function. The thickness of the ferroelectric film is 600nm.

The time to maximum τ_{max} as a function of external voltages is plotted in Fig. 6.5. At low applied fields the switching time can be fitted by the Merz's empirical law [41],

$$\tau_s = \tau_0 \exp\left(\frac{\alpha}{E}\right) \quad (6.16)$$

where τ_0 and α are constants and is regarded as activation field. E is the applied field. At high applied fields, the data points slightly deviate from the exponential fitting and they are best fit by the power law function,

$$\tau_s = \frac{1}{\mu(E - E')} \quad (6.17)$$

The parameter μ is the mobility of the domain walls and E' is a limiting field strength defining the range of validity of Eq. (6.17). The different switching behaviour for low and high electrical field regions, which separate out around 90MV/m, can be explained by a change of the switching kinetics, that is, polarization reversal is governed by the nucleation of new domains at low applied fields, which has an exponential dependence on field strength, and by the domain-wall motion at higher applied fields, which has a power law or linear dependence [101].

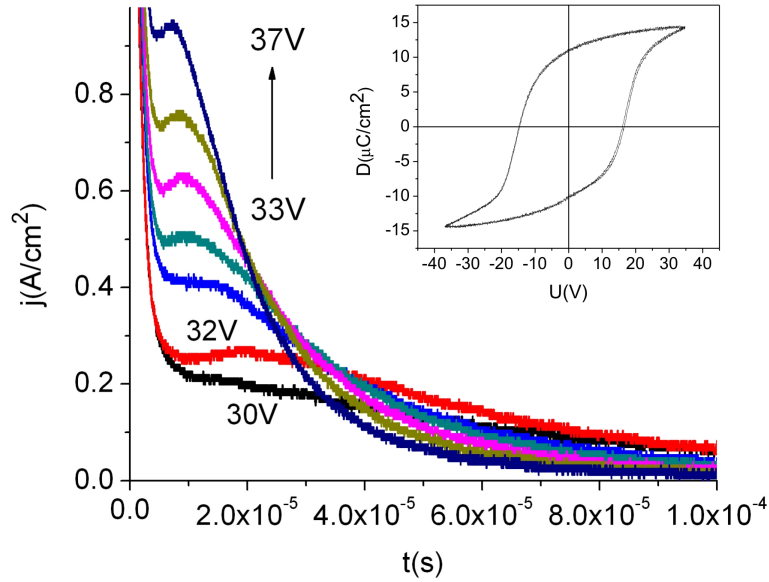


Figure 6.6: Switching current transients for the P(VDF-TrFE) film with a thickness of 320nm under various applied voltages, a peak in the current is only observed at fields above 100MV/m. Inset shows the hysteresis loop of the sample measured with a triangular signal at 1 Hz (coercive voltage is 15V).

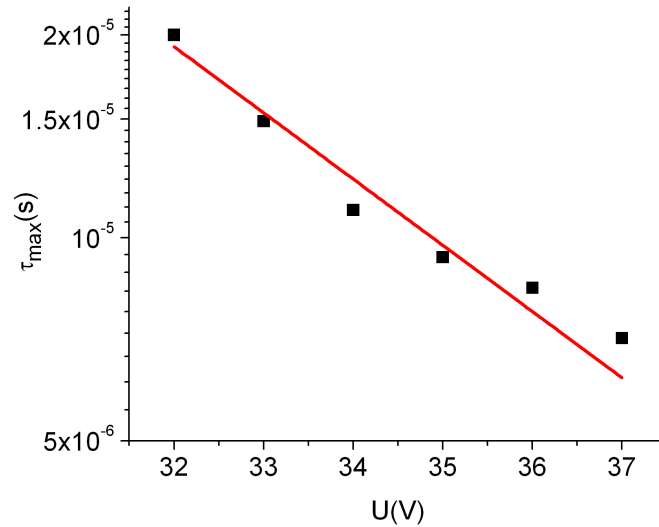


Figure 6.7: Voltage dependence of the peak time, the data points are fitted with an exponential function.

As the film thickness decreases to 320nm, we obtain the applied voltage dependence of switching current transients depicted in Fig. 6.6. The current peak is only observed at high fields exceeding 100MV/m (more than twice of the sample's coercive field, as shown in the inset of Fig. 6.6), which suggests that the critical field for the appearance of the current peak is much higher than its coercive field here. Moreover, the peak is less pronounced as compared to that of the sample of 600nm (Fig. 6.4). The time to maximum τ_{max} as a function of external voltages is plotted in Fig. 6.7, which can be fitted with an exponential function. The reduction of the film thickness leads to a change of switching kinetics.

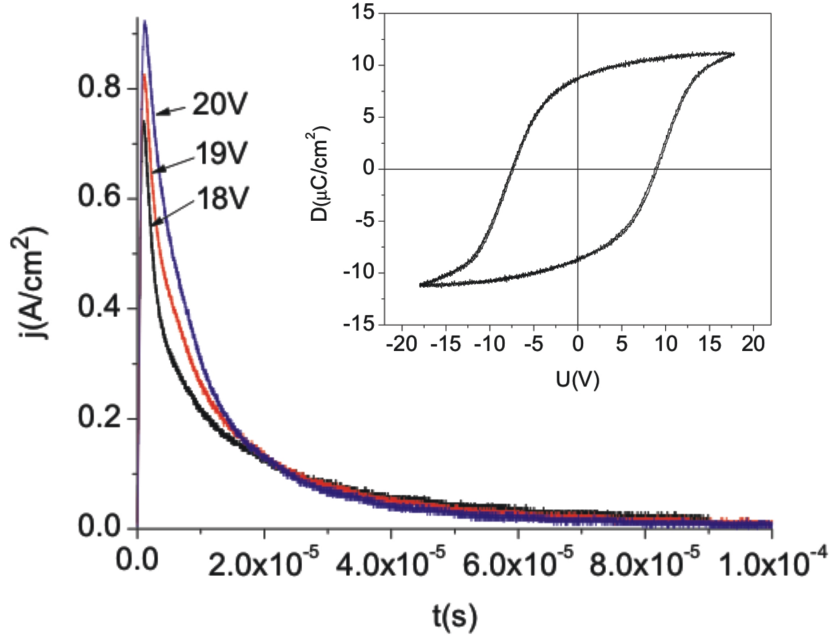


Figure 6.8: Switching current transients for the P(VDF-TrFE) film with a thickness of 158nm under various applied voltages. There is no peak in the current transient even at high applied voltages. Inset shows the hysteresis loop of the sample measured with a triangular signal at 1 Hz (coercive voltage is 8.1V).

For films thinner than 300nm, we observed a monotonic decrease in the switching current without maximum even at high field strengths. Fig. 6.8 shows the switching current responses of the P(VDF-TrFE) film with a thickness of 158nm. There is no peak in the current observed for fields more than twice of the sample's coercive field (extracted from the hysteresis loop shown in the inset). It is worth noting that

there is also no current maximum observed in sub-300nm films prepared by Langmuir-Blodgett deposition, which indicates that the above measurement results are regardless of preparation method. In fact, we have already studied that the spun films and LB films basically have the same switching behaviour [110], despite LB films are found to exhibit higher crystallinity [18].

So far, we are not successful in developing a quantitative model to describe the thickness dependence of switching current profiles. The switching process in ferroelectrics with a maximum in time for the switching current as observed by Merz can be simulated in the framework of the Weiss molecular mean field model with homogeneous state and single domain [154]. This is also in accordance to our measurements in P(VDF-TrFE) thin films as thick as 600nm described above. The introduction of interfacial dielectric layer between the ferroelectric film and the electrode can generate a depolarization field, which becomes the higher the thinner the ferroelectric film is. The current maximum in time disappears with decreasing the ferroelectric film thickness for a constant interface layer thickness. However, at the same time, the hysteresis loop in the sample will also disappear as a result of high depolarization field [170]. In addition, in the framework of KAI model, it is not possible to identify a current maximum for $n \leq 1$ according to Eq. (6.8). For $n > 1$, a peak occurs in the current similar to the experiment results in Fig. 6.4. However, there is no physical meaning in the framework of KAI model for an n value less than 1 since the sample dimensionality could never be less than 1. Numerical simulations in small systems using a local field method combined with dynamic Monte Carlo steps results in a monotonic decrease in the switching current [100]. A model for the thickness dependence of switching current profiles is needed in the future. Probably, a dynamic simulation in Weiss model would be the direction.

6.3 Temperature dependence of switching process

Fig. 6.9 shows the temperature dependence of switching current transients for the 600nm-P(VDF-TrFE) film at a constant applied field of 100MV/m. As the temperature increases, the current maximum increases and shifts simultaneously to shorter times indicating a faster switching at higher temperature. The inset in Fig. 6.9 clearly reveals that when the temperature approaches to the Curie point, the peak is less pronounced and becomes a shoulder and finally disappears above the Curie point due to the loss of ferroelectricity. An Arrhenius plot of the time to maximum in Fig. 6.10 presents that

the data points are best fit by a thermal activation law,

$$\tau_s = \tau_0 \exp\left(\frac{W}{kT}\right) \quad (6.18)$$

with $\tau_0 = 5 \times 10^{-14}$ s, and $W = 0.54$ eV for the sample's activation energy. This is consistent with the Arrhenius behaviour of the peak time simulated by the Weiss model in Ref. [154].

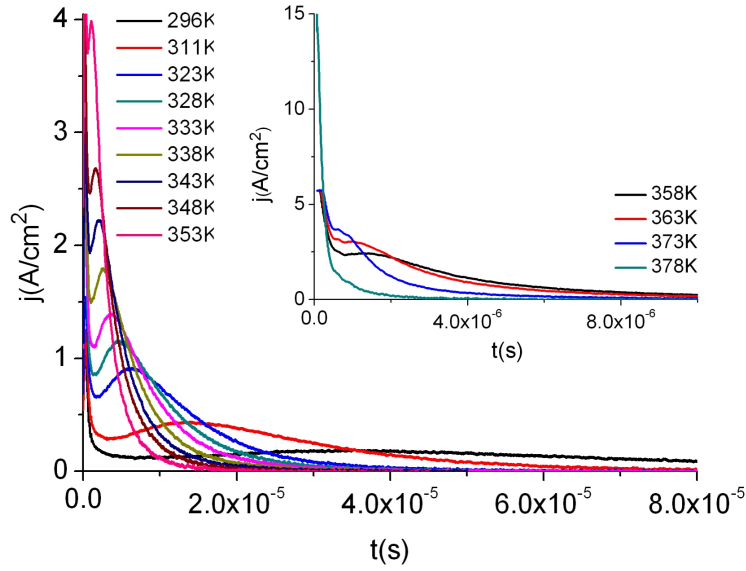


Figure 6.9: Temperature dependence of switching currents for a 600nm-P(VDF-TrFE) film at 100MV/m.

The time dependence of polarization build up for the 600nm-P(VDF-TrFE) film at 100MV/m over a wide temperature range is presented in Fig. 6.11. With increasing temperature, the curve shifts to the left side along the time axis. The saturation value of polarization is nearly constant until about 333K where it starts to decrease due to the loss of ferroelectricity. Meanwhile the conduction current becomes noticeable at longer times and high temperature. The polarization transients can be approximately described by the phenomenological formula of Eq. (4.6). The extracted turning point of the switching time τ_{tp} is plotted in Fig. 6.12, which has an Arrhenius dependence on temperature over the entire temperature range (from low temperature of 218K to high temperature of 353K) as expected for a thermally activated process. As discussed in chapter 4, the peak time τ_p should be slightly smaller than the turning point τ_{tp} formally.

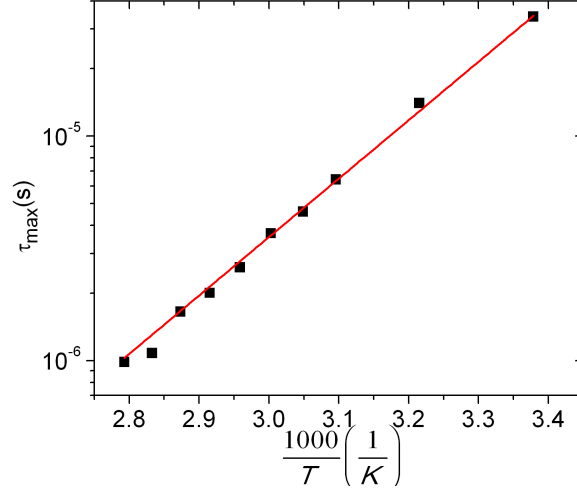


Figure 6.10: Arrhenius plot of the time to maximum in the temperature dependence of switching currents for a 600nm-P(VDF-TrFE) film at 100MV/m. The red line indicates a fitting by Eq. (6.24).

Compared Fig. 6.10 and Fig. 6.12 from room temperature to high temperature region, the time to maximum is also slightly smaller than τ_{tp} . The fitting by the thermal activation law in Eq. (6.18) gives $\tau_0 = 1 \times 10^{-14}s$, and $W = 0.58eV$, which are similar to the values deduced in the temperature dependence of peak time (Fig. 6.10).

On the other hand, the extracted stretching factor α which characterizes the profile of the polarization transient is shown in Fig. 6.13. α increases with increasing temperature. An exponential fitting can roughly describe the temperature dependence tendency of α . For a constant applied field, polarization switching occurs over a very wide time scale at low temperature, i.e. from 10^{-6} to 10s, related to the smaller value of α . As the temperature increases, a complete polarization switching occurs within shorter time scale, e.g. 1 to 2 decades above 307K. For $T < 280K$, $\alpha < 1$ which indicates the current maximum disappears at low temperature. Since the coercive field increases with decreasing temperature (see later in Fig. 6.21), the critical field for the appearance of current maximum in the switching transient is expected to be higher. However, this needs to be proved by low temperature measurements in the future.

We observed different temperature dependence of switching behavior for films thinner than 300nm. The switching current transients with a variation of temperature for a 98nm-P(VDF-TrFE) film at 150MV/m is depicted in Fig. 6.14. We have checked carefully that there is also no current maximum in the switching transients at higher

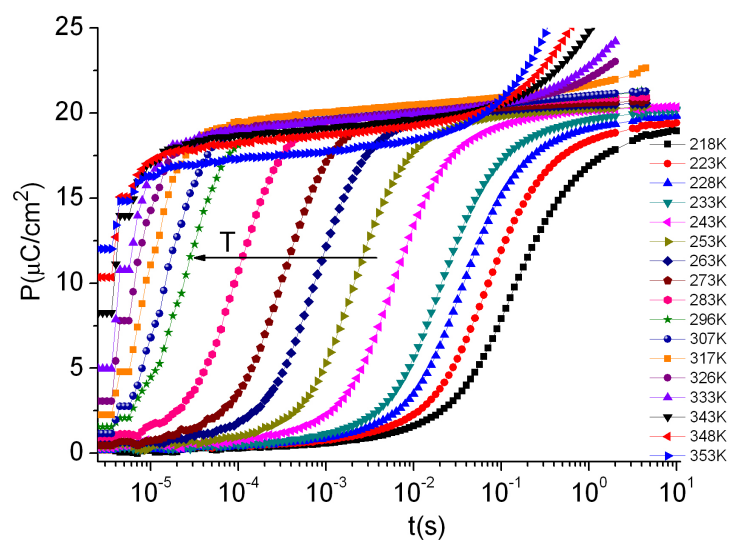


Figure 6.11: Time dependence of polarization build up for a 600nm P(VDF-TrFE) film at 100MV/m in a wide temperature range from 218K to 353K.

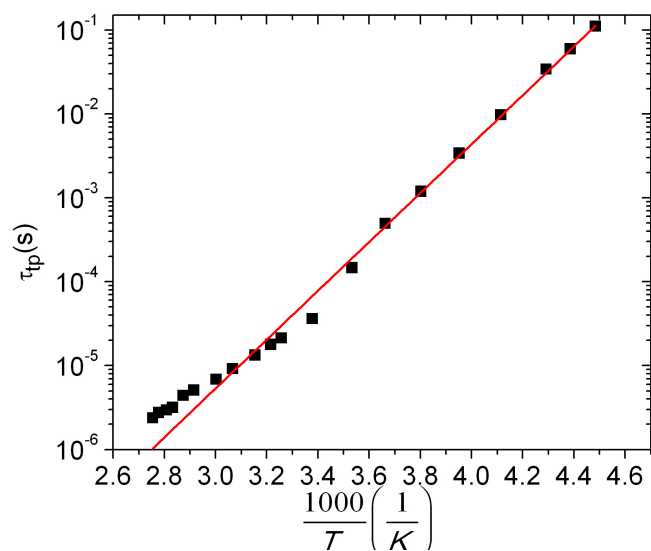


Figure 6.12: Arrhenius plot for the switching time of the turning point in the polarization transients for a 600nm P(VDF-TrFE) film at 100MV/m. The red line indicates a fitting by Eq. (6.18).

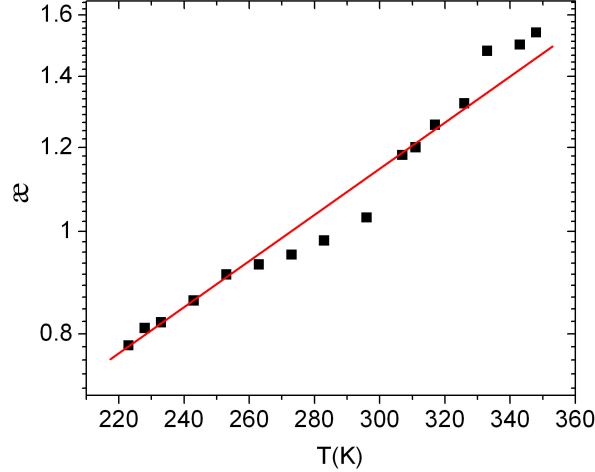


Figure 6.13: The shape factor α extracted from the temperature dependence of polarization build up for a 600nm P(VDF-TrFE) film at 100MV/m. The red line is an exponential fitting.

temperature. The current drops faster at shorter times with increasing temperature which indicates an accelerated switching event at higher temperature.

The time dependence of polarization build up from room temperature to high temperature of 365K is checked in Fig. 6.15. The curve firstly shifts to the left side with increasing temperature which is of thermal activated nature. However, further increasing temperature causes a slanted curve. This could be due to the ferroelectricity loss when the temperature approaches to the Curie point. At the same time, the remanent polarization degrades and the conduction current becomes pronounced with increasing temperature. It turns out that for thinner films the acceleration of the switching time by temperature has an upper limit due to the loss of ferroelectricity.

Furthermore, the switching kinetics in thinner films is investigated in low temperature region down to 218K, which is shown in Fig. 6.16. With decreasing temperature, the switching curves shift to the right side along the time axis indicating a slower switching. Moreover, the saturation value of the polarization decreases with decreasing temperature. This could be due to the pinning effect of domain walls and the increase of coercive field at lower temperature (determined by the hysteresis loop). A long poling time of 1000s is applied to the sample at low temperature of 223K and the polarization transient in time domain over 9 decades is shown in Fig. 6.17. There is no second step of polarization increase for poling time up to 1000s which indicates that the

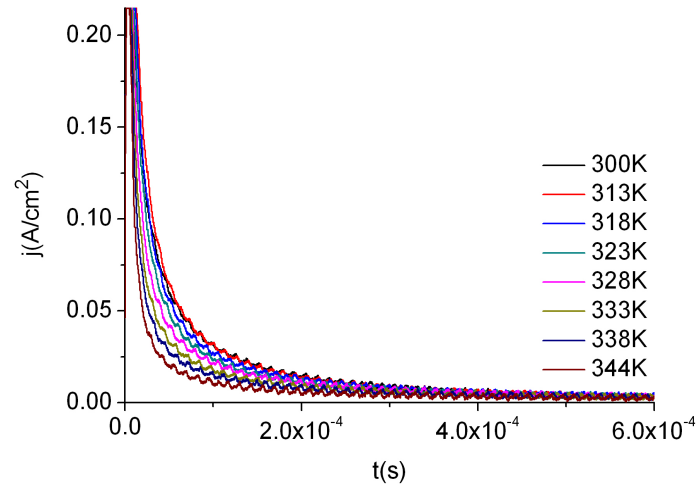


Figure 6.14: Temperature dependence of switching currents for a 98nm-P(VDF-TrFE) film at 150MV/m (from room temperature to 344K).

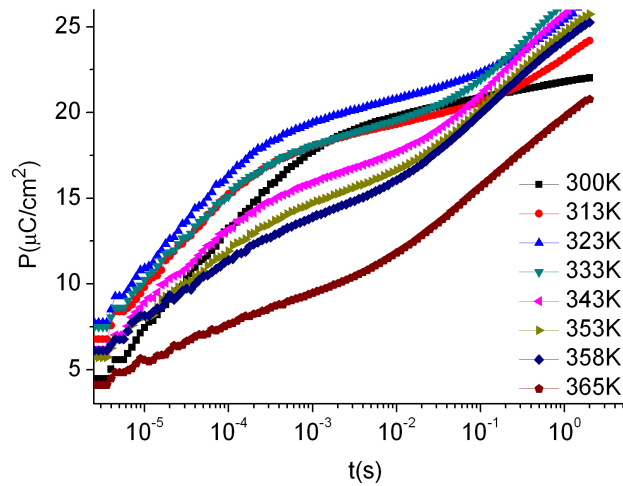


Figure 6.15: Temperature dependence of polarization transients for a 98nm-P(VDF-TrFE) film at 150MV/m.

energy provided by the electric field at this temperature is not high enough to depin the domain walls. In general, defects, imperfections, interfaces and grain boundaries can serve as the pinning centers. Domain pinning centers are distributed in the ferroelectric in a random manner. A certain fraction of switchable polarization is reduced by capturing an electron by a pinning center. Domain depinning can be achieved by either sufficiently strong field or thermal fluctuations [171]. At the interface, the dipoles are pinned by their image charges. The ratio of the pinned dipoles to the switchable dipoles in the bulk is the higher the thinner the film is. Therefore domain pinning effect in thin films is usually stronger than in thick films. Monte Carlo simulations of ferroelectric properties based on a microscopic model also reveal that in thin films the pinning effect due to the image dipole prevails and the pinning effect of the image dipoles is more pronounced with decreasing temperature [152,172]. This effect partly contributes to the lower saturation polarization with decreasing temperature under a constant applied field in Fig. 6.16.

Fig. 6.18 exhibits the switching times of the turning point for the thin sample in the entire temperature range. The data points can be fitted by the thermal activation law of Eq. (6.18), revealing that the thermal activation nature also governs thin films below the Curie point. The shape factor α for the thin sample (Fig. 6.19), in striking contrast to the thick film in Fig. 6.13, is more or less constant, which indicates the switching kinetics in thin films is different from thick films.

The coercive field E_c is a function of frequency and amplitude of the input signal as discussed in chapter 4. Besides, E_c changes considerably with temperature as it approaches to the Curie point. The value of E_c at a given frequency, amplitude and temperature, is related to the switching mechanism being dominant under the given conditions [173]. Fig. 6.20 shows the evolution of hysteresis loops in dependence of temperature for a 600nm-P(VDF-TrFE) film. All the hysteresis loops have a similar shape. The coercive field E_c increases with decreasing temperature. The extracted coercive voltage U_c and remanent polarization P_r are shown in Fig. 6.21. The remanent polarization P_r remains nearly constant in the temperature range from 296K to 243K. P_r slightly decreases from $10.1\mu C/cm^2$ at 233K to $9.6\mu C/cm^2$ at 218K due to the domain pinning at low temperature which requires a higher applied voltage. The coercive voltage U_c can be fitted with a linear line. This is in agreement with the prediction of Landau-Ginzburg (LG) phenomenology of the first order, which is well approximated by [116],

$$E_c \approx 2\beta(3|\beta|/5\gamma)^{3/2} (1 - 25(T - T_0)\gamma/(6C\beta^2)) \quad (6.19)$$

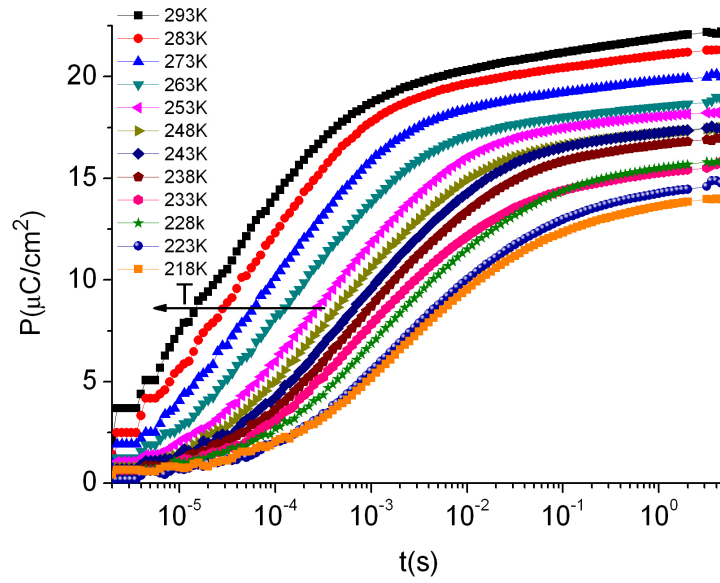


Figure 6.16: Time dependence of polarization build up for a 98nm-P(VDF-TrFE) film at 150MV/m in low temperature region.

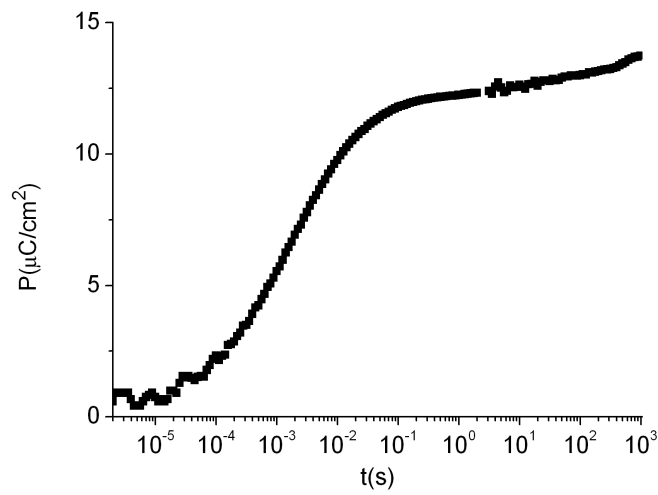


Figure 6.17: Time dependence of polarization build up for a 98nm-P(VDF-TrFE) film at 150MV/m at a low temperature of 223K for 1000s over 9 decades in the time domain.

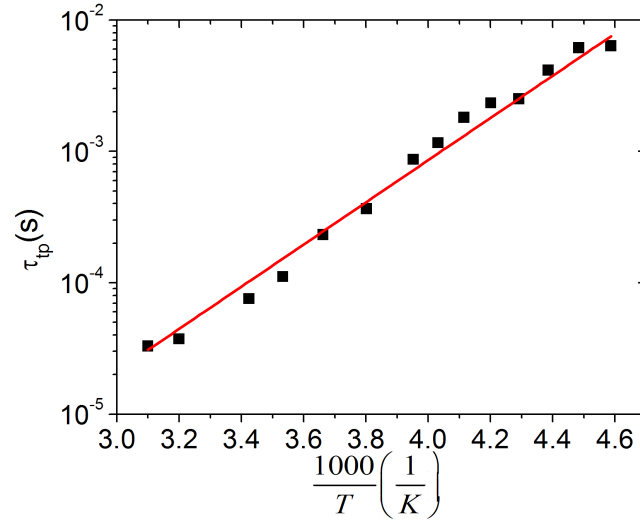


Figure 6.18: Arrhenius plot for switching time τ_{tp} of the turning points in the polarization transients for a 98nm-P(VDF-TrFE) film at 150MV/m over the entire temperature range.

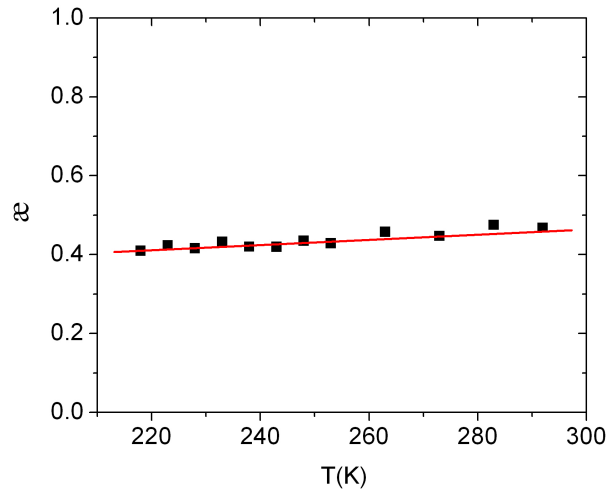


Figure 6.19: The shape factor α extracted from the temperature dependence of polarization build up for a 98nm-P(VDF-TrFE) film at 150MV/m. The red line is a guide for eyes.

where β , γ are LG coefficients, C is the Curie constant and T_0 is the Curie temperature. The intercept of the linear fitting at x axis is 366K, which is close to the Curie point of the sample (see also Fig. 7.3 in chapter 7). The simulation in Weiss model taking into account the piezoeffect which induces a first order transition gives a temperature dependence of coercive field in a power law form $E_c(T) = const.(\theta - T)^\beta$, with the exponent $\beta \approx 1.17$ [167]. In addition, the Landau-Ginzburg (LG) phenomenology of the second order and the Ising-Devonshire model both expect a power law dependence on the temperature with the former having form of Eq. (6.20) and the latter having form of Eq. (6.21) [116],

$$E_c = 2\beta ((T_0 - T)/(3C\beta))^{3/2} \quad (6.20)$$

$$E_c \approx (2kT_0/(3p_0)) (1 - T/T_0)^{3/2} \quad (6.21)$$

In Eq. (6.21), k is the Boltzmann constant and p_0 is the dipole moment. The fitting curve for the temperature dependence of the coercive field $E_c(T)$ in the simulation by the Weiss mean field model yields the same power law function for the second order transition [153]. Compared to Eq. (4.11) in chapter 4, the coercive field also has a power law dependence on temperature with the exponent equal to 3/2, the same as Eqs. (6.20) and (6.21). Therefore, the temperature dependence of E_C generally can be expressed as $E_c = C_1(T_0 - T)^\beta + C_2$, with C_1 and C_2 being constants. For second order transition, $\beta = 3/2$; for first order transition, β is approximate to 1 (linear dependence).

Since E_c increases with decreasing temperature, polarization transients are also examined at a constant field normalized to the coercive field at different temperatures, i.e. $\frac{E_a}{E_c(T)} = const.$. Fig. 6.22 shows the polarization in time domain for the 600nm-film at a constant normalized field. In the low temperature range from 218K to 243K, the sample almost exhibits the same switching behavior. As temperature increases, the curve shifts to the left side slightly. The saturation polarization is nearly constant. The shape factor α only slightly increases with increasing temperature in this case and has a value of $0.9 \leq \alpha \leq 1.1$.

Fig. 6.23 shows the polarization transients for the 98nm-film at a constant normalized field. The sample has the same switching time in the temperature range from 233K to 273K. As temperature increases, the switching is slightly faster. Compared to Fig. 6.16, the reduce of saturation polarization is less pronounced for a normalized field which indicates that the increase of coercive field at low temperature contributes to the decrease of saturation polarization with decreasing temperature. The shape factor α

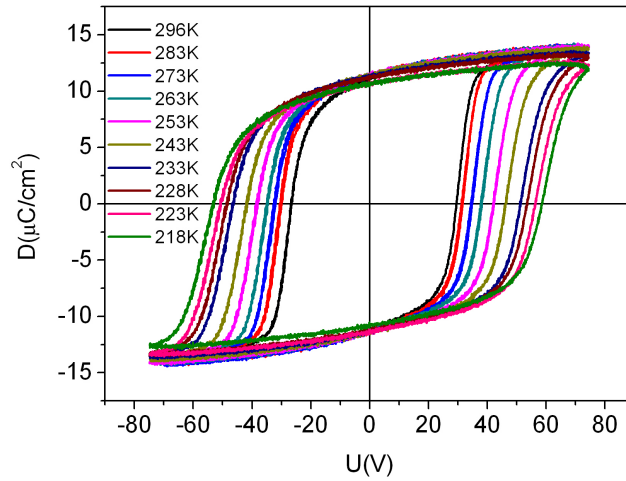


Figure 6.20: Temperature scaling of hysteresis loop for a 600nm-P(VDF-TrFE) film at 1 Hz.

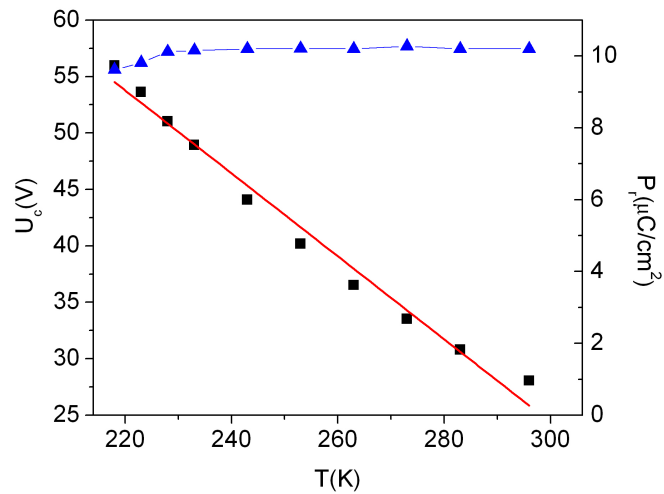


Figure 6.21: The temperature dependence of coercive voltage (left Y axis) and remanent polarization (right Y axis) for a 600nm-P(VDF-TrFE) film. The red line for the coercive voltage is a linear fitting.

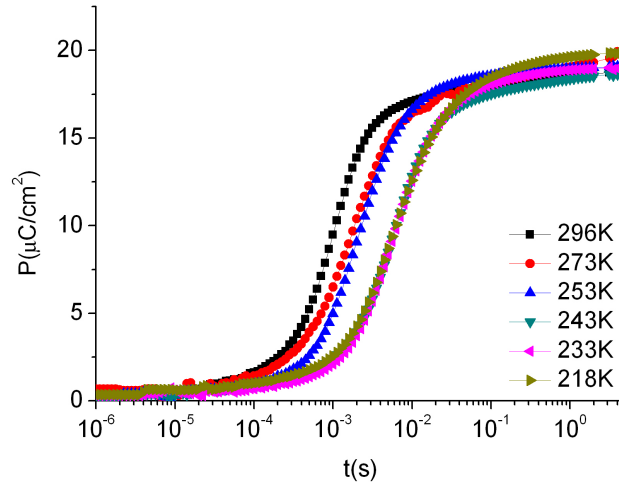


Figure 6.22: Time dependence of polarization build up for a 600nm-P(VDF-TrFE) film at a constant normalized field of 1.5 times of the coercive field at different temperatures, compared to Fig. 6.11.

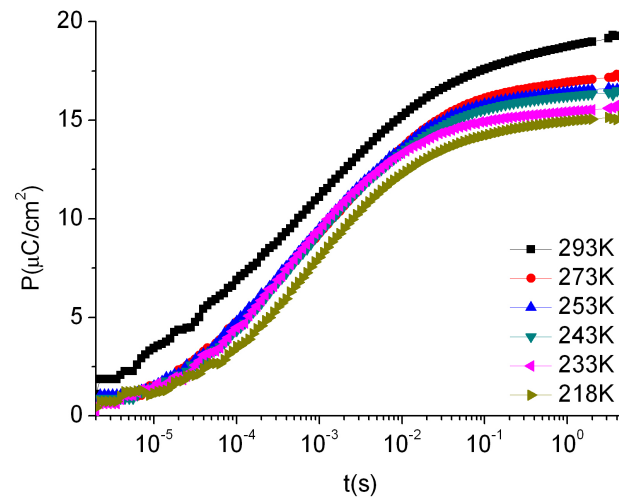


Figure 6.23: Time dependence of polarization build up for a 98nm-P(VDF-TrFE) film at a constant normalized field of two times of the coercive field at different temperatures, compared to Fig. 6.16.

is more or less constant as in Fig. 6.19 and has a value of $0.4 \leq \alpha \leq 0.5$.

6.4 Extrinsic switching vs. intrinsic switching

To examine if there is a transition from extrinsic domain switching to intrinsic spinodal switching with a decrease of sample thickness in ferroelectric films of P(VDF-TrFE) copolymer, thin samples with thicknesses ranging from 30 to 44nm prepared by Langmuir-Blodgett deposition and thicker films in the range of 320-412nm prepared by spin coating are investigated mainly through hysteresis loop and switching transient measurements.

Fig. 6.24 shows the polarization transients for a 412nm sample at different applied voltages. The coercive voltage and remanent polarization are determined from the hysteresis loop with $U_c = 23.6V$ and $P_r = 8\mu C/cm^2$. For applied voltage below the coercive voltage, there is a switching crossing the zero point polarizing up to 20s (from negative remanent polarization $-P_r$ to zero polarization $P = 0$). This is consistent with extrinsic domain switching which has no critical switching.

In striking contrast to the sample of 412nm, the thin film of 37nm has no switching (no crossing to the zero point) below its coercive voltage (6V) which shows intrinsic spinodal switching behavior with switching threshold (Fig. 6.25). The same behavior is also found in thin films of 30nm and 44nm with a critical switching at the coercive voltage.

Switching time here is defined as the zero crossing point in the switching transients from the negative remanent polarization to the positive polarization. Dependence of the reciprocal switching time $1/\tau$ on the normalized applied voltage U/U_c for samples with different thicknesses is summarized in Fig. 6.26. The thicker film follows an exponential law with no apparent critical switching. The thinner films can be fitted with a square root function referring to Eq. (6.15) which is a characteristic of intrinsic spinodal switching.

However, the switching transient measurement alone cannot give enough evidence to determine the intrinsic/extrinsic switching. The coercive field determined from the hysteresis loop also depends on frequency. Fig. 6.27 and Fig. 6.28 show dependence of the polarization on the applied voltage at different constant times for the samples of 412nm and 37nm obtained from the switching transient curves. In both samples, the voltage threshold which is defined as the crossing point from the negative polarization to the positive polarization exhibits a time dependence. The voltage threshold increases with decreasing pulse length. For example, as shown in Fig. 6.28, the 37nm

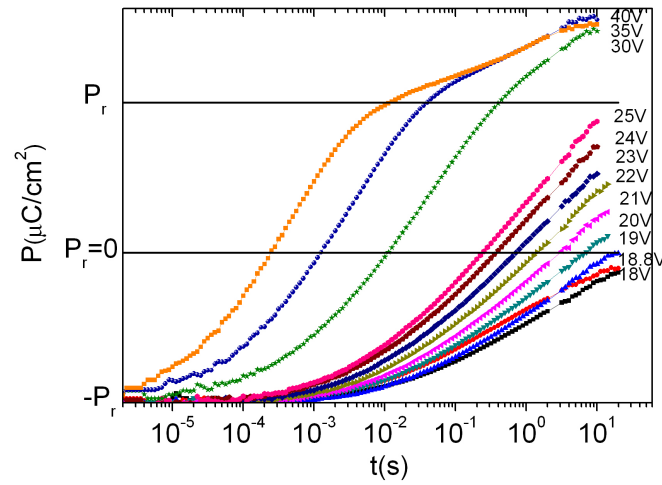


Figure 6.24: The switching transients of a spun film with 412nm at different applied voltages. There is switching below the coercive voltage of 23.6V.

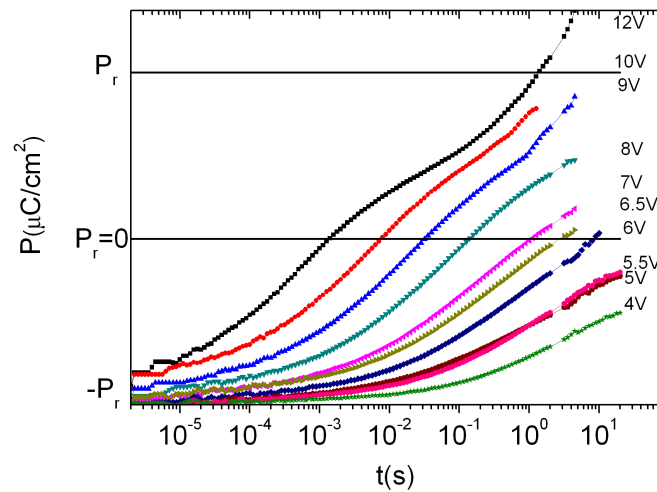


Figure 6.25: The switching transients of a LB film with 37nm at different applied voltages. There is no switching below the coercive voltage of 6V.

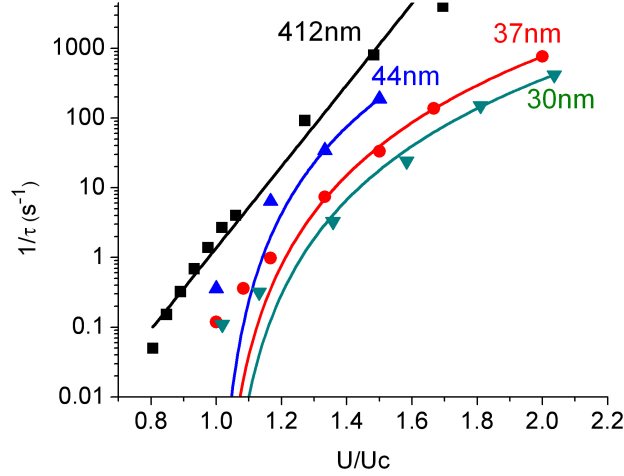


Figure 6.26: Dependence of the reciprocal switching time $1/\tau$ on the normalized applied voltage U/U_c for samples with different thicknesses. The data points for the thicker sample of 412nm are fitted with an exponential function showing no apparent critical switching. The data points for the thinner samples are fitted with a square root function (Eq. (6.15)) showing critical switching above the coercive field.

film has no switching after polarizing for 1ms at applied step of 12V but switching becomes achievable for longer polarizing time at the same applied voltage. Therefore, this experiment alone could not determine the switching mechanism without ambiguity since switching could happen for longer time with lower applied voltages.

Another experiment is devised to try to distinguish whether the switching mechanism is different in thin films and thicker films, which is shown in Fig. 6.29. A triangle voltage is applied to the sample to obtain the hysteresis loop and then the voltage is stopped at a value below the coercive voltage (V_2) and kept for a constant time. Polarization is recorded as a function of time during the set applied voltage step. For extrinsic switching, a zero crossing of the polarization is expected while there should be no zero crossing of the polarization for intrinsic switching.

Fig. 6.30 shows the hysteresis loop under the above described applied voltage sequence for a 320nm sample. After the recording of hysteresis loop, the voltage is kept at 10V ($0.7U_c$) for 5s. The polarization value changes from point A to point B, which has a switching at the zero crossing as predicted by the extrinsic domain switching with nucleation and domain motion process. On the other hand, in the hysteresis loop of the 30nm sample (Fig. 6.31), when the applied voltage is stopped at 2V ($0.7U_c$) and kept for

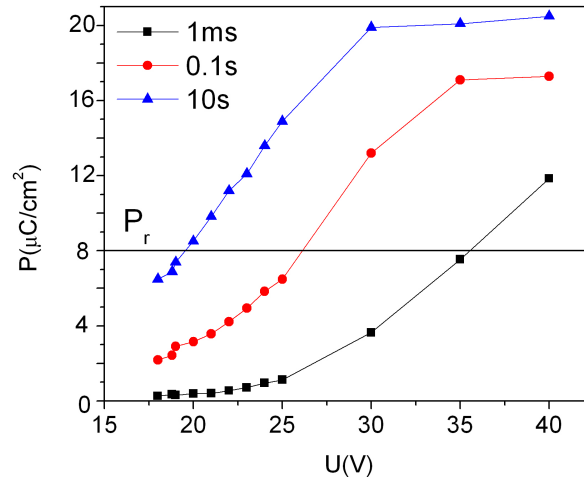


Figure 6.27: Dependence of the polarization on the applied voltage at different constant times for the 412nm spun film.

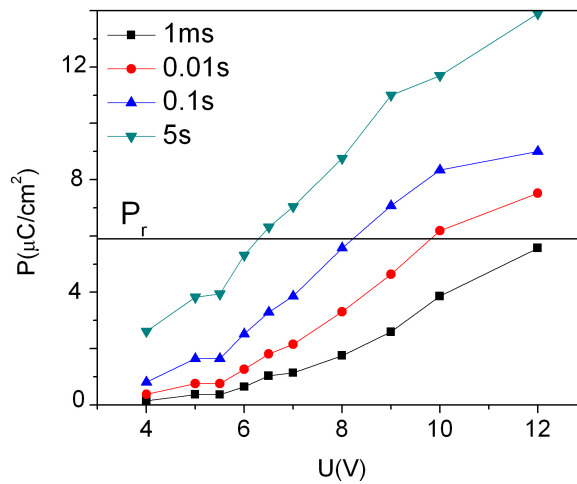


Figure 6.28: Dependence of the polarization on the applied voltage at different constant times for the 37nm LB film.

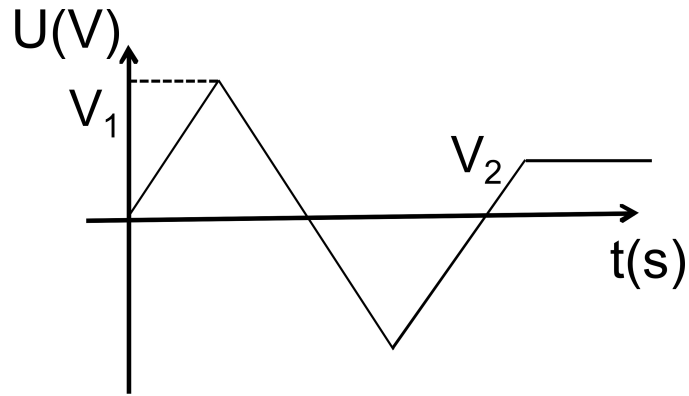


Figure 6.29: Schematic diagram of the applied voltage sequence.

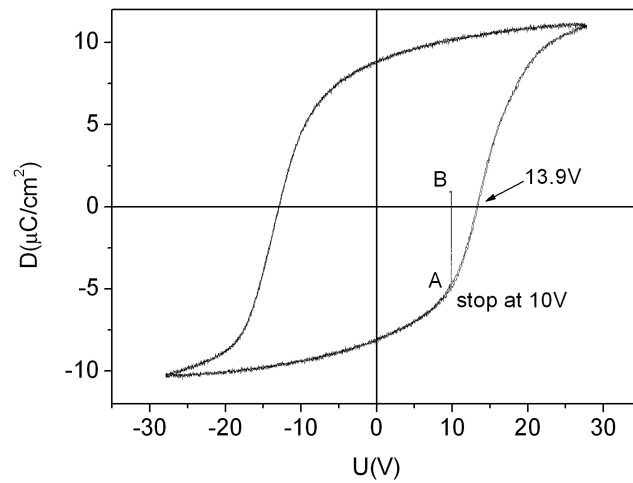


Figure 6.30: The hysteresis loop for a spun film of 320nm measured at 1 Hz. The applied voltage was stopped at 10V for 5s while polarization changing from point A to point B with a switching zero crossing.

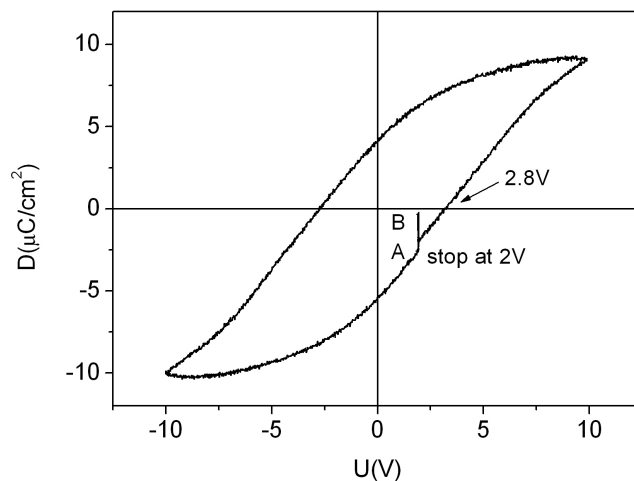


Figure 6.31: The hysteresis loop for a LB film of 30nm measured at 1Hz. The applied voltage was stopped at 2V for 5s while polarization changing from point A to point B without a switching zero crossing.

5s, the polarization value changes from point A to point B. No switching is observed in this case. However bear in mind that this experiment cannot exclude the side effects including conduction and dielectric relaxation. For thinner samples, space charge polarization would be pronounced as polarizing for longer time since leakage current is higher in thinner samples. Therefore, it is possible to observe a zero crossing in thinner films for longer step length. Unfortunately, this experiment cannot distinguish the switching mechanism without doubt. In the future, investigations of the local switching behavior performed by PFM probably can give an answer.

6.5 Conclusions

We have studied the important characteristics of switching process in P(VDF-TrFE) thin films with different thicknesses. An interesting size dependent effect is found in the profiles of the switching current transients. The switching behavior for P(VDF-TrFE) films as thick as 600nm is similar to that observed in ferroelectric single crystals, that is, a current maximum occurs during polarization switching above the coercive field indicating a critical switching. As the sample thickness decreases, the field dependent switching current profiles have changed which results from a transformation of switching kinetics. For P(VDF-TrFE) films as thin as 320nm, a less pronounced maximum

appears only at fields more than twice of the sample's coercive field. In contrast, there is a monotonic decrease in the switching current without maximum for samples thinner than 300nm. A quantitative model to describe this behavior is needed in the future.

The temperature dependence of switching process in thick films is thermally activated over the entire temperature range. The current maximum disappears above the Curie temperature due to the loss of ferroelectricity. In addition, it also disappears at low temperature under a constant applied field. The critical field for the appearance of current maximum is expected to be higher since the coercive field increases with decreasing temperature, which needs to be proved in the future experiments. Switching in thinner films is also thermally activated below the Curie point. The reduction of saturated polarization at low temperature is caused by domain pinning effect and the increase of coercive field at low temperature. The temperature dependence of coercive field exhibits an almost linear increase of coercive field with decreasing temperature. The switching transients under a constant normalized field to the coercive field at different temperatures have a smaller variation of switching time and saturated polarization.

At last, dynamic switching measurements including polarization transients in time domain and hysteresis loops with modified applied voltage sequence are employed to try to determine intrinsic/extrinsic switching in samples with different thicknesses. However, the present experiment evidence is not convincing and new experiment approach is needed in the future.

Chapter 7

Phase transition

In this chapter, the phase transition in PVDF and P(VDF-TrFE) copolymer films is studied. The important features which characterize phase transition including dielectric thermal hysteresis, temperature dependence of hysteresis loop and remanent polarization are investigated. The shift of the phase transition temperature in dependence of film thickness in PVDF is demonstrated and explained by theoretical models. The thermal Barkhausen effect in PVDF copolymer films is observed for the first time.

7.1 Phase transition in P(VDF-TrFE) thin films

The phase transition behavior in ferroelectric systems can be described by Landau phenomenological theory [36,174] and dipolar theory such as Weiss mean field model [153,165]. P(VDF-TrFE) copolymers (70/30) have been shown to have a first order phase transition [6], which is characterized by a discontinuity of P_s at T_c and the presence of double hysteresis loop close to T_c . The shift of the phase transition temperature in P(VDF-TrFE) copolymers can be induced by the application of electric field [175] and strain [176]. It has been reported that there is a phase transition in the surface region with transition temperature lower than that in the bulk in P(VDF-TrFE) thin films [18,177]. Here the phase transition behavior including the thermal hysteresis and temperature dependence of hysteresis loop in P(VDF-TrFE) thin films with different thicknesses is examined.

Fig. 7.1 shows the strong thermal hysteresis of the dielectric constant at zero bias for a 50ML P(VDF-TrFE) thin film at 1 kHz. The sample was heated and cooled with a constant rate of 1K/min. The Curie-temperature is at 377K during heating. At this temperature, the phase transition from the ferroelectric region to the paraelectric

region occurs. On the cooling process, the dielectric constant peaks at 347K indicating a paraelectric to ferroelectric transition. The large thermal hysteresis of $\Delta T = 30K$ is a clear indication of the first-order nature of the phase transition. The phase transition temperature revealing in $\epsilon(T)$ in P(VDF-TrFE) is almost constant in a broad range of sample thicknesses from 6.5nm to hundreds of micron [85]. In contrast, PVDF exhibits a strong finite size effect at the nanoscale, which will be discussed in section 2. It should be noted that the phase transition temperature in P(VDF-TrFE) is also independent of substrate since the dielectric constant peaks at the same positions in $\epsilon(T)$ using polyimide and silicon substrates.

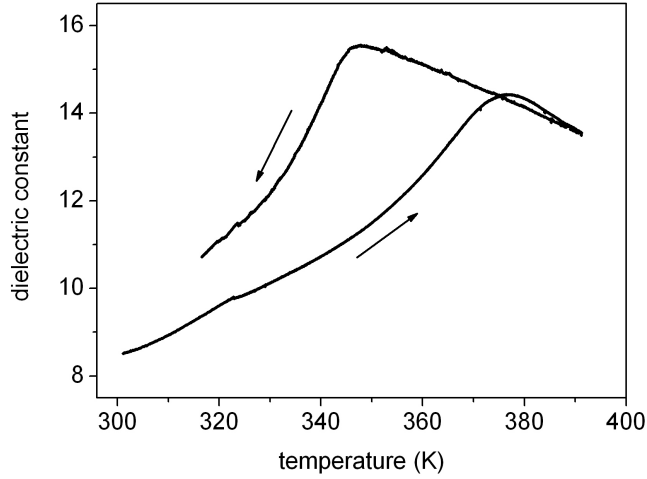


Figure 7.1: Dielectric constant for a 50ML P(VDF-TrFE) thin film (65nm) with a variation of the temperature at 1 kHz. Arrows indicate heating and cooling direction.

The dynamic hysteresis loops with a variation of the temperature during heating for a 600nm thick sample are shown in Fig. 7.2. As temperature increases, the hysteresis shrinks and both the values of the remanent polarization and coercive field decrease. Below a critical temperature of 358K, a single hysteresis loop is obtained. This critical point is close to the value found in the butterfly loop measurements [178]. A double hysteresis loop is observed in the temperature range of 358K-363K adjacent to the phase transition, as shown in the inset. The double hysteresis loop indicates the coexistence of the paraelectric and field-induced ferroelectric phase. Above 363K, a non-hysteretic single curve is found referring to the true paraelectric state.

The temperature dependence of the remanent polarization P_r and the coercive field E_c as derived from the hysteresis loops is exhibited in Fig. 7.3. There is a sharp jump

of P_r at temperature of 353K characterizing a first order ferroelectric phase transition. The coercive field E_c exhibits a linear decrease with increasing temperature before reaching the critical point, which has the same temperature dependence tendency as in low temperature region discussed in chapter 6 (Eq. (6.19)). A first order phase transition with a double hysteresis loop close to T_c can be simulated using the Weiss field model taking into account that strain in the ferroelectric induced by the polarization via the piezoeffect [167].

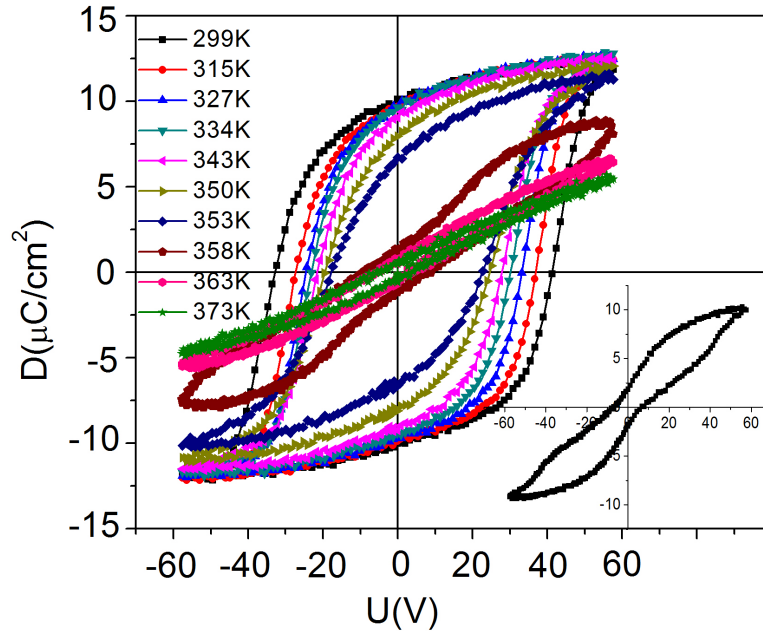


Figure 7.2: The variation of the hysteresis loops during heating for a 600nm thick sample at 500 Hz.

For a first order phase transition, the sample's behavior depends on whether it is approaching the Curie point from lower or higher temperature. Fig. 7.4 shows the temperature dependence of the hysteresis loop during cooling for the 600nm thick sample. The double hysteresis loop appears in the temperature interval of 361K-350K, which is larger than the temperature region for the double hysteresis loop in the heating process. The sample undergoes a paraelectric state to ferroelectric state transition during cooling. At sufficiently high field, the ferroelectric state is induced before reaching the Curie point. The temperature dependence of P_r during cooling together with the values during heating exhibit a thermal hysteresis of $P_r(T)$, which is shown in Fig. 7.5. P_r

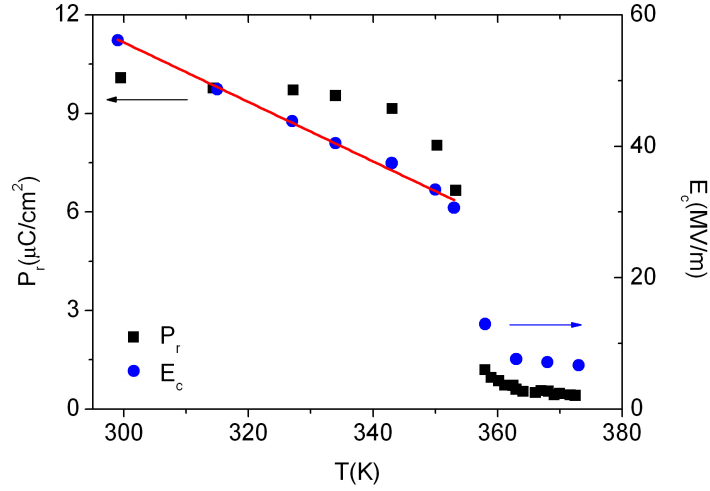


Figure 7.3: The temperature dependence of P_r and E_c determined from the hysteresis loops during heating for a 600nm-thick sample. The red line is a linear fitting.

decreases steeply at 353K upon heating and at 348K upon cooling, which implies the transition of first order nature. The value of P_r is lower after thermal cycling due to fatigue. However, P_r can mostly recover to the original value after a few days.

The thinner samples exhibit different temperature dependent hystereses close to phase transition from the thick samples. Fig. 7.6 shows the temperature dependence of hysteresis loop during heating for a 90nm thick sample measured at 10 Hz. With increasing temperature, the hysteresis loop shrinks with both remanent polarization and coercive field decreasing. However, there is no double hysteresis loop observed close to the Curie point. The temperature dependence of hysteresis loop with different frequencies from 10 Hz to 500 Hz is checked. Nevertheless, the double hysteresis loop is not found. The change of the remanent polarization P_r in dependence of temperature at different frequencies (Fig. 7.7) is smoother than that in thick samples. The experiment curves of Fig. 7.7 can be obtained by the dynamic Weiss model simulations including the piezoeffect. The method of simulation is described in detail within Ref. [179].

There are two reasons for the absence of double hysteresis loop in the thin samples. First, the frequency of the applied field is not low enough to trace a proper sequence of isothermal equilibrium states. It is expected that the ferroelectric which has a first order phase transition should exhibit double hysteresis close to the Curie temperature. In the dynamic hysteresis, the double hysteresis loop is only observed when the sample is able to take up the stable state which is the minimum of the free energy at every instant

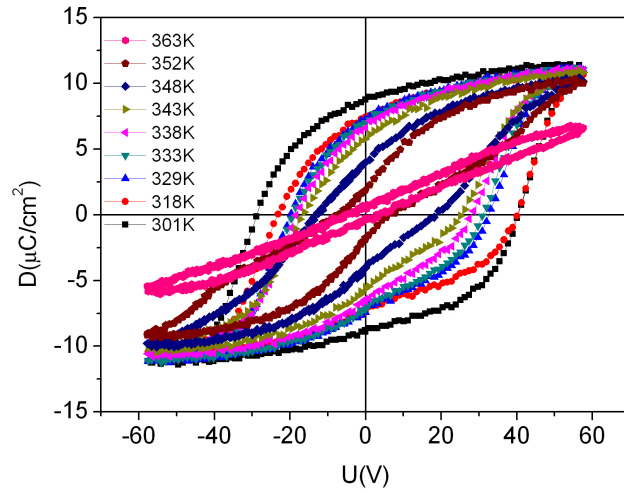


Figure 7.4: The variation of the hysteresis loop during cooling for a 600nm thick sample at 500 Hz.

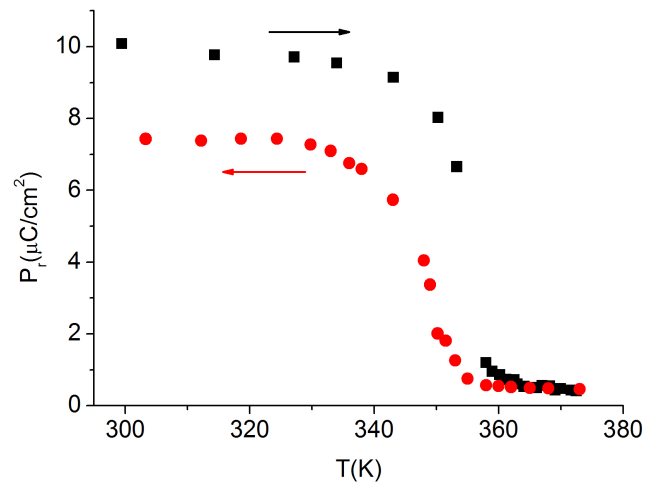


Figure 7.5: The temperature hysteresis of $P_r(T)$ for a 600nm thick sample. The black square denotes the heating process and the red circle denotes the cooling process.

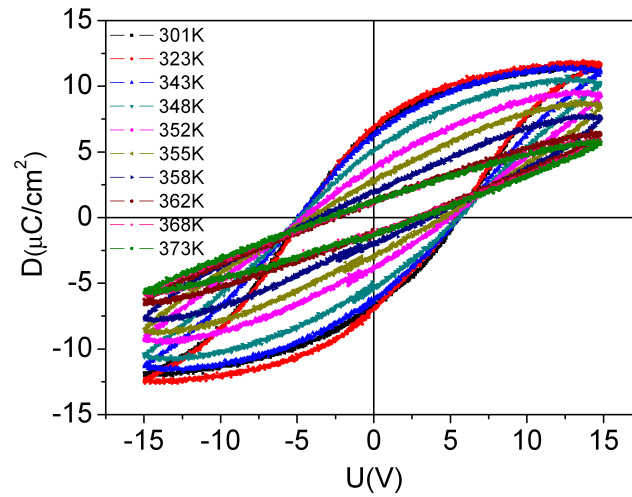


Figure 7.6: The temperature dependence of hysteresis loop during heating for a 90nm thick sample at 10 Hz.

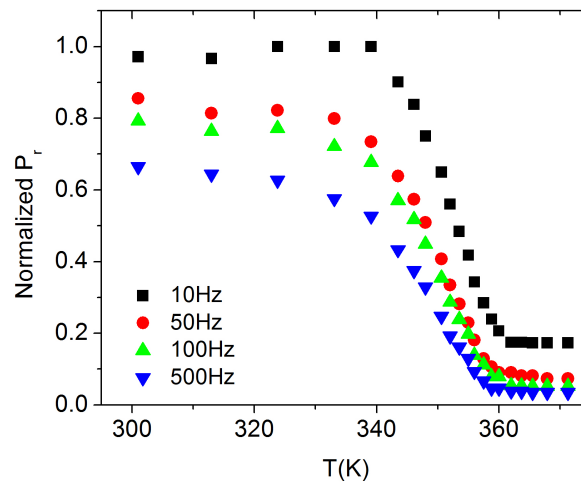


Figure 7.7: The temperature dependence of P_r determined from the hysteresis loops during heating for a 90nm thick sample at different frequencies.

throughout the field cycle. A metastable state persisted in the sample could significantly perturb the double loop. However, in practice, if the measurement frequency is too low the contribution from space charge polarization would become pronounced especially at high temperature, resulting in an elliptical hysteresis. Second, the finite size effects on ferroelectricity near T_c in thin films could play an important role. It has been shown that thin films of ferroelectrics exhibit quite different phase transition characteristics than that of bulk materials [180]. The Tilley-Zeks model can explain two phase transitions in terms of near-surface and interior onsets of ferroelectricity in PVDF copolymer films [20]. An extension by Duiker predicts two ordering temperatures with near-surface ordering lower than the bulk. The presence of a second transition at near-surface is responsible for the experimental broadness in the $P_r(T)$ data though not in $\varepsilon(T)$. Taking into account a dead layer also the Weiss model predicts changes of $P_r(T)$ near the phase transition [192].

7.2 The thickness dependence of the phase transition temperature in PVDF

It was found recently that in the Langmuir-Blodgett ultrathin vinylidene fluoride (PVDF) films there is ferroelectric phase transition of the first order [63]. Earlier in the bulk PVDF this phase transition was not observed because the melting temperature of this ferroelectric polymer ($\sim 170^\circ\text{C}$) is lower than the point of the possible phase transition. Therefore this polymer was treated for a long time as pyroelectric. In the present work the investigation of LB films of PVDF at the nanoscale was performed to obtain the film thickness interval, where ferroelectric phase transition disappears and transition from ferroelectric to pyroelectric state takes place. To get this interval the finite-size theory at the nanoscale using Landau-Ginzburg-Devonshire (LGD) theory [181-183] and by the Weiss mean field model [153,166] are employed.

7.2.1 Thermal hysteresis and butterfly hysteresis

The PVDF films were prepared by Langmuir-Blodgett deposition with transfer number of 10, 20, 30 and 100, yielding sample thicknesses from 7nm to 69nm. The temperature variation of capacitance measurements were performed with an Agilent 4294A impedance analyzer under a small a.c. signal of 100mV at 1 kHz. The electrical contact was obtained using a set of copper pads evaporated onto the aluminum stripes being directly soldered to the inner conductors of coaxial lines [85]. The samples were

heated up to 438K with a heating rate of 1K/min and then cooled down to room temperature to obtain the thermal hysteresis. During these measurements no d.c. bias voltage was applied to the samples. The capacitance-voltage sweeps ('butterfly' hysteresis) were recorded at a frequency of 1 kHz to characterize the change of polarization in the films.

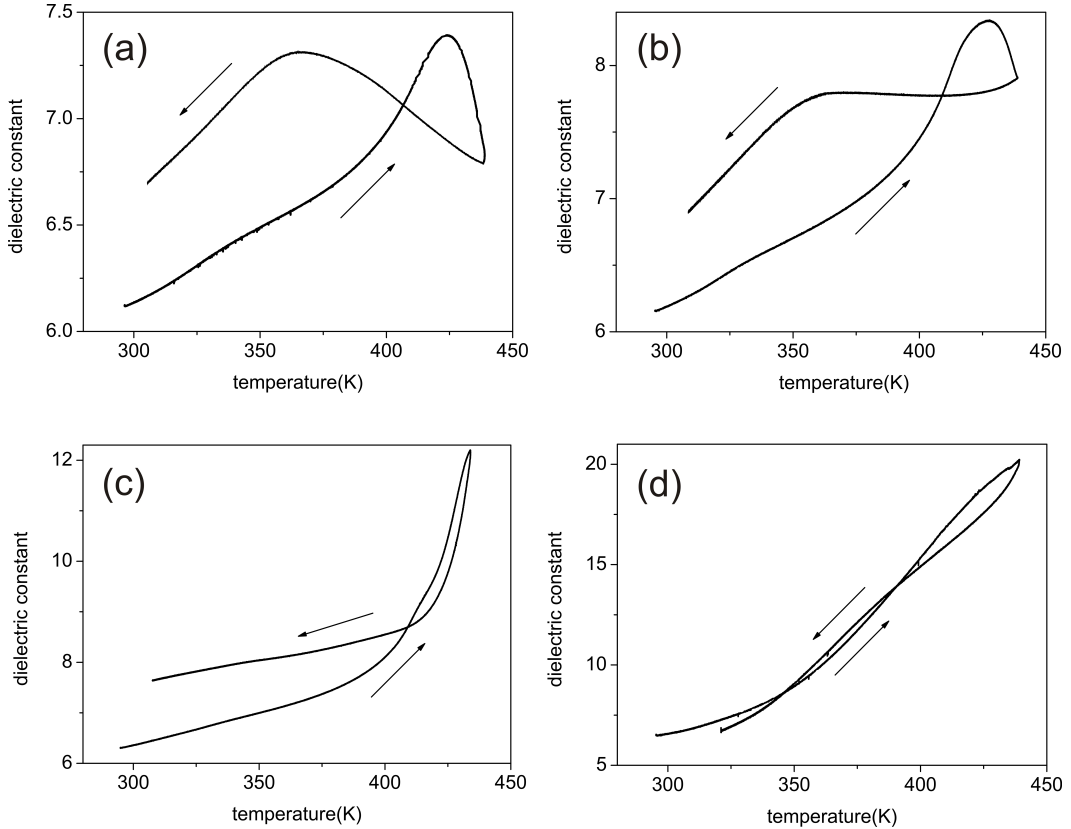


Figure 7.8: Temperature dependence of the dielectric constant for PVDF films with various thicknesses: (a) 10ML with 7nm, (b) 20ML with 13nm, (c) 30ML with 20nm and (d) 100ML with 69nm. Arrows indicate heating and cooling direction.

Fig. 7.8 shows the temperature dependence of the dielectric constant for PVDF films with different thicknesses. The samples with 7nm and 13nm exhibit typical ferroelectric behavior with thermal hysteresis (Fig. 7.8(a) and (b)), which is a manifestation of first order phase transition. During the heating process dielectric constant $\varepsilon(T)$ peaks at $T_{C1} \approx 423K$ and during the cooling process $\varepsilon(T)$ has a maximum at $T_{C2} \approx 374K$ in the 7nm film (Fig. 7.8(a)). The phase transition temperature shifts to $T_{C1} \approx 426K$ during the heating process and to $T_{C2} \approx 371K$ during the cooling process in the 13nm film (Fig. 7.8(b)). Besides, the peaks are broader compared with the sample of 7nm. In contrast,

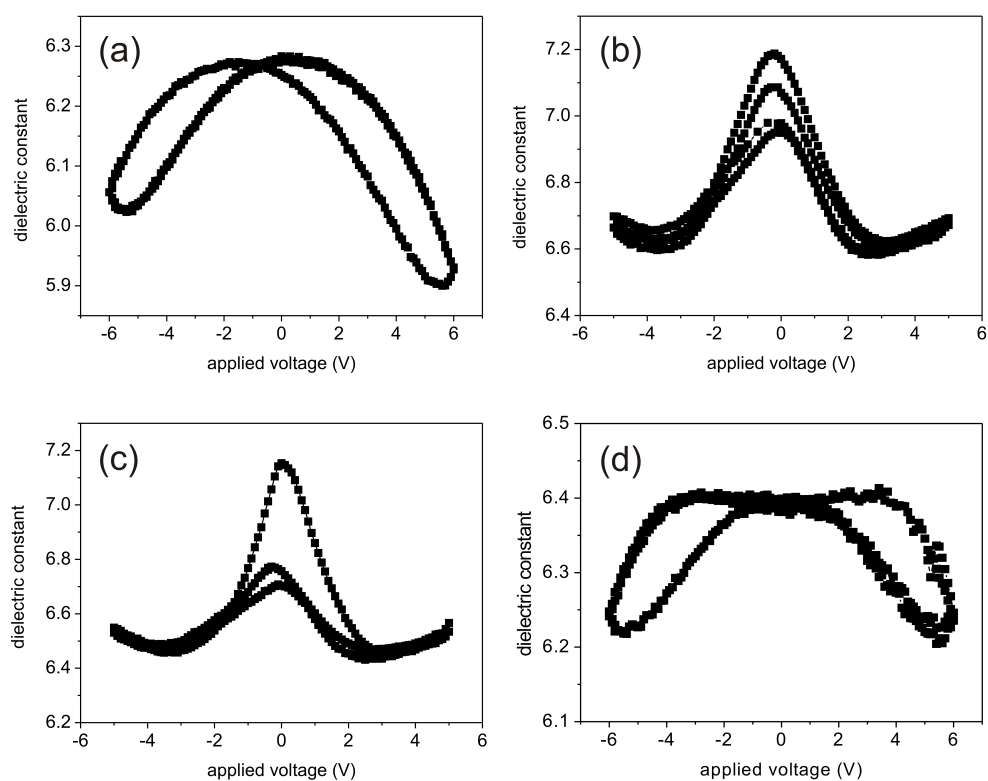


Figure 7.9: The CV characteristic of a 10nm PVDF film at (a) room temperature after anneal, (b) 430K during heating, (c) 420K during cooling, (d) room temperature after cooling down. The ‘butterfly’ shape in (a) and (d) manifests the ferroelectricity in the sample. The disappearance of the ‘butterfly’ shape in (b) and (c) shows a loss of ferroelectricity resulting from phase transition.

there is no phase transition observed in PVDF films of 20nm and 69nm (Fig. 7.8(c) and (d)). The dielectric constant $\varepsilon(T)$ increases monotonically with increasing temperature and then decreases monotonically with decreasing temperature. Comparing with the dielectric constant values we find that there is a smaller change of $\varepsilon(T)$ with variation of the temperature in thinner samples. As film thickness increases, the change of $\varepsilon(T)$ with variation of the temperature becomes larger. The phase transition in PVDF films exhibits a strong size effect at the nanoscale. In the thickness interval of $\Delta l = 13-20nm$ the phase transition in PVDF films disappears.

Fig. 7.9 shows the CV curves of a 10nm PVDF film at different states. At room temperature, the sample exhibits a ‘butterfly’ shape which is a characteristic of ferroelectric behavior (Fig. 7.9(a)). The peaks at voltages of $\sim \pm 1.1V$ correspond to the coercive voltage of the sample. A small shift and asymmetry in the curve is observed which can be caused by the built-in field in the sample. When the sample is heated up to 430K higher than the Curie temperature T_{C1} (423K-426K) the ‘butterfly’ shape in the CV curve disappears (Fig. 7.9(b)), which indicates a paraelectric state here. In the cooling process at 420K before reaching the phase transition temperature T_{C2} (371K-374K) there is also no butterfly hysteresis observed (Fig. 7.9(c)). The butterfly loop appears again when the sample is cooled down to room temperature suggesting a paraelectric to ferroelectric phase transition (Fig. 7.9(d)). The butterfly hysteresis is another strong evidence of the manifestation of a phase transition in thin PVDF films.

7.2.2 Landau-Ginzburg-Devonshire theory

The appearance of the ferroelectric phase transition in PVDF films at the nanoscale could be explained by the finite-size effect and its theory, developed in [182].

There is a polarization distribution in the ferroelectric, as shown in Fig. 7.10. The polarization gradually decreases at the interfaces describing by Landau-Ginzburg-Devonshire theory (Fig. 7.10(a)). In the framework of Weiss model considering a dielectric layer, the polarization has a sharp drop to zero at the dielectric gaps (Fig. 7.10(b)), which will be discussed in the next section. Both theories yield qualitatively the same polarization profile .

The equation of state of Landau-Ginzburg-Devonshire theory (LGD) follows the equation in the Euler-Lagrange form [182]:

$$\alpha P + \beta P^3 - \delta \frac{d^2 P}{dz^2} = E + 4\pi(\bar{P} - P) \quad (7.1)$$

where \bar{P} is the spatial average value of the film polarization P , $\alpha = \alpha_0(T - T_0)$ and β

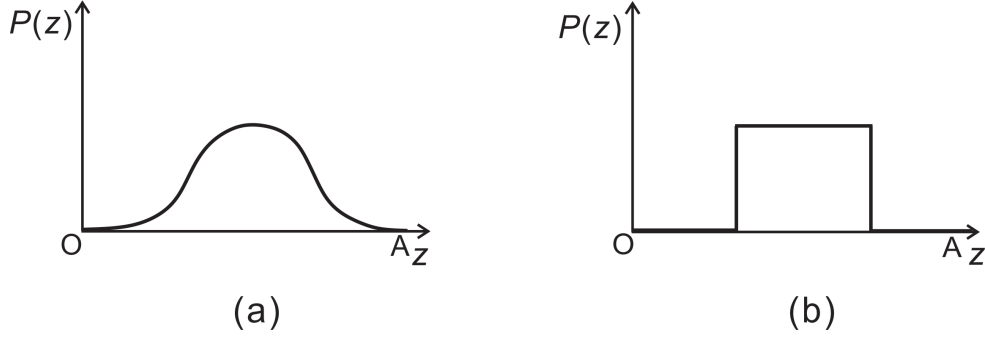


Figure 7.10: The polarization profile in the ferroelectric considered within (a) Landau-Ginzburg-Devonshire theory and (b) the Weiss mean field model. OA is the distance between two metal electrodes.

are Landau-Ginzburg-Devonshire coefficients, $\alpha_0 = C^{-1}$, C is the Curie constant, δ is the gradient energy coefficient and E is the external field, while the interfaces between ferroelectric film and electrodes are characterized by the decay length λ , proposed by Tilley [181]. For simplicity we consider here the second order phase transition and linearized form of equation (7.1). For film thickness l at the nanoscale the mismatch polarization P_m , caused by the film surface must be taken into account [182]. Thus the boundary conditions for the nanoscaled ferroelectric film have a form:

$$\left(P + \lambda \frac{dP}{dz} \right) \Big|_{z=\pm \frac{l}{2}} = -P_m$$

$$P \Big|_{z=0} = P_b \quad (7.2)$$

The importance of the boundary mismatch effect at the nanoscale was first shown in [184], but the boundary conditions in form (7.2) at the nanoscale were first introduced by Glinchuk [182] and later with different interpretation in [185].

The solution of equation (7.1) for the boundary conditions (7.2) was obtained in [182,183]. Equation (7.3) gives scaling $P = P(l)$,

$$P = \frac{E - P_m \Psi(l)/2}{\alpha + \Psi(l)} \quad (7.3)$$

where

$$\Psi(l) = 4\pi \left(\frac{2l_d}{l} \right) \frac{\tanh(l/2l_d)}{1 + (\lambda/l_d) \tanh(l/2l_d)}, l_d = \sqrt{\frac{\delta}{4\pi}} \quad (7.4)$$

Taking into account that $l \gg l_d$, $\lambda \gg l_d$ [181,185-188], $\alpha \ll 4\pi$ [77], we get finally:

$$\Psi(l) \simeq 8\pi \frac{l_d^2}{\lambda l} \quad (7.5)$$

Substituting equation (7.5) in equation (7.3) and using the condition for ferroelectricity in nanoscale $P_m > P_b$ [182,185], we obtain the expression for the dielectric constant:

$$\varepsilon = \frac{dP}{dE} \simeq \frac{1}{\alpha + 2\delta/\lambda l} \quad (7.6)$$

Equation (7.6) gives the dependence of the dielectric constant ε on the film thickness $\varepsilon = \varepsilon(l)$.

Equation (7.6) shows the decrease of phase transition temperature T_0 with the decrease of the thickness l :

$$\Delta T = -2 \frac{\delta C}{\lambda l} \quad (7.7)$$

The decrease ΔT depends on l and grows with decrease of thickness l . Therefore this effect has to be large at the nanoscale.

It should be mentioned that the decrease of phase transition temperature is not found in P(VDF-TrFE) copolymer films [18,85]. The equation (7.6) also shows the smearing of the phase transition at the nanoscale, which has been observed already in [18].

Fig. 7.8 shows that in thickness interval $\Delta l = 13 - 20nm$, the transition from ferroelectric to pyroelectric state takes place. For $l > 13nm$ the phase transition is not observed. Substituting in equation (7.7) the values $C \simeq 1500K$ [77], $\delta \simeq 10^{-18}m^2$ and $l \simeq 10^{-9}m$ [181,185-188] we get for this interval $\delta/\lambda \simeq 10^{-9}m$ which satisfied the literary data. In nanoscaled ferroelectric film with short circuited electrodes there is an internal electric field (see in equation (7.1)). This effect is revealed by the asymmetry of the butterfly curves at the nanoscale (Fig. 7.9). The butterfly curves in the thick pyroelectric films are symmetric.

7.2.3 The Weiss mean field model

Another explanation for the appearance of the phase transition in thin PVDF films can be given by the Weiss model taking into account an interfacial layer [192].

Here, it is assumed that permanent dipoles fluctuate thermally activated over energy barriers in double-well potentials evoking the polarization P and thus a dipolar field.

According to Weiss a local field

$$E_{loc} = E_a + \alpha P \quad (7.8)$$

is introduced. E_a is the applied field. The feedback factor α is a material parameter that describes the strength of the interactions between the dipoles.

The permanent dipoles in the double-wells are assumed again. These dipoles give rise to a polarization

$$P = np \tanh\left(\frac{pE_{loc}}{kT}\right) \quad (7.9)$$

where n is the density of the dipoles, k is the Boltzmann constant, and T is the temperature. The dipole moment p is given by $p = Rq$ with the charge q and with the dipole length R as the distance between the minima in the double-wells.

Now, a dielectric layer with thickness d_{di} and permittivity ε_{di} is introduced in series to the dipole system which is described with the thickness d_{fe} and the permittivity ε_{fe} (Fig. 7.11). This dielectric layer can result from a thin aluminum oxide layer caused by the evaporated aluminum electrodes. The system can be treated in the same way as a stacked capacitor. Thus, the resulting high frequency dielectric permittivity of the system

$$\varepsilon = \frac{(d_{di} + d_{fe})\varepsilon_{di}\varepsilon_{fe}}{\varepsilon_{fe}d_{di} + \varepsilon_{di}d_{fe}} \quad (7.10)$$

is given directly. As found also in experiments the measured dielectric permittivity decreases with decreasing thickness of the ferroelectric in relation to the dielectric layer, especially at the phase transition temperature. For further considerations the equation

$$U = E_{di}d_{di} + E_{fe}d_{fe} \quad (7.11)$$

has to be fulfilled where E_{di} is the mean field in the dielectric layer, E_{fe} the mean field in the ferroelectric, and U is the applied voltage. Additionally, the boundary condition for the dielectric displacement D yields

$$D_{di} = D_{fe} \Rightarrow \varepsilon_{di}\varepsilon_0 E_{di} = \varepsilon_{fe}\varepsilon_0 E_{fe} + P \quad (7.12)$$

where ε_0 is the permittivity of the free space. With equations (7.8)-(7.12) a self consistent equation for the polarization

$$P = np \tanh\left(\frac{p}{kT} \left(\frac{\varepsilon_{di}}{\varepsilon_{fe}d_{di} + \varepsilon_{di}d_{fe}} U + \left[\alpha - \frac{d_{di}}{\varepsilon_0(\varepsilon_{fe}d_{di} + \varepsilon_{di}d_{fe})} \right] P \right)\right) \quad (7.13)$$

is derived. In the present case the Curie temperature, i.e. the temperature where the spontaneous polarization vanishes, is searched for. Therefore, the applied voltage U can be set to zero. Thus, we get

$$P = np \tanh \left(\frac{p\alpha}{kT} \left[1 - \frac{d_{di}}{\alpha \varepsilon_0 (\varepsilon_{fe} d_{di} + \varepsilon_{di} d_{fe})} \right] P \right) \quad (7.14)$$

The polarization is normalized to np :

$$P_n = \frac{P}{np} \quad (7.15)$$

Replacing P in the argument of the tanh-function by P_n yields the Curie temperature of the system for $d_{di} = 0$:

$$T_c = \frac{np^2 \alpha}{k} \quad (7.16)$$

This temperature is shifted to

$$\Theta = T_c \left[1 - \frac{d_{di}}{\alpha \varepsilon_0 (\varepsilon_{fe} d_{di} + \varepsilon_{di} d_{fe})} \right] \quad (7.17)$$

if a dielectric layer of thickness d_{di} is present. The shift of the Curie temperature can be written as

$$\Delta T_c = \Theta - T_c = -\frac{np^2}{k} \frac{d_{di}}{\varepsilon_0 (\varepsilon_{fe} d_{di} + \varepsilon_{di} d_{fe})} \quad (7.18)$$

This shift is the larger the thicker the dielectric layer is. By keeping the thickness of the dielectric layer constant the shift of the Curie temperature increases with decreasing ferroelectric sample thickness as found in the experiments. Thus, the transition from the ferroelectric to the pyroelectric state in the interval from 13nm to 20nm can be explained by the stronger influence of the dielectric layer.

Additionally, the absence of the T_C shift in P(VDF-TrFE) copolymer can be qualitatively explained. In the copolymer, a lower dipole moment p and a lower dipole density n have to be taken into account yielding a smaller shift of the phase transition as revealed by Eq. (7.18).

In the form presented here the Weiss model only yields a phase transition of the second order. A first order phase transition is obtained, if the piezoeffect is taken into account [166] which is omitted here for reasons of simplicity.

The disappearance of the phase transition in PVDF films and their transition to pyroelectric phase in the interval $\Delta l = 13 - 20nm$ can be explained by the finite size effect at the nanoscale using LGD theory and also by the Weiss mean field model.

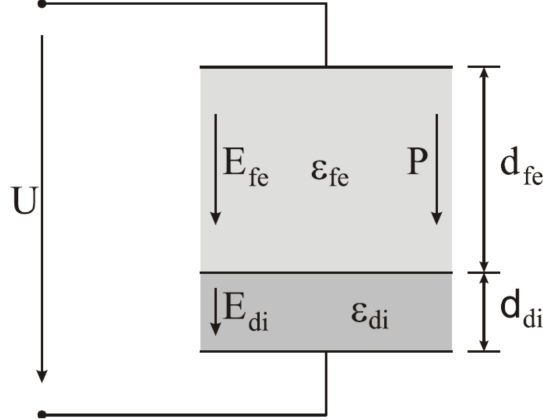


Figure 7.11: Stacked capacitor structure consisting of the ferroelectric layer and the dielectric layer.

Interesting, that this interval coincides roughly with the size of the critical domain nucleus 1-10nm [35,189]. It means, that LGD theory in form (7.1) and (7.2) at $P_m > P_b$ can explain the existence of ferroelectricity and ferroelectric phase transition at the nanoscale, where film thickness is comparable with critical nucleus size.

Actually, the parameters in the Weiss model and the coefficients in the LGD theory are related to each other, which is found in [190]. Both the Weiss model and the LGD phenomenological theory lead to the same ferroelectric behavior.

7.3 Observation of Barkhausen effect

The Barkhausen effect is discovered in 1919 and has been extensively investigated in ferromagnets [195]. Later on, similar phenomena with electrical Barkhausen pulses were observed in barium titanate due to ferroelectric domain switching. When a domain is inverted, the dipole flips induce time-varying charges which cause a current transient, so-called a Barkhausen jump. The Barkhausen jumps in ferroelectrics, associated with nucleation, motion and fusion of domains, are related to the spontaneous polarization change at switching in the external field or at the transition from ferro to paraphase [36].

Polarization reversal jumps during a temperature change within the phase transition range without an external electric field is called thermal Barkhausen effect by Rudyak et al [196], which have been observed in several ferroelectric crystals such as $BaTiO_3$, $SbSI$, TGS , KH_2PO_4 and seignette salt. This effect has high sensitivity to trace the

domain structure transformation in ferroelectric, and therefore can be a direct way to investigate the domain structure dynamics.

Here, thermal Barkhausen effect in ferroelectric copolymer of P(VDF-TrFE) is observed for the first time. The shape of the Barkhausen pulse is analyzed. The Barkhausen pulse is a microscopic phenomenon and can be a direct way to prove the existence of domain. We suggest that the Barkhausen effect can be a new tool to distinguish different switching mechanisms in ferroelectric materials in the future.

7.3.1 Barkhausen pulses of P(VDF-TrFE) on polyimide substrate

The P(VDF-TrFE) copolymer films were prepared by spin coating onto a polyimide substrate carrying evaporated aluminum stripes. The sample was heated up to 393K with a heating rate of 0.5 K/min and then cooled down to room temperature with the same rate. The slow heating and cooling rate can reduce the temperature gradient within the sample caused by the inhomogeneous heat transfer. The current during the temperature change was measured with a Keithley 6514 electrometer under short-circuiting. The top electrode of the sample was connected to the electrometer while the bottom electrode was grounded. The readings from the electrometer were recorded using a computer data acquisition system with a sampling rate of 13 Sa/s. To avoid the contribution of pyroelectric current, preliminary nonpolarized samples were investigated.

Fig. 7.12 shows the current density at heating and cooling for a 500nm film. The heating and cooling are accompanied by background currents in negative direction, which are caused by the charging and discharging effect in polyimide substrate. Similar currents are also present using glass substrates. Before the heating/cooling cycle was started the sample was not polarized by external field. Barkhausen current jumps arise in the temperature range of 378-388K during heating and in the range of 363-337K during cooling. The appearance of Barkhausen jumps is independent of substrate materials as we have also used glass substrates. The Curie point of the sample is determined by the temperature dependence of the dielectric constant $\varepsilon(T)$ with $T_{c1} = 377K$ during heating and $T_{c2} = 347K$ during cooling. Barkhausen jumps occur close to the Curie temperature, which is related to the domain reconstruction or fusion at the phase transition. The temperature range for the Barkhausen jumps is slightly wider at cooling than that at heating process. Barkhausen jumps reveal a local switching of dipoles microscopically while hysteresis loop represents a global switching macroscopically. To develop a physical model to relate Barkhausen jumps with hysteresis loop is a coming

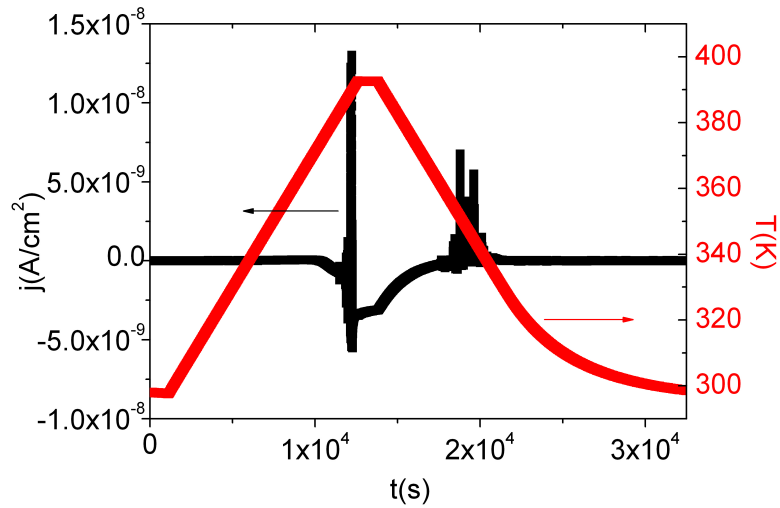
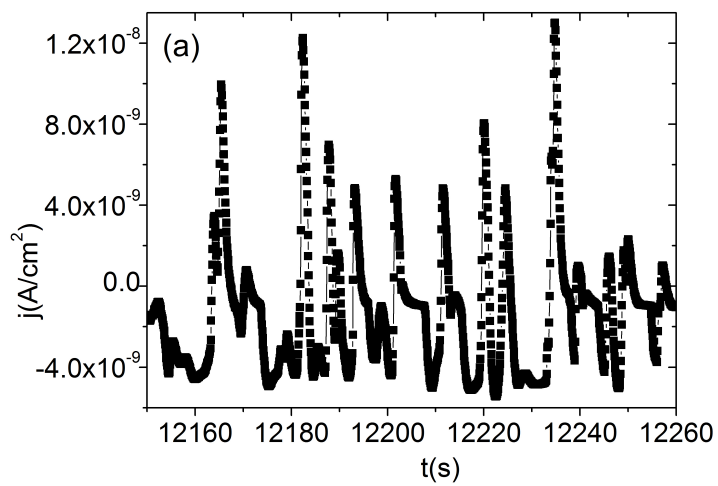


Figure 7.12: The evolution of current density under short circuit as a change of temperature during heating and cooling for a 500nm thick P(VDF-TrFE) film on polyimide. Barkhausen jumps arise in the temperature range close to the Curie point.



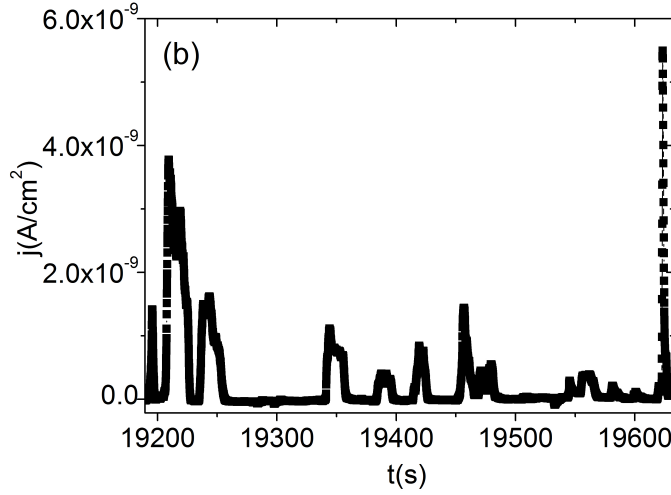


Figure 7.13: The Barkhausen jumps (a) in the time window from 12150s to 12260s during heating and (b) in the time window from 19180s to 19640s during cooling in Fig. 7.12.

future work.

To analyze the Barkhausen jumps, we choose a sampling time window involving a large number of events during heating and cooling (Fig. 7.13). A consecutive pulse train with similar shape is observed during heating (Fig. 7.13(a)). The Barkhausen jumps at cooling are discrete and have lower amplitude (Fig. 7.13(b)). Most of the jumps are in positive direction. It should be noted that a single jump of the Barkhausen effect is not reproducible. The number, amplitude and duration of the pulses are thermally driven statistical phenomena and they differ from cycle to cycle.

There are three types of Barkhausen current jumps observed in P(VDF-TrFE) films, as shown in Fig. 7.14. The first type of jumps has a smooth rising and falling edge with a time period on the order of a few seconds (Fig. 7.14(a)). The second type of jumps has a spike shape with a very sharp rising edge followed by an exponential falling edge (Fig. 7.14(b)). The falling time of this type is slightly shorter than that of the first type. The third type of jumps is a combination of both the first type and second type, which has a longer time period (Fig. 7.14(c)). Jumps of the first and second type have been classified in the early literature [197]. The shape of the current jumps can reveal the microscopic mechanisms of domain reversal. Jumps of the first type are expected during the relatively slow sideways growth of domains [198]. Jumps of the second type with a sharp leading edge are associated with a fast domain nucleation

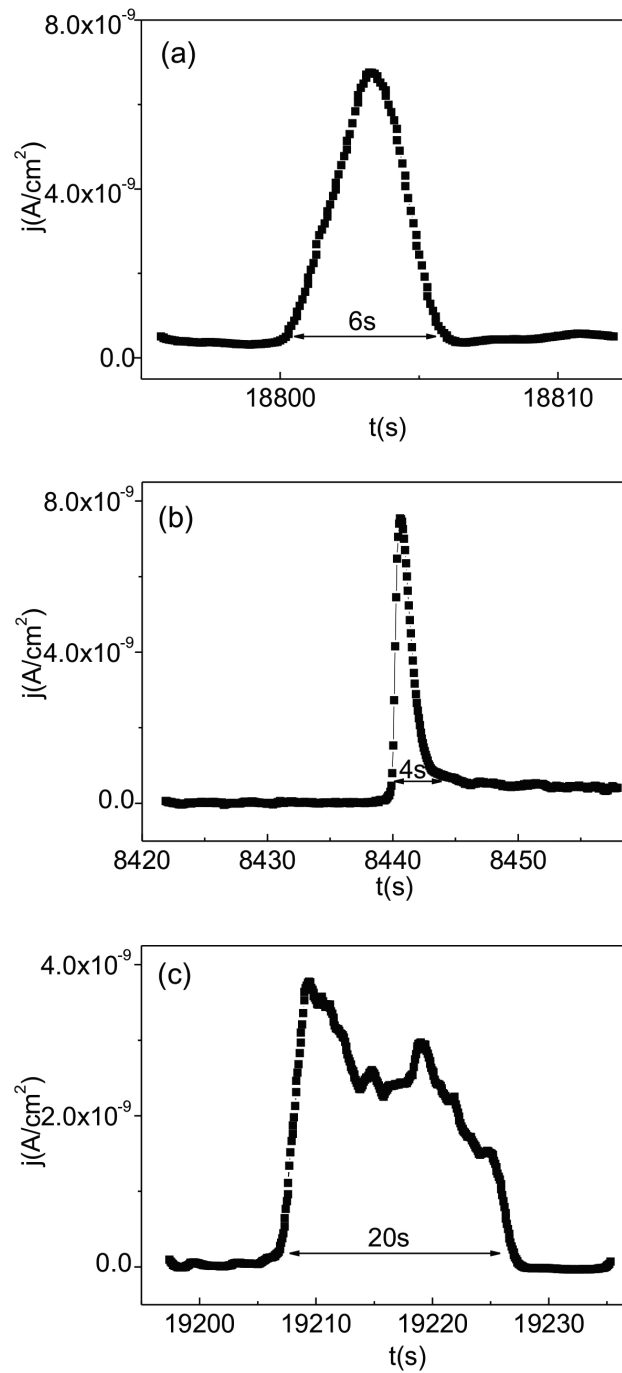


Figure 7.14: Three types of current jumps observed in P(VDF-TrFE) copolymer: (a) first type with a gentle rising and falling edge; (b) second type having a spike shape with a very sharp rising edge followed by an exponential decay; (c) third type being a combination of first type and second type.

and the subsequent exponential decay corresponds to the growth of the domain. The third type of jumps observed here is believed to be multiple domain switching events with nucleation and domain wall motion occurring simultaneously. The Barkhausen jumps can be caused by an elementary switching act or avalanche of many switching acts. The time scale of current pulses in P(VDF-TrFE) films is much longer than that of similar events in barium titanate [197]. We believe that the Barkhausen jumps here correspond to the avalanche of many switching acts.

The dipole number switched within a current spike can be calculated by integrating the total charge under the current spike. The charge density of one current pulse is typical on the order of $10^{-9} - 10^{-8} C/cm^2$, while the saturation polarization is about $10^{-5} C/cm^2$. Thus a fraction of 10^{-4} to 10^{-3} dipoles of the total dipoles in the sample is switched within one pulse. Considering a total dipole density $n = 2 \times 10^{22} cm^{-3}$, a dipole moment of $p = 5 \times 10^{-28} C \cdot cm$, an electrode area of $9 \times 10^{-4} cm^2$ and a sample thickness of 500nm, the absolute number of switched dipoles in one single pulse is $N_{sw} \approx 10^{11} - 10^{12}$. Considering that the copolymer used here has a molecular weight about $10^5 g/mol$, with each pulse a packet of 10^8 to 10^9 chains is rotating.

7.3.2 Barkhausen pulses of P(VDF-TrFE) on glass substrate

The Barkhausen pulses in P(VDF-TrFE) using glass substrate is also checked. Fig. 7.15 shows the current density under a thermal cycle for a 580nm-thick sample previously polarized at positive direction. Similar to the samples on polyimide, the heating and cooling are accompanied by significant background currents in the negative direction which are caused by the ions released in the glass substrate. There are four regions close to the Curie point where Barkhausen jumps are observed during the thermal cycle. Fig. 7.16 shows the enlargement of the Barkhausen jumps corresponding to the four regions in Fig. 7.15. Initially the Barkhausen jumps have a negative direction due to the decrease of polarization (Fig. 7.16(a)). The duration of the jump is about 1-30s with pulse shape mostly of second type (Fig. 7.14(b)). Reversing the previous polarized direction or electrical connection, the jumps change to the other direction which confirms the jumps are connected to the polarization in the sample. At the phase transition, the Barkhausen jumps appear attributed from domain reconstruction and self-polarization, mostly in positive direction (Fig. 7.16(b)-(d)). The charge Q_p integrated in one Barkhausen pulse is similar to that of the samples on polyimide substrates.

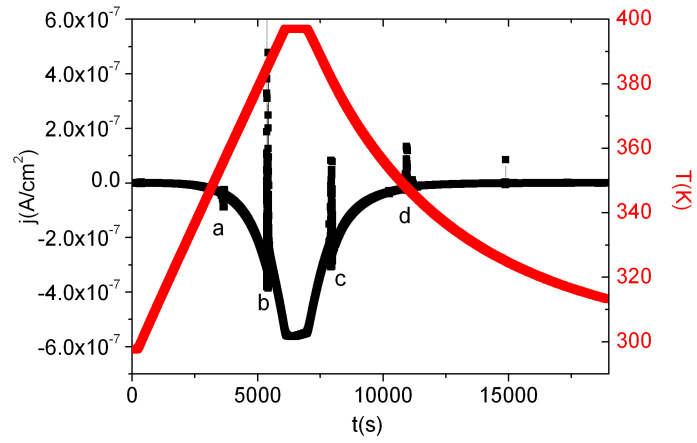


Figure 7.15: The current density upon heating and cooling for a 580nm-thick sample on glass.

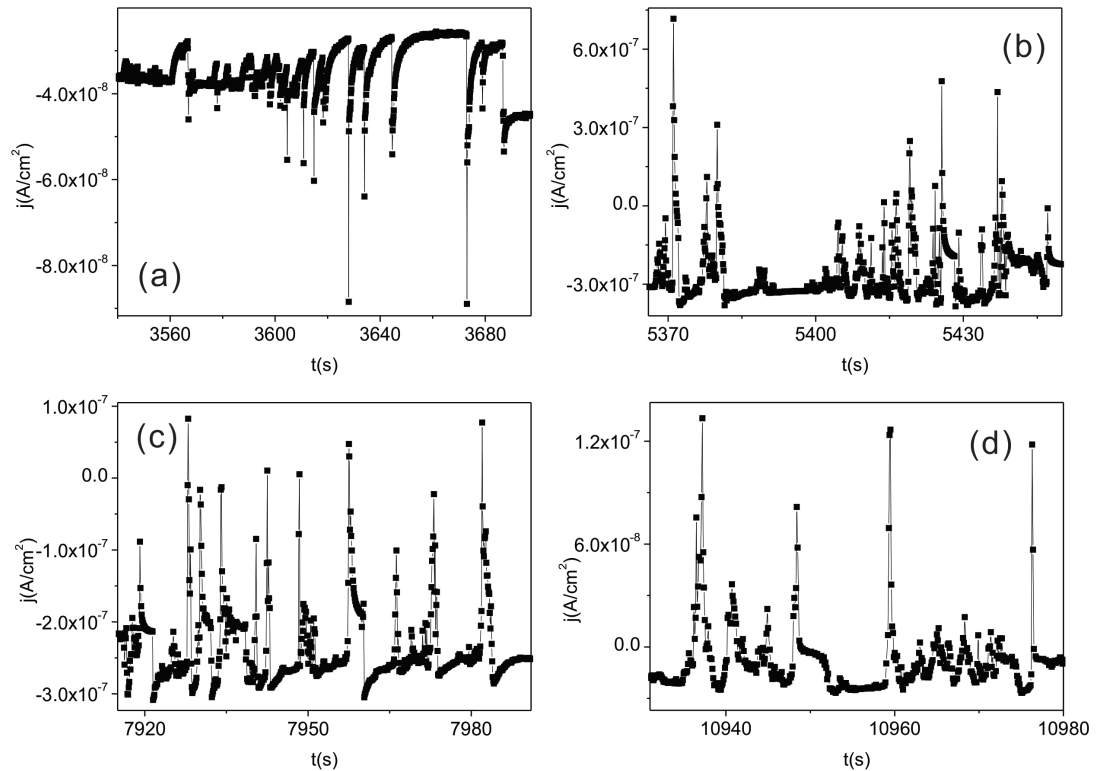


Figure 7.16: The Barkhausen jumps at (a) 355K upon heating, (b) 383K upon heating, (c) 379K upon cooling and (d) 348K upon cooling corresponding to Fig. 7.15.

7.4 Conclusions

We have studied the phase transition behavior in PVDF and P(VDF-TrFE) copolymer films. For P(VDF-TrFE) copolymer films as thick as 600nm a double hysteresis loop is observed close to the Curie point and a sharp jump of the remanent polarization is obtained indicating a first order phase transition. Nevertheless, the double hysteresis loop of the polarization is absent and the change of remanent polarization on temperature is smoother in samples as thin as 90nm which could be due to the finite size effects or that the dynamic hysteresis does not represent the trace of a proper sequence of equilibrium states.

The PVDF LB films are investigated at the nanoscale and the film thickness interval of $\Delta l = 13 - 20nm$, where ferroelectric phase transition disappears and transition from ferroelectric to pyroelectric state takes place, is obtained. This phenomenon is explained by the finite-size effect at the nanoscale using Landau-Ginzburg-Devonshire (LGD) theory and by the Weiss mean field model.

Thermal Barkhausen effect is observed in P(VDF-TrFE) copolymer films for the first time, which is connected to the change of polarization and occurs mostly at the phase transition temperature. Three types of current jumps are observed, which correspond to nucleation and domain wall motion. As a direct way to prove the existence of domain, Barkhausen effect is expected to be able to distinguish different switching mechanisms (intrinsic or extrinsic) in thick and thin films in the future.

Chapter 8

Summary and Outlook

This thesis focuses on the polarization switching in ferroelectric P(VDF-TrFE) films, and seeks to exploit their properties for nonvolatile random access memory applications.

A comprehensive study of ferroelectric properties for LB films and spun films shows both types of films exhibit similar switching behavior. With reducing thickness, the hysteresis loops tend to slant and the switching transients become broader. The thickness dependence of the coercive field follows a power law, whereas the remanent polarization is nearly constant. The switching time decreases with increasing field and it is almost independent of thickness down to 69nm in LB films and 71nm in spun films. Slower switching is observed for a thickness below 60nm in both LB films and spun films. This is due to the depolarization field induced by the surface oxidation layers of Al electrodes which becomes the more pronounced the thinner the sample is. Furthermore, both kinds of films show similar polarization decay tendency of retention and fatigue. Retention behavior is temperature dependent. The thicker films exhibit better retention performance due to the lower depolarization field. The fatigue tests by continued switching show that the thinner films have improved polarization fatigue endurance under the same electric field due to faster heat diffusion out of the sample. The fatigue endurance can be influenced by the waiting time between each switching pulse which induces a change of the local temperature. The above results suggest that thin films in the range of 60-100nm are promising candidates for memory applications with achievable low voltage operation and a relatively fast switching speed.

The electrode and dielectric layer effects are evaluated. Faster polarization switching is observed in metal electrodes with higher work function. Coercive field is lower and switching time is shorter using Cu and Pt electrode. This can be explained by that the higher the work function of the metal is, the thinner the oxide layer becomes. Therefore

the depolarization field is smaller and a faster switching is obtained. CV and PE curves are symmetric with electrodes of same work function and asymmetric with electrodes of different work functions causing a built-in field. The Al_2O_3 dielectric layer can cause a shift and slanted hysteresis loop due to the inducing depolarization field and built-in field. With increasing dielectric layer thickness, the remanent polarization decreases and both coercive field and switching time increase.

Coercive field is a function of both frequency and amplitude of the input signal. For complete switching, the coercive field increases with increasing frequency, which follows a power law. Meanwhile, for a constant frequency the coercive field increases as the maximum electric field increases. These experiments can be described in the framework of Weiss mean field model.

The polarization relaxation effect characterized by a continued increase of polarization build up in the switching transients corresponds to a $t^{-\alpha}$ law of the current density in the long time range, showing a pronounced Kohlrausch behavior. This effect is thickness independent as expected for a relaxational volume polarization. A pronounced saturation effect is observed in both isochronal polarization currents and depolarization currents at high fields. A physical model based on an asymmetric double well potential with dipoles fluctuating between the wells is proposed to explain this behavior. The model assumes a distribution of barrier heights yielding the distribution of transition probabilities which causes the power law current $j \sim t^{-\alpha}$. An asymmetry V causes the nonlinearity in $j(E)|_{t=const.}$. Charge injection sets in at higher temperature during charging. The charging currents deviate from the $t^{-\alpha}$ behavior and become constant at long times. Two relaxation processes are identified in the depolarization currents: the dipole relaxation process with $t^{-\alpha}$ behavior at short times and the space charge relaxation process with a pronounced minimum in time at long times. The time constant of τ_{sc} at which the space charge relaxation process sets in considerably depends on temperature as well as the charging field and it is thermally activated. The mechanism responsible for this behavior appears to be due to injection of charges and their subsequent trappings and retrappings.

The important characteristics of switching process in P(VDF-TrFE) thin films with different thicknesses are studied. The profiles of the current transients show a strong size effect: above the coercive field a maximum in the switching current is observed for samples as thick as 600nm; for samples as thin as 320nm a maximum appears only at fields more than twice of the sample's coercive field, while a monotonic decrease in the switching current without maximum is observed for samples thinner than 300nm. The temperature dependence of switching process in thick films is thermally activated

over the entire temperature range. The current maximum disappears above the Curie temperature due to the loss of ferroelectricity. Switching in thinner films is also thermally activated below the Curie point. The reduction of saturated polarization at low temperature is caused by domain pinning effect and the increase of coercive field at low temperature. The temperature dependence of coercive field exhibits an almost linear increase of coercive field with decreasing temperature. The switching transients under a constant normalized field to the coercive field at different temperatures have a smaller variation of switching time and saturated polarization.

The phase transition behavior in PVDF and P(VDF-TrFE) copolymer films is investigated. For P(VDF-TrFE) copolymer films as thick as 600nm a double hysteresis loop is observed close to the Curie point and a sharp jump of the remanent polarization is obtained indicating a first order phase transition. Nevertheless, the double hysteresis loop of the polarization is absent and the change of remanent polarization on temperature is smoother in samples as thin as 90nm. The PVDF LB films are investigated at the nanoscale and the film thickness interval of $\Delta l = 13 - 20nm$, where ferroelectric phase transition disappears and transition from ferroelectric to pyroelectric state takes place, is obtained. This phenomenon is explained by the finite size effect at the nanoscale using Landau-Ginzburg-Devonshire (LGD) theory and by the Weiss mean field model.

Thermal Barkhausen effect is observed in P(VDF-TrFE) copolymer films for the first time, which is connected to the change of polarization and occurs mostly at the phase transition temperature. Three types of current jumps are observed, which correspond to nucleation and domain wall motion. As a direct way to prove the existence of domain, Barkhausen effect is expected to be able to distinguish different switching mechanisms (intrinsic or extrinsic) in thick and thin films in the future.

There are still some open questions in this work. We suggest the following work for further studies. In chapter 4, we have studied the electrode effects on the ferroelectric response. In the future, electrode effects on the long term properties, i.e. retention and fatigue should be checked. In chapter 5, the proposed physical model for the Kohlrausch relaxations is based on non dipole-dipole interaction, which can qualitatively describe the experiments. However, the field reversal measurements suggest that the Kohlrausch dipole system has interactions. A quantitative model considering the interaction of dipoles should be developed in the future. Furthermore, the pronounced minimum in time in the depolarization current at high temperature should be considered to be simulated quantitatively using the three dimensional hopping model with space charge injection. The polarization current generally has contributions from the

dielectric system, the ferroelectric system as well as the back-switching current if there is a pulse sequence applied before. A method to separate these contributions from different systems should be considered. In chapter 6, we have observed an interesting thickness dependence of switching current profile. A theoretical model to describe this behavior quantitatively is still absent. Meanwhile, the switching current maximum in thick films also disappears at low temperature under a constant applied field. The critical field for the appearance of current maximum is expected to be higher since the coercive field increases with decreasing temperature, which needs to be proved in the future experiments. Barkhausen effect at the nanoscale should be investigated later, which permits to distinguish the different switching mechanisms between the thin and thick films. Also, a physical model should be developed to correlate the microscopic behavior of Barkhausen jumps with the macroscopic behavior of hysteresis loops. Finally, the investigation of local switching behavior, probably by PFM, is also encouraged.

Bibliography

- [1] S. Setter, D. Damjanovic, L. Eng, G. Fox, S. Gevorgian, S. Hong, A. Kingon, H. Kohlstedt, N. Y. Park, G. B. Stephenson, I. Stolitchnov, A. K. Taganstev, D. V. Taylor, T. Yamada and S. Streiffer, *Ferroelectric thin films: Review of materials, properties, and applications*, J. Appl. Phys., vol. 100, p. 051606 (2006).
- [2] C. P. de Araujo, J. F. Scott and G. W. Taylor, *Ferroelectric Thin Films: Synthesis and Basic Properties*, Gordon and Breach Publisher (1996).
- [3] S. Ducharme, T. J. Reece, C. M. Othon and R. K. Rannow, *Ferroelectric polymer Langmuir-Blodgett films for nonvolatile memory applications*, IEEE T. Device Mat. Re., vol. 5, no. 4, p. 720 (2005).
- [4] T. Furukawa, Y. Takahashi and T. Nakajima, *Recent advances in ferroelectric polymer thin films for memory applications*, Curr. Appl. Phys., vol. 10, no. 1, pp. e62-e67 (2010).
- [5] R. C. G. Naber, K. Asadi, P. W. M. Blom, D. M. de Leeuw and B. de Boer, *Organic nonvolatile memory devices based on ferroelectricity*, Adv. mater., vol. 22, no. 9, pp. 933-45 (2010).
- [6] T. Furukawa, *Ferroelectric properties of vinylidene fluoride copolymers*, Phase transit., vol. 18, p. 143 (1989).
- [7] M. Poulsen and S. Ducharme, *Why ferroelectric polyvinylidene fluoride is special*, IEEE T. Dielectr. Electr. Insul., vol. 17, no. 4, pp. 1028-1035 (2010).
- [8] T. J. Reece, S. Ducharme, A. V. Sorokin and M. Poulsen, *Non-volatile memory element based on a ferroelectric polymer Langmuir-Blodgett film*, Appl. Phys. Lett., vol. 82, no. 1, p. 142 (2003).

-
- [9] S. H. Lim, A. C. Rastogi and S. B. Desu, *Electrical properties of metal-ferroelectric-insulator-semiconductor structures based on ferroelectric polyvinylidene fluoride copolymer film gate for nonvolatile random access memory application*, J. Appl. Phys., vol. 96, no. 10, p. 5673 (2004).
- [10] A. Gerber, H. Kohlstedt, M. Fitsilis, R. Waser, T. J. Reece, S. Ducharme and E. Rije, *Low-voltage operation of metal-ferroelectric-insulator-semiconductor diodes incorporating a ferroelectric polyvinylidene fluoride copolymer Langmuir-Blodgett film*, J. Appl. Phys., vol. 100, no. 2, p. 024110 (2006).
- [11] S. Fujisaki, H. Ishiwara and Y. Fujisaki, *Low-voltage operation of ferroelectric poly(vinylidene fluoride-trifluoroethylene) copolymer capacitors and metal-ferroelectric-insulator-semiconductor diodes*, Appl. Phys. Lett., vol. 90, no. 16, p. 162902 (2007).
- [12] Y. J. Park, S. J. Kang, Y. Shin, R. H. Kim, I. Bae and C. Park, *Non-volatile memory characteristics of epitaxially grown PVDF-TrFE thin films and their printed micropattern application*, Curr. Appl. Phys., vol. 11, no. 2, pp. e30-e34 (2011).
- [13] R. Schroeder, L. A. Majewski and M. Grell, *All-organic permanent memory transistor using an amorphous spin-cast ferroelectric-like gate insulator*, Adv. Mater., vol. 16, no. 7, p. 633 (2004).
- [14] R. C. G. Naber, C. Tanase, P. W. M. Blom, G. H. Gelinck, A. W. Marsman, F. J. Touwslager, S. Setayesh and D. M. de Leeuw, *High-performance solution-processed polymer ferroelectric field-effect transistors*, Nat. Mater., vol. 4, no. 3, p. 243 (2005).
- [15] K. N. N. Unni, S. Dabos-Seignon and J. M. Nunzi, *Improved performance of pentacene field-effect transistors using a polyimide gate dielectric layer*, J. Phys. D: Appl. Phys., vol. 38, no. 8, p. 1148 (2005).
- [16] A. Gerber, M. Fitsilis, R. Waser, T. J. Reece, E. Rije, S. Ducharme and H. Kohlstedt, *Ferroelectric field effect transistors using very thin ferroelectric polyvinylidene fluoride copolymer films as gate dielectrics*, J. Appl. Phys., vol. 107, no. 12, p. 124119 (2010).

-
- [17] S. Palto, L. Blinov, a. Bune, E. Dubovik, V. Fridkin, N. Petukhova, K. Verkhovskaya and S. Yudin., *Ferroelectric Langmuir-Blodgett films*, *Ferroelectr. Lett. Sect.*, vol. 19, no. 3-4, pp. 65-68 (1995).
- [18] A. V. Bune, V. M. Fridkin, S. Ducharme, L. M. Blinov, S. P. Palto, A. V. Sorokin, S. G. Yudin and A. Zlatkin, *Two-dimensional ferroelectric films*, *Nature*, vol. 391, pp. 874-877 (1998).
- [19] S. Ducharme, V. Fridkin, A. Bune, S. Palto, L. Blinov, N. Petukhova and S. Yudin, *Intrinsic ferroelectric coercive field*, *Phys. Rev. Lett.*, vol. 84, no. 1, pp. 175-8 (2000).
- [20] J. F. Scott, *Ferroelectrics Domain Wall Kinetics: Nano-Domain Nucleation in Lead Germanate and Tilley-Zeks Theory for PVDF*, *Ferroelectrics*, vol. 291, no. 1, p. 205 (2003).
- [21] H. Kliem and R. Tadros-Morgane, *Extrinsic versus intrinsic ferroelectric switching: experimental investigations using ultra-thin PVDF Langmuir-Blodgett films*, *J. Phys. D: Appl. Phys.*, vol. 38, no. 12, pp. 1860-1868 (2005).
- [22] A. Bratkovsky and A. Levanyuk, *Comment on: Intrinsic Ferroelectric Coercive Field*, *Phys. Rev. Lett.*, vol. 87, no. 1, p. 019701 (2001).
- [23] R. Moreira, *Comment on Intrinsic Ferroelectric Coercive Field*, *Phys. Rev. Lett.*, vol. 88, no. 17, p. 179701 (2002).
- [24] J. F. Scott, M. Dawber, A. Q. Jiang and F. D. Morrison, *New Developments in Ferroelectric Thin Films*, *Ferroelectrics*, vol. 286, p. 223 (2003).
- [25] R. C. G. Naber, P. W. M. Blom and D. M. D. Leeuw, *Comment on 'Extrinsic versus intrinsic ferroelectric switching: experimental investigations using ultra-thin PVDF Langmuir-Blodgett films'*, *J. Phys. D: Appl. Phys.*, vol. 39, no. 9, pp. 1984-1986 (2006).
- [26] R. V. Gaynutdinov, S. Mitko, S. G. Yudin, V. M. Fridkin and S. Ducharme, *Polarization switching at the nanoscale in ferroelectric copolymer thin films*, *Appl. Phys. Lett.*, vol. 99, no. 14, p. 142904 (2011).

-
- [27] R. Gaynutdinov, S. Yudin, S. Ducharme and V. Fridkin, *Homogeneous switching in ultrathin ferroelectric films*, J. phys.: Condens. matt., vol. 24, no. 1, p. 015902 (2012).
- [28] S. Ducharme, V. Fridkin, R. Gaynutdinov, M. Minnekaev, A. Tolstikhina and A. Zenkevich, *Homogeneous switching in ultrathin ferroelectric BaTiO₃ films*, arXiv: 1204.4792 (2012).
- [29] H. Ishiwara, M. Okuyama and Y. Arimoto Ed., *Ferroelectric Random Access Memories: Fundamentals and Applications*, Berlin: Springer (2004).
- [30] J. Van Randerat and R. E. Settingington, *Piezoelectric Ceramics*, London: Mullard Limited Pub. Co. (1974).
- [31] J. Valasek, *Piezoelectric and allied phenomena in Rochelle salt*, Phys. Rev., vol. 15, no. 537 (1920).
- [32] L. E. Cross, *Ferroelectric Ceramics*, Basel, Switzerland: Birkhauser (1993).
- [33] K. C. Kao, *Dielectric Phenomena in Solids*, California: Elsevier Academic Press (2004).
- [34] O. Lohse, D. Bolten, M. Grossman, R. Waser, W. Hartner and G. S. Schindler, *Relaxation mechanisms in ferroelectric thin film capacitors for FeRAM application*, Ferroelectric Thin Films VI Symp. Mater. Res. Soc., vol. 267 (1998).
- [35] A. K. Tagantsev, L. E. Cross and J. Fousek, *Domains in Ferroic Crystals and Thin Films*, New York: Springer (2010).
- [36] M. E. Lines and A. M. Glass, *Principles and Applications of Ferroelectrics and Related Materials*, New York: Oxford University Press (1977).
- [37] E. I. Bondarenko, V. Y. Topolov and A. V. Turik, *The role of 90 degrees domain wall displacements in forming physical properties of perovskite ferroelectric ceramics*, Ferro. Lett. Sect., vol. 13, no. 13 (1991).
- [38] K. Franke, J. Besold, W. Haessler and C. Seegebarth, *Modification and detection of domains on ferroelectric PZT films by scanning force microscopy*, Surf. Sci., vol. 302, p. L283 (1994).

-
- [39] K. S. Lee, J. H. Choi, J. Y. Lee and S. Baik, *Domain formation in epitaxial Pb(Zr,Ti)O₃ thin films*, J. Appl. Phys., vol. 90, p. 4095 (2001).
- [40] H. Odagawa and Y. Cho, *Simultaneous observation of nanometer size ferroelectric domains and surface morphology using scanning nonlinear dielectric microscopy*, Ferroelectrics, vol. 251, p. 29 (2001).
- [41] W. J. Merz, *Domain formation and domain wall motions in ferroelectric BaTiO₃ single crystals*, Phys. Rev., vol. 95, no. 3, p. 690 (1954).
- [42] E. A. Little, *Dynamic behavior of domain walls in barium titanate*, Phys. Rev., vol. 98, no. 4, p. 978 (1955).
- [43] R. C. Miller, *Some experiments on the motion of 180° domain walls in BaTiO₃*, Phys. Rev., vol. 111, no. 3, p. 736 (1958).
- [44] R. C. Miller and G. Weinreich, *Mechanism for the sideways motion of 180° domain walls in barium titanate*, Phys. Rev., vol. 117, no. 6, p. 1460 (1960).
- [45] E. Fatuzzo, *Theoretical considerations on the switching transient in ferroelectrics*, Phys. Rev., vol. 127, no. 6, p. 1999 (1962).
- [46] A. N. Kolmogorov, *A statistical theory for the recrystallization of metals*, Izv. Acad. Nauk USSR, Ser. Math., vol. 3, p. 355 (1937).
- [47] M. Avrami, *Kinetics of phase change. I: General theory*, J. Chem. Phys., vol. 7, p. 1103 (1939).
- [48] A. K. Tagantsev, I. Stolichnov and N. Setter, *Non-Kolmogorov-Avrami switching kinetics in ferroelectric thin films*, Phys. Rev. B, vol. 66, p. 214109 (2002).
- [49] K. M. Rabe and C. H. Ahn, *Physics of Ferroelectrics: A Modern Perspective*, Berlin: Springer-Verlag (2007).
- [50] L. D. Landau, *Theory of phase transformations. I*, Phys. Z. Sowjun, vol. 11, p. 26 (1937).
- [51] L. D. Landau, *Theory of phase transformations. II*, Zh. Eksp. Teor. Fiz., vol. 7, p. 627 (1937).

-
- [52] A. F. Devonshire, *Theory of barium titanate*, Philos. Mag., vol. 40, p. 1040 (1949).
- [53] A. F. Devonshire, *Theory of ferroelectrics*, Adv. Phys., vol. 3, p. 85 (1954).
- [54] E. Fatuzzo and W. J. Merz, *Ferroelectricity*, Amsterdam: North-Holland (1967).
- [55] C. L. Wang, *Theories and methods of first order ferroelectric phase transition*, in Ferroelectrics, I. Coondoo, Ed. Rijeka: InTech (2010).
- [56] E. Riande and R. D. Calleja, *Electrical properties of polymers*, New York: Marcel Dekker Inc. (2004).
- [57] H. Kawai, *The Piezoelectricity of poly(vinylidene fluoride)*, Jpn. J. Appl. Phys., vol. 8, p. 975 (1969).
- [58] J. G. Bergman, J. H. McFee and G. R. Crane, *Pyroelectricity and Optical Second Harmonic Generation in Polyvinylidene Fluoride Films*, Appl. Phys. Lett., vol. 18, p. 203 (1971).
- [59] R. G. Kepler and R. A. Anderson, *Ferroelectricity in polyvinylidene fluoride*, J. Appl. Phys., vol. 49, p. 1232 (1978).
- [60] T. Furukawa, M. Date and E. Fukada, *Hysteresis phenomena in polyvinylidene fluoride under high electric field*, J. Appl. Phys., vol. 51, no. 2, p. 1135 (1980).
- [61] T. Furukawa, G. E. Johnson and H. E. Bair, *Ferroelectric Phase Transition in a Copolymer of Vinylidene Fluoride and Trifluoroethylene*, Ferroelectrics, vol. 32, p. 61 (1981).
- [62] V. V. Kochervinskii, *Ferroelectricity of polymers based on vinylidene fluoride*, Russian chem. Rev., vol. 68, no. 10, p. 821 (1999).
- [63] A. R. Geivandov, S. G. Yudin, V. M. Fridkin and S. Ducharme, *Manifestation of a Ferroelectric Phase Transition in Ultrathin Films of Polyvinylidene Fluoride*, Magn. Ferroelectr., vol. 47, no. 8, p. 1590 (2005).
- [64] N. Takahashi, *X-ray study of ferroelectric twin in poly(vinylidene fluoride)*, Appl. Phys. Lett, vol. 51, p. 970 (1987).

-
- [65] I. L. Guy and J. Unsworth, *Observation of a change in the form of polarization reversal in a vinylidene fluoride/trifluoroethylene copolymer*, Appl. Phys. Lett., vol. 52, p. 532 (1988).
- [66] W. Melitz, J. Shen, A. C. Kummel and S. Lee, *Kelvin probe force microscopy and its application*, Surf. Sci. Rep., vol. 66, p. 1 (2011).
- [67] M. Date and T. Furukawa, *Computer simulation of switching processes in polyvinylidene fluoride and its copolymers*, Ferroelectrics, vol. 57, p. 37 (1984).
- [68] T. Sato, H. Ishikawa and O. Ikeda, *Multilayered deformable mirror using PVDF film*, Appl. Opt., vol. 21, no. 9, p. 3664 (1982).
- [69] W. P. Robbins, *Ferroelectric-based microactuators*, Integ. Ferro., vol. 11, p. 179 (1995).
- [70] Y. Nemirovsky, A. Nemirovsky, P. Muralt and N. Setter, *Design of a novel thin film piezoelectric accelerometer*, Sens. Actuators A, vol. 56, p. 239 (1996).
- [71] L. Dellmann, G. A. Racine and N. F. de Rooij, *Micromachined piezoelectric Elastic Force Motor (EFM)*, IEEE Proc. Micro Electro Mech. Syst. (MEMS), p. 52 (2000).
- [72] A. Sheikholeslami and G. Gulak, *A Survey of Circuit Innovations in Ferroelectric Random-Access Memories*, Proceedings of the IEEE, vol. 88, no. 5, p. 667 (2000).
- [73] G. W. Burr, B. N. Kurdi, J. C. Scott, C. H. Lam, K. Gopalakrishnan and R. S. Shenoy, *Overview of Candidate Device Technologies for Storage-Class Memory*, IBM J. Res. & Dev., vol. 52, p. 449 (2008).
- [74] M. H. Kryder and C. S. Kim, *After hard drives - What comes next?*, IEEE T. Magn., vol. 45, no. 10, p. 3406 (2009).
- [75] M. Mort, G. Schindler, W. Hartner, I. Kasko, M. J. Kastner, T. Mikolajick, C. Dehm and R. Waser, *Low temperature process and thin SBT films for ferroelectric memory devices*, Integr. Ferroelectr., vol. 30, p. 235 (2000).
- [76] P. Martin and M. Szablewski, *Langmuir-Blodgett Troughs Operating Manual*, Nima Technology Ltd (2002).

-
- [77] S. Ducharme, S. P. Palto and V. M. Fridkin, *Ferroelectric and Dielectric Thin Films*, Academic press (2002).
- [78] L. M. Blinov, V. M. Fridkin, S. P. Palto, A. V. Bune, P. A. Dowben and S. Ducharme, *Two-dimensional ferroelectrics*, *Physics-Uspekhi*, vol. 43, no. 3, pp. 243-257 (2000).
- [79] S. A. Jenekhe, *Effect of solvent mass transfer on flow of polymer solution on a flat rotating disk*, *Ind. Eng. Chem. Fundam.*, vol. 23, p. 425 (1984).
- [80] M. Bai, M. Poulsen and S. Ducharme, *Effects of annealing conditions on ferroelectric nanomesa self-assembly*, *J. Phys.: Condens. Matter*, vol. 18, p. 7383 (2006).
- [81] M. Bai and S. Ducharme, *Ferroelectric nanomesa formation from polymer Langmuir-Blodgett films*, *Appl. Phys. Lett.*, vol. 85, no. 16, p. 3528 (2004).
- [82] C. M. Othon, J. Kim, S. Ducharme and V. M. Fridkin, *Switching kinetics of ferroelectric polymer nanomesas*, *J. Appl. Phys.*, vol. 104, no. 5, p. 054109 (2008).
- [83] H. G. Tompkins and E. A. Irene, Ed., *Handbook of Ellipsimetry*, New York: William Andrew Publishing and Springer (2005).
- [84] B. Martin, M. Mai and H. Kliem, *Broadband dielectric relaxation spectra of PVDF copolymer films*, *J. Phys.: Conf. Ser.* 310, p.012001 (2011).
- [85] B. Martin, M. Mai and H. Kliem, *Broadband dielectric dispersion in ferroelectric P(VDF-TrFE) copolymer films*, *Physica B: Condens. Matter*, vol. 407, no. 21, pp. 4398-4404 (2012).
- [86] C. B. Sawyer and C. H. Tower, *Rochelle salt as a dielectric*, *Phys. Rev.*, vol. 35, p. 269 (1930).
- [87] B. Martin and H. Kliem, *Time Domain Polarisation Measurements with the Sawyer-Tower Method*, *IEEE Int. Conf. Solid Dielectr.*, pp. 729-732 (2007).
- [88] L. Gil, M. A. Ramos, A. Bringer and U. Buchenau, *Low-Temperature Specific Heat and Thermal Conductivity of Glasses*, *Phys. Rev. Lett.*, vol. 70, no. 2, pp. 182-185 (1993).

-
- [89] R. Tadros-Morgane and H. Kliem, *Polarization curves of Langmuir-Blodgett PVDF-copolymer films*, J. Phys. D: Appl. Phys., vol. 39, no. 22, pp. 4872-4877 (2006).
- [90] R. V. Gaynutdinov, O. A. Lysova, A. L. Tolstikhina, S. G. Yudin, V. M. Fridkin, and S. Ducharme, *Polarization switching kinetics at the nanoscale in ferroelectric copolymer Langmuir-Blodgett films*, Appl. Phys. Lett., vol. 92, no. 17, p. 172902 (2008).
- [91] S. Horie, K. Ishida, S. Kuwajima, K. Kobayashi, H. Yamada and K. Matsushige, *Effect of Ferroelectric/Metal interface structure on polarization reversal*, Jpn. J. Appl. Phys., vol. 47, no. 2, pp. 1259-1262 (2008).
- [92] T. Nakajima, Y. Takahashi, S. Okamura and T. Furukawa, *Nanosecond switching characteristics of ferroelectric ultrathin vinylidene fluoride/trifluoroethylene copolymer films under extremely high electric field*, Jpn. J. Appl. Phys., vol. 48, no. 9, p. 09KE04 (2009).
- [93] K. Mueller, D. Mandal, K. Henkel, I. Paloumpa and D. Schmeisser, *Ferroelectric properties of spin-coated ultrathin (down to 10 nm) copolymer films*, Appl. Phys. Lett., vol. 93, no. 11, p. 112901 (2008).
- [94] R. C. G. Naber, P. W. M. Blom, A. W. Marsman and D. M. de Leeuw, *Low voltage switching of a spin cast ferroelectric polymer*, Appl. Phys. Lett., vol. 85, no. 11, p. 2032 (2004).
- [95] U. Robels, J. H. Calderwood and G. Arlt, *Shift and deformation of the hysteresis curve of ferroelectric by defects: An electric model*, J. Appl. Phys., vol. 77, no. 8, p. 4002 (1995).
- [96] P. K. Wu, G. R. Yang, X. F. Ma and T. M. Lu, *Interaction of amorphous fluoropolymer with metal*, Appl. Phys. Lett., vol. 65, no. 4, p. 508 (1994).
- [97] V. Janovec, *On the theory of the coercive field of single-domain crystals of BaTiO₃*, Czech. J. Phys., vol. 8, p. 3 (1958).
- [98] J. C. Burfoot and G. W. Taylor, *Polar Dielectrics and Their Applications*, London: Macmillan (1979).

-
- [99] E. K. H. Salje, B. Wruck and H. Thomas, *Order-parameter saturation and low-temperature extension of Landau theory*, Z. Phys. B: Condens. Matt., vol. 82, no. 3, pp. 399-404 (1991).
- [100] M. Kuehn and H. Kliem, *The method of local fields: A bridge between molecular modelling and dielectric theory*, J. Electrostatics, vol. 67, no. 23, pp. 203-208 (2009).
- [101] E. Fatuzzo and W. J. Merz, *Switching mechanism in triglycine sulfate and other ferroelectrics*, Phys. Rev., vol. 116, no. 1, p. 61 (1959).
- [102] G. D. Zhu, X. Y. Luo, J. H. Zhang, Y. Gu and Y. L. Jiang, *Electrical fatigue in ferroelectric P(VDF-TrFE) copolymer films*, IEEE Trans. Dielectr. Electr. Insul., vol. 17, no. 4, p. 1172 (2010).
- [103] X. Lou, M. Zhang, S. Redfern and J. Scott, *Fatigue as a local phase decomposition: A switching-induced charge-injection model*, Phys. Rev. B, vol. 75, no. 22, p. 224104 (2007).
- [104] Y. Chen, *Ferroelectric/electrode interfaces: Polarization switching and reliability of PZT capacitors in nonvolatile memories*, Stanford University (2008).
- [105] C. Duan, R. F. Sabirianov, W. Mei, S. S. Jaswal and E. Y. Wsymbal *Interface effect on ferroelectricity at the nanoscale*, Nano Lett., vol. 6, no. 3, p.483, (2006).
- [106] F. Xia and Q. M. Zhang, *Schottky emission at the metal polymer interface and its effect on the polarization switching of ferroelectric poly(vinylidene fluoride-trifluoroethylene) copolymer thin films*, Appl. Phys. Lett, vol. 85, p. 1719 (2004).
- [107] J. Choi, P. A. Dowben, S. Pebley, A. V. Bune, S. Ducharme, V. M. Fridkin, S. P. Palto and N. Petukhova, *Changes in metallicity and electronic structure across the surface ferroelectric transition of ultrathin crystalline poly(vinylidene fluoride-trifluoroethylene) copolymers*, Phys. Rev. Lett., vol. 80, p. 1328 (1998).
- [108] F. Xia and Q. M. Zhang, *Influence of metal electrodes on the ferroelectric responses of poly(vinylidene fluoride-trifluoroethylene) copolymer thin films*, Mat. Res. Soc. Symp. Proc, p. B9.20.1 (2003).

-
- [109] B. Xu, C. N. Borca, S. Ducharme, A. V. Sorokin, P. A. Dowben, V. M. Fridkin, S. P. Palto, N. N. Petukhova and S. G. Yudin, *Aluminum doping of poly(vinylidene fluoride-trifluoroethylene) copolymer*, J. Chem. Phys., vol. 114, p. 1866 (2001).
- [110] M. Mai, B. Martin and H. Kliem, *Ferroelectric switching in Langmuir-Blodgett and spin-coated thin films of poly(vinylidene fluoride/trifluoroethylene) copolymers*, J. Appl. Phys., vol. 110, no. 6, p. 064101 (2011).
- [111] G. Vizdrik and E. Rije, *Fast polarization switching and influence of platinum electrodes in ultrathin Langmuir films of poly(vinylidene fluoride-trifluoroethylene)*, Ferroelectrics, vol. 370, p. 74 (2006).
- [112] R. C. G. Naber, B. de Boer, and P. W. M. Blom, *Low-voltage polymer field-effect transistors for nonvolatile memories*, Appl. Phys. Lett., vol. 87, p. 203509 (2005).
- [113] B. Xu, J. Choi, P. A. Dowben, A. V. Sorokin, S. P. Palto, N. N. Petukhova, and S. G. Yudin, *Comparison of aluminum and sodium doped poly(vinylidene fluoride-trifluoroethylene) copolymers by x-ray photoemission spectroscopy*, Appl. Phys. Lett., vol. 78, p. 448 (2001).
- [114] P. Gonnard and R. Briot, *Ferroelectrics modelization of the dielectric and mechanical losses in ferroelectric ceramics*, Ferroelectrics, vol. 93, no. 1, p. 117 (1989).
- [115] E. Fatuzzo and W. Merz, *Ferroelectricity*, Amsterdam: North-Holland (1967).
- [116] V. M. Fridkin and S. Ducharme, *General features of the intrinsic ferroelectric coercive field*, Phys. Solid State, vol. 43, no. 7, pp. 1320-1324 (2001).
- [117] Y. Ishibashi and H. Orihara, *A theory of D-E hysteresis loop*, Integr. Ferroelectr., vol. 9, p. 57 (1995).
- [118] J. F. Scott, F. M. Ross, De Araujo, C. A. Paz, M. C. Scott and M. Huffman, *Structure and device characteristics of SrBi₂Ta₂O₉ based nonvolatile random-access memories*, MRS Bulletin, vol. 21, no. 7, p. 33 (1996).
- [119] D. Kim, J. Jo, Y. Kim, Y. Chang, J. Lee, J. G. Yoon, T. Song and T. Noh, *Polarization relaxation induced by a depolarization field in ultrathin ferroelectric BaTiO₃ capacitors*, Phys. Rev. Lett., vol. 95, no. 23, pp. 1-4 (2005).

-
- [120] Y. W. So, D. J. Kim, T. W. Noh, J. G. Yoon and T. K. Song, *Polarization switching kinetics of epitaxial $Pb(Zr_{0.4}Ti_{0.6})O_3$ thin films*, Appl. Phys. Lett., vol. 86, no. 9, p. 092905 (2005).
- [121] W. Li, Z. Chen and O. Auciello, *Calculation of frequency-dependent coercive field based on the investigation of intrinsic switching kinetics of strained $Pb(Zr_{0.2}Ti_{0.8})O_3$ thin films*, J. Phys. D: Appl. Phys., vol. 44, no. 10, p. 105404 (2011).
- [122] S. L. Miller, R. D. Nasby, J. R. Schwank, M. S. Rodgers and P. V. Dressendorfer, *Device modeling of ferroelectric capacitors*, J. Appl. Phys., vol. 68, no. 12, p. 6463 (1990).
- [123] R. Belouadah, D. Kendil, E. Bousbiat, D. Guyomar and B. Guiffard, *Electrical properties of two-dimensional thin films of the ferroelectric material polyvinylidene fluoride as a function of electric field*, Physica B: Condens. Matt., vol. 404, no. 12-13, pp. 1746-1751 (2009).
- [124] A. K. Jonscher, *Dielectric relaxation in solids*, London: Chelsea dielectric press (1983).
- [125] H. Kliem, *Kohlrausch relaxations: New aspects about the everlasting story*, IEEE T. Dielectr. Electr. Insul., vol. 12, no. 4, pp. 709-718 (2005).
- [126] R. Kohlrausch, *Theorie des elektrischen Rueckstandes in der Leidener Flasche*, Pogg. Ann., vol. 91, pp. 56-82, 179-214 (1854).
- [127] H. Kliem and G. Arlt, *On the Curie-von Schweidler law in aluminum oxide*, IEEE CEIDP, pp. 495-503 (1984).
- [128] A. de Polignac and M. Jourdain, *Low frequency dispersion in evaporated silicon oxide films*, Thin Solid Films, vol. 71, pp. 189-199 (1980).
- [129] S. Holten and H. Kliem, *Increased dielectric permittivity of SiO_2 thin films*, J. Appl. Phys., vol. 90, pp. 1941-1949 (2001).
- [130] S. Manzini and F. Volonta, *Charge transport and trapping in silicon nitride-silicon dioxide dielectric double layers*, J. Appl. Phys., vol. 58, pp. 4300-4306 (1985).

-
- [131] M. Homann and H. Kliem, *Relaxational polarization and charge injection in thin films of silicon nitride*, Microelectr. J., vol. 25, no. 7, pp. 559-566 (1994).
- [132] A. Wagner and H. Kliem, *Dispersive space charge relaxation in solid polymer electrolytes, I. Experimental system polyethylene oxide*, J. Appl. Phys., vol. 91, no. 10, p. 6630 (2002).
- [133] H. Kliem, B. Schumacher and G. Arlt, *Transient current measurements in polyimide*, IEEE CEIDP, pp. 168-173 (1986).
- [134] F. C. Aris and T. J. Lewis, *Steady and transient conduction processes in anodic tantalum oxide*, J. Phys. D, vol. 6, pp. 1067-1083 (1973).
- [135] R. M. Faria, B. Gross and G. F. L. Ferreira, *DC conduction and dielectric absorption in PVF₂*, J. Appl. Phys., vol. 55, p. 4130 (1984).
- [136] Y. Takase and A. Odajima, *γ -ray radiation-induced changes in switching current of PVDF*, Jpn. J. Appl. Phys., vol. 22, p. L318 (1983).
- [137] M. Sayer, A. Mansingh, J. M. Reyes and G. Rosenblatt, *Polaronic hopping conduction in vanadium phosphate glasses*, J. Appl. Phys., vol. 42, p. 2857 (1971).
- [138] H. Kliem, *Dielectric small-signal response by protons in amorphous insulators*, IEEE T. Electr. Insul., vol. 24, no. 2, pp. 185-197 (1989).
- [139] T. J. Lewis, *The dielectric behavior of non-crystalline solids*, in Dielectric and Related Molecular Processes, vol. 3, pp. 186-218 (1977).
- [140] M. Kuehn and H. Kliem, *Modelling non-exponential polarization relaxations in interacting dipole systems*, Phys. Status Solid B, vol. 243, no. 12, pp. 2913-2928 (2006).
- [141] A. Wagner and H. Kliem, *Dispersive ionic space charge relaxation in solid polymer electrolytes. II. Model and simulation*, J. Appl. Phys., vol. 91, no. 10, p. 6638 (2002).
- [142] B. Martin and H. Kliem, *The role of image charges in solid electrolyte capacitors*, in IEEE ICSD, vol. 1, pp. 17-20 (2004).
- [143] R. H. Cole, *Physics of dielectric solids*, in IOP Conf. Ser., no.58, p.1 (1980).

-
- [144] Y. Tajitsu, *Effects of thickness on ferroelectricity in vinylidene fluoride and trifluoroethylene copolymers*, Jpn. J. Appl. Phys., vol. 34, p. 5418 (1995).
- [145] H. von Seggern and S. N. Fedosov, *Conductivity-induced polarization buildup in poly(vinylidene fluoride)*, Appl. Phys. Lett., vol. 81, no. 15, p. 2830 (2002).
- [146] R. Gysel, I. Stolichnov, A. K. Tagantsev, N. Setter and P. Mokry, *Restricted domain growth and polarization reversal kinetics in ferroelectric polymer thin films*, J. Appl. Phys., vol. 103, no. 8, p. 084120 (2008).
- [147] H. Kliem and G. Arlt, *Transient reversible currents in MAOS structures*, in Insulating films on semiconductors, p. 211 (1983).
- [148] B. Martin, M. Kuehn and H. Kliem, *Interacting and noninteracting dipole systems in ferroelectric poly(vinylidene fluoride-trifluoroethylene) copolymer*, J. Appl. Phys., vol. 108, no. 8, p. 084109 (2010).
- [149] H. Kliem and G. Arlt, *Observation of non-linear relaxational polarization effects at high electric field strengths*, Solid State Commun., vol. 59, no. 2, pp. 793-795 (1986).
- [150] H. Kliem, *Non-linear dielectric response by protons in amorphous insulators*, Conf. Electri. Insul. Dielectr. Phenom., no. 1, pp. 81-86 (1992).
- [151] H. Froehlich, *Theory of dielectrics*, Oxford University Press (1949).
- [152] M. Kuehn and H. Kliem, *Monte Carlo simulations of ferroelectric properties based on a microscopic model for PVDF*, Phys. Status Solid B, vol. 245, no. 1, pp. 213-223 (2008).
- [153] H. Kliem, M. Kuehn and B. Martin, *The Weiss field revisited*, Ferroelectrics, vol. 400, no. 1, pp. 41-51 (2010).
- [154] H. Kliem and M. Kuehn, *Modeling the switching kinetics in ferroelectrics*, J. Appl. Phys., vol. 110, no. 11, p. 114106 (2011).
- [155] H. Kliem and F. Znidarsic, *Watersensitive conduction and charge relaxation in polyimide*, in CEIDP Ann. Rep., p. 89 (1991).

-
- [156] Y. Murata and N. Koizumi, *Anomalous discharge current in copolymers of vinylidene fluoride and trifluoroethylene*, IEEE Trans. Electr. Insul., vol. 24, no. 3, pp. 449-455 (1989).
- [157] J. Lindmayer, *Current transients in insulators*, J. Appl. Phys., vol. 36, no. 1, pp. 196-201 (1965).
- [158] S. Hashimoto, H. Orihara and Y. Ishibashi, *Study on D-E hysteresis loop of TGS based on the avrami-type model*, J. Phys. Soc. Jpn., vol. 63, p. 1601 (1994).
- [159] W. Li and M. Alexe, *Investigation on switching kinetics in epitaxial $Pb(Zr_{0.2}Ti_{0.8})O_3$ ferroelectric thin films: Role of the 90° domain walls*, Appl. Phys. Lett., vol. 91, p. 262903 (2007).
- [160] G. Vizdrik, S. Ducharme, V. Fridkin and S. Yudin, *Kinetics of ferroelectric switching in ultrathin films*, Phys. Rev. B, vol. 68, no. 9, pp. 1-6 (2003).
- [161] P. Weiss, *Sur la nature du champ moléculaire*, Archives des Sciences physiques et naturelles, vol. 37, p. 201 (1914).
- [162] P. Weiss, *Sur la Rationalité des rapports des moments magnétiques moléculaires et le Magneton*, Archives des Sciences physiques et naturelles, vol. 4, p. 401 (1911).
- [163] H. A. Lorentz, *The Theory of Electrons*. Teubner (1909).
- [164] M. Kuehn, V. M. Fridkin and H. Kliem, *Influence of an external field on the first order ferroelectric phase transition*, Ferroelectr. Lett. Sec., vol. 37, no. 3, pp. 55-59 (2010).
- [165] M. Kuehn and H. Kliem, *Phase transitions in the modified Weiss model*, Ferroelectrics, vol. 400, no. 1, pp. 52-62 (2010).
- [166] H. Kliem, *Strain induced change from second order to first order ferroelectric phase transition*, Ferroelectrics, vol. 425, no. 1, pp. 54-62 (2011).
- [167] H. Kliem, A. Leschhorn and T. Edbauer, *A model for the double loop of ferroelectric polarization close to T_c* , J. Appl. Phys., vol. 113, p. 104102 (2013).

-
- [168] M. Highland, T. Fister, M. I. Richard, D. Fong, P. Fuoss, C. Thompson, J. Eastman, S. Streiffer and G. Stephenson, *Polarization switching without domain formation at the intrinsic coercive field in ultrathin ferroelectric PbTiO₃*, Phys. Rev. Lett., vol. 105, no. 16, p. 167601 (2010).
- [169] C. F. Pulvari and W. Kuebler, *Polarization reversal in triglycine fluoberyllate and triglycine sulfate single crystals*, J. Appl. Phys., vol. 29, no. 12, p. 1742 (1958).
- [170] A. Leschhorn, *Private communication* (2012).
- [171] T. Nattermann, Y. Shapir and I. Vilfan, *Interface pinning and dynamics in random systems*, Phys. Rev. B, vol. 42, no. 13, p. 8577 (1990).
- [172] M. Kuehn and H. Kliem, *Monte carlo simulations of ferroelectric properties for PVDF and BaTiO₃*, Ferroelectrics, vol. 370, no. 1, pp. 207-218 (2008).
- [173] J. L. Martinez and J. A. Gonzalo, *Well behaved temperature dependence of the ferroelectric coercive field near T_c in T_{gs}*, Ferroelectrics, vol. 44, no. 1, p. 5 (1982).
- [174] T. Furukawa, *Phenomenological aspect of a ferroelectric vinylidene fluoride trifluoroethylene copolymer*, Ferroelectrics, vol. 57, pp. 63-72 (1984).
- [175] M. Poulsen, A. V. Sorokin, S. Adenwalla, S. Ducharme and V. M. Fridkin, *Effects of an external electric field on the ferroelectric-paraelectric phase transition in polyvinylidene fluoride-trifluoroethylene copolymer Langmuir-Blodgett films*, J. Appl. Phys., vol. 103, no. 3, p. 034116 (2008).
- [176] Q. M. Zhang, *Giant electrostriction and relaxor ferroelectric behavior in electron-irradiated poly(vinylidene fluoride-trifluoroethylene) copolymer*, Science, vol. 280, no. 5372, pp. 2101-2104 (1998).
- [177] J. Choi, C. N. Borca, P. A. Dowben, A. Bune, M. Poulsen, S. Pebley, S. Adenwalla, S. Ducharme, L. Robertson, V. M. Fridkin, S. P. Palto, N. N. Petukhova and S. G. Yudin, *Phase transition in the surface structure in copolymer films of vinylidene fluoride (70%) with trifluoroethylene (30%)*, Phys. Rev. B, vol. 61, no. 8, p. 5760 (2000).

-
- [178] S. Ducharme, A. Bune, L. Blinov, V. Fridkin, S. Palto, A. Sorokin and S. Yudin, *Critical point in ferroelectric Langmuir-Blodgett polymer films*, Phys. Rev. B, vol. 57, no. 1, pp. 25-28 (1998).
- [179] A. Leschhorn and H. Kliem, *Influence of the piezoeffect on static and dynamic ferroelectric properties*, J. Appl. Phys., vol. 114, p. 094105 (2013).
- [180] J. F. Scott, *Phase transitions in ferroelectric thin films*, Phase transit., vol. 30, p. 107 (1991).
- [181] D. R. Tilley, *Ferroelectrics*, Amsterdam: Gordon and Breach, pp. 11-45 (1996).
- [182] M. D. Glinchuk and A. N. Morozovska, *The internal electric field originating from the mismatch effect and its influence on ferroelectric thin film properties*, J. Phys.: Condens. Matt., vol. 16, no. 21, pp. 3517-3531 (2004).
- [183] A. Tolstousov, R. V. Gaynutdinov, R. Tadros-Morgane, S. G. Yudin, A. L. Tolstikhina, H. Kliem, S. Ducharme and V. M. Fridkin, *Ferroelectric properties of Langmuir-Blodgett copolymer films at the nanoscale*, Ferroelectrics, vol. 354, no. 1, pp. 99-105 (2007).
- [184] A. G. Zembilgotov, N. A. Pertsev, H. Kohlstedt and R. Waser, *Ultrathin epitaxial ferroelectric films grown on compressive substrates: Competition between the surface and strain effects*, J. Appl. Phys., vol. 91, no. 4, p. 2247 (2002).
- [185] A. Bratkovsky and A. Levanyuk, *Smearing of phase transition due to a surface effect or a bulk inhomogeneity in ferroelectric nanostructures*, Phys. Rev. Lett., vol. 94, no. 10, p. 107601 (2005).
- [186] C. Lichtensteiger, J. M. Triscone, J. Junquera and P. Ghosez, *Ferroelectricity and tetragonality in ultrathin $PbTiO_3$ films*, Phys. Rev. Lett., vol. 94, no. 4, p. 047603 (2005).
- [187] V. M. Fridkin, *Critical size in ferroelectric nanostructures*, Physics-Uspekhi, vol. 49, pp. 193-202 (2006).
- [188] C. G. Duan, S. Jaswal, and E. Tsymbal, *Predicted magnetoelectric effect in $Fe/BaTiO_3$ multilayers: Ferroelectric control of magnetism*, Phys. Rev. Lett., vol. 97, no. 4, p. 047201 (2006).

-
- [189] J. F. Scott, *Ferroelectric Memories*. Berlin: Springer (2000).
- [190] V. Fridkin, M. Kuehn and H. Kliem, *The Weiss model and the Landau-Khalatnikov model for the switching of ferroelectrics*, Phys. B: Condens. Matt., vol. 407, no. 12, pp. 2211-2214 (2012).
- [191] M. Mai, B. Martin and H. Kliem, *Polarization relaxation and charge injection in thin films of poly(vinylidene fluoride/trifluoroethylene) copolymer*, J. Appl. Phys., vol. 114, no. 5, p. 054104 (2013).
- [192] M. Mai, V. Fridkin, B. Martin, A. Leschhorn and H. Kliem, *The thickness dependence of the phase transition temperature in PVDF*, Phys. B: Condens. Matt., vol. 421, pp. 23-27 (2013).
- [193] A. M. Bratkovsky and A. P. Levanyuk, *Depolarizing field and 'real' hysteresis loops in nanometer-scale ferroelectric films*, Appl. Phys. Lett., vol. 89, no. 25, p. 253108 (2006).
- [194] A. M. Bratkovsky and A. P. Levanyuk, *Very large dielectric response of thin ferroelectric films with the dead layers*, Phys. Rev. B, vol. 63, no. 13, p. 132103 (2001).
- [195] G. Durin and S. Zapperi, *The Barkhausen effect*, arXiv: cond-mat/0404512v1 [cond-mat.mtrl-sci] (2004).
- [196] V. S. Rumyantsev and V. M. Rudyak, *Domain restructurization in ferroelectrics within the transition range*, Fizika, no. 5, pp. 122-124 (1975).
- [197] A. G. Chynoweth, *Barkhausen pulses in barium titanate*, Phys. Rev., vol. 110, no. 6, p. 1316 (1958).
- [198] V. M. Rudyak, A. Y. Kudzin and T. V. Panchenko, *Barkhausen jumps and stabilization of the spontaneous polarization of single crystals of BaTiO₃*, Sov. Phys. Solid State, vol. 14, p. 2112 (1973).

Publications

Articles

1. **Manfang Mai**, Bjoern Martin and Herbert Kliem, *Polarization relaxation and charge injection in thin films of poly(vinylidene fluoride/trifluoroethylene) copolymer*, J. Appl. Phys., 114, 5, 054104 (2013).
2. **Manfang Mai**, Vladimir Fridkin, Bjoern Martin, Andreas Leschhorn and Herbert Kliem, *The thickness dependence of the phase transition temperature in PVDF*, Phys. B: Condens. Matt., 421, 23 (2013).
3. Bjoern Martin, **Manfang Mai** and Herbert Kliem, *Broadband dielectric dispersion in ferroelectric P(VDF-TrFE) copolymer film*, Phys. B: Condens. Matt., 407, 4398 (2012).
4. **Manfang Mai**, Bjoern Martin and Herbert Kliem, *Ferroelectric switching in Langmuir-Blodgett and spin-coated thin films of poly(vinylidene fluoride/trifluoroethylene) copolymers*, J. Appl. Phys., 110, 6, 064101 (2011).
5. Bjoern Martin, **Manfang Mai** and Herbert Kliem, *Broadband dielectric relaxation spectra of PVDF copolymer films*, J. Phys.: Conf. Ser., 310, 012001 (2011).
6. **Manfang Mai** and Herbert Kliem, *Observation of thermal Barkhausen effect in ferroelectric films of P(VDF-TrFE) copolymer*, accepted by J. Appl. Phys..
7. **Manfang Mai**, Andreas Leschhorn and Herbert Kliem, *The field and temperature dependence of hysteresis loop in P(VDF-TrFE) copolymer films*, to be submitted.

8. **Manfang Mai**, Andreas Leschhorn, Bjoern Martin and Herbert Kliem, *Switching current characteristics in ferroelectric films of P(VDF-TrFE) copolymer*, to be submitted.

Conference contributions

1. 22st IEEE International Symposium on Applications of Ferroelectrics (ISAF), Prague, Czech Republic, 2013.
Poster: **Manfang Mai**, Andreas Leschhorn and Herbert Kliem, *The frequency and temperature dependence of hysteresis loop in P(VDF-TrFE) copolymer films*.
2. 21st IEEE International Symposium on Applications of Ferroelectrics (ISAF), Aveiro, Portugal, 2012.
Talk: **Manfang Mai**, Andreas Leschhorn, Bjoern Martin and Herbert Kliem, *Polarization switching current in ferroelectric films of P(VDF-TrFE) copolymers*.
3. International Symposium on Integrated Functionalities (ISIF), Cambridge, UK, 2011.
Talk: **Manfang Mai**, Bjoern Martin and Herbert Kliem, *Polarization relaxation and charge injection in thin films of P(VDF-TrFE) copolymer*.
4. German Physical Society 75th annual spring meeting (DPG), Dresden, Germany, 2011.
Talk: **Manfang Mai**, Bjoern Martin and Herbert Kliem, *Comparative study of ferroelectric properties in Langmuir-Blodgett and spin-coated thin films of poly(vinylidene fluoride/trifluoroethylene) copolymers*.

Acknowledgments

I would like to first acknowledge the support of my supervisor, Prof. Herbert Kliem. I want to thank him for guidance throughout the years and for all the hardwork that made my research possible. Prof. Kliem can always grasp the essentials and suggest new ideas. The questions he asked made me think further and beyond. I have learned so much in the valuable discussions with him. His passion and preciseness for science have a great influence on my academic life.

I would like to thank Dr. Björn Martin for his help and guidance. I could not have asked for a better mentor and a colleague. I am truly indebted to him for his generosity in teaching me so much about equipments and research. I am also grateful to Robert Florange for the technical help. There has not been one time that Robert has not helped me. I also want to thank Gudrun Vogelgesang for the administrative help, and being very kind to me.

I would like to thank all my colleagues in institute of electrical engineering physics, both past and present: Dr. Markus Kühn, Dr. Andreas Leschhorn, Dr. Gennady Vizdrik, Tobias Edtbauer, Nina Reifferscheid, Dr. Laxman Kantkate, Christian Peter and Dishant Kumar. My special thanks go to Markus for his help and friendship. Markus has a great sense of humor, and the rivaled qualities are his intellect and kindness. I would like to thank Andreas for many fruitful discussions on the theories. Andy is a limitless source of knowledge in both science and history. I want to thank Dr. Gennady Vizdrik for his introduction on the Langmuir-Blodgett technique. I also want to thank Prof. Vladimir Fridkin for his generous advice and encouragement. Tobias was always being extremely kind to me. Nina, my former officemate, is a strong and amazing woman. I would like to thank Laxman and Christian for introducing the culture of their countries. It has been my pleasure working with all of you. I enjoyed all the talks and laughs at lunch time, and after. Those are good memories. I will surely miss it, a lot.

Acknowledgments

I would like to thank China Scholarship Council for the financial support.

Finally, I would like to thank my parents for their unconditional love and never-ending support. Without their love and support, I would have not come this far. I also would like to thank my husband, Dr. Xinzhou Ma, for his love, support and understanding. Thanks Xinzhou, for great advice and encouragement. Thank you for reminding me to eat good food and keep in good spirits. Thank you so much for always being there for me.